2017 Workshop on Innovative Nanoscale Devices and Systems

WINDS

Booklet of Abstracts

Edited by
Kazuhiko Matsumoto
Berry Jonker
Josef Weinbub
Tomoki Machida
Siegfried Selberherr
Stephen Goodnick

Hapuna Beach Prince Hotel
Kohala Coast, Hawaii, USA

November 26 - December 1, 2017

2017 Workshop on Innovative
Nanoscale Devices and Systems

WINDS

2017
Booklet of Abstracts

Hapuna Beach Prince Hotel
Kohala Coast, Hawaii, USA

November 26 - December 1 , 2017

ISBN 978-3-901578-31-1

c/o Technische Universität Wien
Gußhausstraße 27-29, 1040 Wien, Austria

Preface

The **Workshop on Innovative Nanoscale Devices and Systems (WINDS)** is a week long symposium of morning and evening sessions, with afternoons free for ad hoc meetings to encourage extended interaction and discussion among participants. This annual workshop is the successor of the original WINDS and the International Symposium on Advanced Nanodevices and Nanotechnology (ISANN), which were held on alternate years. This merging of the two allows for a single international conference to be held each year in Hawaii in late November or early December. WINDS itself began as an outgrowth of the successful Advanced Heterostructures Workshop, which has a long history dating from the 1980s. In 2008, the name changed from AHW to WINDS in order to recognize the importance of nanotechnology in general, and the applications to systems.

Every nanoscale device today is a heterostructure of one form or another. The properties of the interfaces often determine the functionality and properties of the nanoscale system. WINDS is an international, interactive workshop designed to explore the fundamental properties of such nanoscale heterostructures and potential device applications. This year the program includes two special sessions, i.e., 2D materials session organized by Berry Jonker, and quantum computing session by Koji Ishibashi and Matthew Gilbert.

WINDS2017 was supported by American Vacuum Society (AVS) and Japan Science and Technology Agency (JST). We greatly appreciate their support to WINDS 2017.

Conference Committee

General Chair
Kazuhiko Matsumoto
Osaka University
Japan

US Co-Chair
Berry Jonker
Naval Research Laboratories
USA

Europe Co-Chair
Josef Weinbub
Technical University Vienna
Austria

Japan CO-Chair
Tomoki Machida
University of Tokyo
Japan

Publication-Chair
Siegfried Selberherr
Technical UniversityVienna
Austria

Local Arrangements
Stephen Goodnick
Arizona State University
USA

Sponsored Topical Conference
www.avs.org

Program Committee Members

- Alex Balandin, University California, Riverside, USA
- John F. Conley, Oregon State University, USA
- David Ferry , Arizona State University, USA
- Matthew Gilbert, University of Illinois, USA
- Stephen Goodnick, Arizona State University, USA
- Koji Ishibashi, RIKEN, Japan
- David Janes, Purdue University, USA
- Berry Jonker, U.S. Naval Research Laboratories, USA
- Akinobu Kanda, University of Tsukuba, Japan
- Viktor I Klimov, Los Alamos National Laboratory, USA
- Tomoki Machida,The University of Tokyo, Japan
- Kazuhiko Matsumoto, Osaka University, Japan
- Wolfgang Porod, University of Notre Dame, USA
- Mark Reed,Yale University, USA
- Henning Riechert, Paul Drude Institute, Germany
- Siegfried Selberherr, Technical University Vienna, Austria
- Viktor Sverdlov, Technical University Vienna, Austria
- Josef Weinbub, Technical University Vienna, Austria

November 26th 2017（Sunday）

Registration （15:00-18：00）

Welcome Reception （18:00-20：00）

November 27th 2017 （Monday）

8:30-8：45	**Welcome Address** （**Kazuhiko Matsumoto, Stephen Goodnick**）	

Session 2D Materials (Berry Jonker, Tomoki Machida)

8：45-9:15	**Curt A. Richter** (NIST, USA) “Landau Level Edge-State Transport in Graphene p-n Junctions in the Quantum Hall Regime”	1
9：15-9:45	**Xiang Zhang** (University of California, Berkeley, USA) “Discovery of Intrinsic Ferromagnetism in Two-Dimensional van der Waals Crystals”	3
9：45-10:00	**Tomoki Machida** (The University of Tokyo, Japan) “Quantum Transport and Optoelectronic Application in van der Waals Junctions of 2D Materials”	5
10:00-10:30	**A. Nick Vamivakas** (University of Rochester, USA) “Quantum Photonics with van der Waals Heterostructures”	7
10:30-10:45	**Coffee Break**	
10:45-11:15	**Deep Jariwala** (California Institute of Technology, USA) “Ultrathin van der Waals Photovoltaics”	9
11:15-11:30	**Berry Jonker** (Naval Research Laboratory, USA) “Ferroelectric Domain Control of Photoluminescence in Monolayer WS$_2$ / PZT Hybrid Structures”	11
11:30-11:45	**Athos Petrou** (State University of New York, Buffalo, USA) “Exchange Field Induced Valley Splitting Enhancement in WSe$_2$ and WS$_2$”	13
11:45-12:00	**Richard C. Ordonez** (Space and Naval Warfare Systems Center Pacific, USA) “Adaptive Control of Graphene Surface Charge Distribution with Suspended Gates in an Electrolytic Gate Dielectric”	15

Session Solar Cell (Stephen Goodnick)

12:00-12:30	**Joseph M. Luther** (National Renewable Energy Laboratory, USA) “Quantum Dots and Perovskites – Realizing the Best of Both Worlds for Revolutionary Optoelectronic Applications”	17
12:30-12:45	**Stephen Goodnick** (Arizona State University, USA) “InGaN Multi-Quantum Well Solar Cells for High Temperature Applications”	19
12:45-13:15	**Masakazu Sugiyama** (The University of Tokyo, Japan) “InGaAs/GaAsP Quantum Well Superlattice for 1.15-eV Middle Cell in 4-Junction Solar Cell”	21
13:15-13:30	**Takeyoshi Sugaya** (AIST, Japan) “High-Efficiency Heterogeneous Multijunction Solar Cells Fabricated by Smart Stack Technology Using Metal Nanoparticle Arrays”	23

Ad hoc Session

Session Oxide & THz (Kazuhiko Matsumoto)

19:00-19:30	**Alexander A. Demkov** (The University of Texas, Austin, USA) “Integrated Oxide Heterostructures for Electronics and Photonics”	25
19:30-20:00	**Masataka Higashiwaki** (NICT, Japan) “Recent Achievements in Ga$_2$O$_3$ MOSFET Technology”	27
20:00-20:15	**Taiichi Otsuji** (Tohoku University, Japan) “Terahertz Light Emission and Lasing in Graphene-Based van der Waals 2D Heterostructures”	29
20:15-20:30	**Victor Ryzhii** (Tohoku University, Japan) “Concepts of Infrared and Terahertz Photodetectors Based on van der Waals Heterostructures with Graphene Layers”	31
20:30-21:00	**Jeremy Levy** (University of Pittsburgh, USA) “Quantized Ballistic Transport of Electrons and Electron Pairs in an Electron Waveguide”	33
21:00-21:15	**Ya Zhang** (The University of Tokyo, Japan) “Enhanced Sensitivity of MEMS-based Terahertz Bolometers by Introducing Two-Dimensional Phononic Crystal Structures”	35
21:15-21:30	**Shiro Kawabata** (AIST, Japan) “Thermal Manipulation of THz Wave from High-Tc Superconducting Emitters”	37

November 28th 2017（Tuesday）

Session 2D Materials & Quantum Dot (Taiichi Otsuji)

8:30-9：00	**Hui Zhao** (University of Kansas, USA) "Ultrafast Electron Transfer in van der Waals Multilayers"	39
9:00-9：30	**Yasumitsu Miyata** (Tokyo Metropolitan University, Japan) "Semiconductor Heterojunctions Based on 2D Materials"	41
9:30-9:45	**Victor I. Klimov** (Los Alamos National Laboratory, USA) "Recent Advances in Colloidal-Quantum-Dot Lasing: From Zero-Threshold Optical Gain to Solution-Processible Laser Diodes"	43
9:45-10:00	**Akira Oiwa** (Osaka University, Japan) "Electrical Transport Though a SiGe Self-Assembled Quantum Dot"	45
10:00-10:30	**Saptarshi Das** (Pennsylvania State University, USA) "2D Materials for Ubiquitous Electronics"	47
10:30-10:45	**Coffee Break**	

Session 2D Materials & Quantum Computing (Viktor I Klimov)

10:45-11:15	**Hiroki Takesue** (NTT Corporation, Japan) "A Coherent Ising Machine for Solving Combinatorial Optimization Problems"	49
11:15-11:30	**Kouichi Semba** (NICT, Japan) "Superradiance Phase Transition in the Presence of Parameter Fluctuations"	51
11:30-12:00	**Robert A. Wolkow** (University of Alberta /National Research Council / Quantum Silicon, Inc.,Canada) "Binary Atomic Silicon Logic for WINDS 2017"	53
12:00-12:15	**Susumu Okada** (University of Tsukuba, Japan) "Band-Gap Engineering of Graphene Heterostructures via Substitutional Doping with B_3N_3"	55
12:15-12:30	**Atsushi Ando** (AIST, Japan) "Surface Modification Processes of Transition Metal Dichalcogenides for Field-Effect-Transistor Fabrication"	57
12:30-13:00	**Shintaro Sato** (Fujitsu Laboratories Ltd., Japan) "Application of Graphene and Graphene Nanoribbons to Electronic Devices"	59
13:00-13:15	**Taichi Inoue** (Osaka Prefecture University, Japan) "MoS_2/Graphene Stacked Electromechanical Resonator"	61
13:15-13:30	**Felix Jaetae Seo** (Hampton University, USA) "A Single Atom Shift in 2D MoS_2 Supercell"	63

Ad hoc Session

Session Molecular & Quantum Dot (David Janes)

19:00-19:30	**Naoya Fukui** (The University of Tokyo, Japan) "Electronic Properties and Charge Transport of Coordination Nanosheet (CONASH)"	65
19:30-19:45	**Yoshio Aso** (Osaka Uviversity, Japan) "Development of Electron-Accepting π-Conjugated Units for Organic Electronics"	67
19:45-20:00	**David B. Janes** (Purdue University, USA) "Real-Time Measurements of Hydrogen Peroxide Uptake in 2D Cell Cultures Using On-Chip Microelectrode Arrays"	69
20:00-20:30	**Changhee Lee** (Seoul National University, Korea) "Recent Progress in Quantum Dot LEDs and Their Future Prospects for Displays"	71
20:30-20:45	**William S. Wong** (University of Waterloo, Canada) "Electrical and Optical Characteristics of Nanowire LEDs Under Mechanical Bending"	73
20:45-21:00	**Andrew Sachrajda** (National Research Council, Canada) "Properties of A Few Hole Gated Double Quantum Dot"	75
21:00-21:30	**Alexei O. Orlov** (University of Notre Dame, USA) "Metal-Insulator-Metal Single Electron Tunneling Transistors Featuring Non-Native Dielectrics"	77

November 29th 2017（Wednesday）

Session Spin & Nano Magnet (Josef Weinbub, Wolfgang Porod, Siegfried Selberherr)

8:30-9：00	**Roland K. Kawakami** (The Ohio State University, USA) “Optospintronics and 2D Magnets”	79
9：00-9：15	**Alexander Khitun** (University of California,Riverside, USA) “Magnetometer Based on Spin Wave Interferometer”	81
9：15-9：30	**Jaroslav Fabian** (University of Regensburg, Germany) “Field-Effect Spin-Orbit Valve and Spin Transistor Based on Proximity Bilayer Graphene”	83
9：30-10：00	**Masashi Shiraishi** (Kyoto University, Japan) “Spin Current Propagation in a 2-Dimensional Electron Gas”	85
10：00-10：15	**Siegfried Selberherr** (TU Wien, Austria) “Current in Magnetic Tunnel Junctions at Spin-Dependent Hopping”	87
10：15-10：30	**Igor Žutić** (University at Buffalo, SUNY, USA) “Magnetic Proximity Effects in Two-Dimensional Materials”	89
10：30-10：45	**Coffee Break**	
10：45-11：15	**Richard Kiehl** (Arizona State University, USA) “Proximity Induced Ferromagnetism in Graphene from a Magnetic-Nanoparticle Array”	91
11：15-11：30	**Viktor Sverdlov** (TU Wien, Austria) “A Single-Spin Switch”	93
11：30-11：45	**Ece Aytan** (University of California, Riverside, USA) “Ultraviolet Raman Spectroscopy of NiO: Spin – Phonon Interactions and Implications for Antiferromagnetic Spintronics”	95
11：45-12：15	**Scott Crooker** (Los Alamos National Laboratory, USA) “Light, Spin, and Magnetization in Magnetically-Doped Semiconductor Nanocrystals”	97
12：15-12：30	**Giorgos Giavaras** (University of Tsukuba, Japan) “Spin Resonance in Spin-Orbit-Coupled Quantum Dots in the Weak and Strong Driving Regimes”	99
12:30-12：45	**David K. Ferry** (Arizona State University, USA) “Landauer and NEGF: Plain Talk on the Proper Approach”	101
12：45-13：00	**Slava V. Rotkin** (The Pennsylvania State University, USA) “Novel Polaritonic Modes in Subwavelength Antenna:Applications for Nanotube Plasmonic Sensing”	103
13：00-13：15	**Josef Weinbub** (TU Wien, Austria) “Classical and Quantum Electron Evolution with a Repulsive Dopant”	105
13：15-13：45	**Roman M. Lutchyn** (Station Q, Microsoft Research, Santa Barbara, USA) “Coulomb Blockade Effect in Proximitized Nanowires”	107

Ad hoc Session

Banquet at Night（18:30-21：00）

November 30th 2017（Thursday）

Session Topological (John F.Conley)

8:30-9:00 **Junji Tominaga** (AIST, Japan) ········ 109
"Chalcogenide Phase Change Device with Topological Functionalities"

9:00-9:15 **Taylor L. Hughes** (University of Illinois at Urbana-Champaign, USA) 111
"Topological Quadrupole and Octupole Insulators"

9:15-9:30 **Satoshi Fujimoto** (Osaka University, Japan) ········ 113
"Geometrically-Induced Transport Phenomena in Weyl Semimetals and Weyl Superconductors"

9:30-10:00 **Masashi Kawasaki** (The University of Tokyo, Japan) ········ 115
"Quantum Transport in Heterostructured Topological Materials"

10:00-10:15 **Walter Pötz** (Karl-Franzens University of Graz, Austria) ········ 117
"Pure- and Mixed-State Simulation of Dirac Fermion Dynamics in Electromagnetic Textures"

10:15-10:30 **Nina Markovic** (Johns Hopkins University, USA)··········· ··· 119
"Patterning Superconductivity in a Topological Insulator"

10:30-10:45 **Coffee Break**

Session Topological & Nano Magnet (Viktor Sverdlov)

10:45-11:15 **Axel Hoffmann** (Argonne National Laboratory, USA) ········ 121
"Topological Quasiparticles: Magnetic Skyrmions"

11:15-11:30 **Vito Scarola** (Virginia Tech, USA) ········ 123
"Topological Mott Insulators in Certain Frustrated Lattices"

11:30-11:45 **Wolfgang Porod** (University of Notre Dame, USA) ········ 125
"Towards Low-Damping Spin-Wave Media for Magnonics"

11:45-12:15 **Edoardo Albisetti** (City University of New York, USA / Politecnico di Milano, Italy) 127
"Towards Reconfigurable Nanomagnonic Devices Based on Patterned Spin-Textures"

12:15-12:30 **Goran Rasic** (North Carolina Central University, USA) ········ 129
"Surface Patterned Magnetic Thin Films for Multiferroic and Exchange Bias Device Application"

12:30-12:45 **Ewelina Hankiewicz** (Würzburg University, Germany) ········ 131
"Transport in Topological Insulators and Topological Superconductors"

12:45-13:00 **Leonid P. Rokhinson** (Purdue University, USA) ········ 133
"Development of a New Platform to Realize High Order Non-Abelian Excitations"

13:00-13:15 **John F. Conley, Jr.** (Oregon State University, USA) ········ 135
"High-Voltage Al_2O_3/Ta_2O_5 Heterostructure Metal/Insulator/Insulator/Metal (MIIM) Diodes"

Ad hoc Session

Poster Session (19:00-21:30)

November 30th 2017（Thursday） Continued 1/2

Poster Session (19:00-21:30)

P-1 **Dragica Vasileska** (Arizona State University, USA) ······ 137
"Cu Migration During Light-Soaking Experiments"

P-2 **Takuya Igarashi** (Tohoku University, Japan) ······ 139
"Computational Analysis of Chemical Mechanical Polishing Process for GaN Substrate with Step Structure"

P-3 **Naoki Takahashi** (Tohoku University, Japan) ······ 141
"Molecular Dynamics Study on Chemical Wear Process of Amorphous Silica in Humidity Environment"

P-4 **Miho Nakamura** (Tohoku University, Japan) ······ 143
"Effect of Tribochemical Reactions on Super-Low Friction Properties of Carbon Nitride Thin Films as Investigated by Tight-Binding Quantum Chemical Molecular Dynamics Simulations"

P-5 **Haruka Omachi** (Nagoya University, Japan) ······ 145
"Oxidative Degradation of Carbon Nanotubes and Extraction of Encapsulated 1D Materials"

P-6 **Tomohiro Yamaguchi** (RIKEN, Japan) ······ 147
"Tunnel Barrier Formation in Suspended Multi-Walled Carbon Nanotubes by Ga Focused Ion Beam Irradiation."

P-7 **Shinichi Hirose** (Fujitsu Laboratories Ltd., Japan) ······ 149
"High Thermal Conductivity of Carbon Nanotube Sheets for Future Thermal Interface Materials"

P-8 **Manaho Matsubara** (University of Tsukuba, Japan) ······ 151
"Geometric Structures of Al Nanoparticles Adsorbed on Graphene Under an External Electric Field"

P-9 **Mina Maruyama** (University of Tsukuba, Japan) ······ 153
"Coexistence of Dirac Cones and Kagome Flat Bands in Porous Graphene"

P-10 **Yanlin Gao** (University of Tsukuba, Japan) ······ 155
"Electrostatic Potential Properties of Edge-Functionalized Graphene Nanoribbon Under the External Electric Field"

P-11 **Hideyuki Jippo** (Fujitsu Laboratories Ltd., Japan) ······ 157
"Bottom-Up Approach for Edge-Fluorinated Graphene Nanoribbons"

P-12 **Nguyen Thanh Cuong** (NIMS/University of Tsukuba, Japan) ······ 159
"High Thermoelectric Power in B_3N_3-doped Graphene"

P-13 **Eun Kyu Kim** (Hanyang University, Korea) ······ 161
"Controllable Tunneling of Electron and Hole in van der Waals Assembly"

P-14 **Chang-Soo Park** (Hanyang University, Korea) ······ 163
"Ferromagnetic and Semiconducting Properties from Cobalt Oxide Adsorbed Graphene"

P-15 **Yuhei Takaguchi** (Tokyo Metropolitan University, Japan) ······ 165
"Electric Double Layer Light Emitting Diode of $WSe_2/MoSe_2$ In-Plane Heterostructures"

P-16 **Shintaro Yoshimura** (Tokyo Metropolitan University, Japan) ······ 167
"Growth and Characterization of Re-Doped MoS_2 Monolayers"

P-17 **Yu Kobayashi** (Tokyo Metropolitan University, Japan) ······ 169
"Growth and Characterization of Transition Metal Dichalcogenides Using Halide-Assisted MOCVD"

P-18 **Felix Jaetae Seo** (Hampton University, USA) ······ 171
"Cubic Nonlinearity of Transition Metal Dichalcogenides Atomic layer"

P-19 **Felix Jaetae Seo** (Hampton University, USA) ······ 173
"Phonon and Intensity induced Exciton Dephasing of TMDC Atomic Layer"

P-20 **Felix Jaetae Seo** (Hampton University, USA) ······ 175
"Piezoelectricity of 2-Dimensional MoS_2/WSe_2 Heterostructure"

November 30th 2017（Thursday） Continued 2/2

Poster Session (19:00-21:30) Continued

P-21 **Yasuhide Ohno** (Tokushima University, Japan) ······ 177
“Electrical Characteristics of Positively and Negatively Charged Protein Adsorption to Epitaxial Graphene Film on SiC Substrate”

P-22 **Guram T. Adamashvili** (Technical University of Georgia, Georgia) ······ 179
“Surface Resonance Soliton in Phosphorene”

P-23 **Daiki Yoshikawa** (Osaka Prefecture University, Japan) ······ 181
“Amplitude Control of MoS_2 Cantilever by Electrostatic Driving”

P-24 **David B. Janes** (Purdue University, USA) ······ 183
“Universality of Self-Heating in Disordered Transparent Conductor Networks”

P-25 **Ryuji Takahashi** (RIKEN, Japan) ······ 185
“Landau-Zener Tunneling Problem for Particles in Periodic Systems”

P-26 **Tomosuke Aono** (Ibaraki University, Japan) ······ 187
“Nuclear Spin Polarization and Resistively-Detected Nuclear Magnetic Resonance in Quantum Point Contact”

P-27 **Walter Pötz** (Karl-Franzens University of Graz, Austria) ······ 189
“Numerical Simulation of s- and p-Wave Superconductor Heterostructures within the (1+1)D Bogoliubov-de Gennes Equation”

P-28 **Aymen Yangui** (The University of Tokyo, Japan) ······ 191
“Thermionic Cooling Devices Based On AlGaAs/GaAs Heterostructures”

P-29 **Yasuyuki Sanari** (Kyoto University, Japan) ······ 193
“Field-Induced Crystallization of $Ge_2Sb_2Te_5$ Amorphous Studied by Strong THz Pulses”

P-30 **Peng Zhang** (Michigan State University, USA) ······ 195
“Inverse Tunneling of Free Vacuum Electrons into a Solid”

P-31 **Yasushi Shoji** (The University of Tokyo, Japan) ······ 197
“Growth and Characterization of GaSb Quantum Nanostructures by Solid-Source Molecular Beam Epitaxy”

P-32 **Sim-Hoon Youk** (SPRC, Chonbuk National University, Korea) ······ 199
“Effect of Sulfur Passivation Using Aqueous and Alcoholic Ammonium Sulfide Solutions on the Specific Contact Resistivity of Ni Contact to InAs Layer Epitaxially Grown on $In_{0.56}Ga_{0.47}As$ Epilayer.”

P-33 **Han-Soo Jang** (SPRC, Chonbuk National University, Korea) ······ 201
“Microstructural and Electrical Properties of Ni Stanogermanides Formed on $Ge_{0.92}Sn_{0.08}$ Epi-Layer Grown on Si(100) Substrate”

P-34 **Katsuhisa Yoshida** (The University of Tokyo, Japan) ······ 203
“Numerical Study of Quantum Efficiency of Quantum-Dot Intermediate-Band Solar Cells under Infrared Light Illumination”

P-35 **Jongsoon Park** (Samsung Electronics / Sungkyunkwan University, Republic of Korea) ······ 205
“A Method of Predicting Pattern with Etch Rate of Non-Pattern Wafer Using Ion Beam Etching”

December 1st 2017（Friday）

Session Quantum Computing (Koji Ishibashi, Matthew Gilbert)

8:30-9:00	**Gregory D. Fuchs** (Cornell University, USA) …… “Quantum Control Over Diamond Qubits Using a Mechanical Resonator”	207
9:00-9:15	**Matthew J. Gilbert** (University of Illinois,USA) …… “Modular Anomalies in (2+1) and (3+1)-Dimensional Edge Theories”	209
9:15-9:45	**Satoshi Moriyama** (NIMS, Japan) …… “Quantum Dots and Spin Qubits based on Silicon Tunnel Field-effect Transistors”	211
9:45-10:00	**Fumiki Yoshihara** (NICT, Japan)…… “Superconducting Qubit-Oscillator Circuit Beyond the Ultrastrong-Coupling Regime”	213
10:00-10:30	**Thomas Schäpers** (JARA-FIT Jülich-Aachen Research Alliance, Germany) …… “Helical States and Spin-Orbit Coupling in InAs Nanowire-Based Devices”	215
10:30-10:45	**Coffee Break**	
10:45-11:00	**Koji Ishibashi** (RIKEN, Japan) …… “Nanowire Quantum Dots Coupled with a Superconducting Microwave Resonator”	217
11:00-11:15	**Yukimi Kanai** (Nara Women’s University, Japan) …… “Full Counting Statistics Theory for Cross Correlation of Quantum Entanglement Current Noise in Double S/N/N Capacitively-Coupled Single Electron Transistor with Ohmic Impedance in Coulomb Blockade Regime”	219
11:15-11:30	**Denis Mamaluy** (Sandia National Laboratories, USA) …… “Beyond Moore’s Computing (BMC): Fundamental Downscaling Limit of Field-effect Transistors and New Possibilities for Continued Increase of Computing Power”	221

Session Roughness & Friction (Matthew Gilbert)

11:30-11:45	**Dragica Vasileska** (Arizona State University, USA) …… “The Role of Interface Roughness on the Electron Mobility in Nanoscale Devices: A Green’s Function Approach”	223
11:45-12:00	**Fumiya Nakamura** (Tohoku University, Japan) …… “Study on Low Friction of Silicon Carbide under Water Lubrication: Molecular Dynamics Analysis”	225
12:00-12:15	**Closing Remarks**	

Landau level edge-state transport in graphene p-n junctions in the quantum Hall regime

Curt A. Richter[1], Son T. Le[1,2], Joseph A. Hagmann[1], Nikolai Klimov[1], Ji Ung Lee[3],
and David Newell[1]

[1] *Physical Measurement Laboratory, NIST, Gaithersburg, Maryland 20899, USA*
[2] *Theiss Research, San Diego, California, USA*
[3] *College of Nanoscale Engineering, SUNY Polytechnic Institute, Albany, New York, USA*
e-mail: curt.richter@NIST.gov

The graphene pn junction (pnJ) is a promising building block for future graphene electronics [1]. Several interesting transport phenomena are predicted for graphene pnJ's owing to the massless Dirac property of carriers including Klein tunneling [2] and Veselago lensing [3]. By harnessing the fundamental physical properties of graphene pnJ's, with their marked difference from conventional semiconductor pnJs, applications are enabled ranging from ultralow power electronics [1] to multi-state, voltage-controlled quantum resistance standards [4,5].

We report on the interaction of quantized Landau level (LL) edge-states in graphene PN junction devices at both the electrostatically defined PN junction and the physical edge of the graphene. In order to probe the transport behavior of charge carriers in graphene at these physically different interfaces, experimental magneto-transport measurements were made on a single graphene pnJ device embedded within a Hall bar geometry (Fig. 1) and a double pnJ device with a ring shape geometry (Fig. 2) in the quantum Hall regime. When analyzed with a Landauer-Buttiker edge-state formalism [6], our measurements show that, while the lowest LL edge state is decoupled from the other LL's at the electrostatic junction [5], all of the LL edge states strongly equilibrate along the physical edge of the graphene despite the relatively short distance that they travel along this edge. Figs. 1 (b) and 2 (b) show edge state schematics and Figs. 1 (d) and 2 (d) show calculated resistance values. The ability to tune and understanding LL edge state interactions enables a new degree of freedom to fine tune quantum Hall resistance values for scalable resistance standard applications.

[1] R. N. Sajjad and A. W. Ghosh, Appl. Phys. Lett. **99**, 123101 (2011).
[2] A. F. Young and P. Kim, Nat. Phys. 5, 222 (2009).
[3] V. V. Cheianov, V. Fal'ko, and B. L. Altshuler, Science 315, 1252 (2007).
[4] M. Woszczyna et al., Appl. Phys. Lett. **99**, 022112 (2011).
[5] Nikolai N. Klimov, Son T. Le et al., Phys. Rev. B, **92**, 241301(R) (2015).
[6] M. Buttiker, Phys. Rev. Lett. 57, 1761 (1986).

978-3-901578-31-1

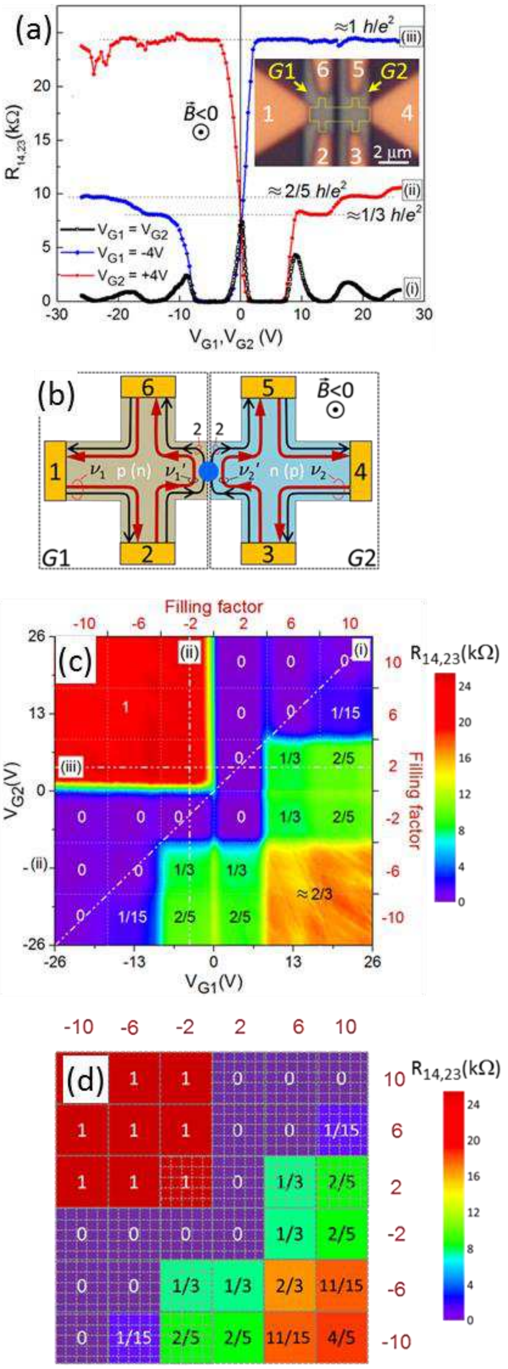

	-10	-6	-2	2	6	10
10	(d)	1	1	0	0	0
6	1	1	1	0	0	1/15
2	1	1	1	0	1/3	2/5
-2	0	0	0	0	1/3	2/5
-6	0	0	1/3	1/3	2/3	11/15
-10	0	1/15	2/5	2/5	11/15	4/5

Fig.1: One pnJ Hall bar device (a) Longitudinal resistance $R_{14,23}$ measured at $T = 0.35$ K and $B = -14$ T as a function of local gate voltages V_{G1} and V_{G2}; insert: Optical image of graphene pnJ device in a Hall-bar geometry outlined in yellow. (b) Schematic of edge-state transport model of longitudinal resistance $R_{14,23}$ in the quantum Hall regime. Model in which only the lowest Landau level edge states on opposite sides of the pnJ equilibrate. Blue dot schematically indicates the region of edge-state equilibration. (c) 2D projection of longitudinal resistance $R_{14,23}$ measured at $T = 0.35$ K and $B = -14$ T as a function of (V_{G1}, V_{G2}) and filling factors (ν_1, ν_2). (d) Calculated 2D resistance map of $R_{14,23}$ as a function of filling factors (ν_1, ν_2) assuming model in (b). Numbers inside the map are plateau resistance values in units of h/e^2.

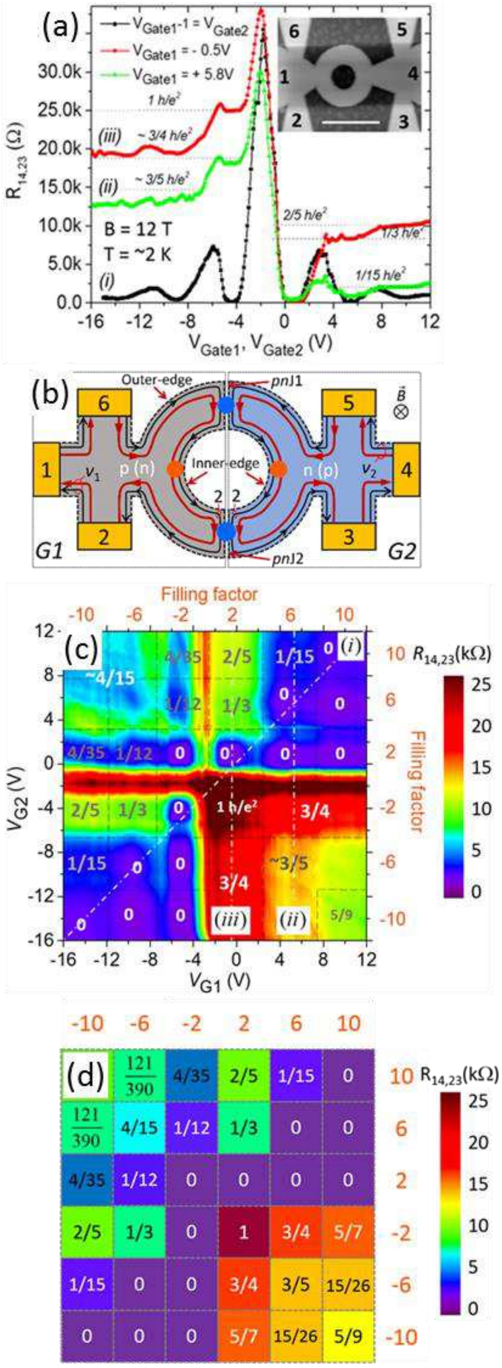

	-10	-6	-2	2	6	10
10	(d)	121/390	4/35	2/5	1/15	0
6	121/390	4/15	1/12	1/3	0	0
2	4/35	1/12	0	0	0	0
-2	2/5	1/3	0	1	3/4	5/7
-6	1/15	0	0	3/4	3/5	15/26
-10	0	0	0	5/7	15/26	5/9

Fig.2: Two pnJ ring device (a) Longitudinal resistance $R_{14,23}$ measured at $T = \sim 2$ K and $B = 12$ T as a function of local gate voltages V_{G1} and V_{G2}; insert: AFM image of ring-shape graphene pnJ device, scale bar is 1 μm. (b) Schematic of edge-state transport model of longitudinal resistance $R_{14,23}$ in the quantum Hall regime. Model in which only the lowest Landau level edge states equilibrate across the junction. all edge states equilibrate along the mechanical edge. Blue and Orange dots schematically indicates the regions of equilibration. (c) 2D projection of longitudinal resistance $R_{14,23}$ measured at $T = 2$ K and $B = 1$ T as a function of (V_{G1}, V_{G2}) and filling factors (ν_1, ν_2). (d) Calculated 2D resistance map of $R_{14,23}$ as a function of filling factors (ν_1, ν_2) assuming model in (b). Numbers inside the map are plateau resistance values in units of h/e^2.

Discovery of Intrinsic Ferromagnetism in Two-Dimensional van der Waals Crystals

Cheng Gong, Yuan Wang, and Xiang Zhang

Nano-scale Science and Engineering Center (NSEC), 3112 Etcheverry Hall, University of California, Berkeley, California 94720, USA
e-mail: xiang@berkeley.edu

Past more than a decade witnessed the explosive exploration of fundamental physics and novel concepts of devices based on two-dimensional (2D) van der Waals (vdW) crystals. It has been long hoped that the realization of long-range ferromagnetic order 2D vdW crystals, combined with their rich electronic and optical properties, would open up new possibilities for magnetic, magnetoelectric and magneto-optic applications. However, in 2D systems, the long-range magnetic order is strongly hampered by thermal fluctuations which may be counteracted by magnetic anisotropy, according to the Mermin-Wagner theorem. Prior efforts via defect and composition engineering, and proximity effect only locally or extrinsically introduce magnetic responses. Recently we reported the first experimental discovery of intrinsic long-range ferromagnetic order in pristine $Cr_2Ge_2Te_6$ atomic layers by scanning magneto-optic Kerr microscopy [1]. In such a 2D vdW soft ferromagnet, for the first time, an unprecedented control of transition temperature is realized via surprisingly small fields (≤ 0.3 Tesla), in stark contrast to the stiffness of the transition temperature to magnetic fields in the three-dimensional regime. We found that the small applied field enables an effective anisotropy far surpassing the tiny magnetocrystalline anisotropy, opening up a sizable spin wave excitation gap. Confirmed by renormalized spin wave theory, we explain the phenomenon and conclude that the unusual field dependence of transition temperature constitutes a hallmark of 2D soft ferromagnetic vdW crystals. Our discovery of 2D soft ferromagnetic $Cr_2Ge_2Te_6$ presents a close-to-ideal 2D Heisenberg ferromagnet for studying fundamental spin behaviors, and opens the door for exploring new applications such as ultra-compact spintronics.

[1] C. Gong et al., Nature, **546**, 265-269 (2017).

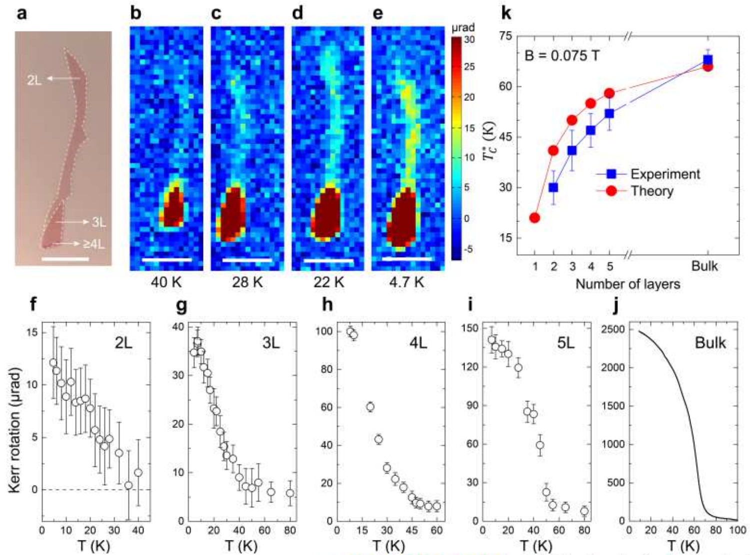

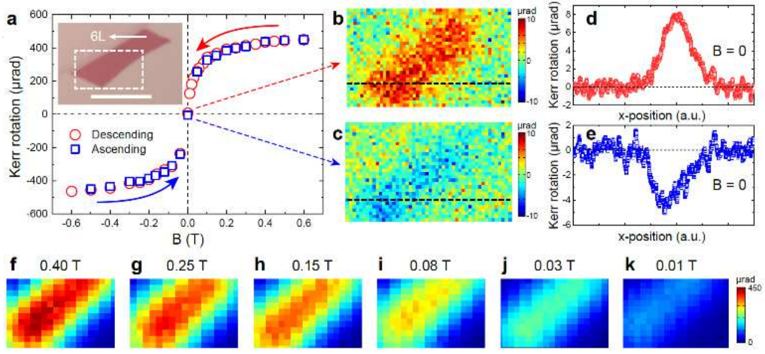

Fig.2 : Ferromagnetic hysteresis loop with single domain remanence in a six-layer (6L) $Cr_2Ge_2Te_6$.

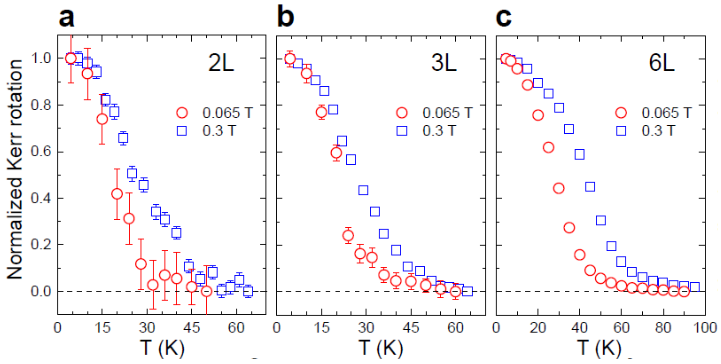

Fig.3: Magnetic field control of transition temperature of few-layer $Cr_2Ge_2Te_6$.

978-3-901578-31-1

Quantum transport and optoelectronic application in van der Waals junctions of 2D materials

Tomoki Machida[1,2]

[1] *Institute of Industrial Science, University of Tokyo, Tokyo 153-8505, Japan*
[2] *CREST, Japan Science and Technology Agency, Japan*
e-mail: tmachida@iis.u-tokyo.ac.jp

Recent advances in mechanical exfoliation and transfer techniques of atomic layers have enabled one to fabricate van der Waals junctions of two-dimensional (2D) materials, such as graphene, hexagonal boron nitride (h-BN), and transition-metal dichalcogenides (TMDs). Here, we present our recent experiments on quantum transport and optoelectronic application in van der Waals junctions of various 2D materials: (i) Dirac fermion reflector in ballistic graphene/h-BN [1], (ii) mechanical exfoliation of magnetic-atom-intercalated transition metal dichalcogenides, $Cr_{1/3}TaS_2$ and $Fe_{1/4}TaS_2$, and their van der Waals assembly to exhibit tunnel magnetoresistance effect [2], (iii) p-type and n-type carrier injection into WSe_2 using $NbSe_2$ and graphite, respectively [3], (iv) suppression of the exciton-exciton annihilation rate in hBN/WS_2/hBN studied by time-resolved photoluminescence spectroscopy [4], (v) inter-subband Landau level couplings induced by in-plane magnetic fields in trilayer graphene [5], (vi) cyclotron resonance absorption in monolayer, bilayer, twisted bilayer, and trilayer graphene, (vii) the influence of the C-doped domains in h-BN on electrical transport and optical properties of 2D materials above.

[1] S. Morikawa, Q. Wilmart S. Masubuchi, K. Watanabe, T. Taniguchi, B. Placais, and T. Machida, Semicond. Sci. and Technol. **32**, 045010 (2017).
[2] Y. Yamasaki, R. Moriya, M. Arai, S. Masubuchi, S. Pyon, T. Tamegai, K. Ueno, and T. Machida, 2D Materials (in press).
[3] Y. Sata, R. Moriya, S. Masubuchi, K. Watanabe, T. Taniguchi, and T. Machida, Jpn. J. Appl. Phys. **56**, 04CK09 (2017).
[4] Y. Hoshi T. Kuroda, M. Okada, R. Moriya, S. Masubuchi, K. Watanabe, T. Taniguchi, R. Kitaura, and T. Machida, Phys. Rev. B **95**, 241403 (2017).
[5] Y. Asakawa, S. Masubuchi, N. Inoue, S. Morikawa, K. Watanabe, T. Taniguchi, and T. Machida (submitted).
[6] Y. Ota, R. Moriya, N. Yabuki, M. Arai, M. Kakuda, S. Iwamoto, T. Machida, and Y. Arakawa, Appl. Phys. Lett. **110**, 223105 (2017).

978-3-901578-31-1

Quantum photonics with van der Waals heterostructures

C. Chakraborty[1,2,3], L. Qiu[1,3], K. Kothasinghe[1,3], A. Mukherjee[1,3], S. Dhara[1,3] and A. N. Vamivakas[1,2,3,4,]

[1]*The Institute of Optics, University of Rochester, Rochester, NY 14627, USA*

[2]*Materials Science, University of Rochester, Rochester, NY 14627, USA*

[3]*Center for Coherence & Quantum Optics, University of Rochester, Rochester, NY 14627, USA*

[4]*Department of Physics, University of Rochester, Rochester, NY 14627, USA*

Two-dimensional, atomically-thin, materials have received enormous interest as a result of their unique mechanical, electrical and optical properties. Particularly exciting are the transition metal dichalcogenides – atomically-thin semiconductors that possess an electronic band gap in the visible. Although these materials have been investigated for applications in opto-electronics, not much work has focused on these systems as a platform for quantum photonics and quantum optics. In this talk I will describe two approaches that leverage atomically thin semiconductors, and other two-dimensional materials, assembled in layered van der Waals heterostructures for applications in these areas. In the first part of the talk I will describe the unique photophysical properties of quantum emitters hosted by single layer transition metal dichalcogenides. I will describe our recent efforts to controllably charge the quantum emitters and realize a localized spin-valley-photon interface (see Fig. 1). I will also present results on realizing negative-mass trion-polaritons that are a manifestation of many body physics arising when coupling the atomically thin semiconductor to a planar optical cavity.

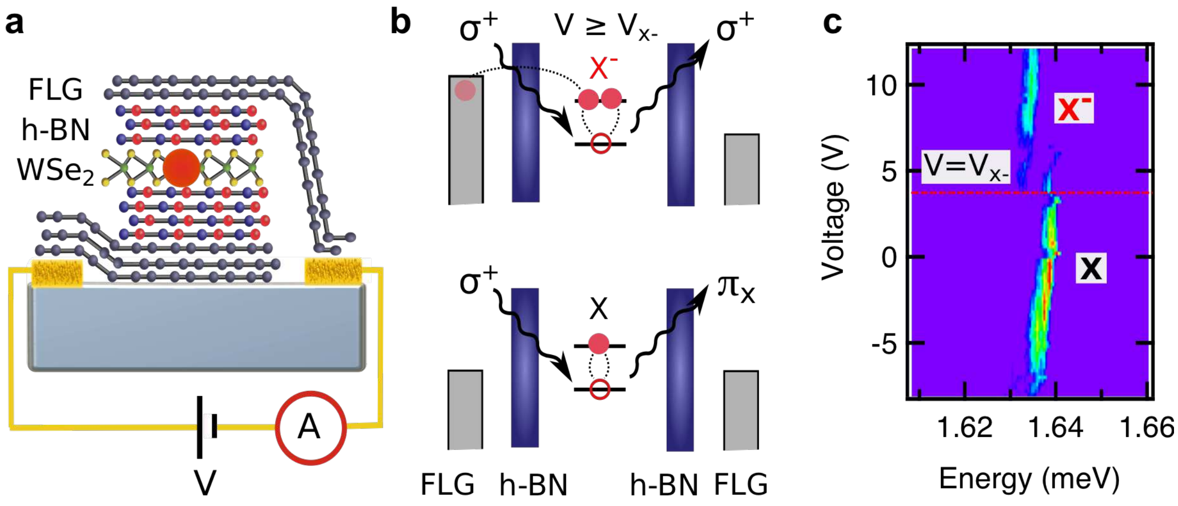

Figure 1. ***a.*** *Illustration of the van der Waals heterostructure used for experiments. The device consisted of (top to bottom) a few layer graphene (FLG) flake contacted to a gold electrode, hexagonal boron nitride (hBN), tungsten diselenide (WSe_2), hBN and a FLG contacted to a gold electrode.* ***b.*** *Illustration of light emission from both a neutral exciton (X; bottom) and trion (X^-;top). The X^- is active for voltages V greater than V_{X-}. The polarization of the emitted photons is determined by the exciton responsible for light emission.* ***c.*** *Voltage controlled photoluminescence exhibiting distinct charging plateaus for the neutral exciton (X) and trion (X^-) emission.*

Ultrathin van der Waals Photovoltaics

Deep Jariwala[1]

[1]*Department of Applied Physics and Materials Science and the Resnick Sustainability Institute, California Institute of Technology, Pasadena, CA-91125, U.S.A.*

e-mail: jariwala@caltech.edu; dmj@seas.upenn.edu

The isolation of stable atomically thin two-dimensional (2D) materials on arbitrary substrates has led to a revolution in solid state physics and semiconductor device research over the past decade.[1] While, graphene is the poster child of 2D materials family, a variety of other 2D materials (including semiconductors) with varying structures and opto-electronic properties have been isolated over the last few years raising the prospects for a new class of devices assembled by van der Waals forces.[2] A fundamental challenge in using 2D materials for opto-electronic devices is enhancing their interaction with light, ultimately responsible for higher performance and efficiency in the devices. In particular, from the perspective of high-efficiency photovoltaics; inorganic materials (e.g., Si, GaAs and GaInP) can achieve maximum above-bandgap absorption as well as carrier-selective charge collection at the cell operating point. But thin film photovoltaic absorbers have lacked the ability to maximize absorption and efficient carrier collection, concurrently often due to due to surface and interface recombination effects. In contrast, Van der Waals semiconductors have naturally passivated surfaces with electronically active edges that allows retention of high electronic quality down-to the atomically thin limit.

In this seminar, I will show our recent work on photovoltaic devices from transition metal dichalcogenides of molybdenum and tungsten such as MoS_2, WSe_2 etc. We have recently demonstrated near-unity absorption in the visible part of the electromagnetic spectrum in < 15 nm films of these semiconductors by placing them on reflecting metal substrates such as gold and silver. We have further shown that these highly absorbing, ultrathin films can be further used for fabrication of simple Schottky junction photovoltaic devices with microfabricated metallic top contacts.[3] While, this work helps solve the light-absorption problem, the external quantum efficiency EQE was < 10% for our Schottky junction devices. Very recently, we have extended this early work to fabricate p-n heterojunctions from p-WSe_2/n-MoS_2 and use graphene as a transparent top contact to amplify our current collection efficiency and push the EQE up to 50%,[4] approaching that of many emerging photovoltaic technologies with active layers in the 100s of nm range. This represents a significant development as both light-absorption and charge collection have been addressed in these devices. Finally, I will present scope for future work using just monolayers of materials to engineer near unity light absorption and collection.

References:

1. Jariwala, D.; Sangwan, V. K.; Lauhon, L. J.; Marks, T. J.; Hersam, M. C. *ACS Nano* **2014,** 8, 1102-1120.
2. Jariwala, D.; Marks, T. J.; Hersam, M. C. *Nat. Mater.* **2017,** 16, 170-181.
3. Jariwala, D.; Davoyan, A. R.; Tagliabue, G.; Sherrott, M. C.; Wong, J.; Atwater, H. A. *Nano Lett.* **2016,** 16, 5482-5487.
4. Wong, J.; Jariwala, D.; Tagliabue, G.; Tat, K.; Davoyan, A. R.; Sherrott, M. C.; Atwater, H. A. *ACS Nano* **2017**.

978-3-901578-31-1

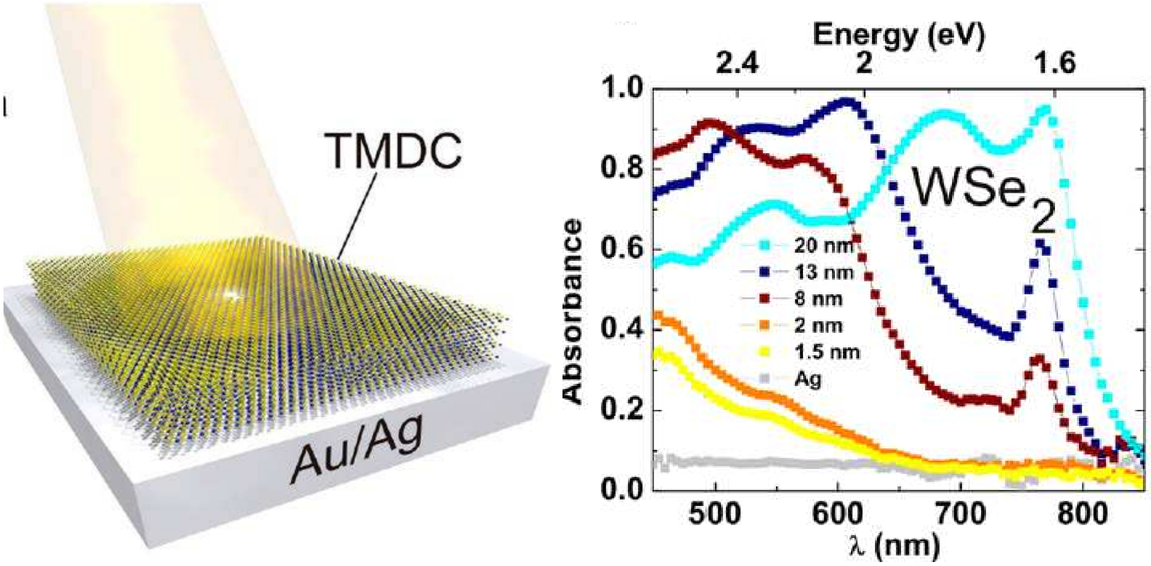

Figure 1. (left) Schematic representation of an ultrathin transition metal dichalcogenide (TMDC) stack on reflective Au or Ag substrates. (right) Experimentally measured absorption of WSe_2 on Ag with varying thickness of the WSe_2 layer. Near unity absorption is observed for WSe_2 layer thickness as low as 8 nm and maximum broadband absorption is observed for ~13 nm WSe_2. For thicker samples the absorption start reducing in the blue part of the spectrum due to increasing reflection.

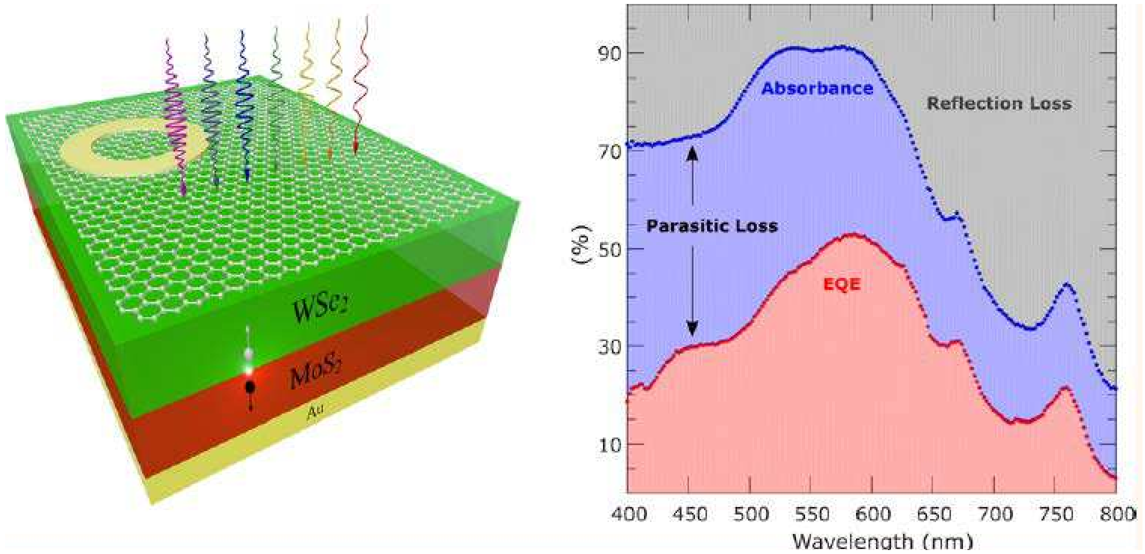

Figure 2. (left) Schematic representation of a WSe_2/MoS_2 p-n heterojunction photovoltaic device stack on reflective Au or Ag substrates as back contacts and graphene as a top conctact. (right) Experimentally measured absorption of the stack (blue) and External quantum efficiency (red) exceeding 50% for 9 nm total thickness of the active layer.

Ferroelectric domain control of photoluminescence in monolayer WS_2 / PZT hybrid structures

Berry Jonker, Connie Li and Kathleen McCreary
Materials Science and Technology Division, Naval Research Laboratory
Washington DC 20375 USA
e-mail: berry.jonker@nrl.navy.mil

Single monolayer transition metal dichalcogenides (TMDs) exhibit exceptionally strong photoluminescence dominated by a combination of distinct neutral and charged exciton contributions. The dielectric screening is very low due to their two-dimensional character relative to bulk material, and their properties are thus strongly affected by their immediate environment. Because the exciton and trion binding energies are very large (~ 600 meV and ~30 meV, respectively), these characteristic emission features persist to room temperature. The samples were fabricated by mechanically transferring large area monolayer WS_2 grown by a CVD process onto a 100 nm thick lead zirconium titanate (PZT) film on a conducting *n*-type strontium titanate wafer. We show here that the surface charge associated with ferroelectric domains patterned into the PZT film with a conductive atomic force microscope laterally control the spatial distribution of neutral and charged exciton populations in the adjacent WS_2 monolayer [1]. This is manifested in the intensity and spectral composition of the photoluminescence measured in air at room temperature from the areas of WS_2 over a ferroelectric domain with polarization dipole pointed either out of the surface plane or into the surface plane. The photoluminescence from areas of the WS_2 over up polarization domains in the PZT are dominated by neutral exciton emission, while those over down domains are dominated by trion emission, consistent with the corresponding charge produced by the domains at the WS_2 / PZT interface. The hysteretic character of ferroelectric materials means that the TMD properties can be selectively reconfigured in a nonvolatile manner by changing the state of the ferroic substrate. This approach enables spatial modulation of TMD properties with a spatial resolution determined by the polarization domains in the underlying ferroelectric layer, with the potential for fabrication of lateral quantum dot arrays or *p-n* junctions in any geometry of choice.

[1] C.H. Li, K.M. McCreary and B.T. Jonker, *ACS Omega* 1, 1075 (2016).

This work was supported by core programs at NRL and the NRL Nanoscience Institute, and by the Air Force Office of Scientific Research #AOARD 14IOA018-134141.

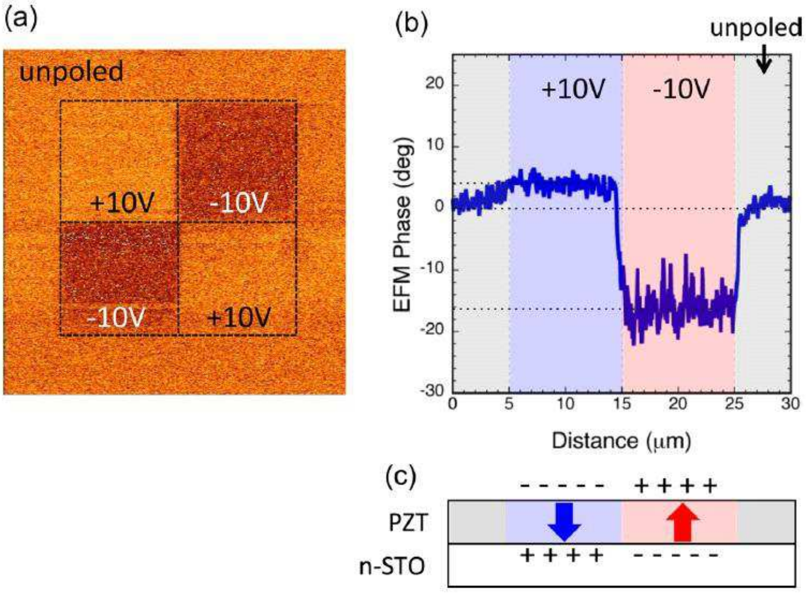

Figure 1. *a) Image of the poled PZT surface obtained with an AFM operated in the electrostatic force microscopy phase mode. The same AFM was used to write the polarization domains into the PZT in a checkerboard pattern with the tip polarities shown. The total image size is 30x30 um, and each poled square is 10x10 um. The dashed lines are a guide to the eye, and the bias voltages applied to the C-AFM tip are indicated. b) Horizontal EFM line scan averaged left to right across the top two panels of the checkerboard. c) Schematic cross section of the PZT film illustrating the orientation of the polarization domains and corresponding surface charge.*

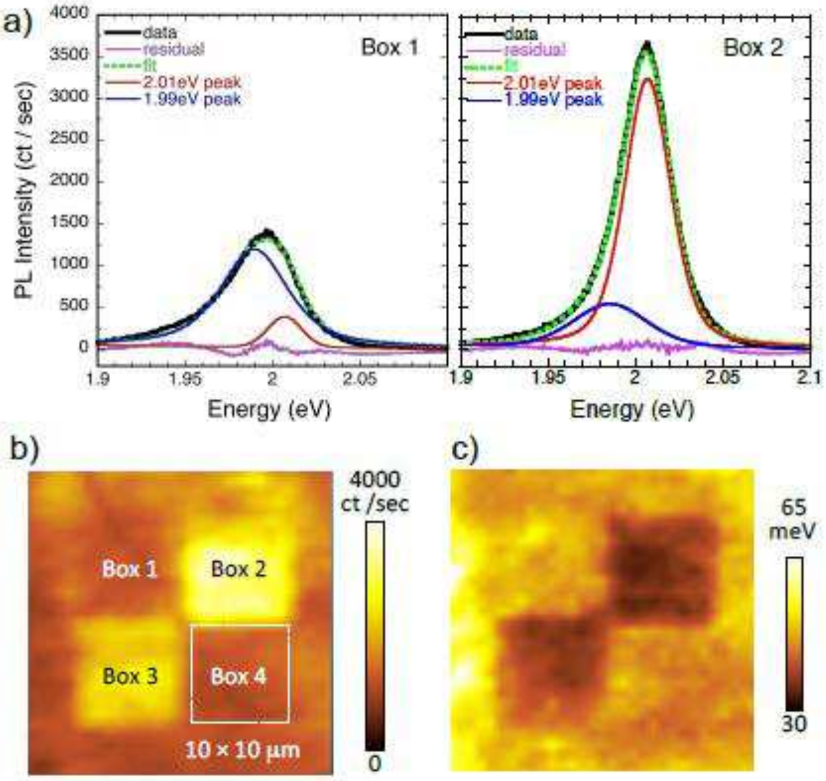

Figure 2. *a) raw PL spectra (solid black line) and fits (dashed green line) using two Lorentzians centered at 2.01 eV (red line) and 1.99 eV (blue line), with the difference between the raw spectra and the fit shown as the purple residual line. b) PL peak intensity map of the raw PL spectra obtained from the* WS_2 *monolayer over a 30x30 um area in the sample plane, acquired from a region of the PZT that was intentionally poled by the AFM with the checkerboard pattern illustrated in Figure 1a. c) spatial map of the raw PL linewidth (FWHM) corresponding to the data of figure 2b.*

Exchange Field Induced Valley Splitting Enhancement in WSe_2 and WS_2

Chuan Zhao[1], Tenzin Norden[1], Peiyao Zhang[1], Puqin Zhao[2,1], Yingchun Cheng[2], Fan Sun[1], James P. Parry[1], Jieqiong Wang[3], Yihang Yang[4], Sen Yang[3], Guo-xing Miao[4], Renat Sabirianov[5], George Kioseoglou[6], Athos Petrou[1], and Hao Zeng[1,3]

[1] *Department of Physics, University at Buffalo, State University of New York, Buffalo, New York 14260, USA*
[2] *Key Laboratory of Flexible Electronics and Institute of Advanced Materials, Jiangsu National Synergetic Innovation Center for Advanced Materials, Nanjing Technical University, Nanjing 211816, China*
[3] *School of Science, MOE Key Laboratory of Nonequilibrium Synthesis and Modulation of Condensed Matter, Xi'an Jiaotong University, Xi'an 710049, China*
[4] *Institute of Quantum Computing, University of Waterloo, Waterloo, Ontario, Canada*
[5] *Department of Physics, University of Nebraska-Omaha, Omaha, Nebraska 68182, USA*
[6] *Department of Material Science and Technology, University of Crete, Heraklion, GR 71003, Greece*

The Zeeman splitting in WSe_2 and WS_2 monolayers deposited in SiO_2 is only 0.20 meV/T [1-3]. In contrast, when these monolayers are deposited on ferromagnetic EuS we observe a significant enhancement of the A exciton slope (2.5 meV/T) [4] as is shown in fig.1. This corresponds to an exchange field of 12 T. In fig.2 we have subtracted the non-magnetic slope of 0.20 meV/T leaving only the contribution ΔE_{ex} to the A exciton due to the interaction of WSe_2 with the EuS substrate. This component of the Zeeman splitting follows the normalized EuS magnetization indicated by the solid lines. We also measured the Zeeman splitting of the B-exciton in WSe_2/EuS samples and observed an enhancement, accompanied by an unexpected slope sign change, as shown in fig.3. This trend is opposite to the Zeeman splitting of the A- and B-excitons from an external magnetic field, which shows identical sign and magnitude. DFT calculations confirmed the sign reversal, and further suggested that the exchange interactions in the conduction and valence bands are opposite in signs. We further show that the A-exciton Zeeman splitting in WS_2/EuS samples (see fig.4) also exhibits an enhancement with a sign reversal of the slope dE/dB compared to the WS_2/SiO_2 samples. The sign reversal of B-exiton of WSe_2 and A-exciton of WS_2 reveals the rich valley physics resulting from the exchange field of a magnetic substrate.

This work has been supported by NSF MRI-1229208, DMR-1104994 and CBET-1510121.

[1] K. F. Mak et al, Nat. Nanotech., **7**, 494 (2012)
[2] G. Aivazian et al, Nat. Phy., **11**, 148 (2015)
[3] A.V. Stier et al, Nat. Commun., **7,** 10643 (2016)
[4] C. Zhao et al, Nat. Nanotech., **12**, 757 (2017)

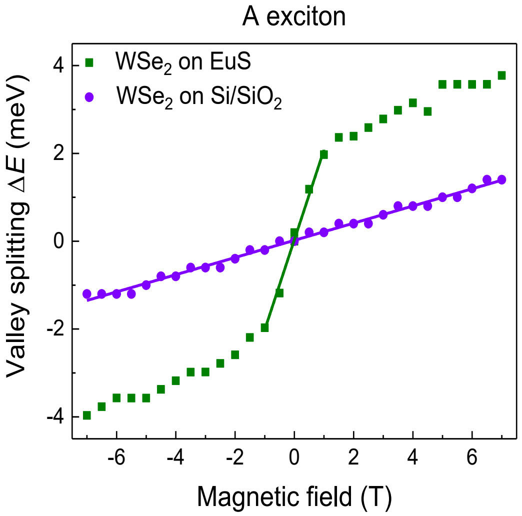

Fig. 1: WSe_2 on EuS versus SiO_2 substrates for A exciton. Purple circles, Si/SiO_2 substrate; green squares, EuS substrate.

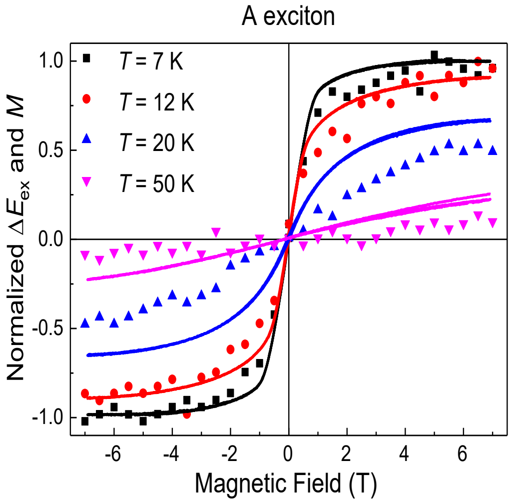

Fig. 2: Field-dependent ΔE_{ex} of WSe_2 and M of EuS superimposed on each other for A exciton. Both ΔE_{ex} and M are normalized by their saturated values at 7 K. Points, normalized ΔE_{ex}; lines, normalized M.

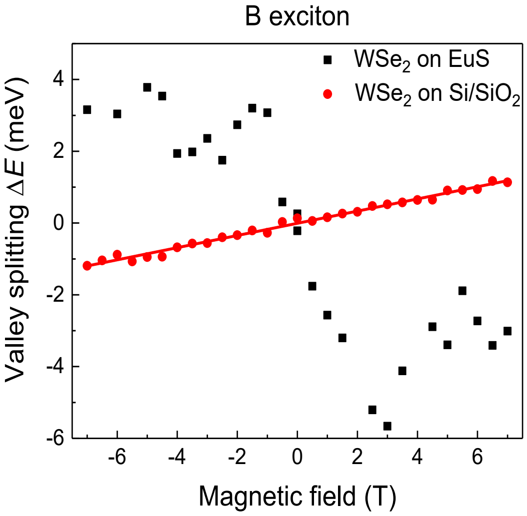

Fig. 3: WSe_2 on EuS versus SiO_2 substrates for B exciton. Red circles, Si/SiO_2 substrate; black squares, EuS substrate.

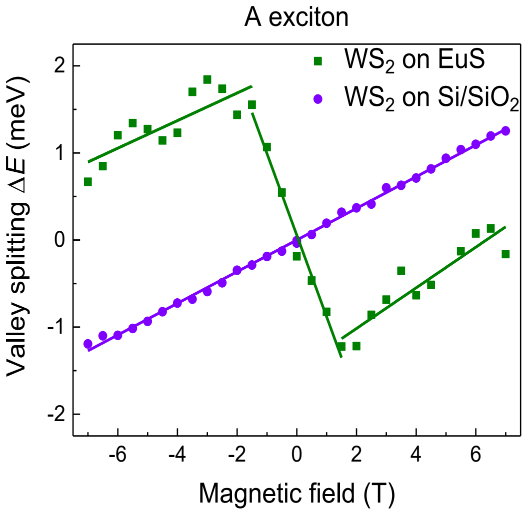

Fig. 4: WS_2 on EuS versus SiO_2 substrates for A exciton. Purple circles, Si/SiO_2 substrate; green squares, EuS substrate.

Adaptive Control of Graphene Surface Charge Distribution with Suspended Gates in an Electrolytic Gate Dielectric

Richard C. Ordonez[1], Cody K. Hayashi[1], Jordan Melcher[2] , Nackieb Kamin[1],
Carlos M. Torres Jr.[3], and David Garmire[2]

[1] *Graphene Microfluidics Laboratory, Space and Naval Warfare Systems Center Pacific,*
Pearl City, Hawai'i, 96782, USA
[2] *Dept. of Electrical Engineering, University of Hawai'i at Mānoa, Honolulu, Hawai'i, 96822*
[3] *Advanced Photonics Branch, Space and Naval Warfare Systems Center Pacific, San Diego,*
California, 92152, USA
e-mail: Richard.c.ordonez@navy.mil

We demonstrate dynamic control of abrupt graphene junction formation with the use of suspended gates in a single electrolytic gate dielectric. Typically, graphene junctions are formed via electrostatic doping with top gates fabricated on thermal oxides and separated by a nominal separation distance [1]. However, current fabrication processes yield a minimum separation distance between top gates. When such gates are used to form junctions on graphene, the regions under the gates become doped, but the intermediate region between gates does not and results in non-ideal charge distribution. This undesired charge distribution can hinder device performance, as it provides an intermediate energy-band level that compromises the otherwise sharp junction barrier height. Consequently, this places performance limitations on electrical switching applications. In addition, due to standard dielectric breakdown of thermal oxides, the induced carrier density $(n < 10^{13} cm^{-2})$ and corresponding junction barrier height are limited. Electrolytic gate dielectrics provide the necessary high gate-capacitances required to induce large carrier densities $(n > 10^{14} cm^{-2})$,which is a direct result of the formation of an electric double layer with nanometer separation at the interface of charged surfaces. Recent attempts to utilize electrolytic gating in literature have only demonstrated a single top gate [2]. We show multiple conductive wires can be suspended within an electrolytic gate dielectric to alter the surface charge distribution of an underlying graphene sheet. As compared to traditional methods, our embedded architecture utilizes the ionic conductivity of the electrolytic gate dielectric to provide a pure junction that is unhindered from junction separation distance. Furthermore, with our methods a designer can carefully optimize ambipolar junction transport characteristics for a variety of applications that include diodes, rectifiers, and bipolar junction transistors.

[1] J. Liu et al., Electronic Letters, **50(23)**, 1724-1726 (2014).

[2] S. Grover et al., Scientific Reports, **7**, (2017).

978-3-901578-31-1

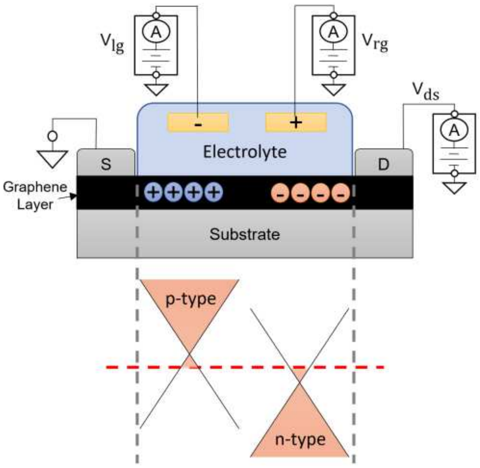

Fig.1: (Top) Visualization of graphene field-effect transistor with two suspended gates. (Bottom) Energy band diagram of graphene p-n junction.

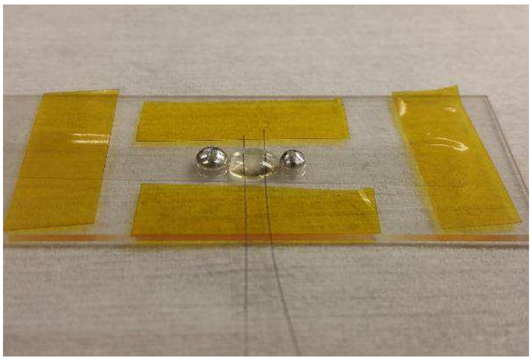

Fig 2: Graphene field-effect transistor with two suspended gates in electrolytic gate dielectric

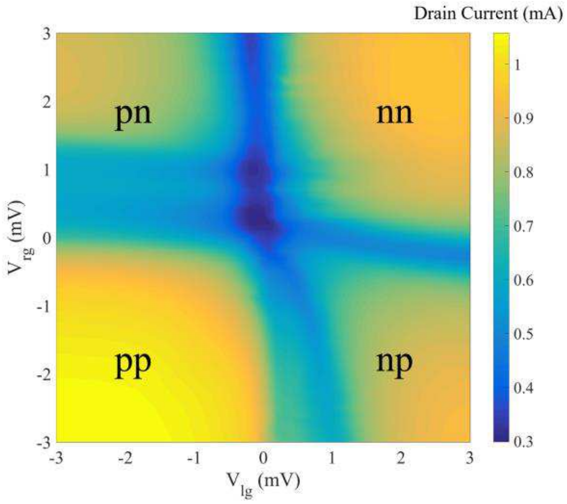

Fig.3: Bi-variable sweep of graphene field-effect transistor drain current as a function of top gate-voltage with biasing schemes identified for both left and right top-gates of Fig. 1.

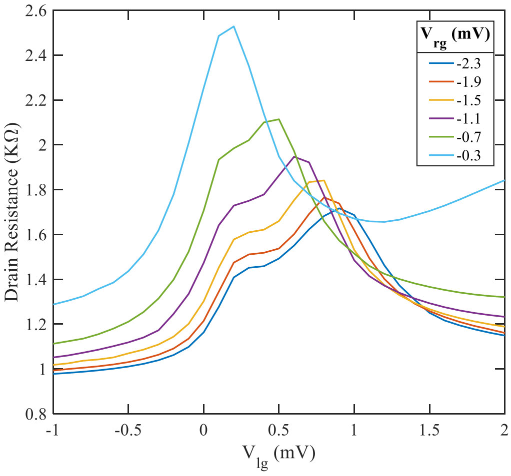

Fig.4 Adaptive control of p-n junction characteristics as the left top gate voltage of Fig. 1 is varied and right top gate is held at constant. Note the difference in drain resistance of each dirac peak changes with corresponding changes in top-gate voltages.

Quantum Dots and Perovskites – Realizing the Best of Both Worlds for Revolutionary Optoelectronic Applications

Erin M. Sanehira,[1,2] Ashley R. Marshall,[1,3] Jeffrey A. Christians,[1] Steven P. Harvey,[1] Peter N. Ciesielski,[1] Lance M. Wheeler,[1] Philip Schulz,[1] Lih Y. Lin,[2] Matthew C. Beard,[1] and Joseph M. Luther[1]*

[1]*National Renewable Energy Laboratory, Golden, CO, 80401, USA*
[2]*Department of Electrical Engineering, University of Washington, Seattle, WA 98195, USA*
[3]*Department of Chemistry and Biochemistry, University of Colorado, Boulder, CO, 80309, USA*

**Correspondence to: joey.luther@nrel.gov*

We demonstrate QD photovoltaic cells made from $CsPbI_3$ colloidal nanocrystals with an open-circuit voltage of 1.23 volts and power conversion efficiency of 13.4%. Despite very little research on this specific material system to date, the performance surpasses that of any other QD solar cell. This new material system has incredible potential for many applications in optoelectronics, including multijunction photovoltaics, solid state lighting and display technology. Here, I will present the basics behind the perovskite revolution over the past several years and a forward look into where this technology could make the greatest impact.

$CsPbI_3$ is an all-inorganic analog to the hybrid organic cation halide perovskites, but the cubic phase of bulk $CsPbI_3$ (a-$CsPbI_3$)—the variant with desirable band gap—is only stable at high temperatures under conventional constructs. We describe the formation of α-$CsPbI_3$ QD films through a colloidal quantum dot route that are phase-stable for months in ambient air. The films exhibit long-range electronic transport and are used to fabricate colloidal perovskite quantum dot solar cells. The modified size/phase stability will be discussed.

978-3-901578-31-1

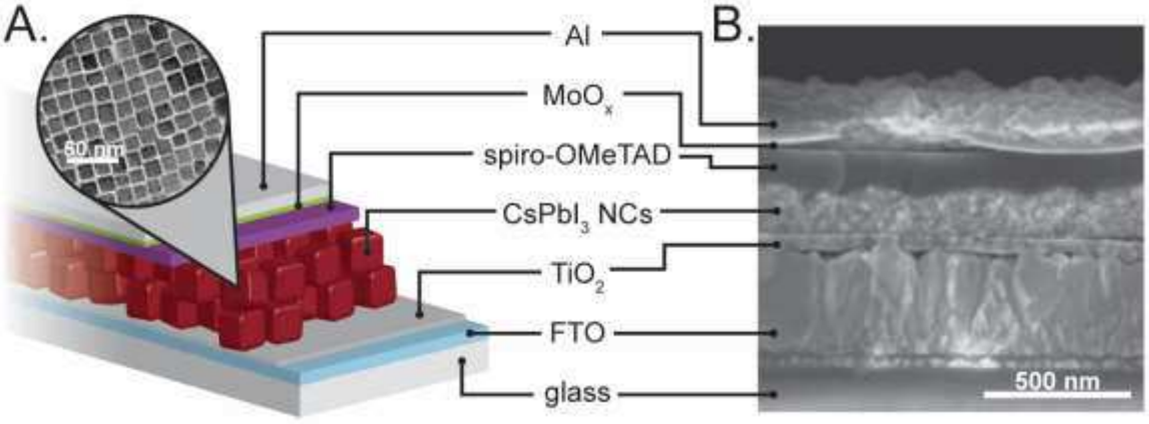

Figure 1. Device structure of CsPbI$_3$ quantum dot solar cells. The inset in A) shows a TEM image of the nanocrystals. B) shows an SEM image of the cross section of a typical solar cell.

978-3-901578-31-1

InGaN Multi-Quantum Well Solar Cells for High Temperature Applications

Joshua Williams[1], Yi Fang[2], Alec Fischer[2], Christiana Honsberg[1], Fernando Ponce[2], Dragica Vasileska[1], and Stephen Goodnick[1]

[1] *School of Electrical Computer and Energy Engineering, Arizona State University, Tempe AZ 85287-5706*

[2] *Department of Physics, Arizona State University, Tempe AZ 85287-1504*

The $In_xGa_{1-x}N$ material system is of great interest for optical applications such as LEDs and photovoltaic devices due to its continuously tunable band gap from near-UV to mid-IR. Another benefit of this system is its high temperature robustness, due both to the wide bandgap and chemical stability of the nitrides. Here we discuss recent results on the high temperature performance of multi-quantum well (MQW) $In_{0.12}Ga_{.88}N$/GaN solar cells grown by MOCVD [1], for applications as topping cells for hybrid photovoltaic/concentrating solar thermal (CSP) applications, as well as for space exploration applications for near solar missions.

A MQW structure was employed in order to maintain a high V_{oc} at high temperature, which is the main parameter affected by temperature, while taking advantage of increased collection efficiency at higher temperatures due to thermionic emission out of the wells into the continuum. The structure of the as grown material and fabricated devices (Fig. 1) used between 10 and 40 periods of an alternating InGaN/GaN MQW system, with the thicknesses of the layers varying from 1-3 nm. Typical results on the best material are shown by the 1 sun I-V characteristics in Fig. 2 for various temperatures from room temperature to 600 C. At 300x concentration, the cells show a V_{oc} greater than 1.8 V, which is very near ideal. Very little degradation is observed after cycling to 600 C and back (shown in Fig. 2), and systematic studies show that even the amount of degradation indicated in Fig. 2 is reversible. Cycling up to 700 C shows in fact little degradation, which is a record for any solar cell technology, and indicative of the robustness of the nitride material system for high temperature operation.

Cathodoluminescence studies coupled with HREM characterization of the cell structure shown in Fig. 1 show in fact that the material system itself is robust up to 1100 C, and that any degradation in performance at the highest temperatures is associated with the contact metallurgy, and not the intrinsic material itself. Modeling results are also presented showing good agreement with the experimental data in terms of current voltage characteristics as a function of temperature for the current-voltage and spectral response characteristics.

[1] J. J. Williams *et al.*, Proceedings of the 2016 IEEE 43rd Photovoltaic Specialists Conference (PVSC),0193-5, 2016; DOI: 10.1109/PVSC.2016.7749576.

978-3-901578-31-1

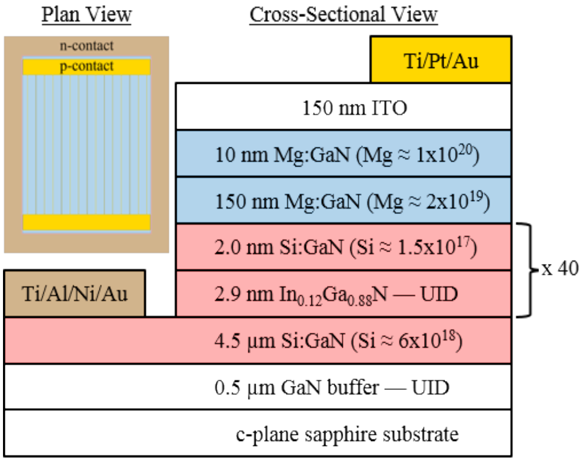
Plan View
n-contact
p-contact
Cross-Sectional View
Ti/Pt/Au
150 nm ITO
10 nm Mg:GaN (Mg ≈ 1x10^20)
150 nm Mg:GaN (Mg ≈ 2x10^19)
2.0 nm Si:GaN (Si ≈ 1.5x10^17)
2.9 nm In0.12Ga0.88N — UID
x 40
Ti/Al/Ni/Au
4.5 µm Si:GaN (Si ≈ 6x10^18)
0.5 µm GaN buffer — UID
c-plane sapphire substrate

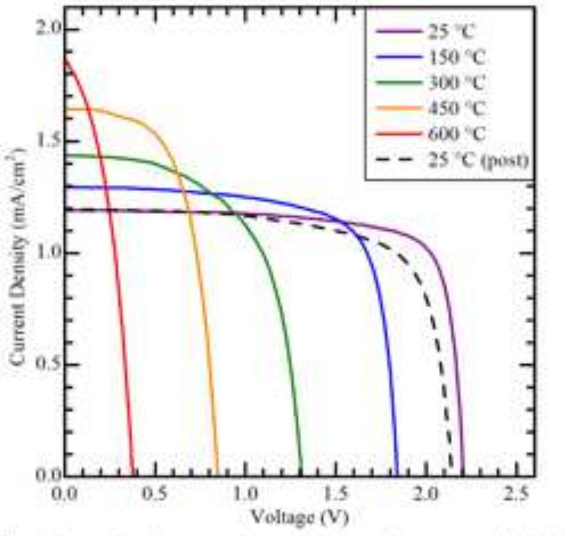
25 °C
150 °C
300 °C
450 °C
600 °C
25 °C (post)
Current Density (mA/cm²)
0.0
0.5
1.0
1.5
2.0
Voltage (V)
0.0
0.5
1.0
1.5
2.0
2.5

InGaAs/GaAsP quantum well superlattice for 1.15-eV middle cell in 4-junction solar cell

Masakazu Sugiyama[1], Takanori Usuki[2], Kasidit Toprasertpong[2], Kentaroh Watanabe[1],
Yoshiaki Nakano[2]

[1]*Reserach Center for Advanced Science and Technology, The University of Tokyo,*
4-6-1 Komaba, Meguro-ku, Tokyo 153-8904, Japan
[2]*Department of Electrical Engineering and Information Systems, School of Engineering,*
The University of Tokyo, Japan
e-mail: sugiyama@ee.t.u-tokyo.ac.jp

As a structure to realize 50% efficiency, 4-junction cell has been proposed with the subcell bandgaps of 1.99/1.51/1.15/0.66 eV from the top to the bottom (**Fig. 1**) [1]. The top two cells consisting of AlInGaP and AlGaAs bulk, respectively, can be grown epitaxially on a Ge bottom cell, whereas the 3rd cell with 1.15 eV bandgap is the bottleneck for the realization of the lattice-matched 4-junction cell, the fabrication of which is expected to be easier than the case of preceding 4-junction cells by wafer bonding [2] and inverse metamorphic (IMM) growth [3]. Using InGaAsP alloys which can be grown with metal-organic vapor-phase epitaxy (MOVPE) with high quality and productivity, strain-balanced InGaAs/GaAsP quantum well superlattice can extend the absorption edge to 1.15 eV. There are two design strategies (**Fig. 2**). The thin barrier facilitated tunneling-assisted carrier transport and significant current enhancement was obtained for this structure under a 800-nm filter which mimics the situation under the 2nd subcell (**Fig. 3**).

When such a superlattice structure is grown on a vicinal substrate, the corrugated layer thickness along the bunching steps on the substrate results in lateral nanowires aligned on the planar well: a “Wire on Well (WoW)” structure (**Fig. 4**). In order to clarify the advantage of the WoW structure over a planar superlattice, GaAs pin solar cells were fabricated with identical structures except for the nanostructure embedded in the intrinsic region. The WoW structure resulted in better fill factor in current-voltage characteristics (**Fig. 5**) and long photoluminescence lifetime (~10 ns) even at room temperature.

[1] T. Thomas et al., 6th *WCPEC*, Kyoto, Japan (2014).
[2] F. Dimroth et al., *IEEE J. Photovoltaic* **6**, 343 (2016).
[3] R. France et al., *IEEE J. Photovoltaic* **6**, 578 (2016).

978-3-901578-31-1

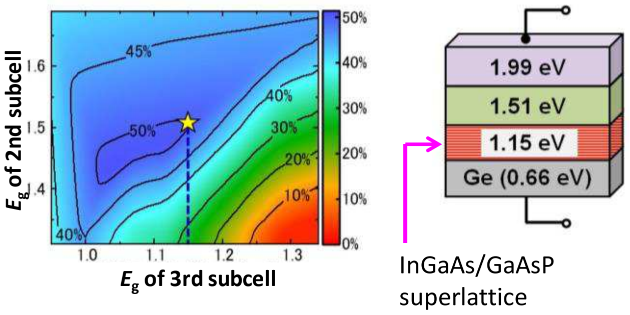

Fig.1: A 4-junction cell with a predicted efficiency of 50%. The 3rd is with a strain-balanced superlattice and an entire structure can be grown on a Ge substrate.

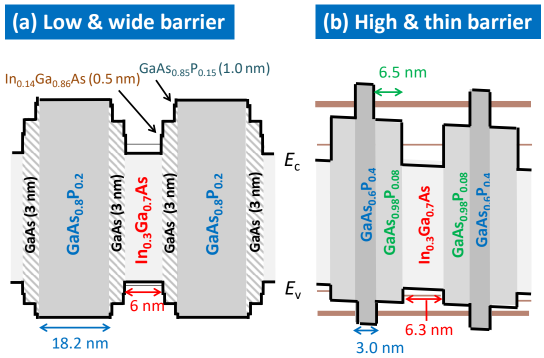

Fig.2: The layer structures and the schematic band alignments of InGaAs/GaAsP strain-balanced superlattice.

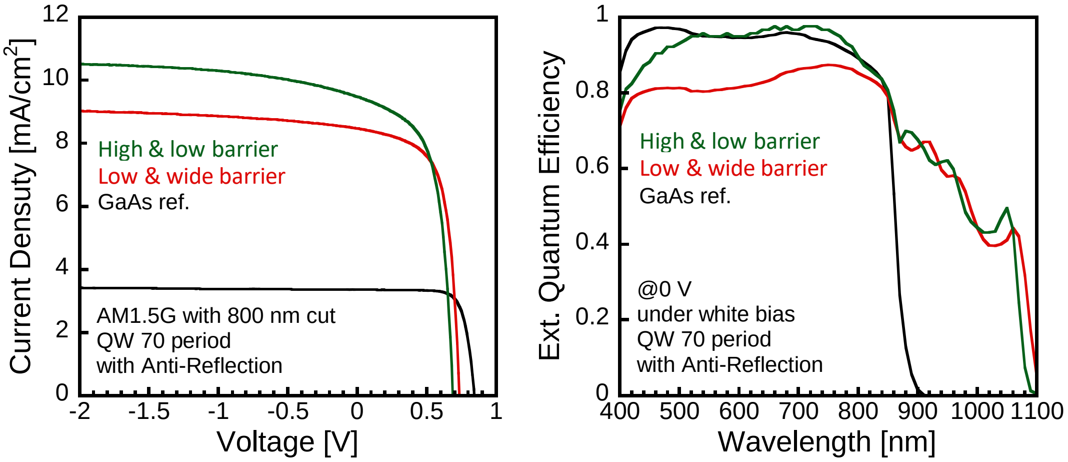

Fig.3: Current-voltage characteristics under a 800-nm filter (corresponding to the transmission of the 2nd subcell) and quantum efficiency for GaAs single-junction cells with the superlattices in Fig. 2. A cell without a superlattice was characterized for comparison.

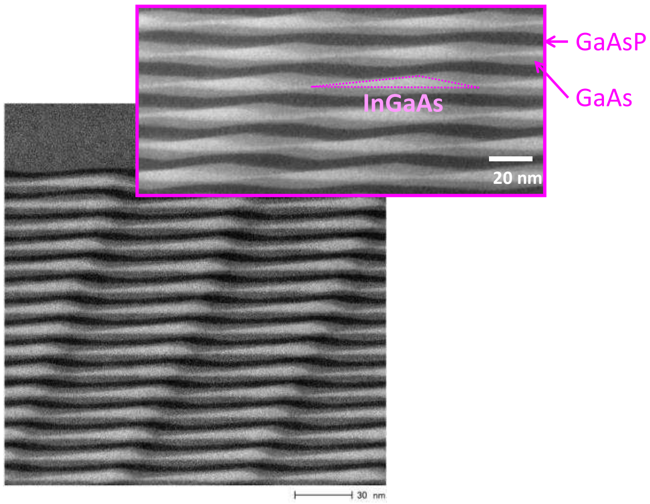

Fig.4: Cross-sectional TEM images of the "Wire on Well" (WoW) structure.

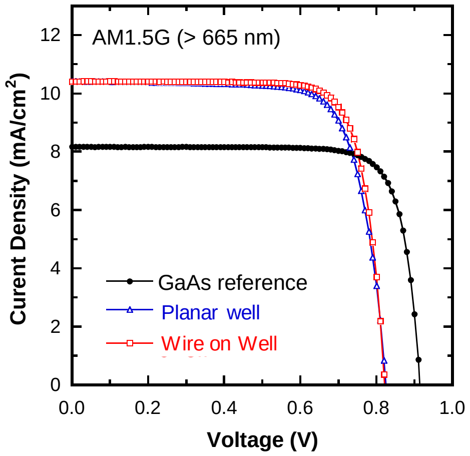

Fig.5: Current-voltage characteristics under a 665-nm filter (corresponding to the transmission of the top cell of a 3-junction cell) for GaAs single-junction cells with a planar superlattice and a WoW structure.

978-3-901578-31-1

High-efficiency heterogeneous multijunction solar cells fabricated by smart stack technology using metal nanoparticle arrays

Takeyoshi Sugaya, Ryuji Oshima, Hidenori Mizuno, Kikuo Makita, Toshimitsu Mochizuki,
and Takeshi Tayagaki

National Institute of Advanced Industrial Science and Technology (AIST),
1-1-1 Umezono, Tsukuba, Ibaraki 305-8568, Japan

Cost reduction and improved conversion efficiency are the most important issues facing the wide-scale deployment of solar photovoltaic systems. Although multijunction solar cells have the highest reported efficiencies and have been commercialized for space and concentrator applications, their use has not become widespread due to their high cost. Our objective is to develop advanced multijunction technologies with extremely low cost and high conversion efficiency.

Multijunction solar cells enable ultra-high efficiencies due to the effective utilization of a solar spectrum by interconnecting different kinds of solar cells. A traditional fabrication method is a monolithic epitaxial growth technique, which is very difficult and limits the choice of materials and cell combinations. We have proposed a novel semiconductor bonding method called smart stack technology for mechanically stacked multijunction solar cells. This technology utilizes Pd nanoparticle alignment to interconnect the top and bottom cells with low bonding resistances and minimal optical absorption losses as shown in Fig. 1 [1]. Pd nanoparticle alignment can be formed by a self-assembled phenomenon using low-cost spin coating method, which is very attractive for interconnecting different kinds of solar cells. We have demonstrated an InGaP(Eg-1.89 eV)/GaAs(Eg-1.42 eV)//InGaAsP(Eg-1.05 eV)/InGaAs (Eg-0.75 eV) 4-junction solar cell with a high efficiency of 32.0% under AM1.5 as shown in Fig. 2 [2]. We also demonstrated an InGaP/GaAs// Si 3-junction solar cell with an efficiency of 25.1% [3]. We describe the thermal reliability test and the stacking mechanisms of smart stack devices. Our method is highly useful to realize the next-generation low-cost and high efficiency multi-junction solar cells with various heterogeneous cell combinations.

[1] H. Mizuno, K. Makita, and K. Matsubara, Appl. Phys. Lett. **101**, 191111 (2012).

[2] H. Mizuno, K. Makita, T. Sugaya, R. Oshima, Y. Hozumi, H. Takato, and K. Matsubara, Jpn. J. Appl. Phys. **55**, 025001 (2016).

[3] H. Mizuno, K. Makita, T. Tayagaki, T. Mochizuki, T. Sugaya, and H. Takato, Applied Physics Express **10**, 072301 (2017).

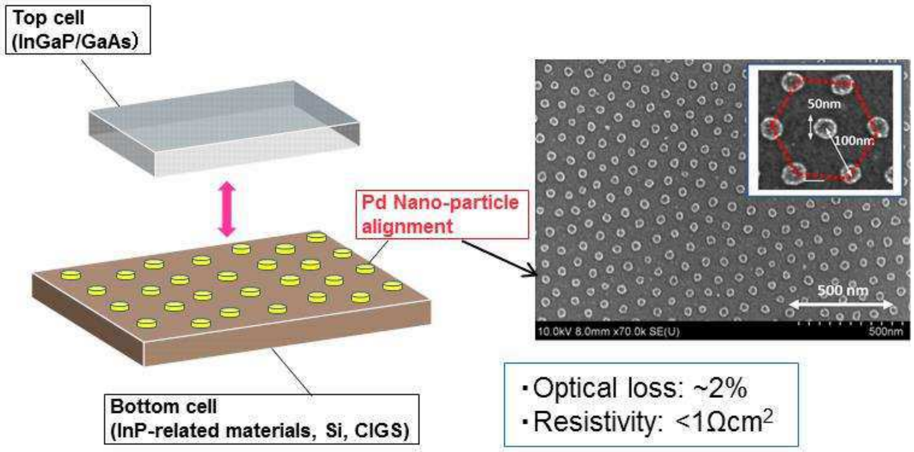

Fig.1: Schematic drawing of a stacking structure and a surface SEM image of Pd nanoparticle alignment.

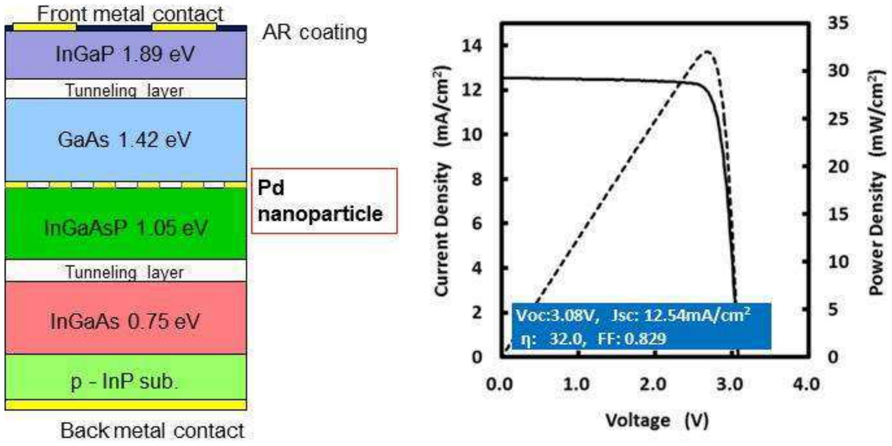

Fig 2: Schematic layer structure of a 4-junction solar cell and its I-V characteristics.

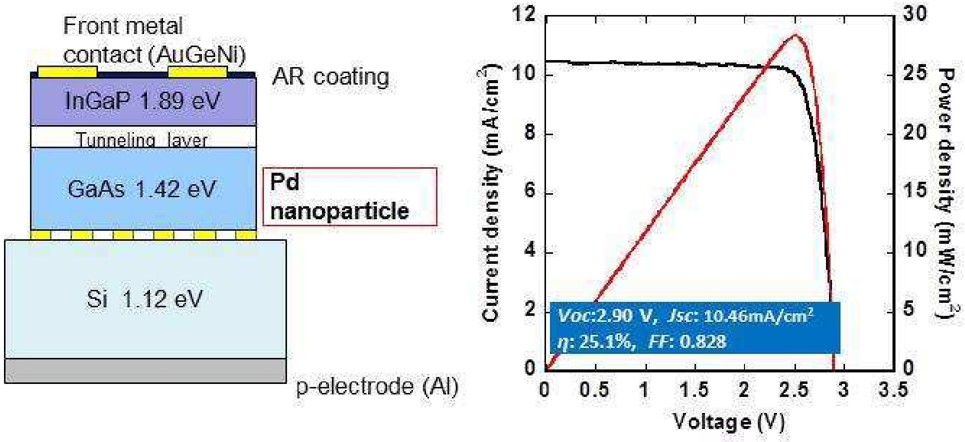

Fig 3: Schematic layer structure of a InGaP/GaAs//Si solar cell and its I-V characteristics.

Integrated Oxide Heterostructures for Electronics and Photonics

Alexander A. Demkov

Department of Physics, The University of Texas, Austin, Texas 78712, USA
e-mail: demkov@physics.utexas.edu

Compared to their better known semiconductor counterparts, heterostructures of transition metal oxides (TMO) offer many new possibilities in various device applications. In addition to quantum confinement that enables band engineering, these materials have several additional degrees of freedom that can be controlled, such as orbital, spin and polar orders, each of which can couple to external fields and strain, and sometimes to each other. Despite significant differences between the internal chemistry and physics, some TMOs can be integrated with common semiconductors, paving the way to hybrid technologies. In this talk I will briefly talk about our recent work on 2DEG at oxide interfaces such as γ-alumina/$SrTiO_3$ [1] (see Figures 1 and 2), applications of ferroelectrics integrated with semiconductors for carrier density modulation in FerroFET [2]. And then I will discuss applications of monolithically integrated bulk TMO films [3] and TMO quantum wells (QW) [4,5] in silicon photonics. The electro-optical (Pockels) effect in $BaTiO_3$ grown on Si is many times larger than that in commercially used $LiNbO_3$, and room-temperature intersubband absorption in $SrTiO_3$/$LaAlO_3$ QW heterostructures (see figure 3) is approaching the critically important telecom wavelength of 1.55 μm.

[1] K. J. Kormondy, A. B. Posadas, T. Q. Ngo, S. Lu, N. Goble, J. Jordan-Sweet, X. P. A. Gao, D. J. Smith, M. R. McCartney, J. G. Ekerdt, and A. A. Demkov, J. Appl. Phys. **117**, 095303 (2015).

[2] P. Ponath, K. Fredrickson, A. B. Posadas, Y. Ren, X. Wu, R. K. Vasudevan, M. B. Okatan, S. Jesse, T. Aoki, M. R. McCartney, D. J. Smith, S. V. Kalinin, K. Lai, and A. A. Demkov, Nature Comm. **6**, 6067 (2015).

[3] K. J. Kormondy, Y. Popoff, M. Sousa, F. Eltes, D. Caimi, M. D. Rossell, M. Fiebig, P. Hoffmann, C. Marchiori, M. Reinke, M. Trassin, A. A. Demkov, J. Fompeyrine and S. Abel, *Nanotechnology* **28**, 075706 (2017).

[4] C. Lin, A. B. Posadas, M. Choi, and A. A. Demkov, J. Appl. Phys. **117**, 034304 (2015).

[5] M. Choi, C. Lin, M. Butcher**,** C. Rodriguez, Q. He, A. B. Posadas, A. Y. Borisevich, S. Zollner, and A. A. Demkov, Appl. Phys. Lett. **106**, 192902 (2015).

978-3-901578-31-1

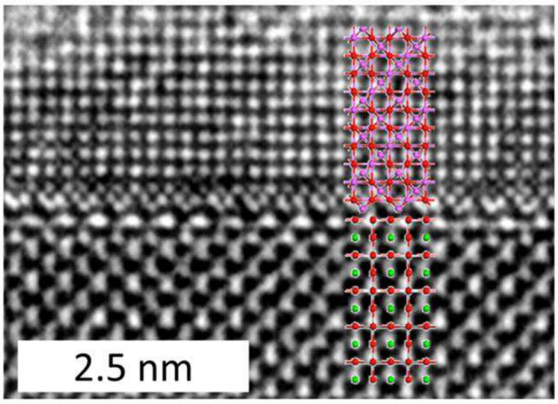

Fig.1: High-resolution electron micrograph in cross-section geometry confirming abrupt interface between highly crystalline epitaxial alumina on STO substrate.

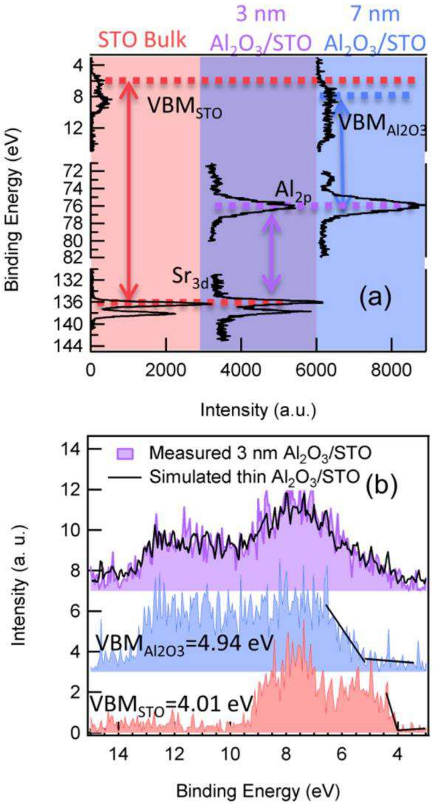

Fig.2: Core level (a) and valence band (b) spectroscopy for the following: STO substrate (red), 3 nm alumina/STO (purple), and 7 nm alumina/STO (blue).

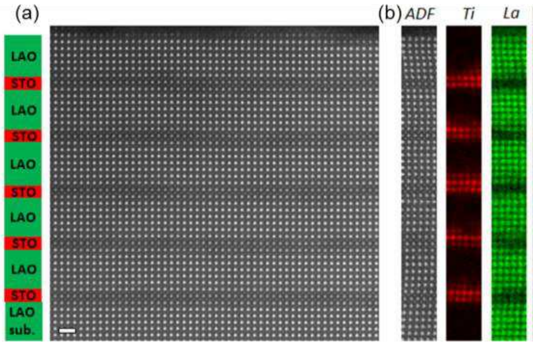

Fig.3: a) A representative STEM-HAADF image (Z-contrast) and a schematic of a [7 uc LAO/2 uc STO]$_5$ superlattice structure on LAO substrate, with schematic on the left. The scale bar is 1 nm. (b) STEM-EELS elemental maps of integrated intensities of Ti L (red) and La M (green) edges and the simultaneously acquired ADF signal. The top interfaces for each STO layer appear to be rough, while the corresponding bottom interfaces are much sharper.

Recent achievements in Ga_2O_3 MOSFET technology

Masataka Higashiwaki[1], Man Hoi Wong[1], Yoshiaki Nakata[1], Chia-Hung Lin[1],
Akinori Takeyama[2], Takahiro Makino[2], Takeshi Ohshima[2], Naoki Hatta[3],
Kuniaki Yagi[3], Ken Goto[4,5], Kohei Sasaki[4], Akito Kuramata[4],
Shigenobu Yamakoshi[4], Hisashi Murakami[5], and Yoshinao Kumagai[5]

[1] *National Institute of Information and Communications Technology, Koganei, Tokyo 184-8795, Japan*

[2] *National Institutes for Quantum and Radiological Science and Technology, Takasaki, Gunma 370-1292, Japan*

[3] *SICOXS Corporation, Chiyoda, Tokyo 101-8629, Japan*

[4] *Tamura Corporation, Sayama, Saitama 350-1328, Japan*

[5] *Tokyo University of Agriculture and Technology, Koganei, Tokyo 184-8588, Japan*

e-mail: mhigashi@nict.go.jp

Gallium oxide (Ga_2O_3) has not only attractive material properties represented by an extremely large bandgap of about 4.5 eV, but also bulk single crystals synthesized by melt growth methods that will enable future mass production of large-size, high-quality, and economical Ga_2O_3 wafers. In this talk, we will introduce our state-of-the-art Ga_2O_3 metal-oxide-semiconductor field-effect transistor (MOSFET) technologies developed for applications to power and harsh environment electronics.

Figure 1 shows a schematic cross section of Ga_2O_3 MOSFETs with a gate-connected field plate (FP) [1]. The FP-MOSFETs demonstrated a large off-state breakdown voltage of 755 V (Fig. 2), a large drain current (I_d) on/off ratio of over nine orders of magnitude at room temperature, stable device operation at temperatures up to 300°C, and negligible DC-RF dispersion (Fig. 3). We also investigated the radiation resistance of the MOSFETs. The devices were highly tolerant to gamma-ray irradiation by virtue of showing very little degradation in on-resistance and threshold voltage shift (Fig. 4) [2].

Recently, we fabricated and characterized first-generation vertical Ga_2O_3 MOSFETs as schematically illustrated in Fig. 5, wherein the source was electrically isolated from the drain by a current blocking layer (CBL) except at an aperture opening through which I_d was conducted [3]. Despite a large source-drain leakage current due to an imperfect function of the CBL, the I_d modulation by gate bias was successfully demonstrated as shown in Fig. 6.

This work was partially supported by Council for Science, Technology, and Innovation (CSTI), Cross-ministerial Strategic Innovation Promotion Program (SIP), "Next-generation power electronics" (funding agency: NEDO).

[1] M. H. Wong, M. H. *et al.*, IEEE Electron Device Lett. **37**, 212 (2016).
[2] M. H. Wong, M. H. *et al.*, *75th Device Research Conference, II-B.4, 2017.*
[3] M. H. Wong, M. H. *et al.*, *75th Device Research Conference, III-B.6 (Late news), 2017.*

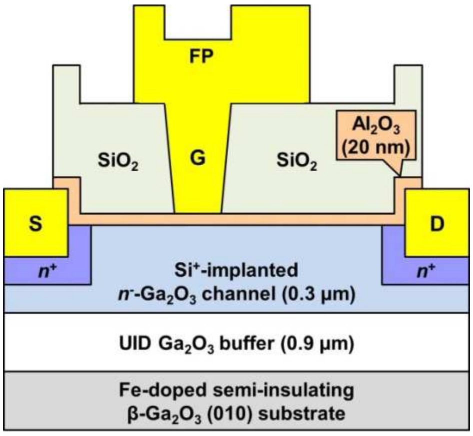

Fig.1: Schematic cross section of Ga_2O_3 FP-MOSFET.

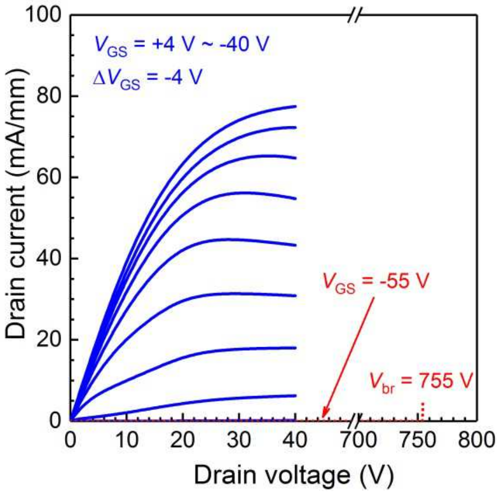

Fig.2: Room-temperature DC I_d-V_d characteristics of Ga_2O_3 FP-MOSFET.

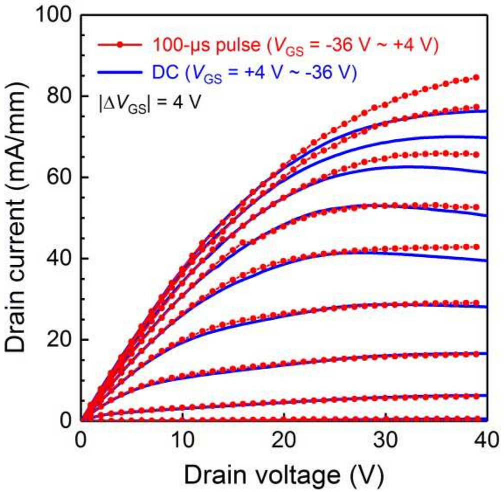

Fig.3: DC and pulsed I_d-V_d characteristics of Ga_2O_3 FP-MOSFET showing non-dispersive behavior.

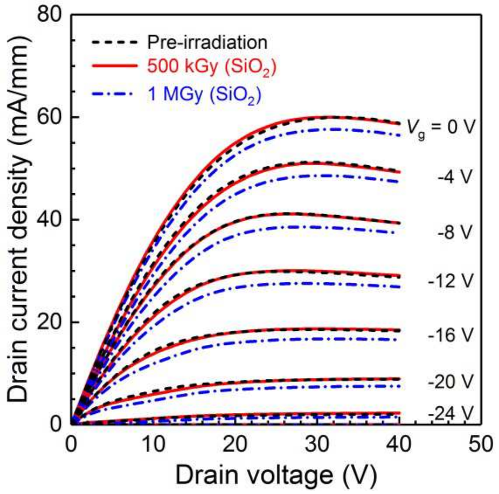

Fig.4: DC I_d-V_d characteristics of Ga_2O_3 FP-MOSFET before and after gamma-ray irradiation with total doses of 500 kGy and 1 MGy.

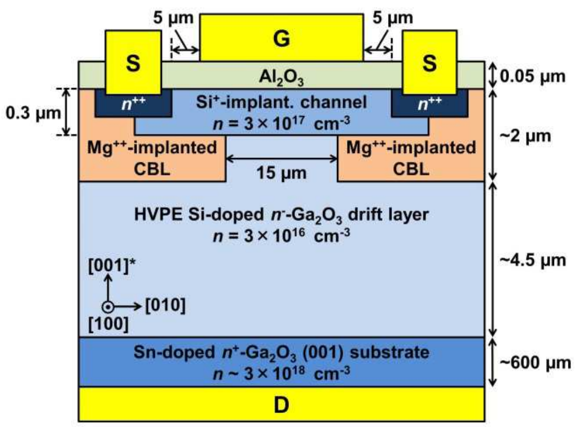

Fig.5: Schematic cross section of depletion-mode vertical Ga_2O_3 MOSFET.

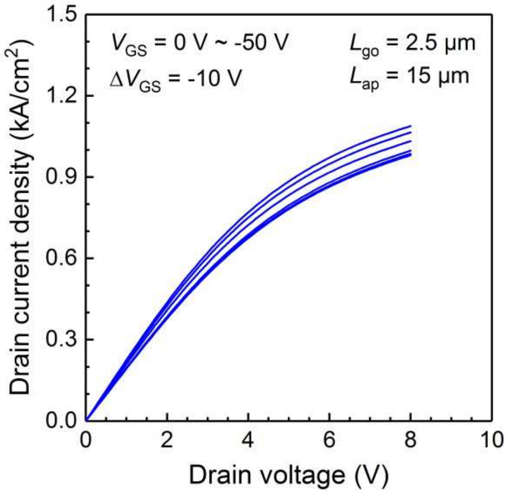

Fig.6: Room-temperature DC I_d-V_d characteristics of vertical Ga_2O_3 MOSFET.

978-3-901578-31-1

Terahertz light emission and lasing in graphene-based van der Waals 2D heterostructures

Deepika Yadav[1], Takayuki Watanabe[1], Stephane Boubanga-Tombet[1], Akira Satou[1],
Victor Ryzhii[1], and Taiichi Otsuji[1]

[1] *Research Institute of Electrical Communication, Tohoku University,*
Sendai, Miyagi 980-8577, Japan
e-mail: otsuji@riec.tohoku.ac.jp

Graphene has attracted considerable attention due to its massless and gapless energy spectrum. We designed and fabricated our original distributed-feedback dual-gate graphene-channel field-effect transistor (DFB-DG-GFET) [1, 2]. The DG-GFET structure serves carrier population inversion in the lateral p-i-n junctions under complementary dual-gate ($V_{g1,2}$) biased and forward drain-source (V_d) biased conditions, promoting spontaneous broadband incoherent THz light emission. The tooth-brash-shaped DG forms the DFB cavity having the fundamental mode at 4.96 THz, which can transcend the incoherent broadband LED to the single-mode lasing action (Fig. 1). The GFET channel consists of a few layer (non-Bernal) highest-quality epitaxial graphene [3], providing an intrinsic field-effect mobility exceeding 100,000 cm^2/Vs [4]. Fourier-transform far-infrared spectroscopy revealed the THz emission spectra for the fabricated samples under population inversion conditions; one sample exhibited a 1-7.6-THz broadband, rather intense (~80 μW) amplified spontaneous emission [1] and the other sample did a weak (~0.1 μW) single mode lasing at 5.2 THz [2] both at 100K. Introduction of the graphene plasmonics in vdW 2D heterostructures is a key to increase the operating temperature and radiation intensity. Asymmetric dual-grating-gate metasurface structures may promote plasmonic superradiance [5] and/or plasmonic instabilities [6], giving rise to giant THz gain enhancement at plasmonic resonant frequencies (Fig. 2). Further improvement will be given by a gated double-graphene-layer (G-DGL) nanocapacitor vdW 2D heterostructures [7,8]. Exploitation of the graphene plasmonics in vdW 2D heterostructures [9] will be the key to realize room-temperature, intense THz lasing (Fig. 3).

The authors thank A.A. Dubinov, D. Svintsov, M. Ryzhii, V. Mitin, and M.S. Shur for their contributions. Financial support: JSPS KAKENHI Nos. 16H06361 and 16K14243, Japan.

[1] D. Yadav et al., CLEO 2017 Dig., **1**, AM2B.7 (2017); [2] G. Tamamushi, et al., 74th Dev. Res. Conf. Dig., **1**, 225 (2016); [3] T. Someya et al., Phys. Rev. B, **95**, 165303 (2017); [4] A. Satou et al., IEEE Trans. Electron Dev., **63**, 330 (2016); [5] V.V. Popov et al., Phys. Rev. B, **86**, 195437 (2012); [6] Y. Koseki et al., Phys. Rev. B, **93**, 245408 (2016); [7] V. Ryzhii et al., Opt. Exp., **21**, 31569 (2013); [8] D. Yadav et al., 2D Mater., **3**, 045009 (2016); [9] D. Svintsov et al., Phys. Rev. B, **94** , 115301 (2016).

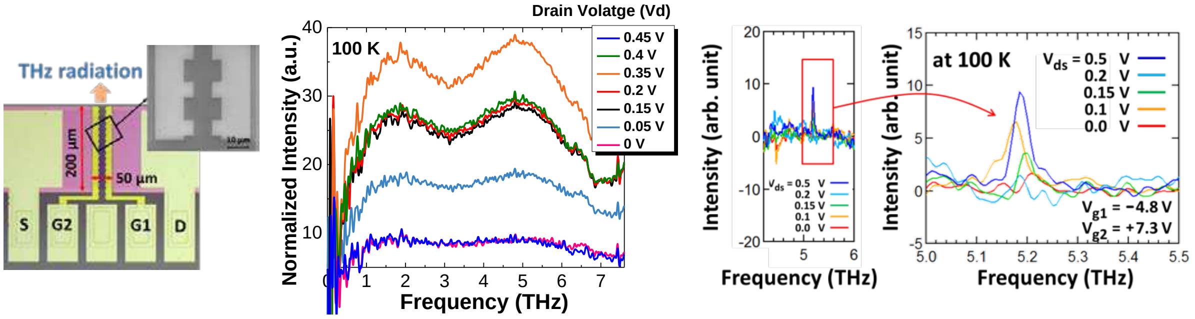

(a) (b) (c)

Figure 1: *DFB-DG-GFET. (a) Micro-photo image. (b) LED-like broadband THz emission. (c) Laser-like single-mode emission at 5.2 THz.*

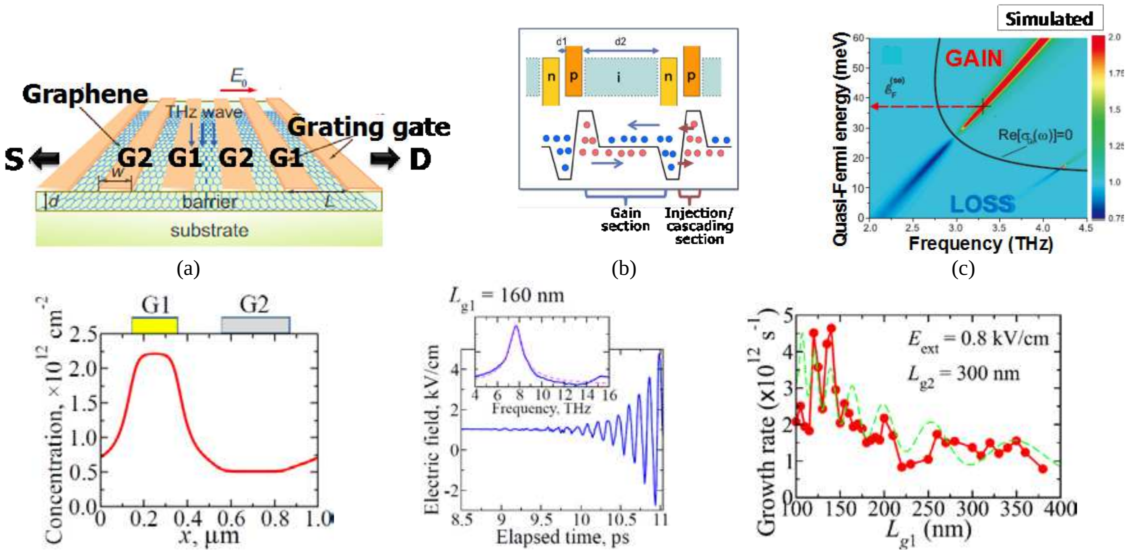

(a) (b) (c)

(d) (e) (f)

Figure 2: *ADGG-GFET. (a)Birds view structure. (b) Comprementary biasing for current-injection pumping scheme. (c) Simulated resonant enhancement on gain for superradiant plasmonic lasing. (d) Unipolar/depletion biasing for instability-driven scheme. (e) Simulated time evoluved self-oscillation at ~8 THz. (f) Simulated voltage amplitude growth rate of the instability-driven oscillation as a function of the plasmon cavity length* L_{g1}.

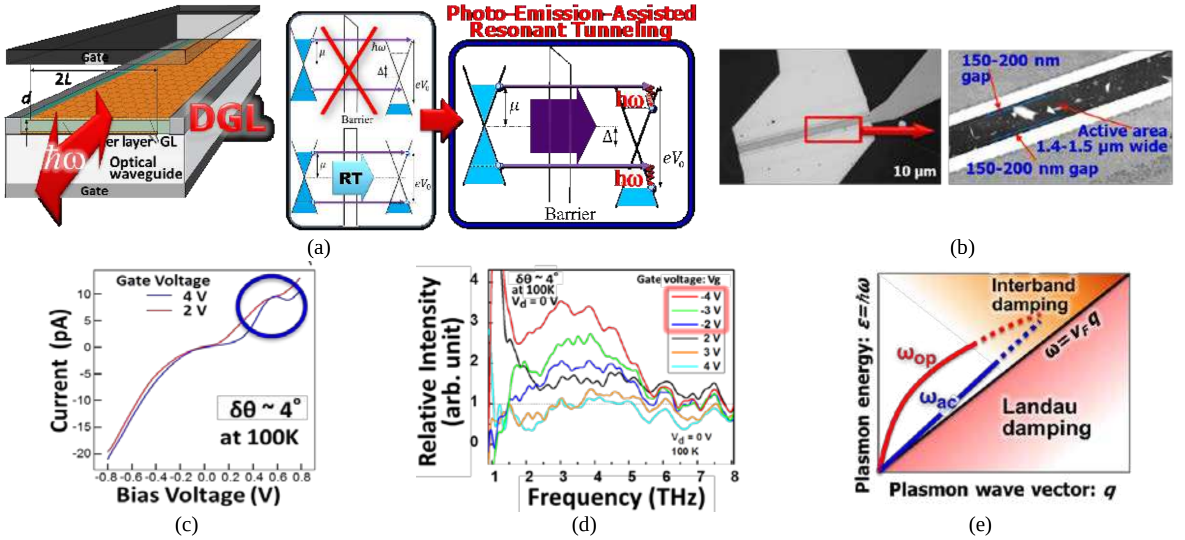

(a) (b)

(c) (d) (e)

Figure 3: Gated DGL vdW 2D heterostructure. *(a) Device structure and band diagrams showing photo-emission-assisted resonant tunneling. (b) Microphoto images of a fabricated device. (c) Measured current-voltage characteristic exhibiting a weak negative-differential conductance profile at 100K. (d) Measured THz emission spectra. (e) Dispersions for optical and acoustic plasmons in a DGL.*

Concepts of infrared and terahertz photodetectors based on van der Waals heterostructures with graphene layers

Victor Ryzhii[1,2,3], Taiichi Otsuji[1], and Michael S. Shur[4]

[1] *Research Institute of Electrical Communication,*
Tohoku University, Sendai 980-8577, Japan
[2] *Institute of Ultra High Frequency Semiconductor Electronics of RAS,*
Moscow 117105, Russia
[3] *Center for Photonics and Infrared Engineering,*
Bauman Moscow State Technical University, Moscow 111005, Russia
[4] *Department of Electrical, Electronics, and Systems Engineering,*
Rensselaer Polytechnic Institute, Troy, New York 12180, USA
e-mail: v-ryzhii@riec.tohoku.ac.jp

The absence of the energy gap in graphene layers (GLs) enables their use in the interband detectors and sources of infrared (IR) and terahertz (THz) radiation. The incorporation of the GLs into the van der Waals (vdW) heterostructures [1] based on such materials as hBN, WS_2, InSe, GaSe, and similar materials can promote the creation of novel IR and THz devices with the elevated performance. Contrary to the heterostructures grown epitaxially using traditional materials, the vdW heterostructures do not require the lattice-match condition. This is due to the weak inter-layer bonding. As a result, the layers with different lattice constants can be stacked together. This allows to use a wide family of the vdW materials with diverse electronic properties to produce the heterostructures with desirable properties and perfect layers. Different vdW/GL devices, including transistors, photodetectors, and light-emitting devices have already been fabricated and studied experimentally.

In this communication, we analyze the concept and characteristics of the detectors of IR and THz radiation based on the vertical vdW/GL heterostructures recently proposed by us and our co-workers. The vdW/GL photodetectors can be realized using a single or multiple GLs sandwiched between the vdW material barrier layers. The operation of such vdW/GL photodetectors is associated with the photoassisted escape of electrons from the GLs into the continuum states in the conduction band of the barrier layers due to the interband photon absorption, the propagation photoexicted electrons and the electrons injected from the emitter travel across the heterostructure and their capture into the GLs and collection by the collector contact. The space charge of the holes trapped in the GLs provides a relatively large injection and photoelectric gains. We calculate the vdW/GL photodetector responsivity and dark-current limited detectivity as functions of the energy of incident infrared photons and the structural parameters. The doping engineering provides wide opportunities for the optimization of vdW/GL photodetectors for operation in different radiation spectrum ranges. We compare the characteristics (responsivity, detectivity, and speed of operation) of the vertical vdW/GL photodetectors with some more traditional photodetectors.

The hybrid devices based on the integration of the vdW/GL detectors and light-emitting diodes can be also used for the up-conversion from far- or mid-IR range to near-IR or visible ranges.

[1] A. K. Geim and I. V. Grigoreva, Nature **499**, 419 (2013).

978-3-901578-31-1

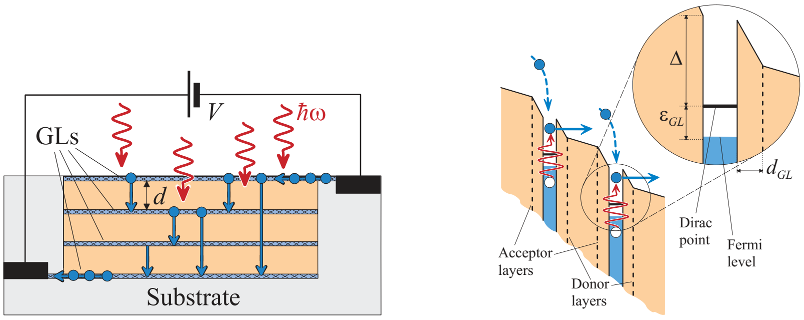

Figure 1: Schematic view of the vdW/GL photodetector (left panel) and the band diagram fragment (right panel) for the particular case of the device with selective dipole doping of GLs and barrier layer. Wavy, solid, and dashed arrows indicate the processes of the electron photoexcitation, tunneling, and capture, respectively.

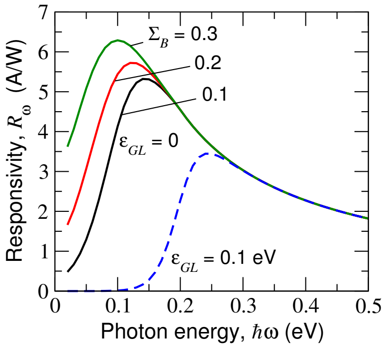

Figure 2: Responsivity of vdW/GL photodetectors with the barrier height (see the inset in Fig. 1) $\Delta = 0.1$ meV, five undoped GLs (electron Fermi energy $\varepsilon_{GL} = 0$), and different donor and acceptor densities in the barriers Σ_B (in units 10^{12} cm^2) versus photon energy at $T = 100$ K and other typical structural parameters. Dashed line corresponds to the doped GL device with the density $\Sigma_{GL} = 0.8 \times 10^{12}$ cm^2 and undoped barrier layers.

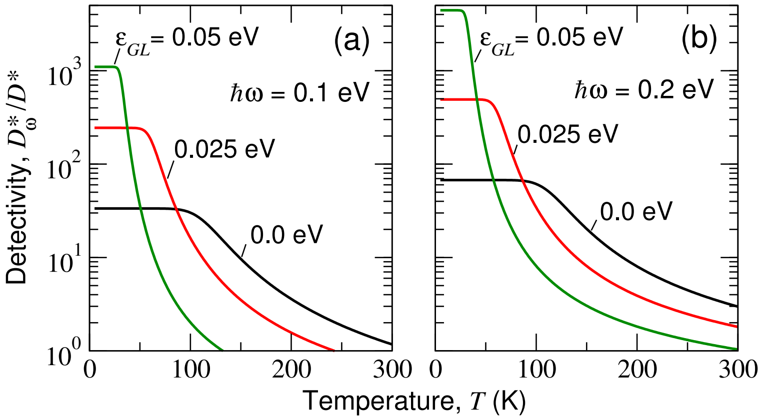

Figure 3: Temperature dependences of the normalized dark-current limited detectivity of vdW/GL photodetectors with $\Delta = 0.1$ eV, undoped barriers and different Fermi energies ε_{GL} for (a) $\hbar\omega = 0.1$ eV and (b) $\hbar\omega = 0.2$ eV ($D^* = (0.5 - 7.0) \times 10^5$ cm$\sqrt{Hz}$/W).

Quantized Ballistic Transport of Electrons and Electron Pairs in an Electron Waveguide

Anil Annadi[1,2], Shicheng Lu[1,2], Hyungwoo Lee[3], Jung-Woo Lee[3], Guanglei Cheng[1,2], Anthony Tylan-Tyler[1,2], Megan Briggeman[1,2], Michelle Tomczyk[1,2], Mengchen Huang[1,2], David Pekker[1,2], Chang-Beom Eom[3], Patrick Irvin[1,2], Jeremy Levy[1,2*]

[1]Department of Physics and Astronomy, University of Pittsburgh, Pittsburgh, PA 15260, USA.
[2]Pittsburgh Quantum Institute, Pittsburgh, PA, 15260 USA. [3]Department of Materials Science and Engineering, University of Wisconsin-Madison, Madison, WI 53706, USA.
E-mail: jlevy@pitt.edu

Electrons undergo profound changes in their behavior when constrained to move along a single axis. Theories of one-dimensional (1D) transport of interacting electron systems depend crucially on the sign of the electron-electron interaction. To date, 1D electron transport has only been explored within material systems with repulsive electron-electron interactions. $SrTiO_3$-based heterointerfaces support quasi-two-dimensional (2D) electron systems that are analogous to III-V semiconductor heterostructures, but also possess superconducting, magnetic, spintronic, ferroelectric and ferroelastic degrees of freedom. Despite these rich properties, the relatively low mobilities of 2D complex-oxide interfaces appear to preclude ballistic transport in 1D. Here we show [1] that nearly ideal 1D electron waveguides exhibiting quantized ballistic transport of electrons and (non-superconducting) electron pairs can be formed at the interface between the two band insulators $LaAlO_3$ and $SrTiO_3$. These electron waveguides are created using a well-established conductive atomic-force microscope (c-AFM) lithography technique that enables nanoscale control of the metal-insulator transition at the $LaAlO_3/SrTiO_3$ interface. Quantized ballistic transport within conducting nanowires at low temperature ranges from truly single-mode (1D) to three-dimensional (3D), depending on the applied magnetic field and gate voltage. Quantization of the lowest e^2/h plateau indicate a ballistic mean-free path $l_{MF} \sim 20\ \mu m$, with comparable values for ballistic electron pair transport. These results yield new insights into the electronic structure of the $LaAlO_3/SrTiO_3$ system and offer a new platform for the study of strongly interacting 1D electronic systems.

[1] https://arxiv.org/abs/1611.05127

978-3-901578-31-1

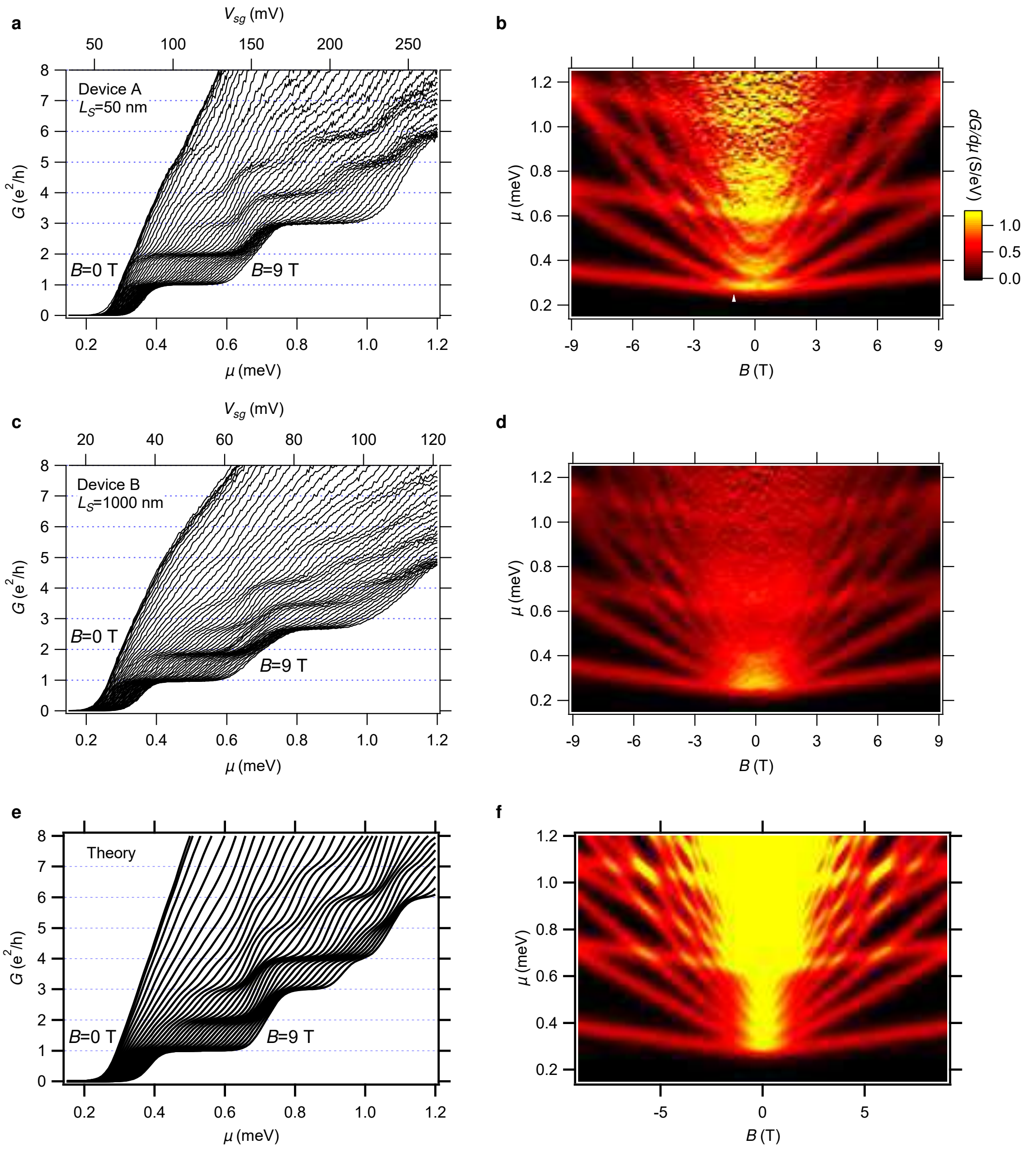

Conductance and transconductance of devices A and B, and comparison with theory. (a and c) Zero-bias conductance of device A ($L_B = 20\,\mathrm{nm}, L_C = 500\,\mathrm{nm}, L_s = 50\,\mathrm{nm}$) (a) and device B ($L_B = 20\,\mathrm{nm}, L_C = 1{,}800\,\mathrm{nm}, L_S = 1{,}000\,\mathrm{nm}$) (b) as a function of chemical potential μ and magnetic fields B in the range 0-9 T. (b and d) Transconductance $dG/d\mu$ shown as a function of μ and B for device A (b) and device B (d). Each bright band marks the crossing of a subband, and the white arrow in (b) indicates the pairing field B_P ≈1 T. The revealed subband structures show remarkable similarity between these two devices. (e) Theoretical zero-bias conductance curves, modeling device A, for a non-interacting channel as a function of the chemical potential and magnetic field. (f) Corresponding transconductance $dG/d\mu$ as a function of μ and B. Transitions have been broadened by a 65 μeV-wide Lorentzian.

Enhanced sensitivity of MEMS-based terahertz bolometers by introducing two-dimensional phononic crystal structures

Y. Zhang[1], B. Qiu[1], N. Nagai[1], M. Nomura[1,2], and K. Hirakawa[1,2]
[1] *Center for Photonics Electronics Convergence, Institute of Industrial Science, University of Tokyo, 4-6-1 Komaba, Meguro-ku, Tokyo 153-8505, Japan*
[2] *Institute for Nano Quantum Information Electronics, University of Tokyo, 4-6-1 Komaba, Meguro-ku, Tokyo 153-8505, Japan*
e-mail:zhangya@iis.u-tokyo.ac.jp

Microelectromechanical system (MEMS)-based resonators are very attractive for sensing applications owing to their high sensitivities. Recently, we proposed an uncooled, all electrical driving and detecting, sensitive bolometer by using a doubly clamped GaAs MEMS beam resonator, which is very promising for realizing high sensitivity and fast terahertz (THz) detection at room temperature [1,2]. The sensitivity of the MEMS bolometer is inversely proportional to the thermal conductivity, κ, of the beam. It has been considered that κ is specific to the material and cannot be changed.

In this work, we have fabricated a two-dimensional phononic crystal (PnC) structure on the MEMS beam resonators to modulate their thermal conductances. Since the phonon wavelength at 300 K is much shorter than the period of the fabricated PnCs, the predominant effect of the PnCs is to enhance phonon scattering and reduce the thermal conductance of the beam. Figure 1(a) shows a schematic sample structure. A PnC is fabricated on the beam resonator by electron beam lithography and subsequent reactive ion etching. Figure 1(b) shows an SEM image of the fabricated PnC structure. As seen in the figure, an array of holes was homogenously fabricated on the beam. Figure 1(c) shows the measured thermal conductance as a function of the volume of the remaining material. We have found that the reduction of the thermal conductance is more than what we expect from the material that has been removed by the PnC, indicating that the PnC structure indeed reduces the thermal conductivity of the GaAs beam. Figure 1(d) shows the measured shifts in the resonance frequency of the beam as a function of the applied input heating power. As seen in Fig. 1(d), the samples with PnC show larger thermal sensitivities (1.6~2 times) than that of the reference sample without PnC, indicating effectiveness of PnCs for thermal sensing applications.

[1] Y. Zhang, Y. Watanabe, S. Hosono, Nagai, and K. Hirakawa, Appl. Phys. Lett. **108**, 163503 (2016).
[2] Y. Zhang, S. Hosono, Nagai, and K. Hirakawa, Appl. Phys. Lett. **111**, 023504 (2017).

978-3-901578-31-1

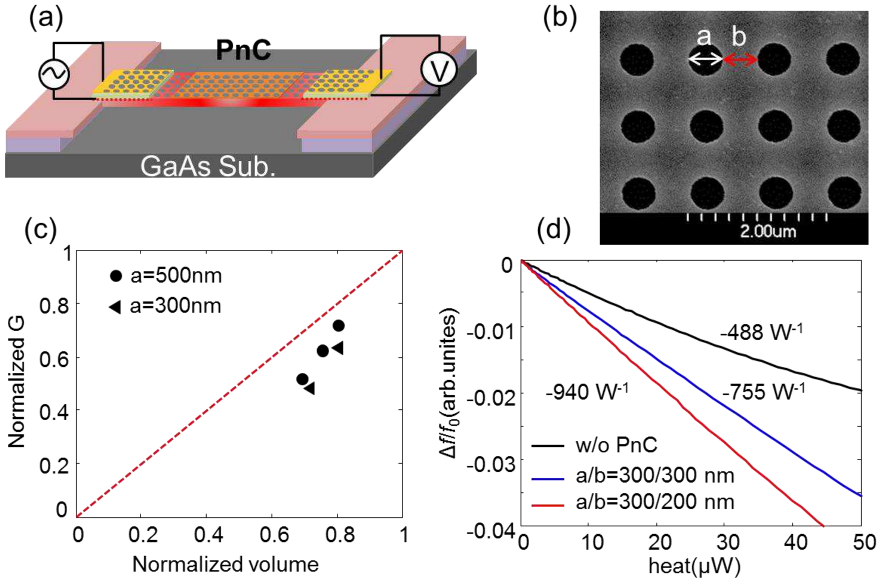

Fig.1 (a) Schematic sample structure of the MEMS resonator integrated with a PnC structure. (b) An SEM image of the fabricated PnC structure (diameter a = 300nm, neck size b = 300nm). (c) The measured thermal conductance as a function of the volume of the remaining material. (d) Frequency responsivity of the MEMS beam resonator samples with and without PnCs.

978-3-901578-31-1

Thermal manipulation of THz wave from high-T_c superconducting emitters

Shiro Kawabata, and Hidehiro Asai

Nanoelectronics Research Institute (NeRI),
National Institute of Advanced Industrial Science and Technology (AIST), Tsukuba, Japan
e-mail: s-kawabata@aist.go.jp

A high Tc superconductor such as $Bi_2Sr_2CaCu_2O_{8+\delta}$ (Bi2212) is comprised of intrinsic Josephson junctions (IJJs), that is, natural stacks of Josephson junctions composed of the stacking of superconducting CuO_2 layers and insulating layers. Thus, the AC Josephson current flows through the crystal under DC bias voltage, and this generates the terahertz (THz) electromagnetic wave. In the last few years, a considerable number of studies have been made on intense THz emission form mesa-structured IJJ [1].

Since we apply a bias voltage to an IJJ mesa in order to generate AC Josephson current, the IJJ mesa is in the resistive state during the THz emission process. Thus, the temperature of the mesa can be higher than the superconducting critical-temperature T_c due to the self-heating effect. Recently the appearance of a “hot spot” in an IJJ mesa during strong THz emission where the temperature is locally higher than T_c has been observed [2]. Therefore, the “inhomogeneity” in the mesa such as hot spot is expected to play a key role in the THz radiation process. In fact, recent theoretical and experimental studies reported that the inhomogeneity coming from local heating of IJJ mesas drastically changes the THz emission power [3,4] (Fig. 1 and 2). Thus, local heating of IJJs by external heat sources is expected to be a promising way to amplify the THz power from IJJ mesas [3].

In this presentation, toward the design of the practical THz emitter, the THz emission from an IJJ mesa which is heated locally by an external thermal source, e.g., laser irradiation, will be discussed (See Fig. 3). We focus on a mesa-structured IJJ whose geometry is slightly deviate from a square and find that the local heating make it possible to emit circularly-polarized THz waves [5]. In this mesa, the inhomogeneity of critical current density induced by the local heating excites the electromagnetic cavity modes TM (1,0) and TM (0,1), whose polarizations are orthogonal to each other. The mixture of these modes results in the generation of circularly-polarized THz waves (Fig. 4). We also show that the circular polarization dramatically changes with the applied voltage. The emitter based on IJJs can emit circularly-polarized and continuum THz waves by the local heating, and will be useful for various technological application.

[1] L. Ozyuzer *et al.*, Science **318**, 1291 (2007).
[2] H. B. Wang *et al.*, Phys. Rev. Lett. **105**, 057002 (2010).
[3] H. Asai and S. Kawabata, Appl. Phys. Lett. **104,** 112601 (2014).
[4] M. Tsujimoto *et al.*, Phys. Rev. Applied **2**, 044016 (2014).
[5] H. Asai and S. Kawabata, Appl. Phys. Lett. **110**, 054021 (2017).

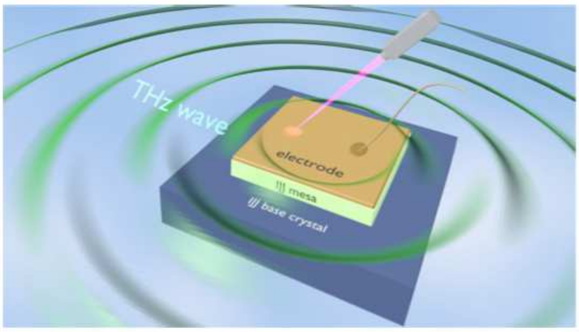

Fig.1: Schematic figure of high-Tc superconductor intrinsic Josephson junction (IJJ) mesa locally heated by laser irradiation.

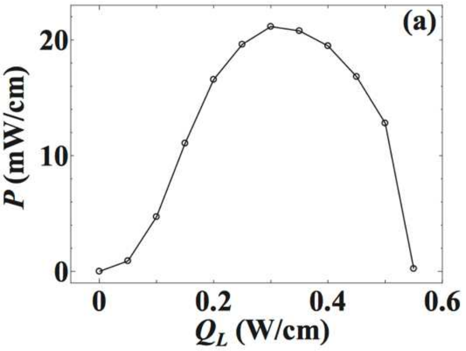

Fig.2: Emission power P as a function of the heating power Q_L of the heating spot.

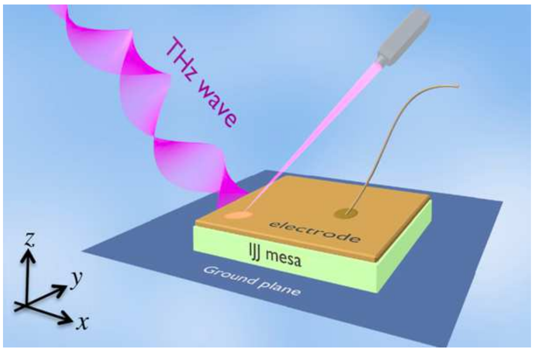

Fig.3: Schematic figure of high-Tc superconductor IJJ mesa whose geometry is almost square and is locally heated by laser irradiation.

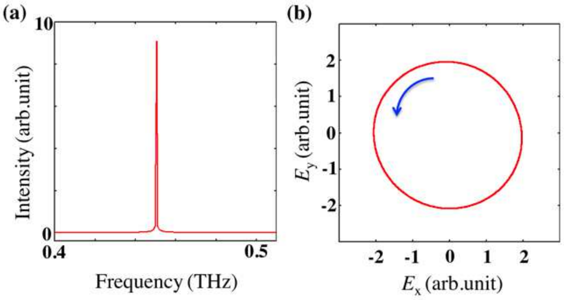

Fig.4 (a) A frequency spectrum of THz waves emitted from the IJJ mesa, and (b) a trajectory of the far electric field along the z axis. A blue arrow indicates the time evolution of the electric field.

Ultrafast Electron Transfer in van der Waals Multilayers

Hui Zhao

Department of Physics and Astronomy, University of Kansas, Lawrence, Kansas 66045, USA
e-mail: huizhao@ku.edu

Recently, heterostructures formed by two-dimensional materials have drawn considerable attention. Such new materials can potential combine novel properties of participating atomic layers and form emergent properties suitable for a number of applications. In developing these materials, one key issue is to understand and control interlayer charge and energy transfer.

In this seminar, I will present recent progress on experimental studies of ultrafast electron transfer between monolayer semiconductors. I will first summarize previous studies by several groups on electron transfer in van der Waals hetero-bilayers, such as $MoS_2/MoSe_2$, WS_2/graphene, and $MoS_2/MoTe_2$. Secondly, I will present latest results on van der Waals bilayers, with emphases on demonstration of a type-I band alignment and study of electron transfer in homo-bilayers. I will then discuss electron transfer in van der Waals trilayers, and show evidence of the coherent nature of the transfer. Such measurements were further expanded to a set of samples, where the electron transfer rate and recombination time are systematically probed as the number of involved atomic layers evolves from one to four. Next, I will show that by band-alignment engineering, it is possible to control the flow and population of electrons in different atomic layers. As an example, we achieved unipolar optical doping of graphene with significantly extended photocarrier lifetimes. Finally, I will report ultrafast measurements of charge transfer in a lateral heterostructure formed by monolayers of MoS_2 and $MoSe_2$.

[1] J. He et al., Nat. Commun. 5, 5622 (2014).
[2] F. Ceballos et al., ACS Nano 8, 12717 (2014).
[3] M. Z. Bellus et al., ACS Nano 9, 6459 (2015).
[4] S. Pan et al., 2D Mater. 4, 015033 (2016).
[5] M. Z. Bellus et al., Nanoscale Horizons 2, 31 (2017)
[6] F. Ceballos et al., Nano Lett. **17**, 1623 (2017).

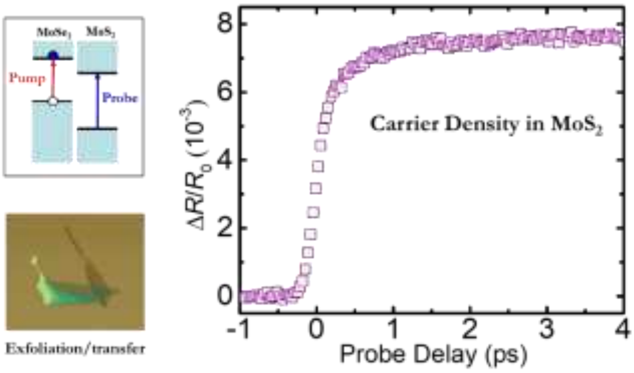

Fig.1: Transient absorption measurement of charge transfer in MoS_2-$MoSe_2$ heterostructures. Electrons and holes are excited in $MoSe_2$. Transfer of electrons to MoS_2 is monitored by probing carrier density in MoS_2.

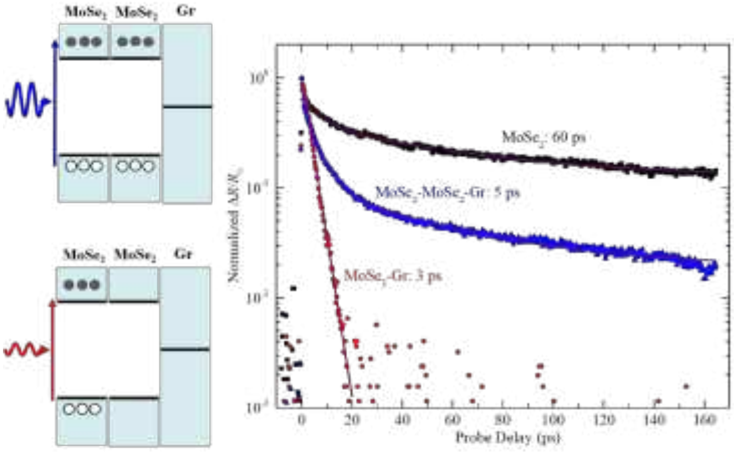

Fig.2: Transient absorption measurement of photocarrier transfer between two randomly stacked $MoSe_2$ monolayers on top of a graphene layer. Carriers excited in the middle layer transfer to graphene quickly (red symbols). The slower decay (blue symbols) is controlled by transfer of photocarriers from the top to the middle $MoSe_2$ layer, since decay of population in $MoSe_2$ monolayer is much slower.

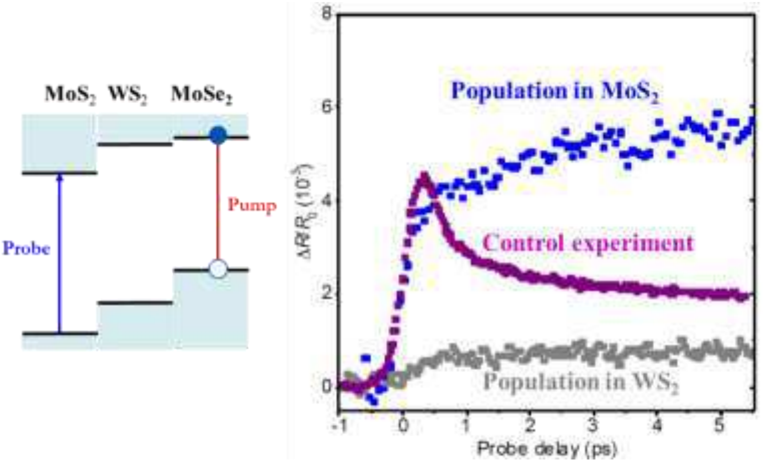

Fig.3: In a trilayer sample formed by MoS_2, WS_2, and $MoSe_2$ monolayers, a pump pulse excites carriers in $MoSe_2$. The transfer process of electrons to MoS_2 is monitored by probing the buildup of carrier density in MoS_2 (blue symbols). The transfer time is about 1.5 ps, which is consistent with first-principle calculations. During the transfer, the electrons never populated the middle WS_2 layer (gray symbols), suggesting the coherent nature of the transfer, which is also confirmed by theory.

Semiconductor heterojunctions based on 2D materials

Yasumitsu Miyata

Department of Physics, Tokyo Metropolitan University, Hachioji, Tokyo 192-0397, Japan
e-mail: ymiyata@tmu.ac.jp

Conventional semiconductor heterojunctions with two-dimensional (2D) interfaces have been an important topic, both in modern solid state physics and in electronics and optoelectronics applications. Recently, the in-plane heterostructures of transition metal dichalcogenide (TMDC) atomic layers are expected to provide a novel one-dimensional (1D) interface with unique physical properties and applications. Even though there have been several reports on the growth and device studies of such atomic-layer heterojunction interfaces, it is still an important challenge to develop a sophisticated growth process and their microscopic basis of electronic properties. For this purpose, we have fabricated high-quality TMDC atomic layers and various heterostructures based on TMDCs [1-5]. Herein, we report on growth and characterization of atomic layer heterostructures based on TMDCs.

Chemical vapor deposition (CVD) was used to prepare high-quality TMDC atomic layers on exfoliated graphite flakes, as reported in our previous paper [1]. As shown in Fig. 1b, WS_2 (or MoS_2) grains are initially synthesized on the graphite, after which the second growth of another TMDCs is conducted. High quality of samples grown on graphite was confirmed from sharp photoluminescence peak (Fig.2) [1]. Scanning tunneling microscopy/spectroscopy (STM/STS) analyses revealed that the monolayer heterojunction has atomically-sharp interface structure, and form conventional type II heterojunction with staggered gap (Fig.3a,b) [3]. Interestingly, we found that the bilayer samples showed the formation of 1D confining potential (potential barrier) in the valence (conduction) band, as well as bandgap narrowing around the heterointerface (Fig.3c) [5]. The present findings indicate that the atomic layer heterojunctions provide a novel system to realize tunable 1D electrical potential for embedded quantum wires and ultrashort barriers of electrical transport.

[1] Y. Kobayashi *et al.*, ***ACS Nano***, 9, 4056 (2015).
[2] Y. Kobayashi *et al*., ***Nano Res***., 8, 3261 (2015).
[3] S. Yoshida, *et al*., ***Sci. Rep.***, 5, 14808 (2015).
[4] S. Sasaki *et al.*, ***Appl. Phys. Express*** 9, 071201 (2016).
[5] Y. Kobayashi *et al*., ***Sci. Rep.***, 6, 31223 (2016).

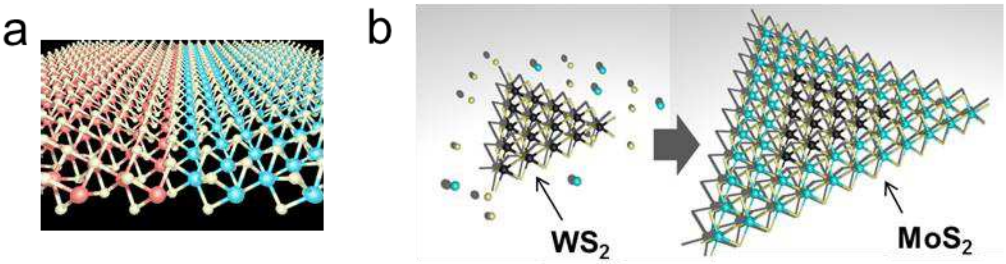

Fig. 1. Structure model of (a) in-plane heterostructure of MoS_2 *and* WS_2 *and (b) their growth process by chemical vapor deposition.*

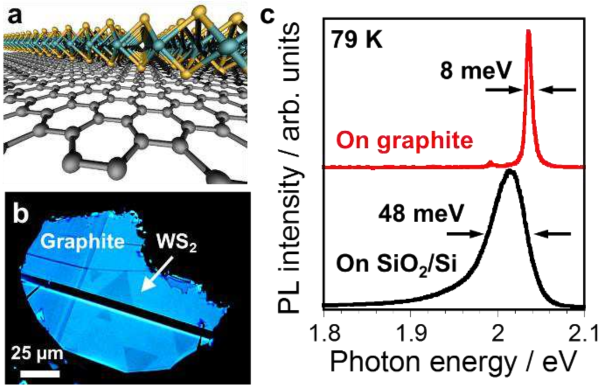

Fig. 2. (a) Structure model and (b) optical image of monolayer WS_2 *grown on graphite. (c) PL spectra of monolayer* WS_2 *on graphite and* SiO_2*/Si substrates at 79 K.*

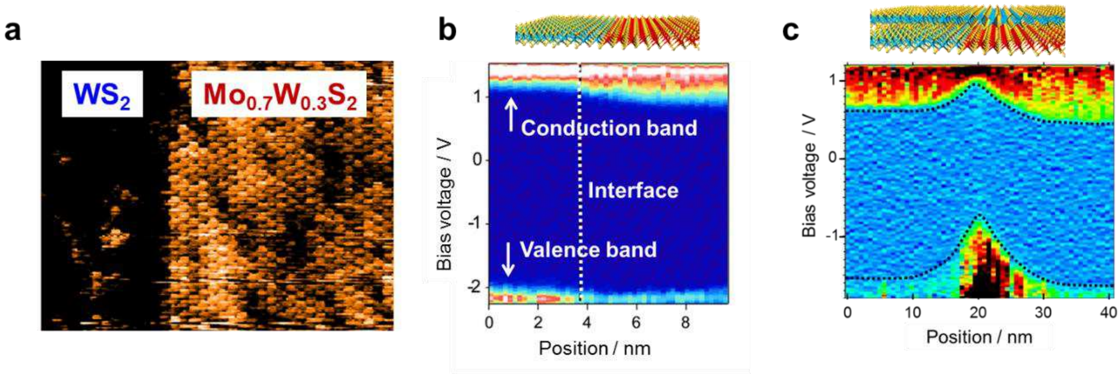

Fig. 3. (a) STM image of interface of $WS_2/Mo_{0.7}W_{0.3}S_2$ *in-plane heterostruture. Structure models and maps of color scale dI/dV curves calculated from the spatially-resolved STS spectra for (a) monolayer- and (c) bilayer-based in-plane heterostructures.*

Recent advances in colloidal-quantum-dot lasing: From zero-threshold optical gain to solution-processible laser diodes

Young-Shin Park, Jaehoon Lim, Kaifeng Wu, and Victor I. Klimov

Los Alamos National Laboratory, Los Alamos, NM 87545, USA
e-mail: klimov@lanl.gov

Chemically synthesized quantum dots (QDs) can potentially enable a new class of highly flexible lasers processible from solutions without complications associated with vacuum-based epitaxial techniques [1,2]. Colloidal QDs feature near-unity emission quantum yields and widely tunable emission wavelengths controlled by their size and/or composition. Further, a wide separation between electronic levels and low degeneracies of band-edge states reduce the lasing threshold and enhance temperature stability compared to semiconductor quantum wells used in traditional laser diodes. Despite a considerable progress over the past years, colloidal-QD lasing is still at the laboratory stage and an important challenge - realization of lasing with electrical injection - is still unresolved. A major complication, which hinders the progress in this field, is fast nonradiative Auger recombination of gain-active multi-carrier species [3,4]. Recently, we explored several approaches for mitigating the problem of Auger decay by taking advantage of a new generation of core/multi-shell QDs with a radially graded composition (Fig. 1a,b) that allow for considerable (nearly complete) suppression of Auger recombination by "softening" the electron and hole confinement potentials. Using these specially engineered QDs, we have been able to achieve two important milestones in the QD field, that is, the first demonstration of continuous-wave colloidal-QD lasing with optical excitation [5] and the first realization of optical gain in colloidal nanostructures with direct-current electrical pumping (Fig. 2) [6]. Further, using these new QDs, we have been able to practically demonstrated the viability of a "zero-threshold-optical-gain" concept using not neutral but negatively charged particles wherein the pre-existing electrons block either partially or completely ground-state absorption [7]. Such charged QDs are optical-gain-ready without excitation and, in principle, can exhibit lasing at vanishingly small pump levels. All of these exciting recent developments demonstrate a considerable promise of colloidal nanomaterials for implementing solution-processible optically and electrically pumped laser devices operating at virtually any wavelength using a verity of optical cavity designs. These materials are also ideally suited for the realization of novel concepts such as laser lighting and displays, on-chip optical interconnects, and multidimensional laser arrays.

[1] Klimov, V. I. *et al.* Optical gain and stimulated emission in nanocrystal quantum dots. *Science* **290**, 314 (2000).
[2] Klimov, V. I. *et al.* Single-exciton optical gain in semiconductor nanocrystals. *Nature* **447**, 441 (2007).
[3] Klimov, V. I., Mikhailovsky, A. A., McBranch, D. W., Leatherdale, C. A. & Bawendi, M. G. Quantization of multiparticle Auger rates in semiconductor quantum dots. *Science* **287**, 1011 (2000).
[4] Robel, I., Gresback, R., Kortshagen, U., Schaller, R. D. & Klimov, V. I. Universal Size-Dependent Trend in Auger Recombination in Direct-Gap and Indirect-Gap Semiconductor Nanocrystals. *Phys. Rev. Lett.* **102**, 177404 (2009).
[5] Fan, F. *et al.* Continuous-Wave Lasing in Colloidal Quantum Dot Solids Enabled by Facet-Selective Epitaxy. *Nature* **544**, 75 (2017).
[6] Lim, J., Park, Y.-S. & Klimov, V. I. Optical Gain in Colloidal Quantum Dots Achieved by Direct-Current Charge Injection. *Nat. Mater.* **in press** (2017).
[7] Wu, K., Park, Y.-S., Lim, J. & Klimov, V. I. Towards zero-threshold optical gain using charged semiconductor quantum dots. *Nat. Nanotechnol.* **in press** (2017).

978-3-901578-31-1

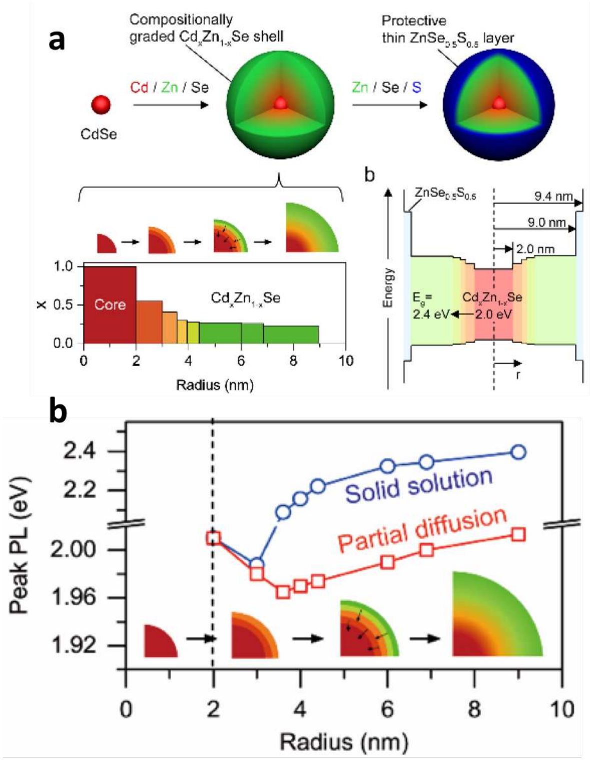

Fig. 1: Compositionally graded core/multi-shell QDs. (a) Reaction schematics (top), radial compositional profile (lower left), and approximate band structure (lower right) of QDs with the 2-nm CdSe core radius, 7-nm $Cd_xZn_{1-x}Se$ shell, and <1-nm final $ZnSe_{0.5}S_{0.5}$ layer. (b) In the case of a uniform alloying (solid solution), the projected band gap (blue circles) is strongly blue-shifted compared to the measured PL energy.

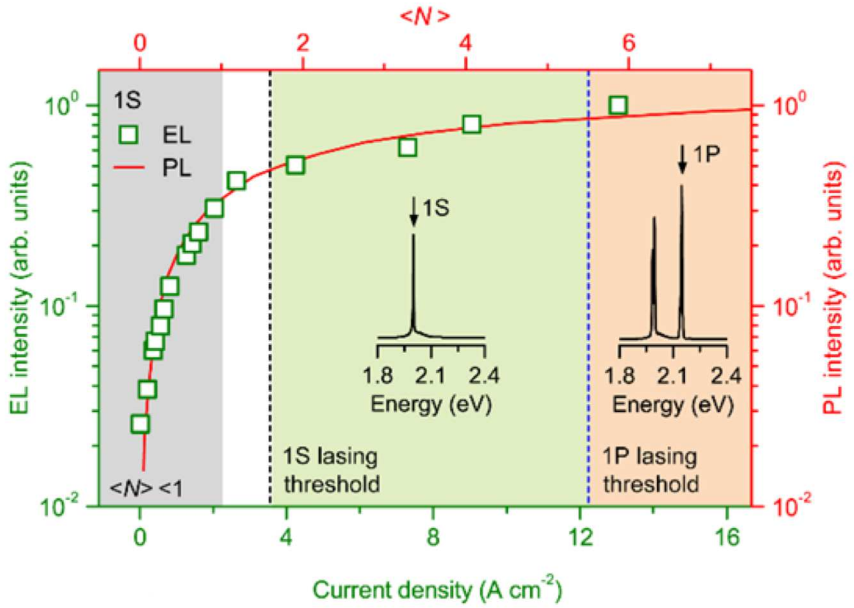

Fig. 2: The pump fluence dependence of the 1S emission intensity from optical measurements (red line) is virtually identical to the dependence on current density observed in the electroluminescence measurements (green squares) suggesting direct linear scaling between the average QD occupancy <N> and current density, j ($\langle N\rangle = \beta \times j$, where $\beta = 0.45\ cm^2\ A^{-1}$). Given this relationship, the maximum QD occupancy realized with electrical pumping is ~6 excitons per dot on average, which is above the thresholds for both 1S lasing (<N> = 1.6; vertical black dashed line) and 1P lasing (<N> = 5.5; vertical blue dashed line); corresponding lasing spectra are shown by black lines.

Electrical transport though a SiGe Self-assembled quantum dot

R. Shikishima[1], T. Kagawaguchi[1], H. Kiyama[1], M. Bamesreiter[2], D. Bougeard[2],
and A. Oiwa[1,3]
[1]The Institute of Scientific and Industrial Research, Osaka University, Osaka, Japan
[2] Institut für Experimentelle und Angewandte Physik, Universität Regensburg, Regensburg, Germany
[3]Center for Spintronics Research Network (CSRN), Graduate School of Engineering Science, Osaka University, Osaka, Japan
e-mail: oiwa@sanken.osaka-u.ac.jp

In group IV quantum dots (QDs), manipulation and detection of single electron spins have been rapidly developed as fundamental technologies of spin-based quantum computing [1]. In contrast to III-V-based QDs, hyperfine interaction with nuclear spins of host crystal is strongly suppressed in isotopically enriched ^{28}Si QDs, resulting in a long electron spin coherence time [2]. Here, we focus on a hole system in SiGe self-assembled QDs (SAQDs) because the confined holes are expected to have very weak contact hyperfine interaction with nuclei and strong SOI due to their p-orbital nature [3]. In this work, we present the superconducting transport and Kondo effect in SiGe SAQDs coupled to superconducting electrodes.

SiGe SAQDs grown by molecular beam epitaxy were contacted by aluminum electrodes as shown in Fig. 1. At magnetic fields higher than 1 T, the source-drain electrodes enters in the normal state. In a negative back-gate voltage region, zero bias conductance peak is observed, which can be attributed to Kondo effect (see Fig. 2). The estimated Kondo temperature was about 5 K. By further increasing magnetic field, the zero bias peak splits owing to Zeeman splitting. From the split Kondo features, we evaluate g-factor for perpendicular magnetic field to be 2.03 similar to the value reported previously [4]. In the superconducting regime at low magnetic fields, quasi-particle tunneling peaks at ± 2Δ are observed as shown in Fig. 3. Additional subgap transport features associated with Andreev transport are visible at ± Δ (see Fig. 3).

*[1] J. J. Pla et al., Nature **496**, 334 (2013).*

*[2] M. Veldhorst et al., Nature Nanotech. **9**, 981 (2014).*

*[3] G. Katsaros et al., Nature Nanotech. **5**, 458 (2010).*

*[4] N. Ares et al., Phys. Rev. Lett. **110**, 046602 (2013).*

978-3-901578-31-1

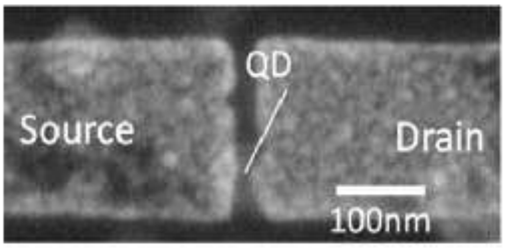

Fig. 1. SEM image of SiGe self-assembled quantum dot contacted to Al electrodes.

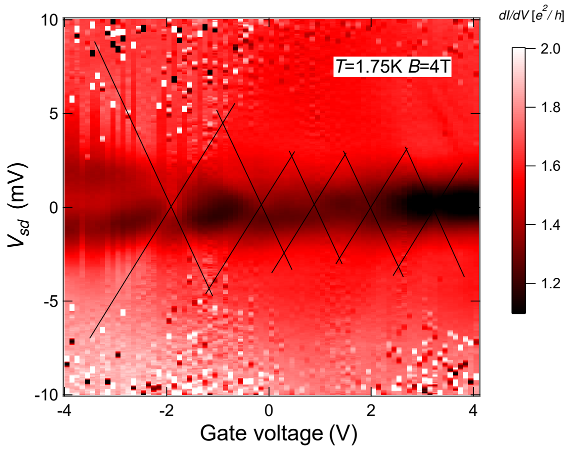

Fig. 2. Differential conductance as a function of the back-gate voltage and source-drain bias. Zero-bias conductance peak is noticeable in the gate voltage range between -2 and -4 V.

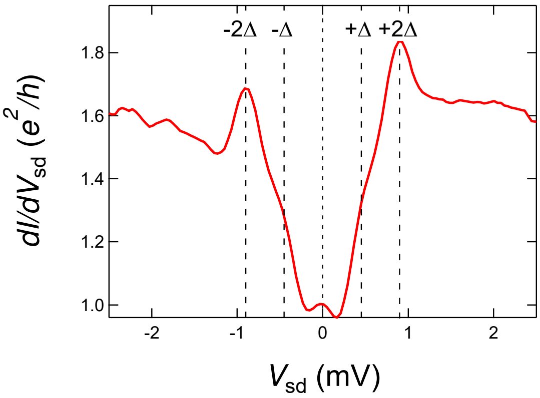

Fig. 3. Differential conductance measured at as a function of source-drain bias at zero magnetic field and 1.75 K.

2D Materials for Ubiquitous Electronics

Saptarshi Das

Department of Engineering Science and Mechanics & Material Research Institute,
Pennsylvania State University, University Park, PA 16802

The interest in two dimensional (2D) materials is rapidly spreading across all scientific and engineering disciplines due to their exquisite physical properties which not only provides a platform to investigate new and intriguing phenomena but also promises solutions to many imminent technological challenges. With the emergence of the era of Internet of Things (IoT), the 2D layered materials like graphene, MoS_2, WSe_2, Black Phosphorus, and many more are finding their widespread applications in conventional electronics, flexible electronics, straintronics, self-powered electronics, optoelectronics and even in brain inspired electronics. Low cost and high yield synthesis of pristine quality of these 2D materials is critical towards their commercial implementation. In my talk, I will provide a holistic understanding of 2D materials starting from a novel electrochemical method of synthesizing monolayers of various 2D materials to their eventual ubiquitous applications in various branches of electronics.

References:

1. Schulman, D. S. *et al.* **IEEE Nanotechnology Magazine, 11 (2), 6-17, 2017.**
2. Arnold, A. J. *et al.* **ACS Nano, 11 (3), 3110–3118, 2017.**
3. Das, S. *et al.* ***Scientific Reports*, 6, 34811, 2016.**
4. Das, S. *et al.* ***Scientific Reports*, 6, 28195, 2016.**
5. Das, S. *et al.* ***Applied Physics Letters*, 106 (17), 2015.**
6. Das, S. *et al.* ***Annual Review of Material Research*, 45 (1), 2015.**
7. Das, S. *et al.* ***ACS Nano*, 8 (11), 2014.**
8. Das, S. *et al.* ***Nano Letters*, 14 (10), 2014.**
9. Das, S. *et al.* ***Nano Letters*,** 14 (5), **2014.**
10. Das, S. *et al.* ***ACS Nano*,** 8 (2), **2014.**
11. Das, S. *et al.* ***Applied Physics Letters***, 103, **2013.**
12. Das, S. *et al.* ***Nano Letters*,** 13(7), **2013.**
13. Das, S. *et al.* ***Physica Status Solidi RRL*,** 7(4), **2013.**
14. Das, S. *et al.* ***Nano Letters***, 13(1), **2013.**

978-3-901578-31-1

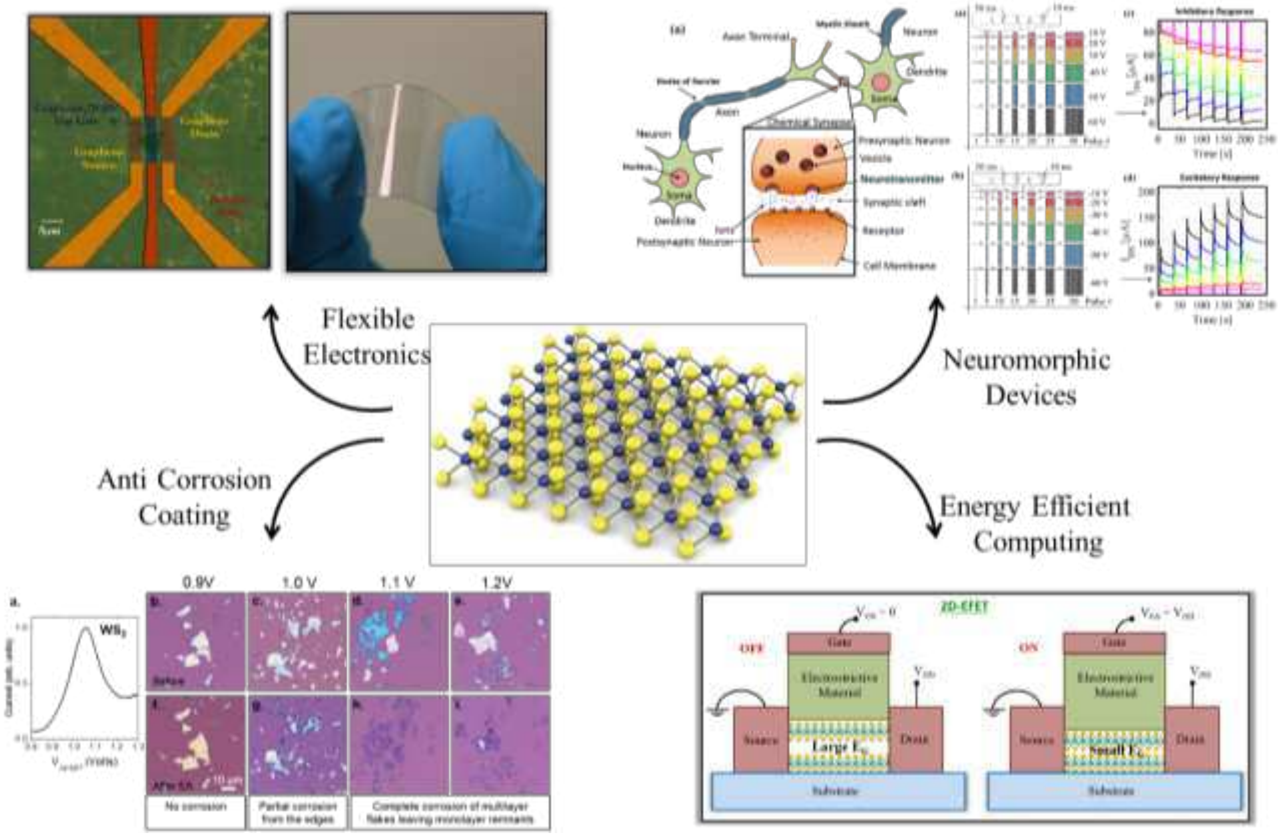

Figure. 2D Materials for Ubiquitous Electronics. ©Das Research Group, Penn State University

A coherent Ising machine for solving combinatorial optimization problems

Hiroki Takesue, Takahiro Inagaki, Kensuke Inaba, Toshimori Honjo

NTT Basic Research Laboratories, NTT Corporation, 3-1 Morinosato Wakamiya, Atsugi,
Kanagawa 243-0198, Japan
e-mail: takesue.hiroki@lab.ntt.co.jp

Simulating the Ising model using controllable spin systems is now drawing attention as a way to realize a new computer for solving combinatorial optimization problems. Here we present a coherent Ising machine (CIM), which is an Ising model simulator that uses degenerate optical parametric oscillators (DOPO) as artificial spins.

A CIM setup is shown in Fig.1. To generate DOPOs, we place a phase sensitive amplifier (PSA) based on signal/idler degenerate parametric amplification in a highly nonlinear fiber [1,2] or a periodically-poled lithium niobate (PPLN) waveguide [3] in an optical cavity. Since a PSA only amplifies lights with 0 or π phases relative to the pump phase, we observe an optical parametric oscillation that can take only 0 or π phases at above the threshold, which can be used to represent an Ising spin. By pumping the PSA with optical pulses whose temporal interval is 1/N of the cavity, we can generate N temporally-multiplexed DOPOs using a single optical system. Our group reported generation of more than thousands of DOPO using long-distance fiber cavities whose cavity lengths are 1 km or more. We have also implemented all-to-all coupling between 2000 DOPOs using the measurement-feedback scheme [3]. We experimentally confirmed that the CIM with measurement-feedback could successfully found solutions to maximum-cut problems of 2000-node graph problems (Fig.2).

This research was supported by ImPACT program of Japan, and has been undertaken as a collaborative research with National Institute of Informatics, Osaka University, The University of Tokyo, and Stanford University.

[1] T. Inagaki, K. Inaba, R. Hamerly, K. Inoue, Y. Yamamoto, and H. Takesue, "Large-scale Ising spin network based on degenerate optical parametric oscillators," Nature Photonics 10, 415-419 (2016).

[2] H. Takesue and T. Inagaki, "10 GHz clock time-multiplexed degenerate optical parametric oscillators for a photonic Ising spin network," Opt. Lett. 41, 4273-4276 (2016).

[3] T. Inagaki, Y. Haribara, K. Igarashi, T. Sonobe, S. Tamate, T. Honjo, A. Marandi, P. L. McMahon, T. Umeki, K. Enbutsu, O. Tadanaga, H. Takenouchi, K. Aihara, K. Kawarabayashi, K. Inoue, S. Utsunomiya, and H. Takesue, "A coherent Ising machine for 2000-node optimization problems," Science Vol. 354, Issue 6312, pp. 603-606 (2016).

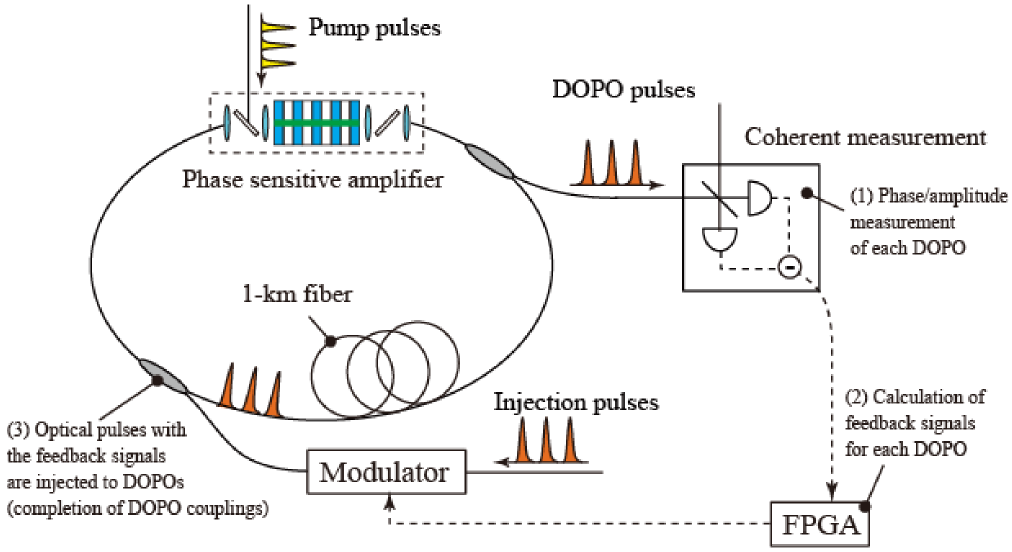

Figure 1: Setup of coherent Ising machine.

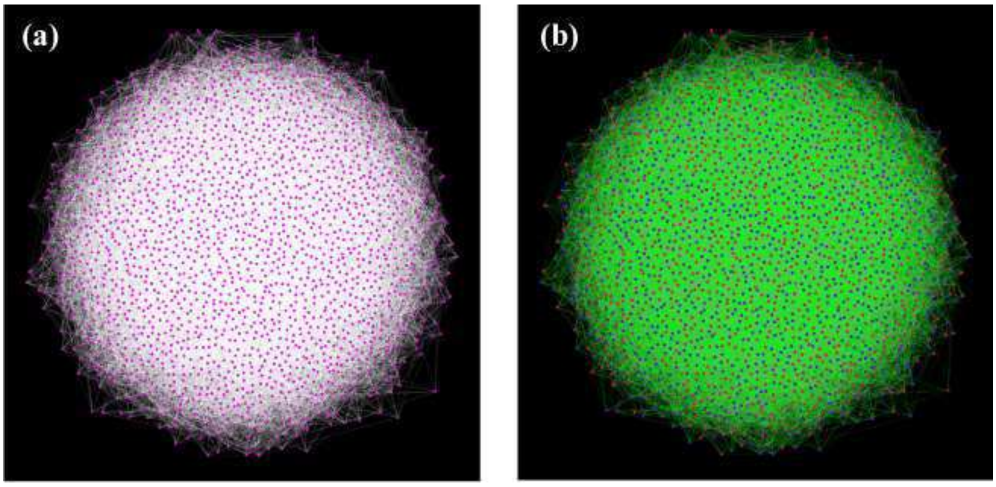

Figure 2: Solution search with CIM. (a) A 2000-node graph problem for maximum cut (G22 graph). Pink dots and white lines correspond to nodes and edges, respectively. (b) A solution of maximum cut problem of the graph shown in (a). Pink dots are divided into red and blue groups, and the edges shown by green lines are cut.

978-3-901578-31-1

Superradiance phase transition in the presence of parameter fluctuations

S. Ashhab[1] and K. Semba[2]

[1] *Qatar Environment and Energy Research Institute, Hamad Bin Khalifa University,*
Qatar Foundation, Doha, Qatar
[2] *National Institute of Information and Communications Technology,*
4-2-1, Nukuikitamachi, Koganei, Tokyo 184-8795, Japan
e-mail: semba@nict.go.jp

Cavity (circuit) quantum electrodynamics (QED), the study of the interaction between matter and the electromagnetic field inside a cavity (or a resonator circuit) at the quantum level, allows the investigation of a variety of physical phenomena involving light-matter interaction. One of these phenomena is the superradiance phase transition, which occurs when the interaction strength between the cavity and an ensemble of atomlike emitters exceeds a certain critical value and the different subsystems form a strongly correlated thermal equilibrium state. The superradiance phase transition has been analyzed and debated theoretically for over 40 years [1-3], and recent experiments have started to observe evidence of the phase transition [4-6].

The recent emergence of superconducting qubits and resonators has enabled circuit-QED systems to access parameter regimes that were inaccessible with other systems. In particular, the coupling strength of a single qubit to a cavity can now be made comparable to the bare energies of qubit and cavity excitations. Unconventional spectra characteristic of the corresponding highly correlated states have been observed in the experiments reported in Ref. [7]. Another recent experiment coupled thousands of qubits to a single cavity, achieving an effective coupling strength that is not far from the theoretically predicted critical value [8]. We theoretically analyze the effect of parameter fluctuations on the superradiance phase transition in a setup where a large number of superconducting qubits are coupled to a single cavity [9].

[1] K. Hepp and E. H. Lieb, Ann. Phys. (NY) **76**, 360 (1973).
[2] K. Rzażewski, K. Wodkiewicz, and W. Źakowicz, Phys. Rev. Lett. **35**, 432 (1975).
[3] S. Ashhab, Phys. Rev. A **87**, 013826 (2013).
[4] K. Baumann, C. Guerlin, F. Brennecke, and T. Esslinger, Nature **464**, 1301 (2010).
[5] G. Scalari, et al., Science **335**, 1323 (2012).
[6] M. P. Baden, et al., Phys. Rev. Lett. **113**, 020408 (2014).
[7] F. Yoshihara, T. Fuse, S. Ashhab, K. Kakuyanagi, S. Saito, and K. Semba, Nat. Phys. **13**, 44 (2017).
[8] K. Kakuyanagi, et al., Phys. Rev. Lett. **117**, 210503 (2016).
[9] S. Ashhab and K. Semba, Phys. Rev. A **95**, 053833 (2017).

978-3-901578-31-1

Binary Atomic Silicon Logic for WINDS 2017

Taleana Huff[1;3], Hatem Labidi[1,2], Mohammad Rashidi[1], Roshan Achal[1;3], Lucian Livadaru[3], Thomas Dienel[1], Jason Pitters[2;3], and Robert A. Wolkow[1;2;3]

1Department of Physics, University of Alberta, Edmonton, Alberta, T6G 2J1, Canada

2National Research Council of Canada, Edmonton, Alberta, T6G 2M9, Canada

3Quantum Silicon, Inc., Edmonton, Alberta, T6G 2M9, Canada,

The ultimate in miniature circuitry, exactingly crafted of single atom building blocks, can unleash a new basis for electronic devices one that is far more energy efficient, while at once much faster and more compact than today's state of the art. A most enticing goal. While examples of atom-crafting with a suitable level of precision and complexity has existed for three decades [1, 2], that control did not extend to electronically useful and also strongly bonded material systems. The attractive idea of forming circuitry of very robust patterned hydrogen atom terminated silicon surface states had been expressed decades ago [3], but, sufficient understanding of single atom states, ensemble states, and the interaction of those with dopants and bulk states was lacking and has only very recently been established [4-6]. That new understanding coupled with greatly improved atomic scale fabrication methods developed just months ago have enabled a great step forward [7]. Here, we report the first example of reversible information transmission through a binary wire - a two state wire made of atomic silicon quantum dots. A binary OR gate and its full truth table has also been demonstrated. Because electrons are merely rearranged and are conserved, and as no conventional current is used, minuscule power consumption is expected. Signal transfer is mediated by electrons confined by and tunneling among constituent dots. The tunneling rate in this strongly coupled, field controlled system is of order 10^{14} s^{-1}, indicating the potential for clocking in the THz regime. An atomic force microscope operating in the non-contact mode was deployed to fabricate these active structures. A variant of that technique, atom resolved Kelvin probe force spectroscopy, records individual atom charge state changes to reveal and verify the inner workings of this approach. Spontaneous spatial charge arrangements in ensembles occur in response to imposed charge inputs, allowing information representation and computation. The recently developed atomic white-out editing technique allowed structure and function alteration and changeable inputs. This approach to electronics we call BASIL for Binary Atomic Silicon Logic.

978-3-901578-31-1

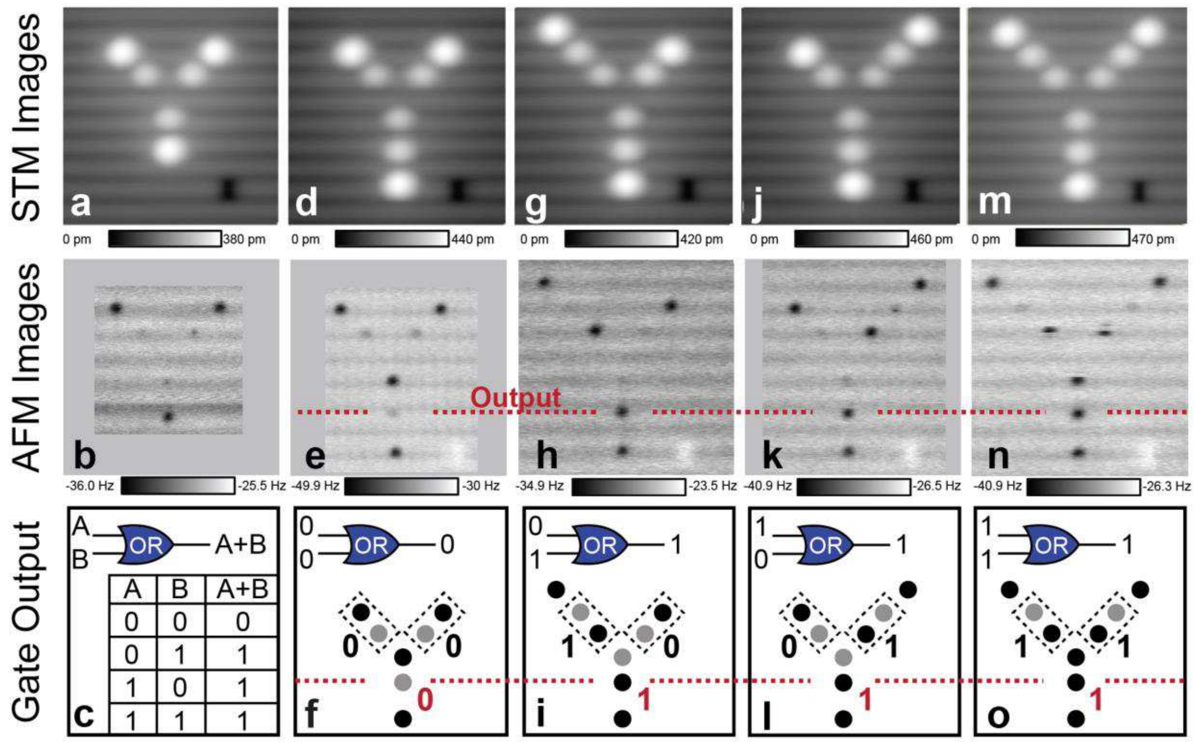

A	B	A+B
0	0	0
0	1	1
1	0	1
1	1	1

Prototype Functional OR gate Constructed of Atomic Silicon Quantum Dots (First row) Constant current filled state STM images (-1.8V, 50pA) of the OR gate in various actuation states. (Second row) corresponding AFM frequency shift maps (0V, Z 3.5 A) of the gates displaying electron location with the output ASiQD marked in red. (Bottom row) The complete truth table of an OR gate (c), with models for the 4 distinct outputs corresponding to the gates displayed vertically above them in rows one and two.

[1] D. M. Eigler and E. K. Schweizer, Nature 344, 524 (1990).

[2] A. J. Heinrich, C. P. Lutz, J. A. Gupta,and D. M. Eigler, Science 298, 1381 (2002).

[3] T. C. Shen, C. Wang, G. C. Abeln, J. R. Tucker, J. W. Lyding, P. Avouris, and R. E. Walkup, Science 268, 1590 (1995).

[4] M. Taucer, L. Livadaru, P. G. Piva, R. Achal, H. Labidi, J. L. Pitters, and R. A.Wolkow, Phys. Rev. Lett. 112 (2014).

[5] M. Rashidi, J. A. Burgess, M. Taucer, R. Achal, J. L. Pitters, S. Loth, and R. A. Wolkow, Nature comm. 7 (2016).

[6] M. Rashidi, M. Taucer, I. Ozfidan, E. Lloyd, M. Koleini, H. Labidi, J. L. Pitters, J. Maciejko, and R. A. Wolkow, Phys. Rev. Lett. 117, 276805 (2016).

[7] T. R. Huff, H. Labidi, M. Rashidi, M. Koleini, R. Achal, M. H. Salomons, and R. A. Wolkow, ACS Nano, http://dx.doi.org/10.1021/acsnano.7b04238

Band-Gap Engineering of Graphene Heterostructures via Substitutional Doping with B_3N_3

Hisaki Sawahata[1], Nguyen Thanh Cuong[2], Mina Maruyama[1], and Susumu Okada[1]

[1] *Graduate School of Pure and Applied Sciences, University of Tsukuba, Tsukuba, Ibaraki 305-8571, Japan*
[2] *International Center for Young Scientists, National Institute for Materials Science, Tsukuba, 305-0044, Japan*
e-mail: sokada@comas.frsc.tsukuba.ac.jp

Since graphene has a peculiar electronic structure at the Fermi level arising from their hexagonal covalent network of C atoms with atom thickness, graphene are keeping a premier position in an emerging material for the semiconductor electronic devices in the near future. On the other hand, the metallic electronic structure makes graphene difficult to utilize the semiconductor switching devices, because they could not guarantee the off states. Thus, the band gap engineering of graphene is mandatory to achieve the practical application of graphene in real semiconductor device. It has been demonstrated that the graphene nanoribbons and nanomeshes have a finite band gap in the resultant nanostructures in some cases. However, the electronic structure of these nanostructures is sensitive to the detail network topology. These facts give us a subject to seek semiconducting graphene nanostructures of which band gap is well controllable by their network topology. In this work, we aim to theoretically design semiconducting graphene nanostructures by substitutional doping with B_3N_3 rings (a borazine structure).

Figure 1 shows an optimized structure of a representative B_3N_3-doped graphene. The doped B_3N_3 rings form triangular lattice in graphene network by forming the heterobonds of BC and NC at their borders. Figure 2 shows the total energy of B_3N_3-doped graphene as a function of the spacing between adjacent B_3N_3 rings. The total energy is found to be inversely proportional to B_3N_3 spacing. Furthermore, the energy also weakly depends on the network topology of the graphene region. The B_3N_3–doped graphene with a Kekulé structure have slightly lower total energy than that without a Kekulé structure in the similar B_3N_3 spacing. All of B_3N_3-doped graphene structures are semiconductor with a finite band gap irrespective of the arrangements of B_3N_3 in graphene. Figure 3 shows the band gap of the B_3N_3-doped graphene as a function of the B_3N_3 spacing. The gap monotonically decreases with increasing the B_3N_3 spacing.

978-3-901578-31-1

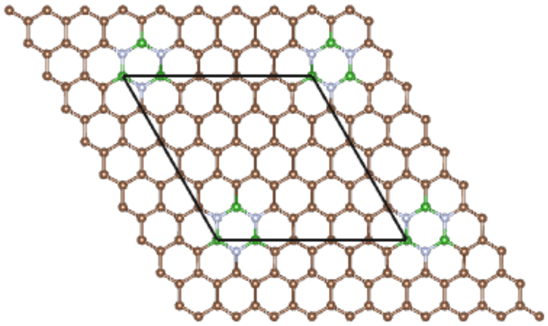

Fig.1: Optimized structure of B3N3-doped graphene. Brown, green, and cyan circles denote C, B, and N atoms, respectively.

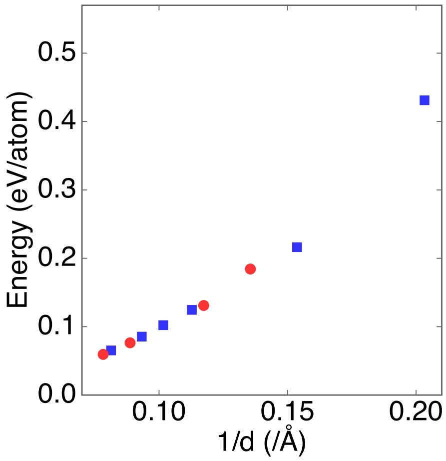

Fig.2: Total energy of B_3N_3-doped graphene as a function of the inverse of the B_3N_3 spacing. Circles and squares denote the energy of the B_3N_3-doped graphene with and without a Kekulé structures, respectively..

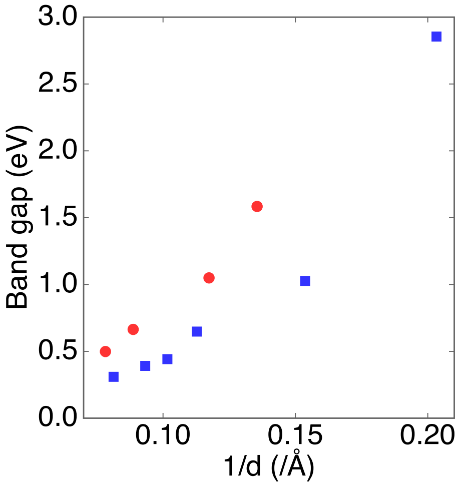

Fig.3: Band gap of B_3N_3-doped graphene as a function of the inverse of the B_3N_3 spacing. Circles and squares denote the band gap of the B_3N_3-doped graphene with and without a Kekulé structures, respectively.

978-3-901578-31-1

Surface modification processes of transition metal dichalcogenides for field-effect-transistor fabrication

Atsushi Ando[1], Toshifumi Irisawa[1], Naoya Okada[1], Jun Miyawaki[1], Toshitaka Kubo[1],
Takahiro Mori[1], Kazuhiro Endo[2],and Kazuhiko Endo[1]

[1] National Institute of Advanced Industrial Science and Technology (AIST),
AIST Tsukuba Central 2, 1-1-1 Umezono, Tsukuba, Ibaraki 305-8568, Japan
[2] Kanazawa Institute of Technology, Hakusan, Ishikawa, Japan
e-mail: atsushi-ando@aist.go.jp

Surface modification processes of the layered materials take an important role to modify intrinsic properties of the materials. In this work, we fabricated the back-gate transition metal dichalcogenides (TMDCs) FETs, and investigated the effect of plasma treatments and/or ultraviolet (UV) light irradiation on morphology and electrical characteristics of TMDCs.

Figure 1 shows a schematic of sectional structure of a back-gate FET for TMDC nanosheets. Micro-mechanically exfoliated TMDC sheets on a 285 nm thick SiO_2 substrate with underlying highly doped silicon [1] were used for a FET channel. For source/drain electrodes, metal electrodes (10 nm Ni/50 nm Au for MoS_2, 10 nm Cr/50 nm Au for WSe_2) formed by e-beam evaporation and lift-off technique [2] were used. Figure 2 (a) shows an optical microscope image of a fabricated FET. Thickness and surface morphology of the TMDC channel were estimated by atomic force microscope measurements. Electrical characterizations of TMDC FETs were performed in room temperature and under ambient conditions. Plasma treatment was performed with a resist strip system (Diener electronics, Nano). UV irradiation was performed under N_2 gas flow (100-300 sccm) in a quartz tube.

By O_2 plasma treatment, oxidation of TMDC and subsequent sublimation of oxide occur. In the case of MoS_2 (Fig.2 (b) and Fig. 3) and WSe_2, the etching proceeds in a nearly layer-by-layer manner on the surface. Defects (dangling bonds) generated by O_2 plasma etching act p-type dopant (Fig.4 and Fig. 5 (a)-(c)). However, the doping is unstable and is deactivate by terminations of the defects with adsorbed molecules (Fig. 5 (d)).

N_2 plasma treatment is available for p-type doping process of MoS_2 (Fig. 6 and Fig. 7 (a)-(c)). With substitution by nitrogen atom, the doping is stable (Fig. 7 (d)). The detailed results will be discussed at the presentation.

A part of this work was supported by JST CREST Grant Numbers JPMJCR16F3, Japan

[1] B. Radisavljevic et al., Nature Nanotech. ***6****, 147 (2011).*
[2] N. Ninomiya et al., Jpn. J. Appl. Phys. ***54****, 046502 (2015).*

978-3-901578-31-1

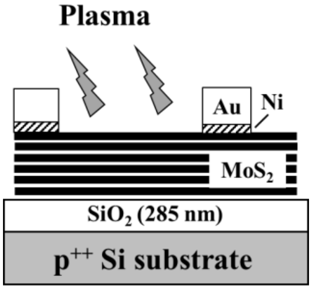

Fig.1: A schematic of sectional structure of a back-gate FET for MoS$_2$ nanosheets.

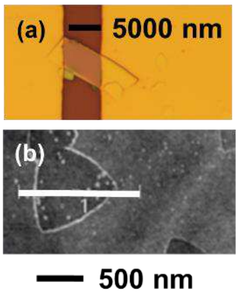

Fig.2: (a) Optical microscope image of a fabricated MoS$_2$ FET, (b) AFM image of MoS$_2$ surface modified by O$_2$ plasma after 90 s.

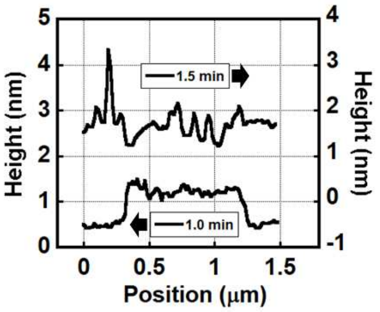

Fig.3: Cross-sections of AFM images of MoS$_2$ surface modified by O$_2$ plasma after 60 s (not shown) and 90 s (as shown in Fig.2 (b)).

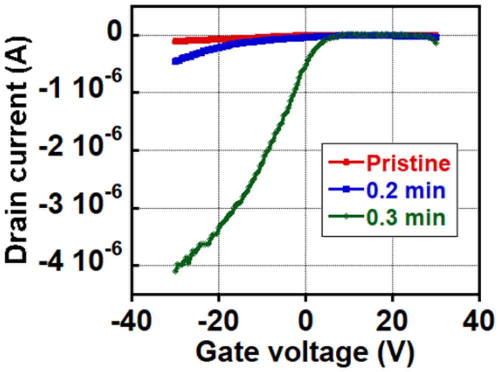

Fig.4: Drain-gate characteristics of pristine WSe$_2$ FET, WSe$_2$ FET irradiated with O$_2$ plasma for 0.2 min, and WSe$_2$ FET irradiated with O$_2$ plasma for 0.3 min.

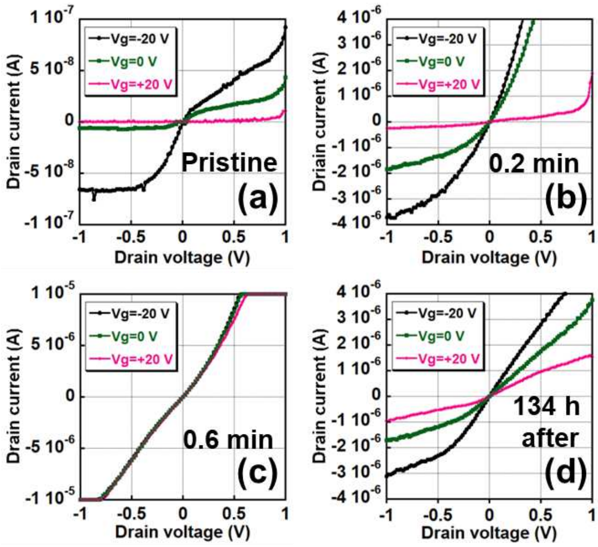

Fig.5: Drain-source characteristics at various gate voltages for (a) pristine WSe$_2$ FET, (b) WSe$_2$ FET irradiated with O$_2$ plasma for 0.2 min, (c) WSe$_2$ FET irradiated with O$_2$ plasma for 0.6 min, (d) WSe$_2$ FET after 134 h of (c).

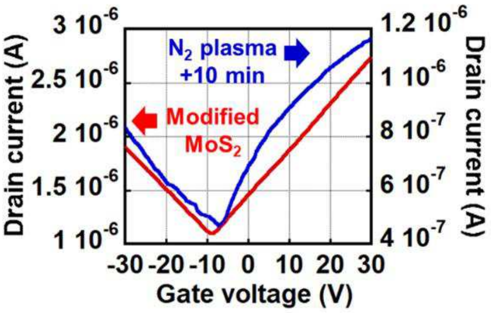

Fig.6: Drain-gate characteristics of modified MoS$_2$ FET and MoS$_2$ FET irradiated with N$_2$ plasma for 10 min.

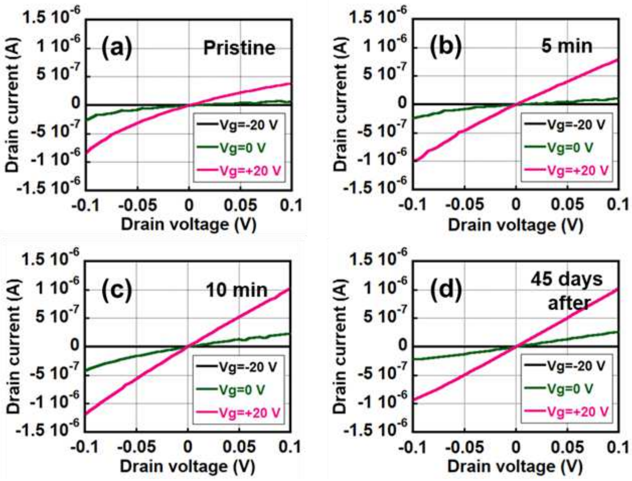

Fig.7: Drain-source characteristics at various gate voltages for (a) pristine MoS$_2$ FET, (b) MoS$_2$ FET irradiated with N$_2$ plasma for 5 min, (c) MoS$_2$ FET irradiated with N$_2$ plasma for 10 min, and (d) MoS$_2$ FET after 45 days of (c).

978-3-901578-31-1

Application of graphene and graphene nanoribbons to electronic devices

Shintaro Sato[1,2]

[1] *Fujitsu Laboratories Ltd.*, [2] *Fujitsu Limited*
10-1 Morinosato-Wakamiya, Atsugi, Kanagawa 243-0197, Japan
e-mail: sato.shintaro@jp.fujitsu.com

Graphene has excellent electrical properties, and is therefore a promising candidate for future electronics materials. While graphene does not have a band gap, a graphene nanoribbon (GNR) does, and can therefore be used for devices such as diodes and transistors. We have been working on growth of nanocarbon materials and their application to electronic devices, including transistors, interconnects, and sensors. We here describe some of the applications.

We recently developed a gas sensor based on a graphene-gate transistor, where the gate of a Si transistor is replaced with single-layer graphene (Fig.1) [1]. If gas molecules adsorb on the graphene-gate surface, the Fermi level or work function of graphene can change, thus shifting the threshold of the Si transistor. This causes changes in the drain current if the gate voltage is kept constant. This graphene-gate sensor was found to be very sensitive to NO_2 and NH_3. As can be seen in the Fig. 2, the sensor can detect NO_2 with concentrations less than 1 ppb.

Graphene can also be used for detecting high-frequency wave [2, 3]. We recently proposed a diode consisting of a GNR heterojunction (Fig. 3) for high-frequency wave detection [4]. The heterojunction consists of a hydrogen-terminated armchair-edge GNR (H-AGNR) and fluorine-terminated armchair-edge GNR (F-AGNR). Since there is a difference in electron affinity between them, we can construct a staggered-type lateral heterojunction p-n diode. First principle calculations show that, due to band-to-band tunneling, the diode has a nonlinear reverse current of the order of kA/m. The junction capacitance is extremely small because of the small junction area. The voltage sensitivities of the GNR-based backward diode as a function of frequency are shown in Fig. 4. The diode can have a much better sensitivity for high-frequency wave than a GaAsSb/InAlAs/InGaAs heterojunction diode [5].

We try to form GNRs having various widths and edge-terminations using a bottom-up approach [6]. Figure 5 shows a scanning tunneling microscope image of H-AGNR we formed. In fact, we used a precursor shown in Fig. 6, aiming at synthesizing partially F-terminated AGNRs. The F atoms at the edges, however, were detached during the cyclodehydrogenation of partially-edge-fluorinated polyanthrylenes to form GNRs. We have found by first principles calculations that a critical intermediate structure, obtained as a result of H atom migration to the terminal carbon of a fluorinated anthracene unit in polyanthrylene, plays a crucial role in significantly lowering the activation energy of carbon−fluorine bond dissociation.

We have also fabricated a transistor using GNRs as a chennel. Transfer characteristics of the transistor are also described in the presentation.

This research was partly supported by JST CREST Grant Number JPMJCR15F1, Japan.

[1] N. Harada, et al., IEDM 2016 p.476 (2016). [2] X. Cai, et al., Nat. Nanotech., **9**, 814 (2014). [3] L. Vicarelli et al., Nat. Mater., **11**, 865 (2012). [4] N. Harada, et al., Appl. Phys. Express, **10**, 074001 (2017). [5] M. Patrashin, et al., IEEE Trans. Electron Devices, 62 (2015) 1068. [6] H. Hayashi, et al., ACS Nano, **11**, 6204 (2017).

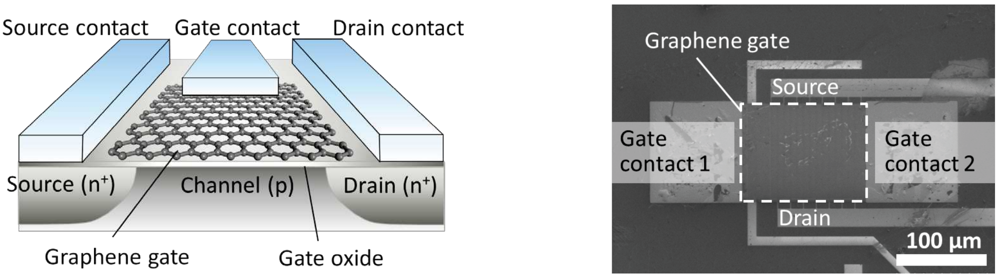

Figure 1: Schematic illustration (left) and scanning electron microscope image (right) of a gas sensor based on a graphene-gate transistor

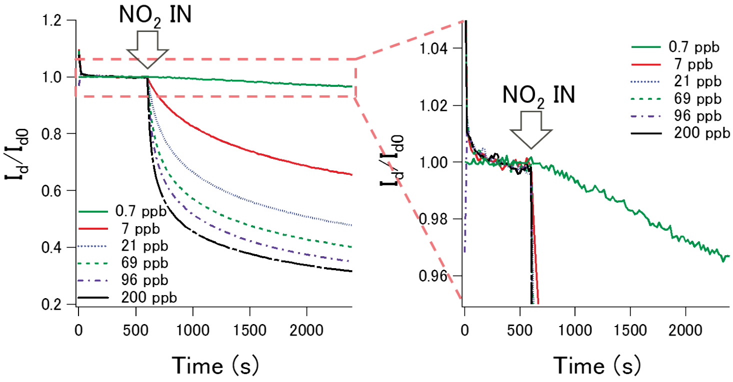

Figure 2: Dependence of the response (normalized drain current, I_d/I_{d0}) of a graphene-gate sensor on NO_2 concentrations.

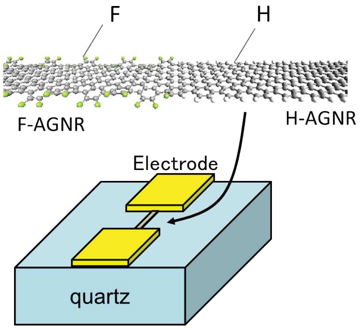

Figure 3: Schemetic llustration of a diode using a heterojunction of F-AGNR and

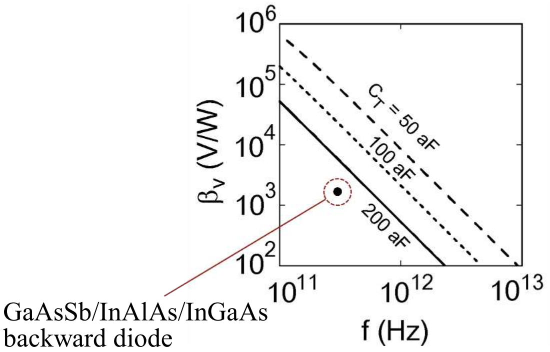

Figure 4: Calculated voltage sensitivity of a GNR backward diode, β_v, as a function of frequency with the total capacitance, C_T, as a parameter. The closed circle indicates β_v of a GaAsSb/InAlAs/InGaAs diode in Ref. 5.

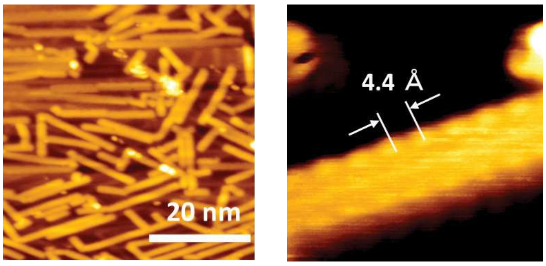

Figure 5: Scanning tunneling microscope images of H-AGNRs

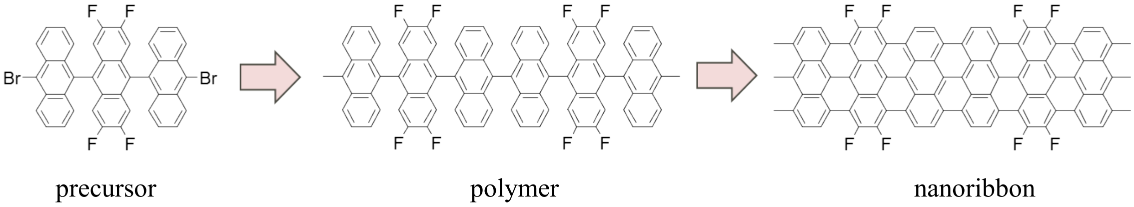

Figure 6: Scheme for synthesizing partially F-terminated AGNRs

978-3-901578-31-1

MoS_2/Graphene stacked electromechanical resonator

Taichi Inoue[1], Yuta Mochizuki[1], Yuki Imakita[1], Kuniharu Takei[1], Takayuki Arie[1], Seiji Akita[1]

[1] *Department of Physics and Electronics, Osaka Prefecture University,*
Sakai 599-8531, Japan
e-mail: t_inoue-4@pe.osakafu-u.ac.jp

Atomically thin 2D layer materials like graphene and MoS_2 are suitable for nano-electro-mechanical systems (NEMS) because of its unique electrical and mechanical properties. Especially, mechanical resonator (MR) made of them is expected for high sensitive sensor and application using nonlinear vibration. To extend further applications, it is necessary to control resonance characteristics of not only single layer MR but also MoS_2/Graphene stacked MR. Here, we demonstrate controlling resonance frequency of graphene/MoS_2 stacked MR by photothermal stress.

Electrodes were fabricated on the Si substrate with a 300 nm-thick SiO_2 layer. Monolayer graphene synthesized by CVD was transferred onto the substrate and trimmed by O_2 plasma. Next, mechanically exfoliated MoS_2 was transferred onto the graphene by PDMS gel stamp. Lastly, SiO_2 layer underneath the graphene was etched by BHF and the substrate was dried by super critical drying to prevent from sticking. Fig.1 shows the SEM image of the drum type graphene/MoS_2 MR. We confirmed whether graphene and MoS_2 exist there by Raman spectrum (Fig.2 and 3). As shown Fig. 4, the resonance of the graphene/MoS_2 resonator was measured electrically by amplitude modulation (AM) method, where the graphene/MoS_2 resonator was irradiated with laser light with different wavelengths (660 or 979 nm). We investigated both of wavelength λ and laser power P dependences of resonance at $V_{sd} = 0.3$ V_{pp} and $V_g^{DC} = 2.5$ V. In the case of 660 nm corresponding to the strongly absorbed light at MoS_2 (Fig.5), resonance frequency shifted from 8.65 MHz to 8.93 MHz as increasing P. While the similar trend that frequency shifts upward with increasing P is observed in the case of 979 nm corresponding to the lower energy than the bandgap of MoS_2 (Fig.6), the frequency shift is smaller than that at $\lambda = 660$ nm. This wavelength dependence implies that the upward shift of resonance frequency is induced by photothermal stress between graphene and MoS_2, namely bi-material effect. Thus, we have successfully controlled the resonance frequency of graphene/MoS_2 bi-material MR by photothermal effect.

Acknowledgemants This study was partially supported by JSPS KAKENHI Grant Numbers JP15H05869, JP16K14259, JP16H00920, JP17H01040

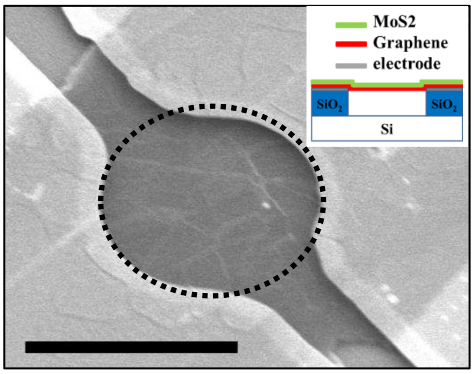

Fig.1: The SEM image of graphene/MoS$_2$ MR. The scale bar is 6 μm. Dotted line indicates resonance part of MR. Inset is sectional image of graphene/MoS$_2$ MR.

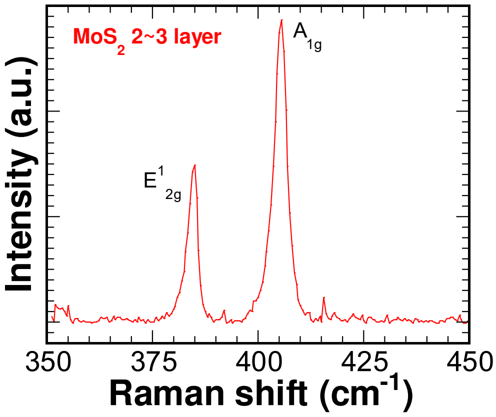

Fig.2: Average Raman spectrum of MoS$_2$ in dotted line in Fig.1. Layer number of MoS$_2$ is two or three by determining Raman shift difference between E^1_{2g} and A_{1g}.

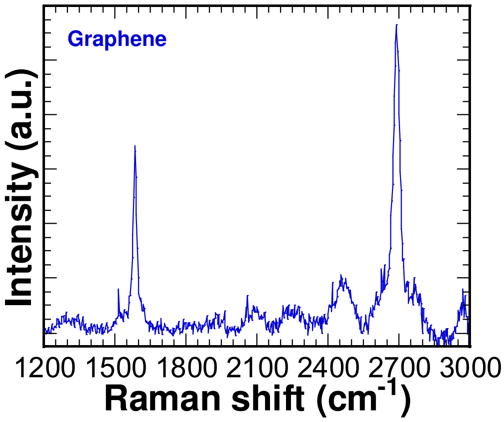

Fig.3: Average Raman spectrum of graphene in dotted line in Fig.1

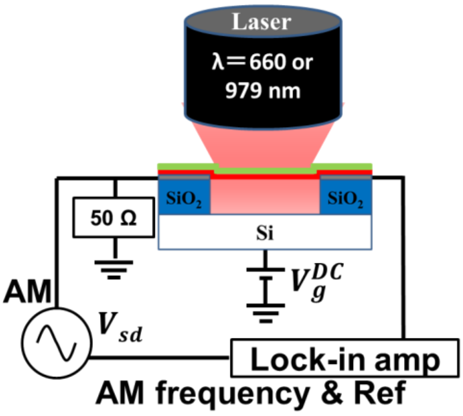

Fig.4: Resonance measurement system. Resonance is actuated and detected electrically by AM method, and laser is used for controlling resonance frequency. Laser wavelength is 660 or 979 nm.

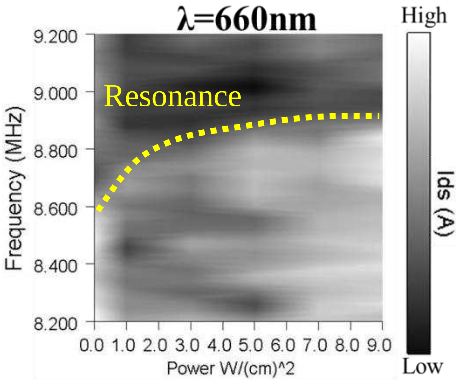

Fig.5 Laser power and frequency dependence of output current in the case of 660 nm. Yellow dotted line indicates resonance.

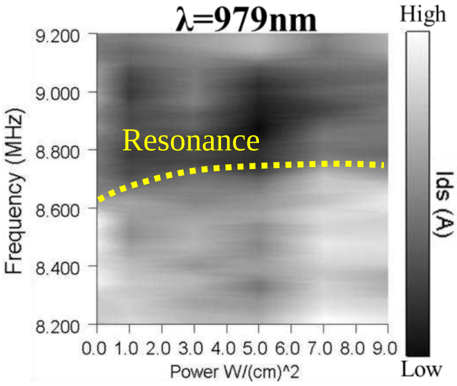

Fig.6: Laser power and frequency dependence of output current in the case of 979 nm. Yellow dotted line indicates resonance.

978-3-901578-31-1

A Single Atom Shift in 2D MoS_2 Supercell

Bagher Tabibi, Sheng Yu, Tikaram Neupane, and Felix Jaetae Seo*
Advanced Center for Laser Science and Spectroscopy, and Center for Atmospheric Research and Education, Department of Physics, Hampton University, Hampton, Virginia 23668, USA,
**jaetae.seo@hamptonu.edu*

Atomic monolayer of transition metal dichalcogenide (TMDC) has a hexagonal structure of transition metal ion that is sandwiched by dichalcognide ions through a covalent bonding. The TMDC atomic monolayer has unique optical, material, and electronic characteristics of emission polarization chirality, time-reversal symmetry, spatial inversion asymmetry, electronic bandstructure with direct transitions at K and K' positions in momentum space, and intrinsic piezoelectricity. This presentation includes the piezoelectricity enhancement, bandstructure modification, and new energy level formation due to a single atom, molybdenum or sulfide, shift along the armchair or zigzag direction in the supercell of 5x5 unit cells of molybdenum disulfide atomic layer [1]. The single atom shift in the supercell modified the piezoelectricity and electronic band structure with the changes of absorption and reflection coefficients. The larger shift of molybdenum or sulfide single atom resulted in the larger reduction in the bandgap. The singe atom shift in the supercell also exhibited new energy levels inside the forbidden band, not in the conduction or valence band. The induced energy levels for a molybdenum atom shift along the armchair direction are relatively deeper than that for a sulfide atom shift along the same direction. The total energy of the supercell with a single atom shift revealed that the single atom shift along the zigzag direction has better structural stability than the single atom shift along the armchair direction. The single atom shift in the supercell also modified the piezoelectricity. The piezoelectricity occurs in the inversion asymmetric crystal that converts mechanical deformational force to electricity. The crystal structure of 2D molybdenum disulfide monolayer or odd layers has an inversion asymmetry. The molybdenum disulfide monolayer has an intrinsic piezoelectricity [2, 3]. The intrinsic piezoelectric coefficient (e_{11}) of MoS_2 monolayer is ～290 pC/m [3]. However, a single atom shift in the supercell of molybdenum disulfide monolayer is obviously a new material system which exhibits its own piezoelectric property. The piezoelectric coefficient of e_{11} in the molybdenum disulfide supercell of 5x5 unit cells is significantly increased by 18% as a single molybdenum shift 20% along the armchair direction which is attributable the large ionic Coulomb interaction. A single atom shift in molybdenum disulfide supercell modified piezoelectric coefficients that change the electronic and ionic polarizations and output voltage. Additional macroscopic strain to the material system of a supercell with a single atom shift also changes the output voltage. The parallel and series connections of devices provide higher electric voltage and current [4] for piezoelectricity, heart rate monitoring, and etc. Therefore, this study paves the realization of piezoelectricity enhancement, energy level formation in the forbidden band, bandstructure modification with Fermi level shift, and ionic Coulomb interaction changes. Acknowledgement: This work at HU is supported by ARO W911NF-15-1-0535, NSF HRD-1137747, and NASA NNX15AQ03A.

References

[1] S. Yu, Q. Rice, T. Neupane, B. Tabibi, Q. Li, and F. J. Seo, Phys. Chem. Chem. Phys. 19, 24271 (2017).
[2] K. N. Duerloo, M. T. Ong, and E. J. Reed, J. Phys. Chem. Lett. 3, 2871 (2012).
[3] S. Yu, K. Eshun, H. Zhu, and Q. Li, Sci. Rep. 5, 12854 (2015).
[4] W. Wu, L. Wang, Y. Li, F. Zhang, L. Lin, S. Niu, D. Chenet, X. Zhang, Y. Hao, T. F. Heinz, J. Hone, and Z. L. Wang, Nature 514, 470 (2014).

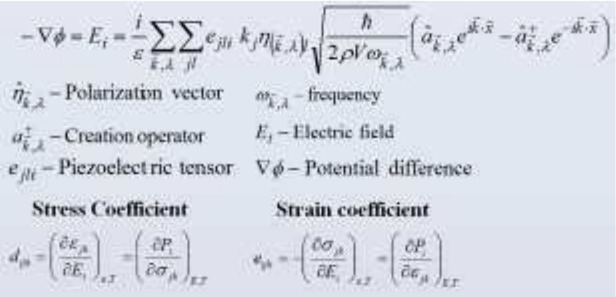

$$-\nabla\phi = E_i = \frac{i}{\varepsilon}\sum_{\vec{k},\lambda}\sum_{jl} e_{jli}\, k_j \eta_{(\vec{k},\lambda)l}\sqrt{\frac{\hbar}{2\rho V\omega_{\vec{k},\lambda}}}\left(\hat{a}_{\vec{k},\lambda}e^{i\vec{k}\cdot\vec{x}} - \hat{a}^{+}_{\vec{k},\lambda}e^{-i\vec{k}\cdot\vec{x}}\right)$$

$\hat{\eta}_{\vec{k},\lambda}$ – Polarization vector

$a^{+}_{\vec{k},\lambda}$ – Creation operator

e_{jli} – Piezoelectric tensor

$\omega_{\vec{k},\lambda}$ – frequency

E_i – Electric field

$\nabla\phi$ – Potential difference

Stress Coefficient

$$d_{ijk} = \left(\frac{\partial\varepsilon_{jk}}{\partial E_i}\right)_{\sigma,T} = \left(\frac{\partial P_i}{\partial\sigma_{jk}}\right)_{E,T}$$

Strain coefficient

$$e_{ijk} = -\left(\frac{\partial\sigma_{jk}}{\partial E_i}\right)_{\varepsilon,T} = \left(\frac{\partial P_i}{\partial\varepsilon_{jk}}\right)_{E,T}$$

Fig.1. Piezo-induced electric field, stress and strain coefficients.

Fig.2. Schematic of PiezoBiosensor for monitoring heart rate.

Electronic properties and charge transport of coordination nanosheet (CONASH)

Naoya Fukui [1], Kazuo Nakazato [2], Sono Sasaki [3], and Hiroshi Nishihara [1]

[1] *Department of Chemistry, Graduate School of Science, The University of Tokyo, Tokyo, Japan*
[2] *Department of Electronic Engineering, Graduate School of Engineering, Nagoya University, Nagoya, Aichi, Japan*
[3] *Faculty of Fiber Science and Engineering, Kyoto Institute of Technology, Kyoto, Japan*
e-mail: nfukui@chem.s.u-tokyo.ac.jp

Monolayer nanosheet materials have attracted significant attention because of their unique physical and chemical properties, which derive from their two-dimensional nature. In such nanosheet materials, coordination nanosheets (CONASHs), which are metal complex π-nanosheets as shown in Figs. 1 and 2, have several advantages [1]. There are numerous combinations of metals and ligands, so that various chemical structures with unique physical properties can be designed. Easy and inexpensive bottom-up synthesis is possible since most coordination reactions proceed in solution under ambient conditions.

Electric conductivity of NiDT (nickel bis(dithiolene)) CONASH was measured by the van der Pauw method using a four-probe set-up under the inspection of scanning electron microscopy as shown in Fig. 3 [2, 3]. To control the Fermi level, nanosheet was doped electrochemically. As-prepared sheet ap-NiDT showed an average oxidation number of -3/4 for the NiDT unit and an electric conductivity of 2.8 $\mathrm{Scm^{-1}}$, whereas oxidized sheet ox-NiDT showed a very high electric conductivity of 160 $\mathrm{Scm^{-1}}$ at 300K. PES and the energy band calculation suggest that both ap-NiDT and ox-NiDT are metallic, although the Arrhenius plot revealed semiconductor behavior. The discrepancy might stem from a structural disorder in the sample. Huang et al. reported that Cu-BHT(benzenhexathiol) CONASH showed room temperature conductivity 1580 $\mathrm{Scm^{-1}}$ and ambipolar charge transport with extremely high electron and hole mobilities, 116 $\mathrm{cm^2V^{-1}s^{-1}}$ and 99 $\mathrm{cm^2V^{-1}s^{-1}}$, respectively [4].

Furthermore, DFT (density functional theory) calculation predicted that the metalladithiolene CONASH is a 2-dimensional topological insulator with a spin-orbital coupling gap of 13.6 mV for NiDT and 22.7 mV for AuDT [5]. This is the first organic topological insulator candidate which can be synthesized.

[1] R. Sakamoto et al., Coord. Chem. Rev. **320-321**, 118 (2016)

[2] T, Kambe et al., J. Am. Chem. Soc. **135**, 2462 (2013)

978-3-901578-31-1

[3] T. Kambe et al., J. Am. Chem. Soc. **136**, 14357 (2014)

[4] X. Huang et al., Nat. Commun. **6**, 7408 (2015)

[5] Z. F. Wang, N. Su, and F. Liu, Nano Lett. **13**, 2842 (2013)

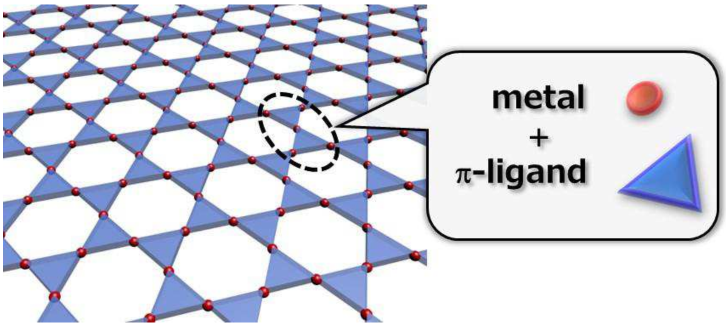

Fig.1: Coordination nanosheet (CONASH)

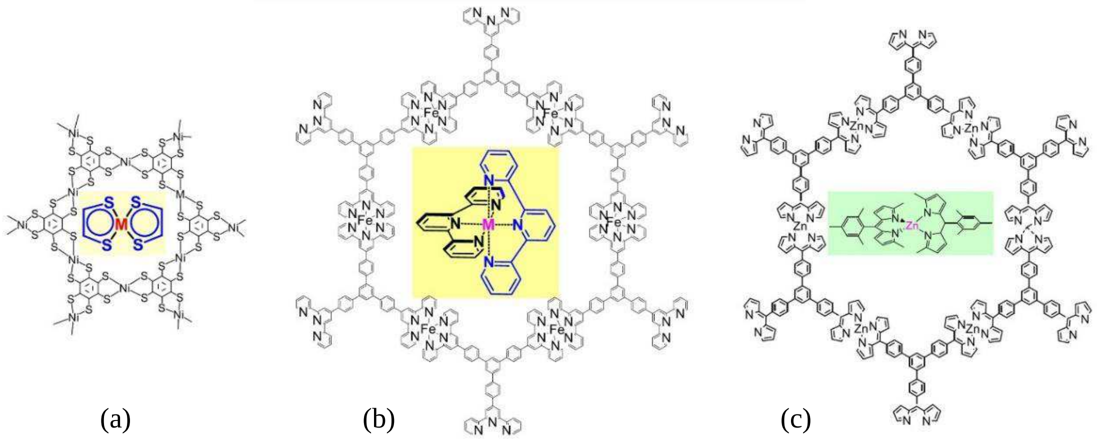

(a) (b) (c)

Fig.2: Functional CONASHs (a) Metalladithiolene CONASH (M = Ni, Pd), (b) Bis(terpyridine) metal CONASH (M = Fe, Co), Bis(dipyrrinato)zinc CONASH.

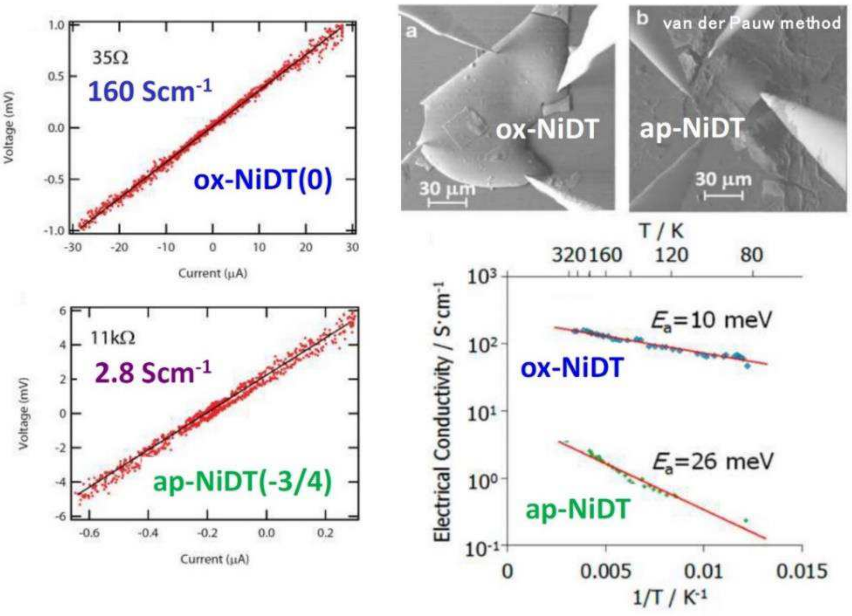

Fig.3: Electric conductivity of NiDT CONASH measured by van der Pauw method.

Development of electron-accepting π-conjugated units for organic electronics

Yutaka Ie, Makoto Karakawa, Masashi Nitani, and Yoshio Aso

The Institute of Scientific and Industrial Research, Osaka University,
Ibaraki, Osaka 567-0047, Japan
e-mail: aso@sanken.osaka-u.ac.jp

*π-Conjugated small molecules and polymers have intensively developed for the application to semiconducting materials in organic thin-film electronics such as organic field-effect transistors (OFETs), light-emitting diodes, and photovoltaic devices (OPVs). Both hole-transporting (p-type) and electron-transporting (n-type) organic semiconductors are required for the fabrication of these devices. Thus, the tuning of the highest occupied molecular orbital (HOMO) and the lowest unoccupied molecular orbital (LUMO) energy level is important. We have developed and systematically investigated five-membered heteroaromatic (thiophene and thiazole) derivatives annelated with a ring containing electron-withdrawing functional groups and proved that the incorporation of these units is effective for increasing the electron deficiency characters of resulting π-conjugated systems without interrupting effective conjugation. Variety π-conjugated compounds were synthesized and characterized as n-type OFET materials with good electron mobility and stable device operation in the air [1]. Complementary inverters fabricated with the carbonyl-bridged bisthiadiazole derivatives (**Ar-CTzTz)** showed high switching properties. Furthermore, in order to apply as p-type semiconductors for bulk-heterojunction (BHJ) OPVs, we have developed novel donor–acceptor π-conjugated copolymers based on benzodioxocyclohexene-annelated thiophene (**C**) as an electron-accepting unit [2]. High power conversion efficiency on BHJ OPVs in a combination with $PC_{71}BM$ was obtained by the optimizations of the chemical structures and active-layer fabrication conditions.*

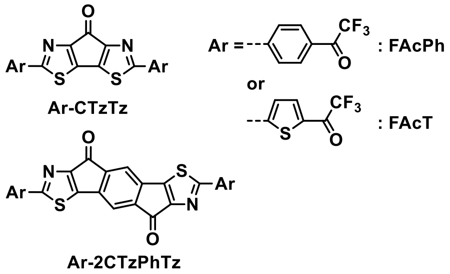

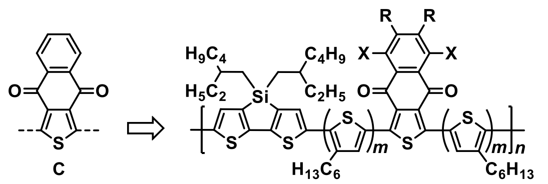

m = 0, X = H, R = C_6H_{13} : DTS-C_6
m = 0, X = F, R = C_6H_{13} : DTS-DFC_6
m = 0, X = F, R = H : DTS-DFC
m = 0, X = R = F : DTS-TFC
m = 1, X = F, R = H : DTS-HT-DFC
m = 1, X = R = F : DTS-HT-TFC

[1] Y. Ie et al., Adv. Funct. Mater., ***20****, 907 (2010); Y. Ie et al., Chem. Mater.,* ***24****, 3285 (2012).*

[2] Y. Ie et al., Macromolecules, ***45****, 4564 (2012); J. Huang et al., Chem. Mater.,* ***26****, 6971 (2014); Y. Ie et al., J. Mater. Chem. A, (2017) DIO: 10.1039/C7TA05822E.*

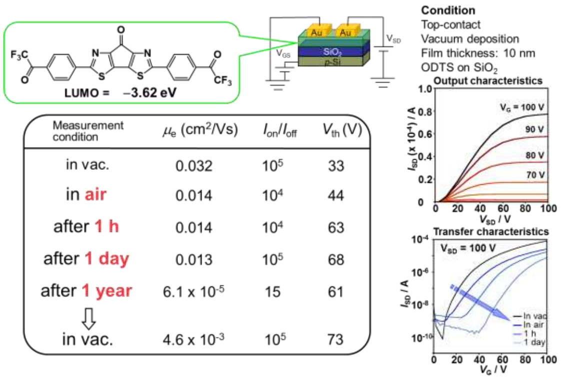

Condition
Top-contact
Vacuum deposition
Film thickness: 10 nm
ODTS on SiO$_2$

Measurement condition	μ_e (cm^2/Vs)	I_{on}/I_{off}	V_{th} (V)
in vac.	0.032	10^5	33
in air	0.014	10^4	44
after 1 h	0.014	10^4	63
after 1 day	0.013	10^5	68
after 1 year	6.1 x 10^{-5}	15	61
⇩ in vac.	4.6 x 10^{-3}	10^5	73

*Fig.1: n-Type OFET performance of carbonyl-bridged bisthiazole-based compound (**FAcPh-CTzTz**) with top-contact configuration.*

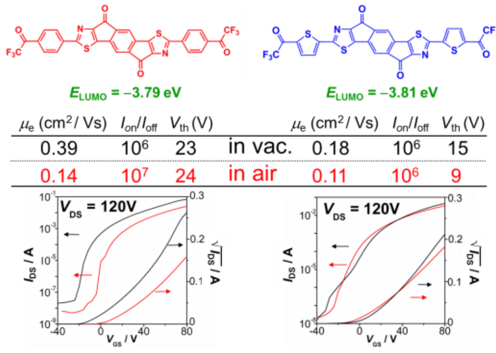

μ_e (cm^2/ Vs)	I_{on}/I_{off}	V_{th} (V)		μ_e (cm^2/ Vs)	I_{on}/I_{off}	V_{th} (V)
0.39	10^6	23	in vac.	0.18	10^6	15
0.14	10^7	24	in air	0.11	10^6	9

*Fig.2: n-Type OFET performance of malti-ring-fused carbonyl-bridged thiazole derivatives (**Ar-2CTzPhTz**) with bottom-contact configuration.*

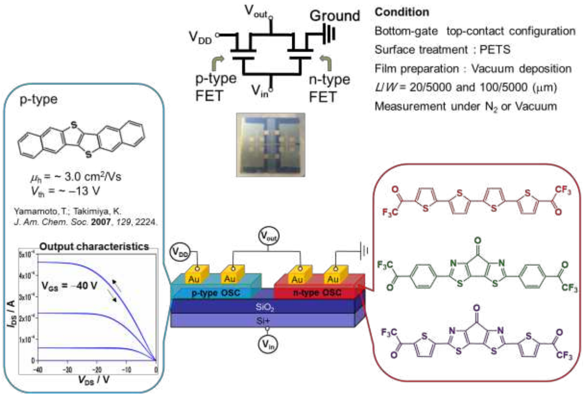

Condition
Bottom-gate top-contact configuration
Surface treatment : PETS
Film preparation : Vacuum deposition
L/W = 20/5000 and 100/5000 (μm)
Measurement under N$_2$ or Vacuum

*Fig.3: Application of carbonyl-bridged bisthiazole-based compounds (**Ar-CTzTz**) to complementary inverters.*

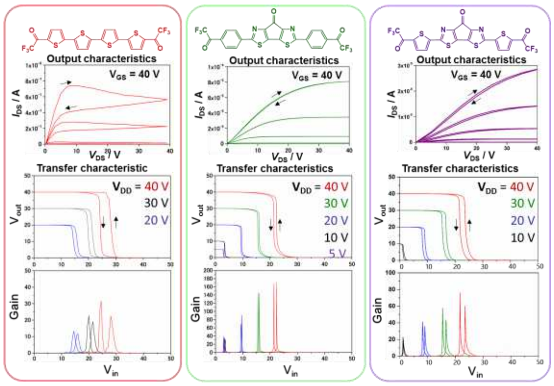

*Fig.4: Performance of complementary inverters using **Ar-CTzTz** as n-type materials.*

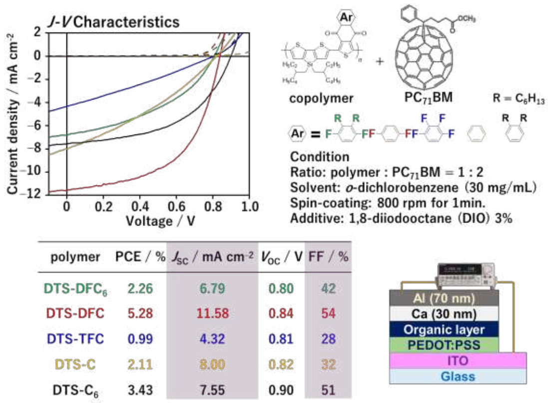

Condition
Ratio: polymer : PC$_{71}$BM = 1 : 2
Solvent: o-dichlorobenzene (30 mg/mL)
Spin-coating: 800 rpm for 1min.
Additive: 1,8-diiodooctane (DIO) 3%

polymer	PCE / %	J_{SC} / mA cm^{-2}	V_{OC} / V	FF / %
DTS-DFC$_6$	2.26	6.79	0.80	42
DTS-DFC	5.28	11.58	0.84	54
DTS-TFC	0.99	4.32	0.81	28
DTS-C	2.11	8.00	0.82	32
DTS-C$_6$	3.43	7.55	0.90	51

*Fig.5: Performance of BHJ OPVs consisting of benzodioxocylohexene-annelated thiophene (**C**) unit-based D–A copolymers as p-type semiconductor and PC$_{71}$BM as n-type semiconductor.*

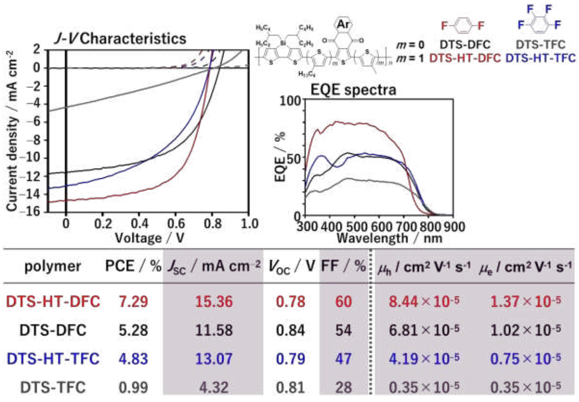

polymer	PCE / %	J_{SC} / mA cm^{-2}	V_{OC} / V	FF / %	μ_h / cm^2 V^{-1} s^{-1}	μ_e / cm^2 V^{-1} s^{-1}
DTS-HT-DFC	7.29	15.36	0.78	60	8.44 × 10^{-5}	1.37 × 10^{-5}
DTS-DFC	5.28	11.58	0.84	54	6.81 × 10^{-5}	1.02 × 10^{-5}
DTS-HT-TFC	4.83	13.07	0.79	47	4.19 × 10^{-5}	0.75 × 10^{-5}
DTS-TFC	0.99	4.32	0.81	28	0.35 × 10^{-5}	0.35 × 10^{-5}

*Fig.6: Performance of BHJ OPVs consisting of π-extended **C** unit-based D–A copolymers as p-type semiconductor and PC$_{71}$BM as n-type semiconductor.*

Real-Time Measurements of Hydrogen Peroxide Uptake in 2D Cell Cultures Using On-Chip Microelectrode Arrays

Siddarth V. Sridharan,[1,6] Jose F. Rivera,[1,6] James Nolan,[2] Stephen Miloro,[2] Xin Jin,[1] Sarah M. Libring,[3,4] Hannah R. Kriscovich,[5] Muhammad A. Alam,[1,6] Jenna L. Rickus,[2,3,6] and David B. Janes[1,6]

[1] *School of Electrical and Computer Engineering, Purdue University, W. Lafayette, IN, US.*
[2] *School of Agricultural and Biological Engineering, Purdue University, W. Lafayette, IN US*
[3]*Welden School of Biomedical Engineering, Purdue University, W. Lafayette, IN US*
[4]*Dept. of Biomedical Engineering, Rutgers University, New Brunswick, New Jersey, US*
[5]*Dept. of Biomedical Engineering, Georgia Institute of Technology, Atlanta, GA, US*
[6] *Birck Nanotechnology Center, Purdue University, W. Lafayette, IN US*

e-mail: janes@purdue.edu

Amperometric microelectrode arrays (MEAs) can potentially measure analyte concentration at multiple positions simultaneously, which should allow determination of transient gradients induced by cellular uptake/release. While MEAs have been used to demonstrate concentration profiles induced by artificial sources/sinks of analytes, their application to physiological measurements, e.g. on 2D cell cultures, has been limited. Typical MEA geometries are not well suited for measurements near cell culture geometries and sensitivity variability, including electrode-to-electrode variability, make it difficult to obtain multi-point concentration values with sufficient accuracy to allow calculation of gradients. This study focuses on the development of on-chip amperometric MEAs and *in-situ* transient calibration approaches to allow measurement of transient concentration gradients near 2D cell cultures. The MEA consists of a 1D array of electrodes fabricated near the edge of a silicon chip to facilitate positioning in a typical 2D cell culture geometry and the calibration approach minimizes the effects of sensitivity variability, thus allowing for determination of gradients and associated fluxes based on concentration differences between adjacent electrodes. Building on prior studies involving artificial sinks, hydrogen peroxide (H_2O_2) consumption is studied in a 2D culture of human astrocyte cells. Astrocytes, a type of glial cell in the central nervous system, consume H_2O_2 in order to protect neurons from the reactive species. Time-dependent concentration profiles were measured at each of the electrodes in the MEA, and gradients/fluxes were determined from the difference in concentration between adjacent electrodes. Extrapolation to the cell surface allows determination of the surface concentration (C_S) and uptake flux, as well as the reaction rate coefficient, for the cells.

978-3-901578-31-1

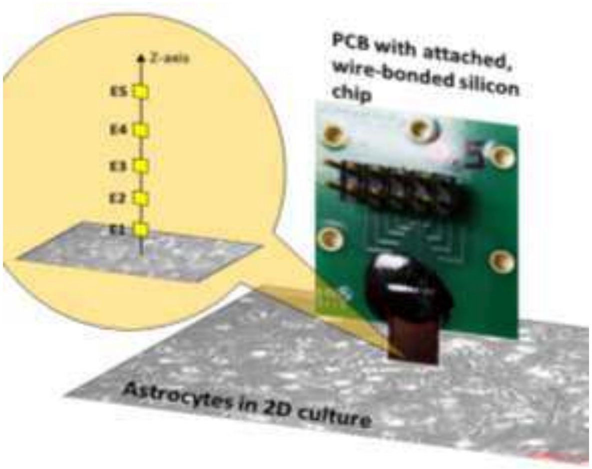

Fig.1: Experimental set-up, showing microelectrode array (MEA) positioned above 2D cell culture. MEA is comprised of 10x10 μm platinum electrodes, with pitch of 140 μm); during transient measurement, nearest electrode (E1) is 100 μm above cell surface.

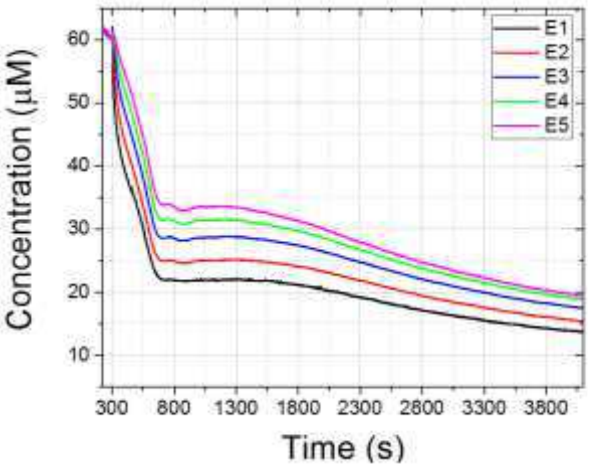

Fig.2: Measured peroxide concentration versus time at each of 5 electrodes in MEA. Initial peroxide concentration of 60 μM is introduced by bolus addition at t = 0s, with MEA positioned 5 mm from cell surface for first 300 s to allow in-situ calibration. Starting at t=300s, MEA is moved to position near cell surface, allowing measurement of time- and spatially- varying local concentration.

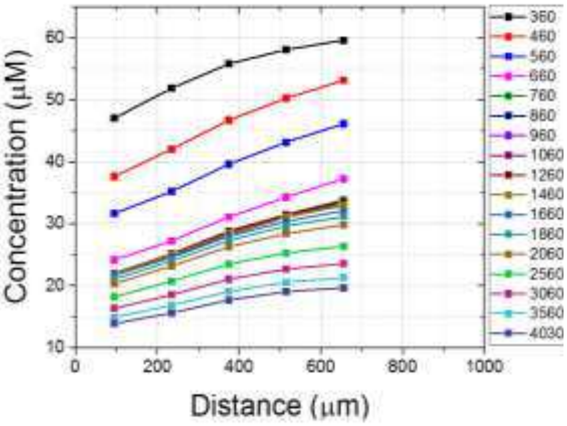

Fig.3. Measured peroxide concentration versus distance (z) at various times (360 to 4000 s) for 60 μM background peroxide concentration. Extrapolation to cell surface (z=0) allows determination of surface concentration (C_S) and uptake rate (flux).

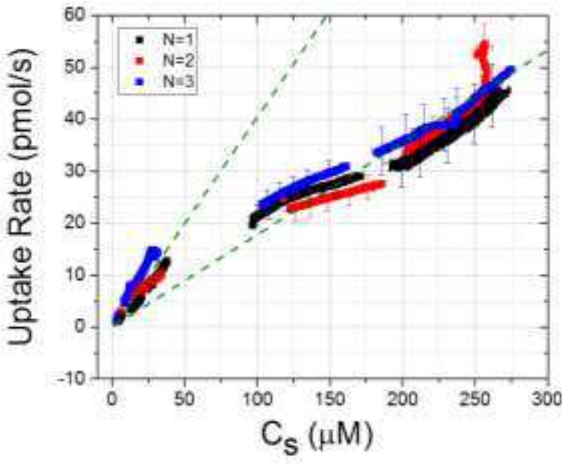

Fig.4 Measured peroxide uptake rate versus surface concentration (C_S) for various background concentrations, showing 3 independent runs for each concentration. Each segment reflects the time-dependent decrease of C_S, which is lower than the original solution concentration. The uptake rate decreases with increasing C_S (dashed lines illustrate two regimes)

Recent progress in quantum dot LEDs and their future prospects for displays

Changhee Lee

School of Electrical and Computer Engineering, Inter-university Semiconductor Research Center (ISRC), Seoul National University, Seoul 08826, Korea

Colloidal quantum dot (QD) is a semiconductor nanoparticle having unique optical properties such as the bandgap tunability and high photoluminescence (PL) quantum efficiency [1]. Especially, QDs have attracted a great interest for developing wide color gamut (WCG) displays since the QD emits light with pure primary colors (RGB). The full-width at half maximum (FWHM) of the PL spectra of CdSe-based QDs is about 20-30 nm, which is narrower than other phosphors. Fig. 1 clearly shows that the FWHM of electroluminescence (EL) spectra of QD light-emitting diodes (QLEDs) are much narrower than phosphorescent organic light-emitting diodes (OLEDs). Thus, QLEDs enable us to make a high-performance WCG display that can meet the Rec.2020 standard as shown in Fig. 2.

The performance of QLEDs have also been greatly improved as a result of remarkable advances in QD synthesis and device engineering since the first report of the QLED in 1994 [2]. The external quantum efficiency (EQE) of the CdSe-based QLEDs is comparable to the EQE of the state-of-the-art phosphorescent OLEDs as shown in Fig. 3 [3-5]. However, the EQE of Cd-free QLEDs is still low even compared with fluorescent OLEDs [6]. In addition the lifetime of QLEDs is far behind the practical requirement. Fig. 4 shows that the lifetime of blue QLEDs is orders of magnitude lower (T_{50}~25 h at 1000 cd/m^2) compared with green and red QLEDs [7]. Another important issue for realizing high-performance QLED displays is high-resolution, full-color patterning of QLED pixels. Currently, transfer printing (Fig. 5) and inkjet printing methods (Fig. 6) are demonstrated for full-color patterning of QLEDs, but mass production technology is not yet established. We think these challenges can be overcome in near future and therefore the future of the QLED technology is bright.

[1] J. Lim, W. K. Bae, J. Kwak, S. Lee, C. Lee, and K. Char, Opt. Mater. Express **2** (5), 594 (2012).

[2] V. L. Colvin, M. C. Schlamp, A. P. Alivisatos, Nature **370**, 354 (1994)

[3] J. Kwak et al., Nano Lett. **12**, 2362 (2012).

[4] X. Dai et al., Nature **515**, 96 (2014).

[5] C. Lee et al., SID Symp. Dig. Tech. Pap. **46**, 685 (2015)

[6] J. Lim,, M. Park, W. K.Bae, D. Lee, S. Lee, C. Lee, and K. Char, ACS Nano **7**, 9019 (2013).

[7] L. Qian et al., SID Symp. Dig. Tech. Pap. **48**, 55 (2017).

978-3-901578-31-1

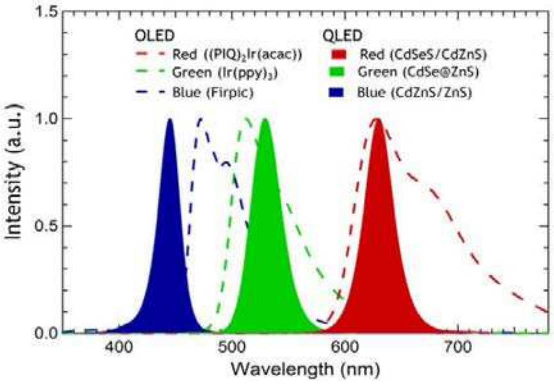

Fig.1: Comparison of the electroluminescence spectra of red, green, and blue phosphorescent OLEDs and CdSe-based QLEDs..

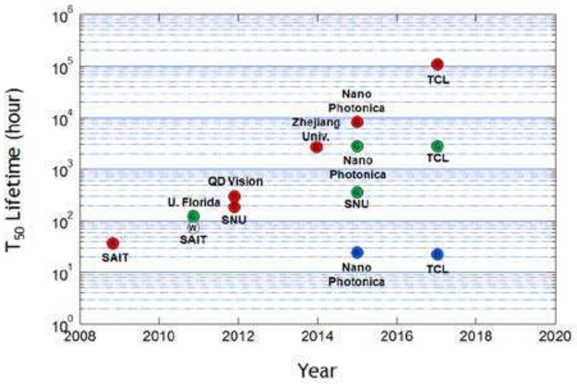

Fig.4: Progress of the lifetime (T_{50}) of red, green, and blue QLEDs measured at an initial luminance of 1000 cd/m^2..

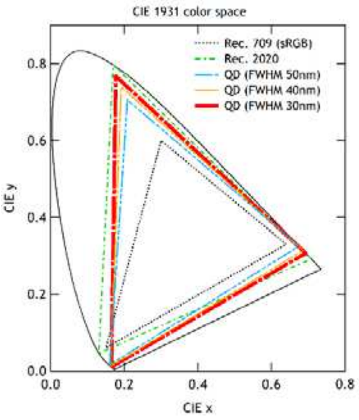

Fig.2: Commission Internationale de l'Eclairage (CIE) 1931 x, y coordinates of red-, green- and blue-QLEDs compared with Rec.709 (sRGB) and Rec.2020 standards..

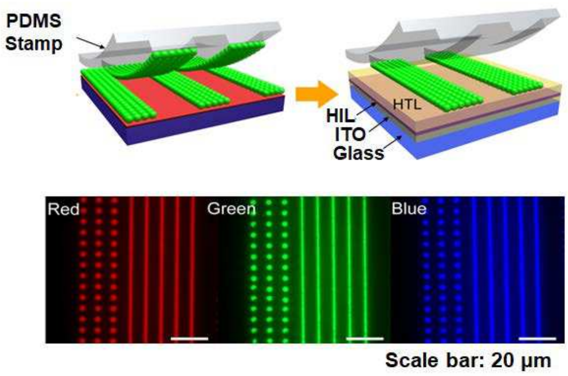

Fig.5 A process scheme of the QD transfer printing on an organic hole-transport layers and the fluorescence optical microscope (FOM) images of red, green and blue QD patterns.

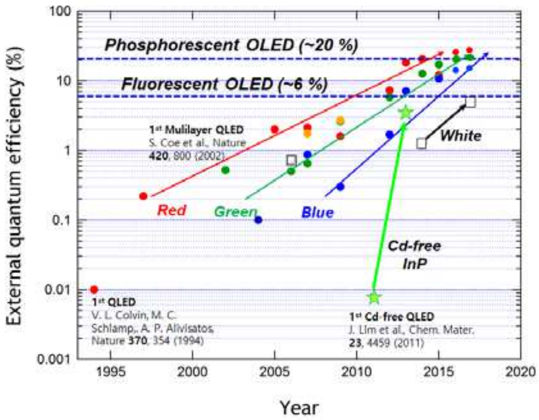

Fig.3: Progress of the external quantum efficiency (EQE) of red, green, blue and white CdSe-based QLEDs and Cd-free InP QLEDs. The theoretical EQE of phosphorescent and fluorescent OLEDs are also plotted with an assumption of out-coupling efficiency of 20 %.

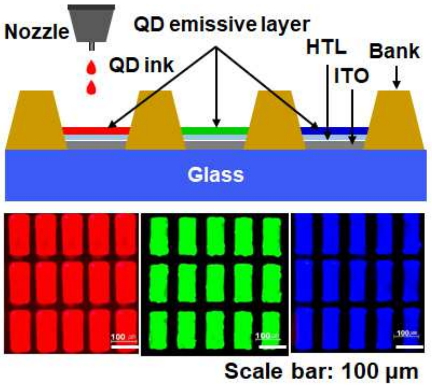

Fig.6: Schematic representation of the inkjet printing process of QDs. FOM images of inkjet-printed QD emitting layers

978-3-901578-31-1

Electrical and Optical Characteristics of Nanowire LEDs Under Mechanical Bending

Mohsen Asad[1], Renjie Wang[2], Zetian Mi,[3] and William S. Wong[1]

[1]*Department of Electrical and Computer Engineering, University of Waterloo, Waterloo, ON, Canada*
[2]*Department of Electrical Engineering, McGill University, Montreal, QC, Canada*
[3]*Department of Electrical Engineering and Computer Science, University of Michigan, Ann Arbor, MI, U.S.A.*
e-mail: wswong@uwaterloo.ca

InGaN dot-in-wire light-emitting diode (LEDs) fabricated on sapphire substrates were transferred onto flexible polyethylene terephthalate (PET) substrates using a “paste-and-cut” transfer process.[1] The GaN-based LEDs are first bonded onto the flexible platform followed by detaching the light emitters from its original process wafer. The I-V characteristics of the nanowire LEDs showed minimal change after transfer onto PET with a turn-on voltage of 2.5 V and a forward current of 400 μA at 4 V. The nanowire structure positioned the active region of the LED away from the plane of bending near the substrate surface, minimizing the effect of mechanical strain on the device operation. Bending the substrates did not affect the I-V characteristics and electroluminescence (EL) peak position while the EL intensity increased when the substrate was bowed in a concave up orientation, tilting the nanowires closer to each other during bending. Three-dimensional finite-difference time-domain modeling of the nanowire LED emission showed that the EL is a function of the distance between adjacent InGaN devices; moving the nanowires closer by substrate bending in a concave up geometry enhances the electromagnetic coupling between the nanowire LEDs leading to an increase in the EL intensity.

[1] W.S. Wong, *et al.* Appl. Phys. Lett. **78**, 1198 (2001).

978-3-901578-31-1

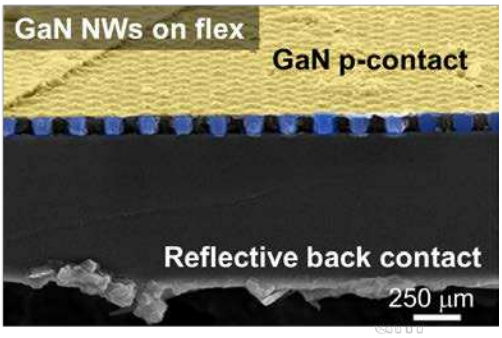

Fig.1: Cross-sectional scanning-electronic microscope micrograph of free standing GaN nanowire light-emitting diodes fabricated on sapphire substrates.

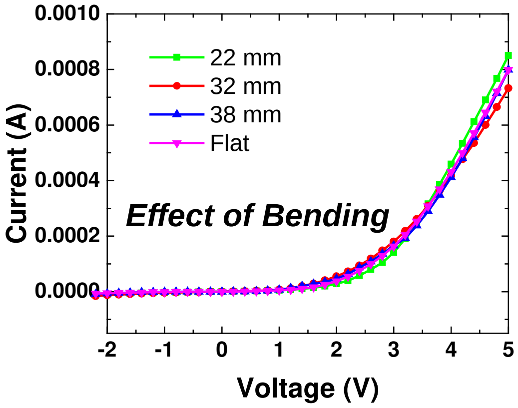

Fig.2: I-V characteristics of GaN LED devices on PET substrates under bending for different radii of curvature.

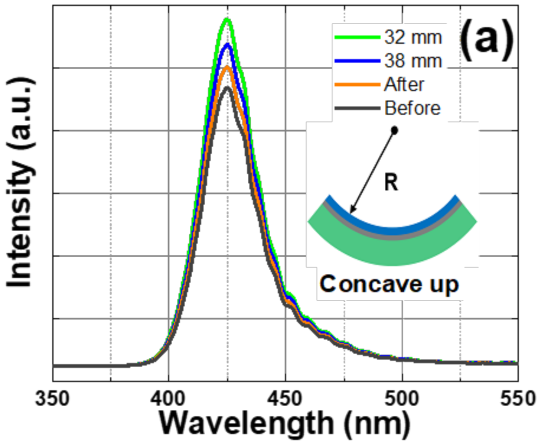

Fig.3: Electroluminescence characteristics of GaN nanowire LEDs under bending for different radii of curvature.

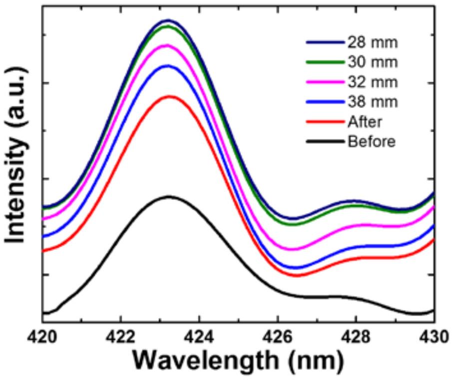

Fig. 4: Finite-difference time-domain calculations of the electroluminescence of an 11×11 array of nanowire LEDs on PET for various radii of bending.

Properties of A Few Hole Gated Double Quantum Dot

A. Bogan[1], S. Studenikin[1], M. Korkusinski[1], G. Aers[1], L. Gaudreau[1], P. Zawadzki[1], A. Sachrajda[1],

[1] [1]*Security and Disruptive Technologies, National Research Council, Ottawa, Canada*

While few electron electrostatic quantum dot devices in GaAs [1] and more recently Silicon have been studied for over a decade, few hole devices have proved surprisingly elusive. Recently L.A. Tracy et al. [2] at Sandia National Laboratories have successfully fabricated few hole devices in GaAs. Since holes are predicted to have lower hyperfine decoherence than electrons this opens up the possibility of spin qubits with long coherence times in a direct bandgap material which is advantageous for linking spin qubit processors to flying qubits (i.e. photons). In this talk results will be presented from transport measurements on the Sandia devices in the one and two hole regimes. The g-factor is found to be very dependent on field orientation due to very weak heavy-light hole mixing with an almost zero g-factor for the in-plane direction[3]. Spin-flip tunneling is found to be very strong in contrast to electron devices. The consequences of this for charge and hybrid spin-charge qubits will be illustrated experimentally using Landau-Zener-Stückelberg interferometry where novel features are observed and will be explained. Finally, we will present results on the spin relaxation time, T1, of a single hole in a quantum dot has been measured as a function of magnetic field.

[1] M.Ciorga et al. PRB **61** (2000) R16315

[2] L.A.Tracy et al. APL **104** (2014) 123101

[3] A.Bogan et al. PRL **118**, (2017) 167701

We acknowledge L. A.Tracy, J. L.Reno, and T. W. Hargett from Sandia National Laboratories in the US for the single hole transistor in p-type GaAs/AlGaAs

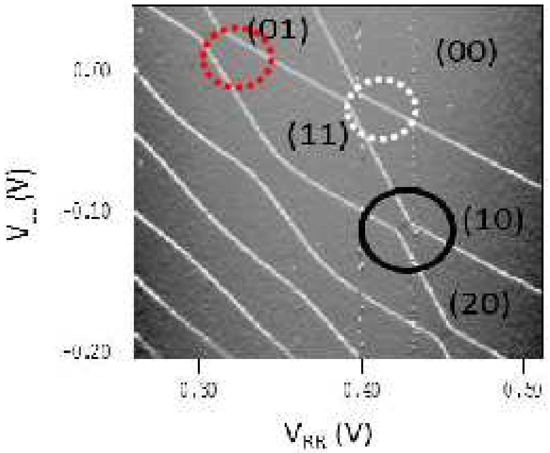

Fig.1 :Stability diagram of a few hole double quantum dot

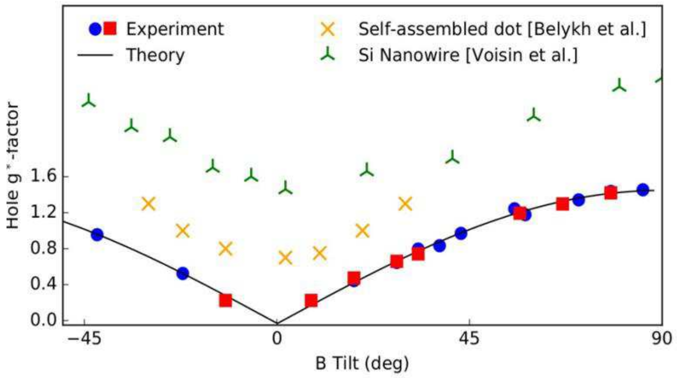

Fig.2 :g-factor of holes confined to a lateral few hole quantum dot. vs field orientation compared to similar results from self-assembled dots and nanowires.

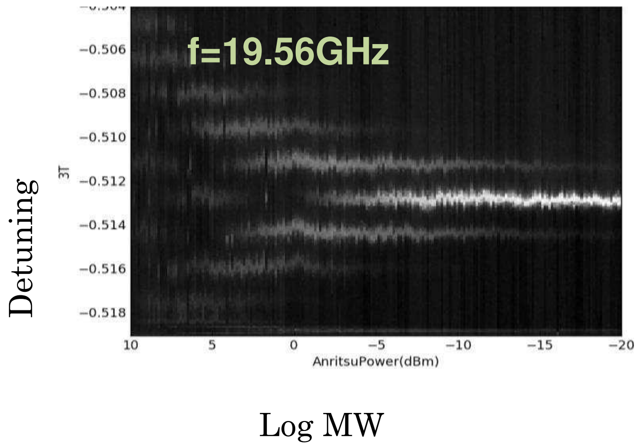

Fig.3 : LZS Interference pattern of a single hole confined to a double quantum dot.

978-3-901578-31-1

Metal-insulator-metal single electron tunneling transistors featuring non-native dielectrics

Mattew Filmer[1], Hubert George[2], Golnaz Karbasian[2], Michael McConnell[1],
Louisa Schneider[4], Alexei N. Nazarov[5], Alexei O. Orlov[1], and Gregory L. Snider[1]

[1] *Department of Electrical Engineering, University of Notre Dame, Notre Dame, Indiana*
[2]*Intel Corporation, Portland, OR, USA;* [3] *Applied Materials, Inc., Santa Clara , CA, USA*
[4] *SkyWater Technology Foundry, Bloomington, MN USA*
[5]*V.E. Lashkaryov Institute of Semiconductor Physics, Kiiv,Ukraine*
email: aorlov@gmail.com

Single electron transistors are nanoscale electron devices that require thin, high-quality tunnel barriers to operate and have potential applications in sensing, metrology and beyond-CMOS computing schemes. While SET performance improves with downscaling, it is critically dependent on the quality of the tunnel barriers. The dominant technique for making the tunnel barriers has been controlled metal oxidation [1]. Here we present the results of a different approach and aim at fabrication of SET devices featuring nanoscale metal-insulator-metal (MIM) tunnel junctions with *non-native* dielectrics. This enables greater flexibility in material choice for device, but it also requires special in-process and post-fabricating treatments of MIM structures to eliminate residual native oxides and to improve the quality of the deposited dielectric. Two basic fabrication schemes for making MIM-SET with thin barrier dielectrics are discussed: atomic layer deposition (ALD) of Al_2O_3, SiO_2, combinations of the two, SiN_x, (an example of a SET with Pt-Al_2O_3-Pt junctions is shown in Fig 1) and physical vapor deposition (PVD) of SiO_2. We demonstrate that the performance of fabricated devices changes radically depending on preparation recipe [2]. In particular, several orders of magnitude difference in the random charge noise was observed in ALD Ni-SiO_2-Ni devices that differ by only a single post-deposition hydrogen treatment step, Fig. 2. Good performance was also obtained for PVD Pt-SiO_2–Pt SETs after hydrogen plasma step, Fig 3. We present a comparative study of several different treatments and discuss potential physical models that explain these observations. This work was supported by NSF grants DMR-1207394 and CHE-1124762.

1. T.A. Fulton and G.H. Dolan, "Observation of Single-Electron Charging Effects in Small Tunnel Junctions". *Phys. Rev. Lett.*, **59**, p. 109-12, 1987.

2. G. Karbasian, M. McConnell, H. George, L. Schneider, M. Filmer, A. Orlov, A. Nazarov, and G. Snider, "Metal-Insulator-Metal Single Electron Transistors with Tunnel Barriers Prepared by Atomic Layer Deposition". *Applied Sciences*, **7**, p. 246, 2017.

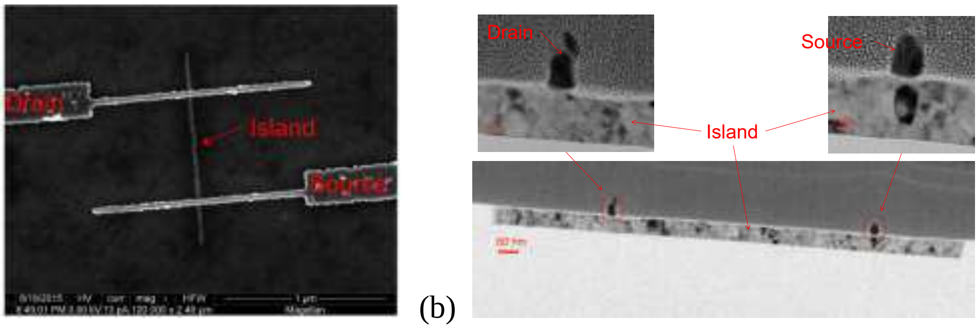

(a) (b)

Figure 1. SEM (a)_and TEM (b) micrographs of the "cross-tie" Pt-Al_2O_3-Pt SET fabricated using 9 cycles of ALD on an oxidized Si substrate

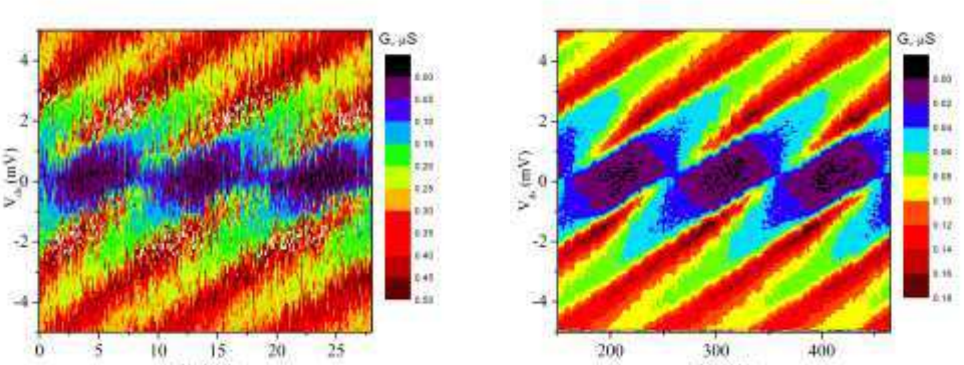

(a) (b)

Figure 2. Coulomb blockade oscillations in the SET with ALD barriers devices in two Ni-SiO_2-NiSETs fabricated using 11 cycles of ALD SiO_2. Two different post-fabrication treatments were used: a) anneal at 375 C in H_2/Ar; b)remote H_2 plasma; T=0.4K

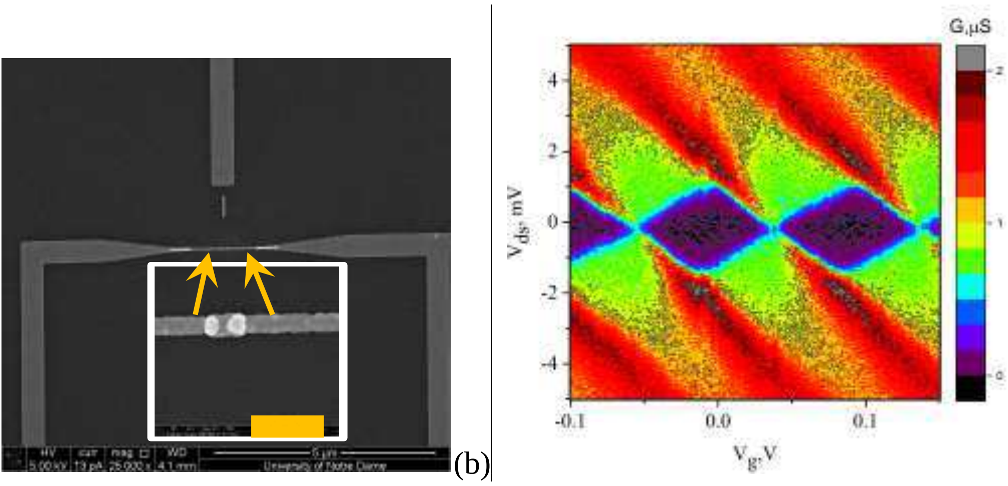

Figure 3. SET with Pt/SiO_2/Pt tunnel junctions made by PVD. a) SEM Micrograph of the device, inset shows SET island and two junctions; b) and Coulomb diamonds of the device measured at T=0.3 K

Optospintronics and 2D Magnets

Roland K. Kawakami

Department of Physics, The Ohio State University, Columbus, OH 43210, USA

Two dimensional (2D) materials provide a unique platform for investigating the properties of spin and valley degrees of freedom, which can be probed by optical methods and electrical transport methods. Graphene provides an excellent medium for spin transport within a low spin orbit coupling (SOC) environment for long spin diffusion lengths at room temperature. Monolayer transition metal dichalcogenides (TMD) provide optical coupling to the spin and valley degrees of freedom within a high SOC environment. Ferromagnetic metals and insulators provide a means for electrical injection, detection, and manipulation of spin and valley degrees of freedom. One distinguishing characteristic of 2D materials is the ability to produce vertical heterostructures that combine vastly different functionalities at the length scale of a few atoms or less. Taking advantage of such an opportunity requires the use and development of advanced synthesis, fabrication, and characterization techniques for creating systems with atomic-scale precision and performing spin/valley-sensitive measurements with high fidelity. In this talk, I will present recent work on some of the first steps toward multifunctional 2D spintronics. This includes optical spin injection into graphene via optical excitation in MoS_2/graphene heterostructures [1], spin/valley dynamics in monolayer TMDs, and room temperature ferromagnetism in monolayer van der Waals magnets.

[1] Y. L. Luo, J. Xu, T. Zhu, G. Wu, E. J. McCormick, W. Zhan, M. R. Neupane and R. K. Kawakami. Nano Lett. **17(6)**, 3877-3883(2017).

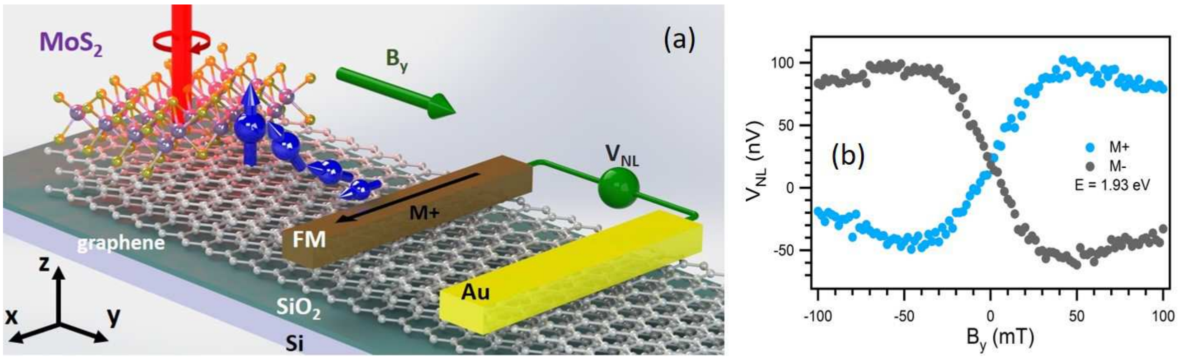

Fig. 1: (a) Illustration of optical spin injection, lateral spin transport, and electrical spin detection in a monolayer MoS_2/few-layer graphene hybrid spin valve structure. (b) Electrical spin signal V_{NL} as a function of B_y exhibits clear antisymmetric Hanle spin precession signals which flip polarity with the Co magnetization direction (M+ vs M−).

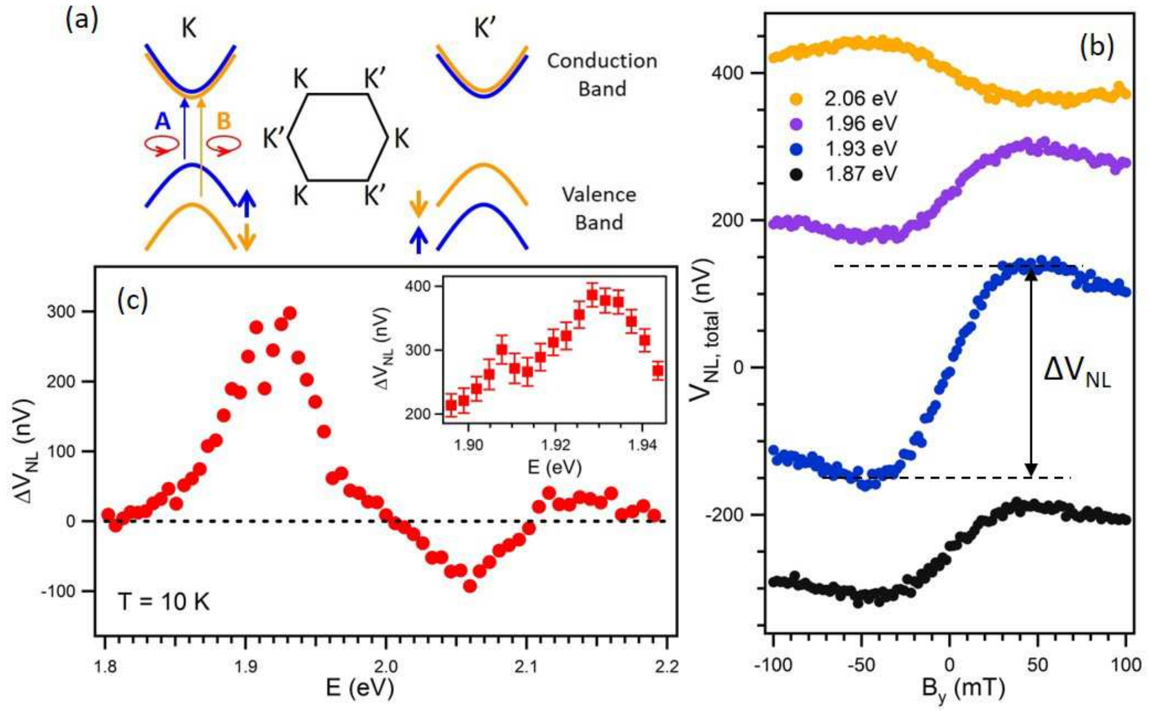

Fig. 2: Photon energy dependence of opto-valleytronic spin injection. (a) Schematic band structure of monolayer MoS_2 at the K and K′ valleys. The valence band of monolayer MoS_2 has a large spin splitting with opposite spin orientation for the A and B optical excitations within the same valley. (b) Representative antisymmetric Hanle curves at four photon energies (1.87, 1.93, 1.96, and 2.06 eV). (c) Spin signal ΔV_{NL} as a function of photon energy. Starting from low photon energy, ΔV_{NL} reaches a maximum positive signal near the A resonance (1.90−1.95 eV) and then decreases with increasing photon energy until ΔV_{NL} flips sign around 2 eV. ΔV_{NL} reaches a minimum near the B resonance at ~2.06 eV. This photon energy dependence clearly reflects the nondegenerate spin-split structure of the valence band, which results from strong spin-orbit coupling and the broken inversion symmetry of the monolayer MoS_2 lattice. Inset shows zoom-in detailed features around the A exciton resonance, consistent with the double peak structure of the A^- trion and A exciton.

978-3-901578-31-1

Magnetometer Based on Spin Wave Interferometer

Michael Balynsky[1], David Gutierrez[1], Howard Chiang [1], Alexander Kozhevnikov[2,3], Galina Dudko[2] , Yuri Filimonov[2,3], Alexander A. Balandin[1], and Alexander Khitun[1]

[1]Department of Electrical and Computer Engineering, University of California -Riverside,
Riverside, California, USA 92521
[2]Kotelnikov Institute of Radioengineering and Electronics of the Russian Academy of Sciences,
Saratov, Russia 410019
[3]Saratov State University, Saratov, Russia 410012
e-mail: akhitun@engr.ucr.edu

We describe a magnetic field sensor based on a spin wave interferometer. Its sensing element consists of a magnetic cross junction with four micro-antennas fabricated at the edges. Two of these antennas are used for spin wave excitation while two other antennas are used for detection of the inductive voltage produced by the interfering spin waves. Two waves propagating in the orthogonal arms of the cross may accumulate significantly different phase shifts depending on the magnitude and direction of the external magnetic field. This phenomenon is utilized for magnetic field sensing. The sensitivity attains its maximum under the destructive interference condition, where a small change in the external magnetic field results in a drastic increase of the inductive voltage, as well as in the change of the output phase. We report experimental data obtained for a micrometer scale $Y_3Fe_2(FeO_4)_3$ cross structure. The change of the inductive voltage near the destructive interference point exceeds 40 dB per 1 Oe. The phase of the output signal exhibits a π-phase shift within 1 Oe. The data are collected at room temperature. Taking into account the low thermal noise in ferrite structures, we estimate that the maximum sensitivity of the spin wave magnetometer may exceed attotesla.

978-3-901578-31-1

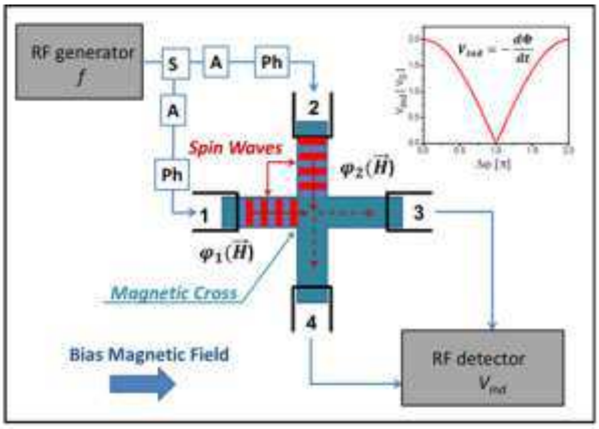

Figure 1. Schematics of the sensing element. It is a spin wave interferometer build on magnetic cross junction. There are four micro-antennas fabricated on the edges of the cross. Two of these antennas (i.e. ports 1 and 2) are used for spin wave excitation, and the other two (i.e. ports 3 and 4) are used for the spin wave detection via the inductive voltage measurements. Sensing element is placed on top of the magnetic substrate, which is aimed to provide a DC bias in-plane magnetic field.

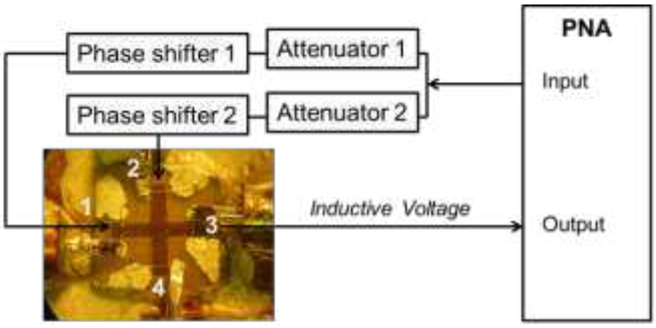

Figure 2. Schematics of the experimental setup. The sensing element is a cross junction made of single crystal $Y_3Fe_2(FeO_4)_3$ film. The YIG cross has the following dimension: the length of the each waveguide is 3.65 mm; the width is 650 μm; and the YIG film thickness is 3.8 μm. There are four Π-shaped micro-antennas fabricated directly on the surface of YIG at the edges of the cross. The antennas are connected to a programmable network analyzer (PNA) Keysight N5241A. There is a set of attenuators (PE7087) and a phase shifters (ARRA 9428A) to independently control input power and the phase of the spin wave signals generated at the input ports 1 and 2. The device is placed inside an electromagnet to control the in-plane bias magnetic field from −1000 Oe to +1000 Oe.

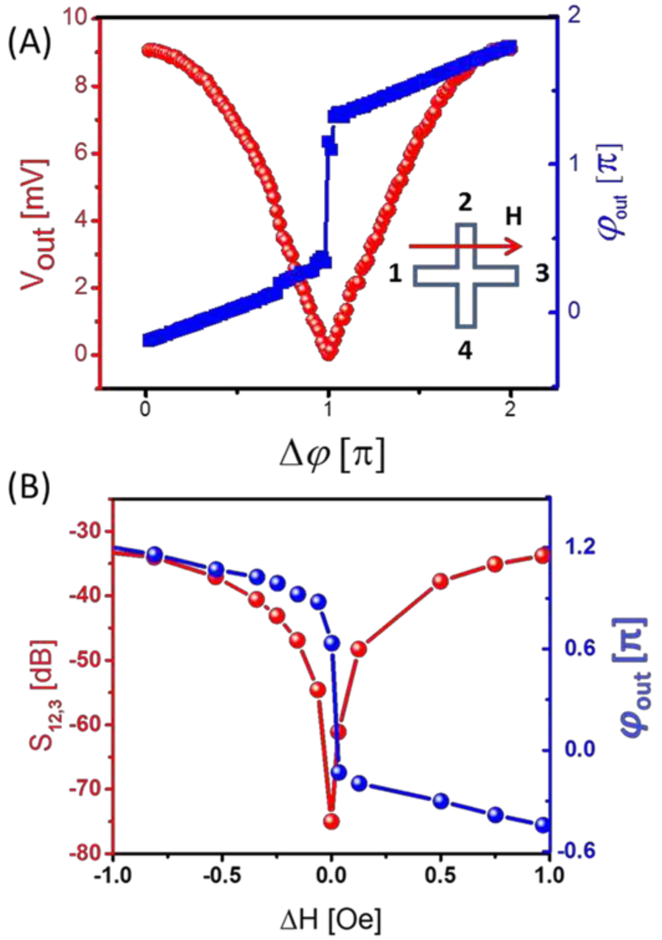

Figure 3. Experimental data obtained for magnetic field directed along the virtual line connected ports 1 and 3. (A) The amplitude (red markers) and the phase (blue markers) of the inductive voltage detected at port 3 as a function of the spin wave phase difference. Output voltage maxima correspond to the constructive spin wave interference. The minimum of the inductive voltage corresponds to the destructive spin wave interference. (B) Output voltage dependence on the magnetic field in the vicinity of the destructive interference point.

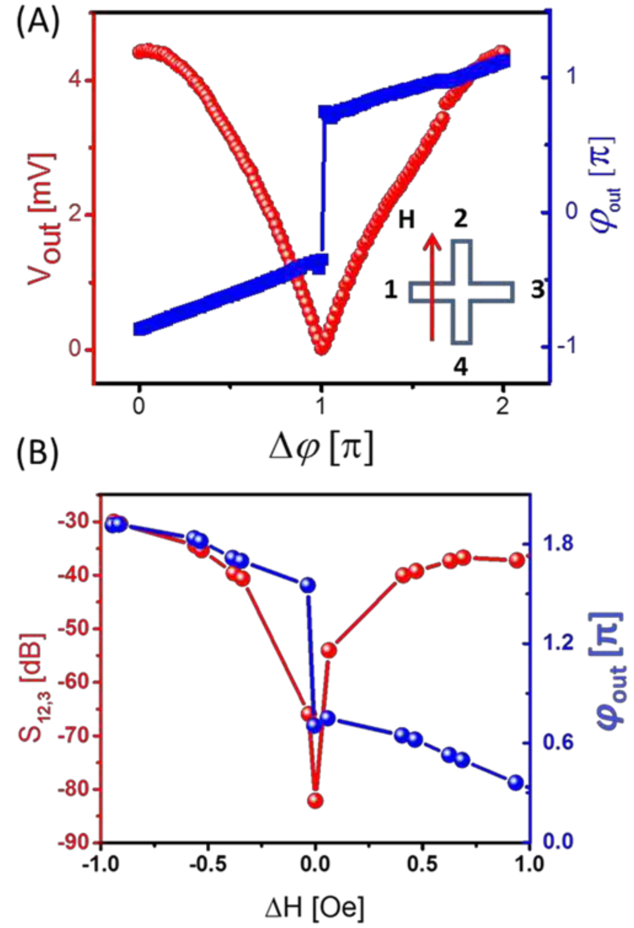

Figure 6. Experimental data obtained for magnetic field directed along the virtual line connected ports 2 and 4. (A) The amplitude (red markers) and the phase (blue markers) of the inductive voltage detected at port 3 as a function of the spin wave phase difference. (B) Output voltage dependence on the magnetic field in the vicinity of the destructive interference point.

978-3-901578-31-1

Field-effect spin-orbit valve and spin transistor based on proximity bilayer graphene

Jaroslav Fabian

Department of Physics, University of Regensburg, 93040 Regensburg, Germany
e-mail: jaroslav.fabian@ur.de

When we place bilayer graphene (BLG) on an insulating or semiconducting substrate, iy can take some properties of the substrates, while keeping its overall electronic band structure. This is common to graphene and 2D materials. What is special about BLG? The fact, that the layers are separated by a weak van der Waals coupling, makes BLG ideal for field-effect manipulations of the proximity effect. Indeed, we find [1] by performing systematic DFT calculations of BLG on monolayer WSe2 (direct gap semiconductor), that the built-in field of the heterostructure induces a strong (few meV) spin-orbit splitting of the valence band of BLG, while the conduction band shows only a pristine splitting of a few micro eV (Fig. 1). Applying an electric field countering the built-in one reverses the splitting: now it is the conduction band that is spin-orbit split, while holes have a weak splitting. This effect is unprecedented, as it allows to change the spin-orbit coupling in BLG by 2 orders of magnitude (and spin relaxation by four!). We also propose that this effect is used as a platform for spin transistors, which are driven by electrically controlling spin relaxation, see Fig. 2 I will also talk about our recent results on spin relaxation in phosphorene [2].

[1] M. Gmitra and J. Fabian, arXiv:1706.06149

[2] A. Avsar et al, Nature Physics, doi:10.1038/nphys4141, (2017)

978-3-901578-31-1

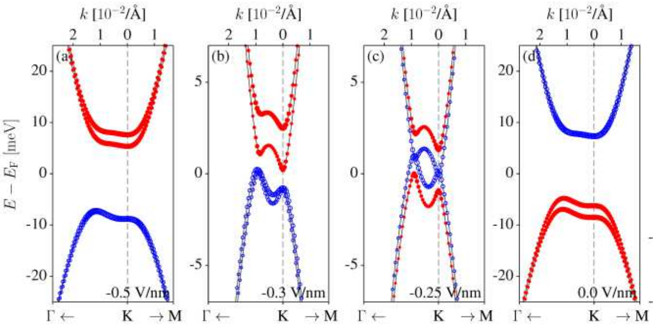

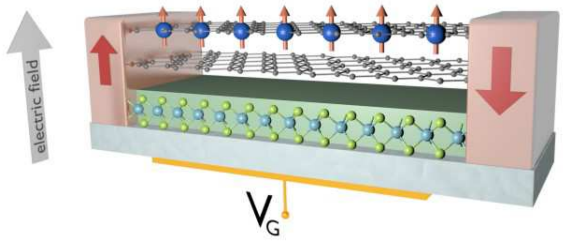

Fig.1: Without electric field (right) the valence band of BLG on WSe2 has strong spin-orbit splitting. If an electric field is applied, the splitting appears in the conduction band (left).

Fig.2: Spin transistor based on field-effect of spin relaxation in BLG on WSe2. In this configuration the spin relaxation is weak since the electrons travel through the upper layer which has weak proximity effect and so induced spin-orbit coupling is weak.

Spin current propagation in a 2-dimensional electron gas

Masashi Shiraishi[1], Ryo Ohshima and Yuichiro Ando

[1] *Department of Electronic Science and Engineering, Kyoto Univ., 6158510, Japan.*
e-mail:mshiraishi@kuee.kyoto-u.ac.jp

Spin transport in condensed matters has been collecting strong attention in spintronics. Nonmagentic metals (Cu, Ag…), semiconductors (Si, Ge, GaAs…) and molecules (graphene, nanotube…) are intensively investigated and room temperature (RT) spin transport is now realized in a wide variety of materials. The realization of RT spin transport enables fabrication of novel functional spin devices, such as spin transistors. In fact, the Sugahara-Tanaka type spin MOSFET [1,2] and the Das-Datta type spin transistor [3] were experimentally demonstrated.

Here in this presentation, we introduce a new material stage for spintronic devices, an oxide 2-dimensional electron gas (2DEG). The 2DEG system formed at an interface between LaAlO (LAO) and SrTiO (STO), insulating oxides, is used for this study. The 2DEG at LAO/STO exhibits a number of attractive and fruitful physics, such as high mobility of carrier [4], superconductivity [5] and so on, and importantly it consists of d-electrons. The purpose of the study is to load a spintronic function to this attractive d-electron 2DEG. NiFe was used for a spin injector and its magnetization dynamics allows spin injection and generation of spin current into the 2DEG. To detect the spin current passing through the 2DEG, the inverse spin Hall effect (ISHE) of Pt and Ta strips equipped on the 2DEG were used. Sign of the spin Hall angle of Pt and Ta are opposite. Thus, the sign of electromotive forces due to the ISHE in the Pt and the Ta is opposite when the spin current successfully propagates in the 2DEG. Consequently, the spin current propagation was demonstrated at RT, and the spin diffusion length was estimated to be about 300 nm from gap length dependence and two different model calculations [6]. The detail is discussed in the presentation.

[1] T. Sasaki, M. Shiraishi et al., Phys. Rev. Applied **2**, 034005 (2014).
[2] T. Tahara, M. Shiraishi et al., Appl. Phys. Express **8**, 113004 (2015).
[3] H.C. Koo et al., Science **325**, 1515 (2009).
[4] A. Ohtomo et al., Nature **427**, 423 (2004).
[5] N. Reyren et al., Science **317**, 1196 (2007).
[6] R. Ohshima, M. Shiraishi et al., Nature Mater. **16**, 609 (2017).

978-3-901578-31-1

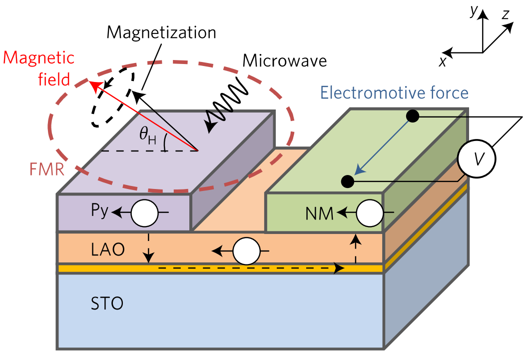

Fig. 1 Schematic image of an LAO/STO device

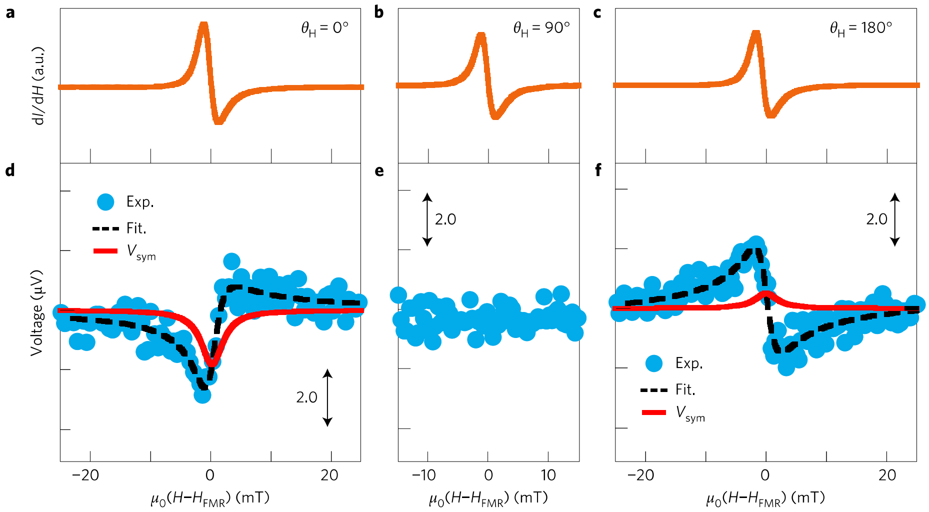

Fig. 2 (a-c) FMR spectra of NiFe on the LAO/STO, (d-f) electromotive forces from the Pt on the LAO/STO.

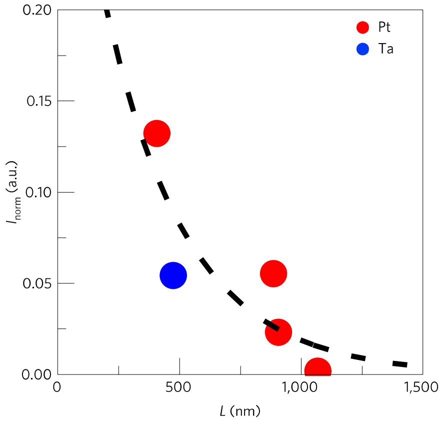

Fig. 3 Gap length dependence of the electromotive forces from the Pt and the Ta.

Current in Magnetic Tunnel Junctions at Spin-Dependent Hopping

Viktor Sverdlov[1], Josef Weinbub[2], and Siegfried Selberherr[1]

[1] *Institute for Microelectronics, TU Wien, Gußhausstr. 27-29, 1040 Wien, Austria*
[2] *Christian Doppler Laboratory for High Performance TCAD, Institute for Microelectronics,*
TU Wien, Gußhausstr. 27-29, 1040 Wien, Austria
e-mail: Selberherr@TUWien.ac.at

Spin correlations at *hopping* are responsible for large effects observed at room temperature in organic light-emitting diodes [1] and also for the large tunnel magnetoresistance (TMR) observed in trap-assisted resonant tunneling between the normal and the ferromagnetic electrode through an oxide [2,3]. The reason for the correlations is the spin-selective escape rate from a trap into the ferromagnet resulting in a non-zero average spin at the trap. The trap occupation n (and thus the current), however, depends on the spin **s**=(s_x, s_y, s_z), which can be determined from the stationary solution of the balance matrix equation generalized to describe spin-dependent hopping in a magnetic tunnel junction (MTJ) sketched in Fig.1.

$$\frac{d}{dt}\begin{pmatrix} n \\ s_x \\ s_y \\ s_z \end{pmatrix} = \Gamma_N(1-n)\begin{pmatrix} 1 \\ \mathrm{p}_2 \sin\zeta\cos\varphi \\ \mathrm{p}_2 \sin\zeta\sin\varphi \\ \mathrm{p}_2 \cos\zeta \end{pmatrix} - \mathrm{A}\begin{pmatrix} n \\ s_x \\ s_y \\ s_z \end{pmatrix},$$

$$\mathrm{A} = \begin{pmatrix} \Gamma_\mathrm{F} & |\mathbf{p}|\Gamma_\mathrm{F}\sin(\Theta) & 0 & |\mathbf{p}|\Gamma_\mathrm{F}|\cos(\Theta) \\ |\mathbf{p}|\Gamma_\mathrm{F}\sin(\Theta) & \Gamma_\mathrm{F} + 1/T_2 & \omega_\mathrm{L} & 0 \\ 0 & -\omega_\mathrm{L} & \Gamma_\mathrm{F} + 1/T_2 & 0 \\ |\mathbf{p}|\Gamma_\mathrm{F}\cos(\Theta) & 0 & 0 & \Gamma_\mathrm{F} + 1/T_1 \end{pmatrix} \qquad (1)$$

Electrons tunnel from the right ferromagnetic contact with the rate Γ_N to the trap, from which they escape with the rate Γ_F to the left ferromagnetic contact. The contacts are characterized by the spin polarizations $\mathbf{p}_2$ and $\mathbf{p}$, to which the electron spins are aligned with the corresponding magnetization directions defined by the polar and azimuthal angles (ζ, φ) and $(\Theta, 0)$ relative to the direction of the magnetic field, respectively. $T_{1,2}$ are the spin relaxation times on the trap, and ω_L is the Larmor frequency.

The stationary solution of (1) for the occupation allows to obtain the current $I = e\Gamma_N(1-n)$:

$$I = e\frac{\Gamma_F(\Theta)\,\Gamma_N}{\Gamma_F(\Theta) + \Gamma_2(\Theta,\zeta,\varphi)} \qquad (2a)$$

$$\Gamma_F(\Theta) = \Gamma_F\left(1 - p^2\,\Gamma_F T_1\left\{\frac{\cos^2\Theta}{\Gamma_F T_1 + 1} + \frac{T_2}{T_1}\frac{\sin^2\Theta(\,\Gamma_F T_2 + 1)}{\omega_L^2 T_2^2 + (\,\Gamma_F T_2 + 1)^2}\right\}\right) \qquad (2b)$$

$$\Gamma_2(\Theta,\zeta,\varphi) = \Gamma_N\left(1 \;- pp_2\,\Gamma_F T_1\left\{\frac{\cos\Theta\cos\zeta}{\Gamma_F T_1 + 1} + \frac{T_2}{T_1}\frac{\sin\Theta\sin\zeta\,(\,\Gamma_F T_2 + 1)}{\omega_L^2 T_2^2 + (\,\Gamma_F T_2 + 1)^2}\left(\cos\varphi - \frac{\omega_L\,T_2}{\Gamma_F T_2 + 1}\sin\varphi\right)\right\}\right) \qquad (2c)$$

978-3-901578-31-1

Fig. 2 shows the dependence of current as a function of Θ for several values of ζ, for $\varphi = 0$ (both magnetizatons are in the same plane, Fig.1), Γ_N=10Γ_F, ω_L=Γ_F, p=p_2=0.9, without spin relaxation. The current has a maximum at $\Theta = \zeta$, when the contact magnetizations are parallel. In addition, there is a smaller current increase at $\Theta = -\zeta$. The second maximum value is found to increase with the magnetic field, when the spin precession is faster. Because the spin precesses within the cone passing through both magnetizations, the rise of the magnetic field and the frequency of precession increases the chance of an electron to escape.

A high magnetic field suppresses the terms with *sinus* functions (2). The terms can also be suppressed by dephasing (T_2=0), which results in the current being symmetric with respect to $\Theta = \pm\zeta$ as shown in Fig.3. Unexpectedly, the stronger dephasing results in a larger current modulation (cf. Fig. 2). Even more surprising, the TMR due to spin-dependent hopping (r≈12) is larger than that of the MTJ (r≈8.5). A 40% TMR boost is important for the improved functionality of MTJs, in particular as a large TMR is paramount for modern MTJ-based MRAM.

[1] Y.Wang et al., Phys. Rev. X 6, 011011 (2016)
[2] Y.Song and H.Dery, PRL 113, 047205 (2014)
[3] Z.Yue et al., Phys. Rev. B 91, 195316 (2015)

Acknowledgment. The financial support by the Austrian Federal Ministry of Science, Research and Economy and the National Foundation for Research, Technology and Development is gratefully acknowledged.

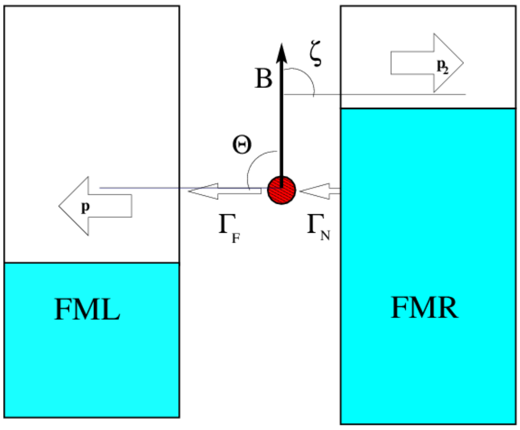

Fig.1 Schematic illustration of the system studied.

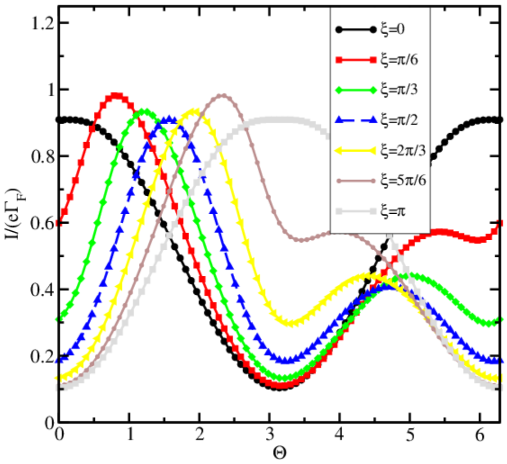

Fig.2 Spin-dependent trap-assisted tunneling without spin relaxation for Γ_N=10Γ_F, ω_L=Γ_F, p=p_2=0.9, $\varphi = 0$.

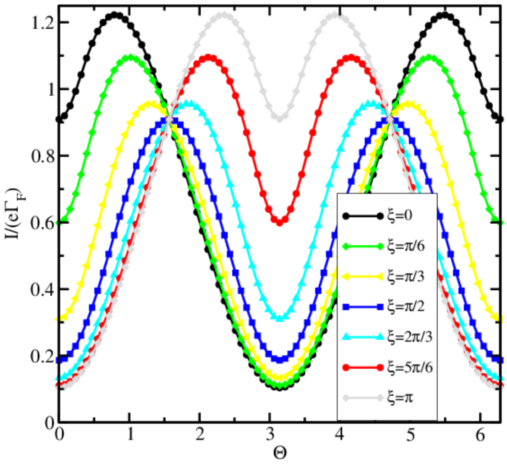

Fig.3 Same as in Fig.2 with strong spin dephasing. TMR at spin-dependent hopping is enhanced as compared to the MTJ's TMR.

978-3-901578-31-1

Magnetic Proximity Effects in Two-Dimensional Materials

Igor Žutić [1]

[1] *Department of Physics, University at Buffalo, SUNY, Buffalo, NY 14260, USA*
e-mail: zigor@buffalo.edu

Proximity effects can transform a given material through its adjacent regions to become superconducting, magnetic, or topologically nontrivial, enabling unexplored device opportunities. In bulk materials, the sample size often dwarfs the characteristic lengths of proximity effects allowing their neglect. However, in two-dimensional materials such as graphene and transition-metal dichalcogenides (TMDs), the situation is drastically different, even short-range magnetic proximity effects exceed their thickness and strongly modify spin transport and optical properties [1-3]. Experimental confirmation by the groups A. Geim [4], B. van Wees [5] and R. Kawakami [6] of our prediction for bias-controlled spin polarization reversal in Co/h-BN/graphene [1] suggest that tunable magnetic proximity effects may overcome the usual need for an applied magnetic field and a magnetization reversal to implement the graphene-based spin logic [7]. One of the TMD hallmarks is their valley-spin coupling which leads to a valley-dependent helicity of interband transitions and important implications for transport. While lifting the degeneracy between valleys K and K' is the key step in manipulating valley degrees of freedom, a common approach requires huge magnetic fields, limited by the small Zeeman splitting ~0.1-0.2 meV/T. However, recent advances demonstrate that using magnetic substrates provides a viable alternative for lifting valley degeneracy [8,9]. Since excitons dominate optical response in TMDs, magnetic proximity effects cannot be described by the widely used single-particle description, but an accurate inclusion of Coulomb interactions is required [3]. We predict a conversion between optically inactive and active excitons by rotating the magnetization of the magnetic substrate [3].

[1] P. Lazić, K. D. Belashchenko, and I. Žutić, Phys. Rev. B **93**, 241401(R) (2016).

[2] P. Lazić, G. M. Sipahi, R. Kawakami, and I. Žutić, Phys. Rev. B **90**, 085429 (2014).

[3] B. Scharf, G. Xu, A. Matos-Abiague, and I. Žutić, Phys. Rev. Lett. in press, arXiv:1704.07984.

[4] P. Asshoff et al., 2D Mater. **4**, 031004 (2017).

[5] M. Gurram, S. Omar, and B. J. van Wees, Nat. Commun. **8**, 248 (2017).

[6] J. Xu, S. Singh, J. Katoch, G. Wu, T. Zhu, I. Žutić, and R. Kawakami, submitted to Nat. Nanotech.

[7] H. Wen et al., Phys. Rev. Appl. **5**, 044003 (2016).

[8] C. Zhao et al., Nat. Nanotech. **12**, 757 (2017).

[9] D. Zhong et al., Science Adv. **3**, 1603113 (2017).

978-3-901578-31-1

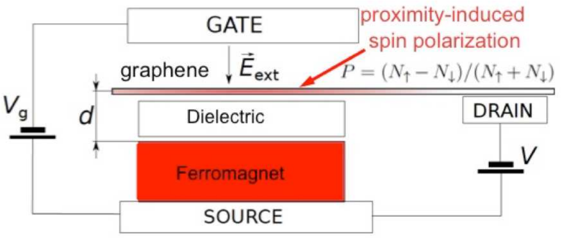

Fig.1: Device schematic. V_g *is the gate voltage and* E_{ext} *related electric field. P proximity-induced spin polarization in graphene.*

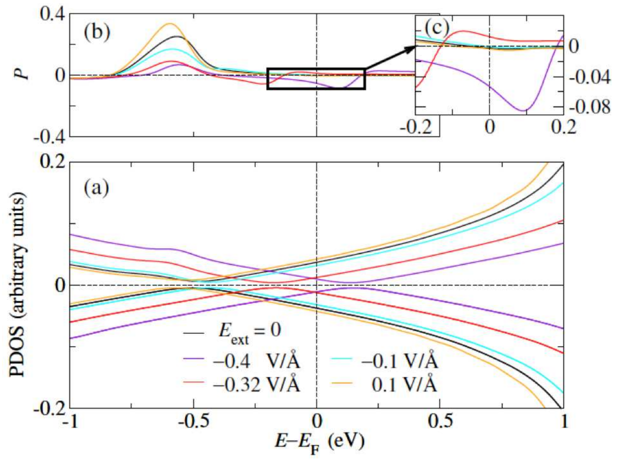

Fig.2: (a) Field-dependent projected DOS and (b) P for graphene in Co/h-BN/graphene system calculated from first principles. (c) Zoom of the P which reveals that its magnitude and sign is gate-controlled [1].

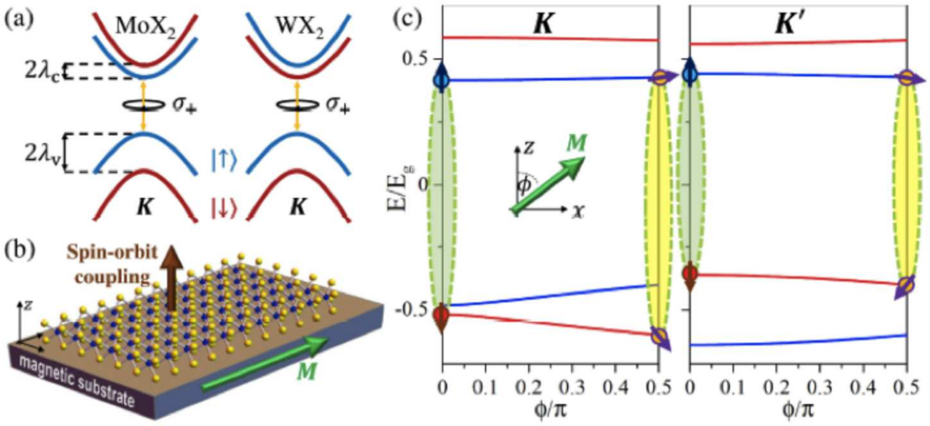

Fig.3: Spin-valley coupling in monolayer TMDs: Conduction, valence band (CB,VB) is spin-split in the K valley due to strong spin-orbit coupling with the CB ordering reversed between MoX_2 *and* WX_2*. Emitted/absorbed light has valley-selective helicity,* $\sigma_{\pm}$*. (b) TMD on a magnetic substrate. (c) The K and K' band edges as the substrate's magnetization, M, is rotated, shown for* $MoTe_2$*/EuO parameters. One dark exciton for K and K' and the spin direction for selected band edges are depicted [3].*

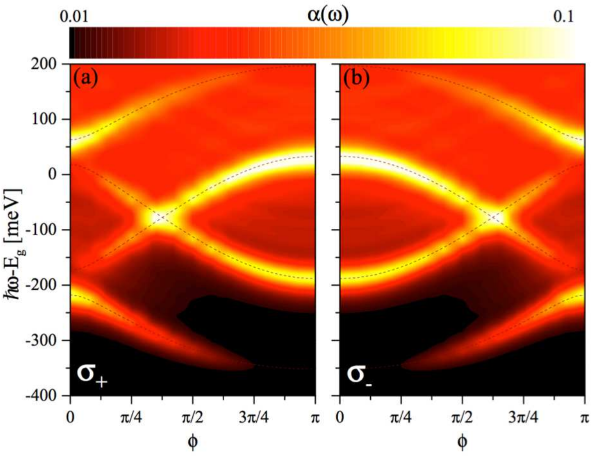

Fig.4: Evolution of the absorption of monolayer $MoTe_2$ *on EuO as M is rotated from out-of-plane* ($\phi = 0$) *to in-plane* ($\phi = \pi/2$) *and out-of-plane, but with reversed M* ($\phi = \pi$) *for (a)* $\sigma+$ *and (b)* $\sigma-$ *[3].*

978-3-901578-31-1

Proximity Induced Ferromagnetism in Graphene from a Magnetic-Nanoparticle Array

Guibin Song[1], Mojtaba Ranjbar[1], Nicholas Rizzo[1], David Daughton[2] and Richard Kiehl[1]

[1] *Electrical, Computer and Energy Engineering, Arizona State University, Tempe, AZ, USA*
[2] *Lake Shore Cryotronics, Westerville, OH USA*
e-mail: richard.kiehl@asu.edu

Graphene's long spin diffusion length, high carrier mobility, and gateablity are attractive features for spintronics, but weak spin-orbit coupling limits graphene's capabilities for generating and manipulating spin polarized currents. This limitation has motivated interest in *inducing* ferromagnetism in graphene by proximity induced ferromagnetism (PIFM) from an adjacent ferromagnetic insulator (FMI). Two critical requirements for PIFM are 1) a strong exchange interaction at the FMI/graphene interface and 2) a highly insulating FMI to prevent shorting of the graphene current. PIFM has been studied for graphene with the FMIs $LaMnO_3$ [1], $Y_3Fe_5O_{12}$ [2], EuS [3] and EuO [4]. Here, we present a novel approach for achieving PIFM in graphene from a "layer" comprised of a *magnetic nanoparticle (MNP) array*, rather than a continuous magnetic insulator film. One important advantage of this approach is that the separation between MNPs provides insulation within the layer, thereby greatly extending the range of suitable FM materials to *conductive* semiconductors and metals. This materials flexibility extends possibilities for optimization of both the magnetic properties of the FM layer and the electronic properties at the critical FM/graphene interface. Moreover, the ability to achieve PIFM in graphene from such a *patterned* magnetic nanostructure opens new possibilities for developing spintronic *circuits* in which individual, or clusters of, nanoparticles serve as magnetically coupled device elements that can be electrically controlled by gated graphene transport. In this talk, we will present results demonstrating PIFM in self-assembled arrays of 18-nm Fe_3O_4 MNPs integrated with a graphene field-effect transistor. Aspects of the device fabrication (Fig. 1), characterization of FM/graphene coupling (Fig. 2), and Hall effect data (Fig. 3) over wide ranges of gated electron and hole transport from 10 to 300 K will be discussed. Possibilities for non-Boolean information processing with such structures (Fig. 4.) will also be addressed.

[1] G. Geng et al., Appl. Phys. Lett., **105**, 133111 (2014).

[2] Z. Wang et al., Phys. Rev. Lett., **114**, 016603 (2015).

[3] P. Wei et al., Nature Mat., **15**, DOI: 10.1038/NMAT4603 (2016).

[4] S. Su et al., Phys. Rev. B., **95**, 075418 (2017).

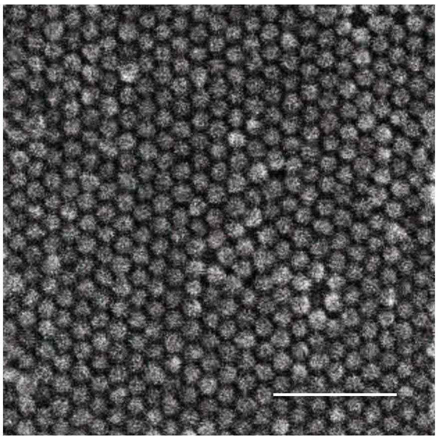

Fig.1: Scanning electron micrograph of a self-assembled array of 18-nm Fe_3O_4 MNPs on graphene after pyrolytic removal of 1-nm oleic acid shells. (Scale bar 100 nm.)

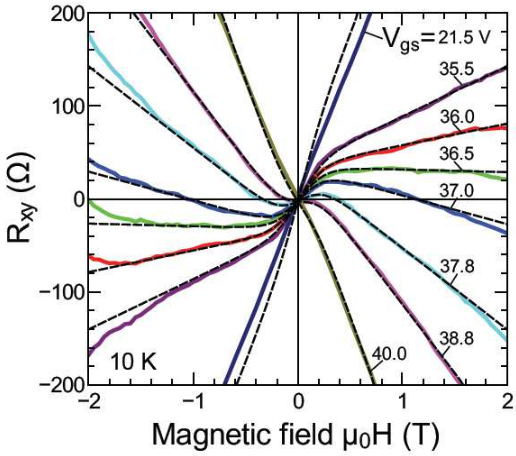

Fig.4: Hall resistance R_{xy} vs magnetic field H for an Fe_3O_4 MNP array on graphene at various back-gate biases V_{gs} above (electron transport) and below (hole transport) the Dirac point of approximately 36.5 V. The sharp nonlinearities are signatures of the anomalous Hall effect, which is attributed to proximity induced ferromagnetism in the graphene due to exchange coupling with the MNP array. .

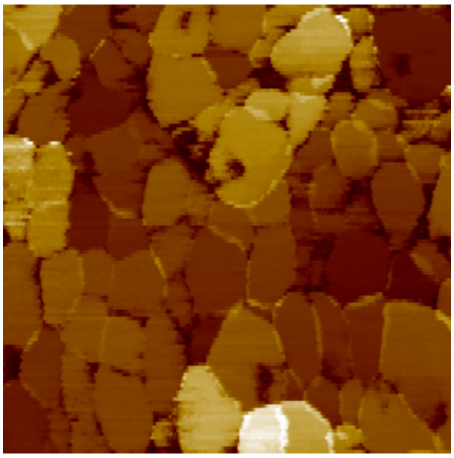

Fig.2: Conductive atomic force microscopy image of Fe_3O_4 magnetic nanoparticles on graphene after pyrolytic removal of oleic acid shells. This current map confirms that electrical contact is achieved at the nanoparticle/graphene interface. Post-deposition removal of the organic shells by pyrolysis is required to produce atomic contact, and hence exchange coupling, between the Fe_3O_4 nanoparticle cores and graphene, as demonstrated by control experiments in this study.

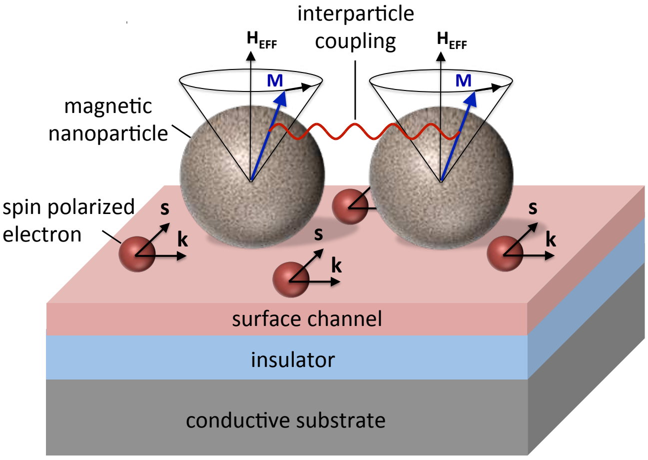

Fig.4: Illustration of coupled spin torque oscillators based on an array of magnetic nanoparticles that are in close proximity and exchange-coupled to graphene, as in the proximity induced ferromagnetism experiments described here. In the depicted device concept, spin-polarized surface current drives magnetic precession in the MNPs by spin torque transfer, while electronic and magnetic interparticle coupling mechanisms provide phase-locking and control of the oscillations, potentially providing the basis for non-Boolean information processing circuitry.

A Single-Spin Switch

Viktor Sverdlov and Siegfried Selberherr
Institute for Microelectronics, TU Wien, Gußhausstr. 27-29, 1040Wien, Austria
e-mail: {Sverdlov|Selberherr}@TUWien.ac.at

With magnetic tunnel junctions scaling down, new phenomena due to the correlated charge transport are anticipated. One relevant phenomenon is associated to the non-avoidable traps in the insulator. In particular, the Coulomb interaction leads to a strong repulsion on a trap, a Coulomb blockade, while the Pauli blockade results in spin-dependent correlations at the transport through quantum dots and traps [1,2]. Spin-dependent hopping is responsible for large magnetoresistance in ferromagnet-insulator-metal structures [3] and magnetic tunnel junctions, due to the strong dependence of the trap occupation n and the current on the avareage spin $\mathbf{s}$ of the trap, which are determined by the solution of the system:

$$\frac{d}{dt}n = \Gamma_{\mathrm{S}}(1-n) - \Gamma_{\mathrm{D}}n - \Gamma_{\mathrm{D}}\mathbf{p}_{\mathrm{D}}\mathbf{s}, \quad \frac{d}{dt}\mathbf{s} = \mathbf{p}_S\Gamma_{\mathrm{S}}(1-n) - \Gamma_{\mathrm{D}}\mathbf{s} - \mathbf{p}_{\mathrm{D}}\Gamma_{\mathrm{D}}n + [\mathbf{s}\times\boldsymbol{\omega}_L]$$

Here $\boldsymbol{\omega}_{\mathrm{L}}$is the Larmor frequency vector pointing along the magnetic field $\mathbf{B}$, $\Gamma_{\mathrm{S,D}}$ and $\mathbf{p}_{\mathrm{S,D}}$ are the tunneling rates and the degrees to which the electron spins are polarized along the corresponding magnetization direction in the source and drain electrodes, respectively.

Since the spin on the trap is a vector quantity, it results in unusual correlations in *multi-terminal* devices. Here we analyze a three-terminal device in the configuration shown in Fig.1, where the source (1), the gate (2), and the drain (3) are ferromagnets, each described by the corresponding spin polarization $\mathbf{p}_{\mathrm{i}}$ (i = 1,2,3). The potential at the trap is determined by the gate voltage $V_{\mathrm{GS},}$ the drain-source voltage $V_{\mathrm{DS},}$ and the capacitances C_{i} (i=1,2,3), which are assumed equal. The current I_α from an electrode α=G(Gate), S(Source), or D(Drain) to the trap is defined positive, if it flows from the electrode to the trap. The current continuity $I_{\mathrm{G}}+I_{\mathrm{S}}+I_{\mathrm{D}}=0$ is thus automatically ensured. In our investigations a constant gate voltage V_{GS} is applied. For $V_{\mathrm{DS}} < V_{\mathrm{GS}}/2$ the junctions “source-trap” and “trap-drain” are biased in opposite direction. Then, in single-electron transistor (SET) configuration ($\Gamma_2 = 0,\ p_i = 0$) the drain current is zero (Fig.2), while the current “drain-trap” I_{D} is negative at $V_{\mathrm{DS}} < V_{\mathrm{GS}}/2$, if all $\Gamma_{\mathrm{i}} = \Gamma$ and p_2=0, for any value of p_1, p_3 (Fig.2). The ferromagnetic gate (p_2=0.99) suppresses I_{D} and I_{G} at $V_{\mathrm{DS}} < V_{\mathrm{GS}}/2$, however, a large I_{G} comparable to I_{D} is obtained (Fig.3, Fig.4), unless the source is also ferromagnetic (p_1=0.99) (Fig.5). The value of I_{D} is further boosted, if all p_{i}=0.99 (Fig.6). We note that, although the behavior in Fig.6 is similar to that of a SET (Fig.2), the switching is due to the *spin correlations* and *spin blockade* alone.

[1] K. Ono et al., Science 297, 1313 (2002).

[2] Y. Wang et al., Phys. Rev. X 6, 011011 (2016).

[3] Y. Song and H. Dery, PRL 113, 047205 (2014).

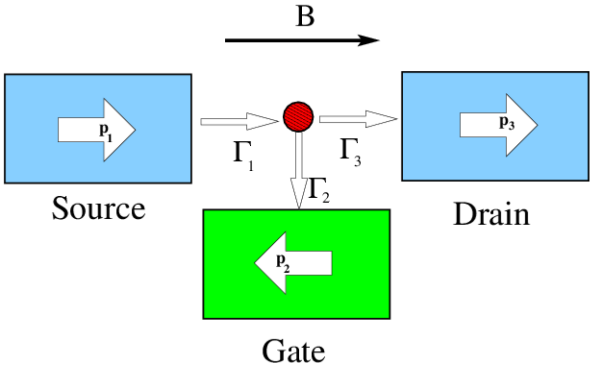

Fig.1: Schematic illustration of the device. Electron transport is caused by spin-dependent hopping between the ferromagnetic contacts.

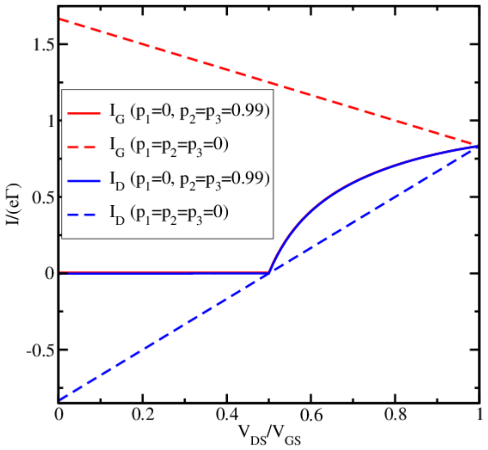

Fig.4: The currents are similar to those in Fig.3, when, in addition to the gate, the drain is ferromagnetic (p_2=p_3=0.99).

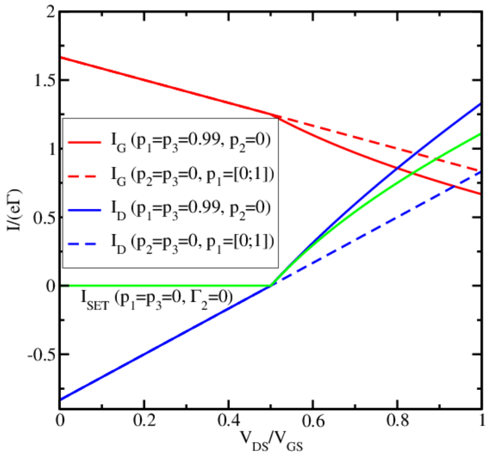

Fig.2: Gate and drain currents, when the gate is non-ferromagnetic (p_2=0). The SET drain current is also shown.

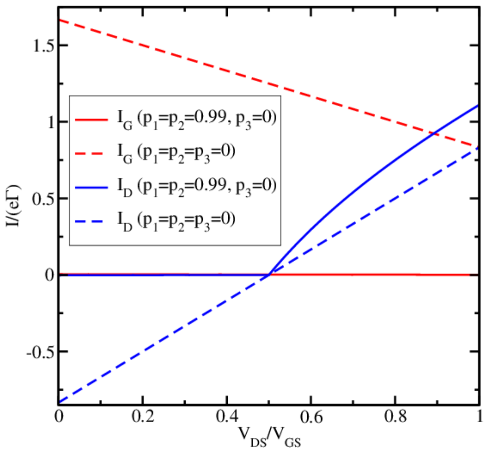

Fig.5 The gate current is suppressed, when the source and the gate are ferromagnetic (p_1=p_2=0.99).

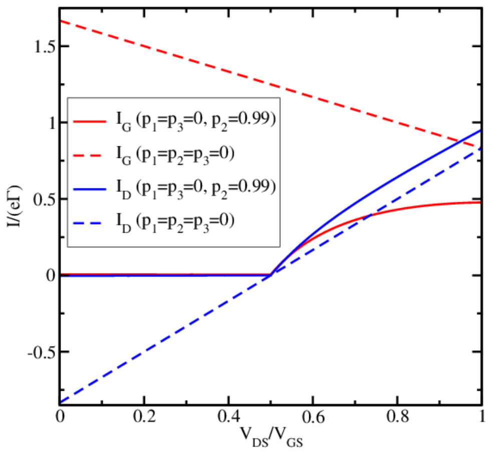

Fig.3: The drain and gate currents are suppressed, if the trap-drain junction is backward biased and the gate is ferromagnetic (p2=0.99). The gate current is nonzero for V_{DS}>V_{GS}/2.

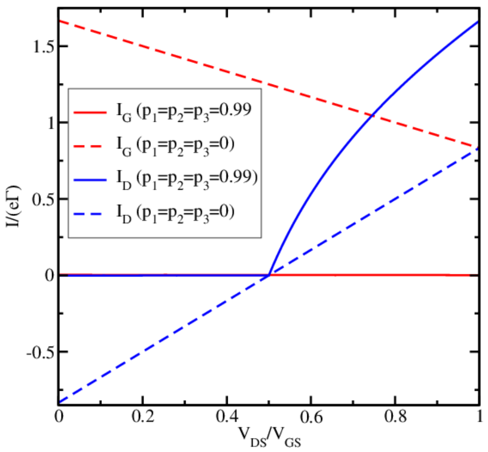

Fig.6: The drain current is the largest, while the gate current is suppressed, when all electrodes are ferromagnetic (p_1=p_2=p_3=0.99) in the configuration shown in Fig.1.

Ultraviolet Raman Spectroscopy of NiO: Spin – Phonon Interactions and Implications for Antiferromagnetic Spintronics

Ece Aytan[1], Bishwajit Debnath[2], Fariborz Kargar[1], Yafis Barlas[2], Junxue Li[3], Roger Lake[2],
Jing Shi[3] and Alexander A. Balandin[1]

[1]Nano-Device Laboratory (NDL), Department of Electrical and Computer Engineering,
University of California, Riverside, CA 92521 USA
[2]Laboratory for Terascale and Terahertz Electronics (LATTE), Department of Electrical and
Computer Engineering, University of California, Riverside, CA 92521 USA
[3]Department of Physics and Astronomy, University of California, Riverside, CA 92521 USA
e-mail: eayta001@ucr.edu

Nickel oxide (NiO) has recently attracted attention as an antiferromagnetic (AF) insulator material for spintronic applications and THz control of AF spin waves. The unusually high Néel temperature of this material (T_N=523 K) allows for device operation in AF state at room temperature (RT) and above. It is beneficial for the proposed spintronic applications that the magnetic ordering of NiO can only be changed by very large magnetic fields, *i.e.* stable against external magnetic perturbations. Understanding the spin – phonon coupling in NiO is important for material's functionalization, and for enabling ultra-high-speed and low-power dissipation. However, until today, little is known about spin – phonon interactions, and an associated magnon damping, in this material system. We used temperature-dependent ultraviolet (UV) Raman spectroscopy to determine the spin – phonon coupling in NiO. The UV excitation was essential for obtaining spectrum, which is not dominated by the two-magnon (2M) band [1]. It was established that both longitudinal optical (LO) and transverse optical (TO) phonons interact with the spin of Ni atoms. At the same time, the spin – LO and spin – TO interactions are of different strengths and have opposite effects on the phonon energies. The coupling strength was explained using the density functional theory (DFT). The obtained results shed light on spin – phonon interactions in AF insulators and may help in optimizing spintronic and THz devices.

This work was supported as part of the Spins and Heat in Nanoscale Electronic Systems (SHINES), an Energy Frontier Research Center funded by the U.S. Department of Energy, Office of Science, Basic Energy Sciences (BES) under Award # SC0012670.

[1] M. M. Lacerda, F. Kargar, E. Aytan, R. Samnakay, B. Debnath, J. X. Li, A. Khitun, R. K. Lake, J. Shi, and A. A. Balandin, Appl. Phys. Lett., 110, 202406 (2017).

978-3-901578-31-1

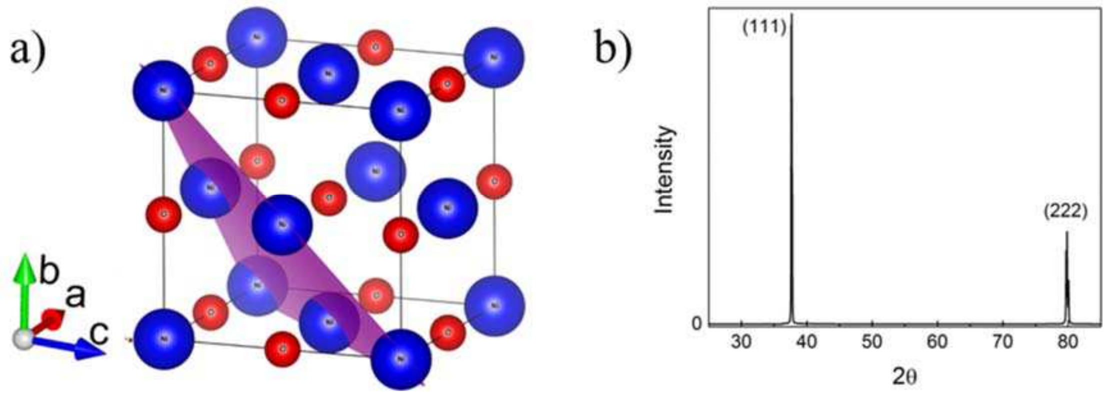

Figure 1: (a) Schematic of the crystal structure of NiO oxide showing antiferromagnetic ordering along [111] direction. A purple plane respresents the (111) plane. (b) X-ray difraction spectrum of the sample confirming its crystallinity.

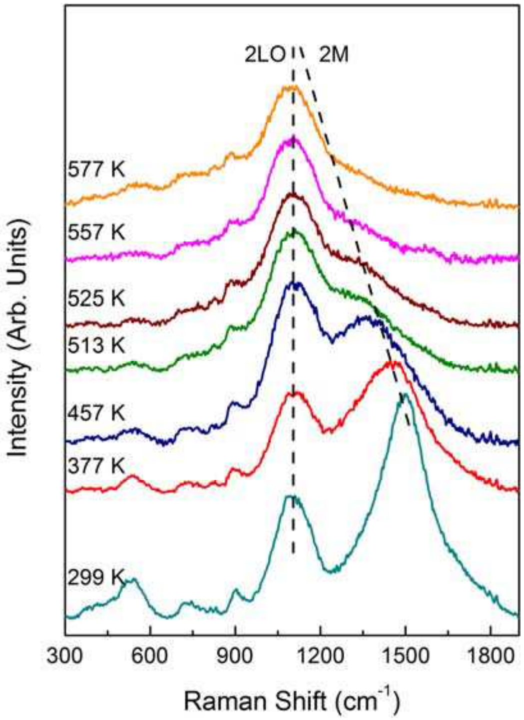

Figure 2: Evolution of visible Raman spectrum of NiO at different temperatures. Note that the visible Raman spectrum is dominated by the 2M band, which does not allow for the accurate 2LO or 2TO peak position extraction.

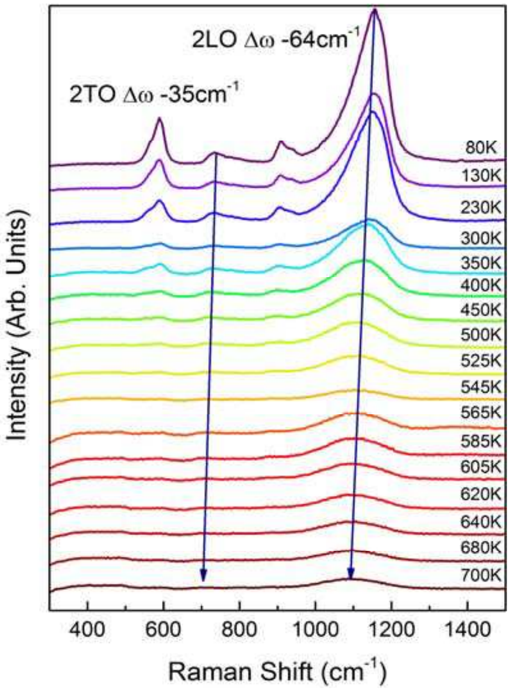

Figure 3: Evolution of UV Raman spectrum of NiO at different temperatures. The 2M band is absent in the UV Raman spectrum allowing for an accurate extraction of the 2LO and 2TO peak positions. The temperature dependence of the 2LO and 2TO bands can be used for determining the spin – phonon coupling coefficients.

Light, Spin, and Magnetization in Magnetically-Doped Semiconductor Nanocrystals

Scott Crooker[1], Bill Rice[1], Wenyong Liu[2], Dmitri Yakovlev[3], and Victor Klimov[2]

[1] *National High Magnetic Field Laboratory, Los Alamos, NM 87545, USA*
[2] *Chemistry Division, Los Alamos National Laboratory, Los Alamos, NM 87545, USA*
[3] *Experimentelle Physik 2, Technische Universitat Dortmund, D-44221 Dortmund, Germany*
e-mail: crooker@lanl.gov

The past decade has witnessed a resurgent interest in magnetically-doped semiconductors, motivated in part by the ability to tailor, via quantum confinement and wavefunction engineering, the *sp-d* spin interactions between embedded magnetic atoms and band carriers (electrons and holes). Materials for spin-based electronic and photonic applications include magnetically-doped nanoribbons, nanowires, quantum dots, and nanocrystals. In these structures, strong quantum confinement can compress the carrier wavefunctions $\Psi_{e,h}(\mathbf{r})$ to nanometer-scale volumes, significantly enhancing their interactions with dopants such as Mn^{2+} or Co^{2+}. Giant magneto-optical effects can therefore be realized in nanoscale devices using few or even single dopants. Importantly, however, thermodynamic spin fluctuations become increasingly relevant in this few-spin limit. In nanoscale volumes, the statistical sqrt(N) fluctuations of N embedded dopant spins are expected to generate giant effective magnetic fields B_{eff} which dramatically impact carrier spin dynamics, even in the absence of any external applied field. Using ultrafast optical spectroscopy we directly reveal the very large (~30 tesla) effective fields B_{eff} that are "seen" by electrons in Mn^{2+}-doped CdSe nanocrystals, which are due to statistically-incomplete cancellation of the randomly-oriented Mn^{2+} spins [1]. These measurements reveal the initial coherent dynamics of magnetic polaron formation and highlight the importance of magnetization fluctuations on carrier spin dynamics in nanoscale devices.

Separately, we also explore the flip-side of the strong *sp-d* exchange interaction: the effective magnetic exchange field, B_{ex}, that is felt by the Mn^{2+} spins due to the spin of a single photogenerated electron-hole pair (*i.e.*, an exciton). Using resonant PL studies we show that B_{ex}~10 T, in agreement with theoretical expectations [2]. B_{ex} is sufficient to induce a collective and spontaneous ferromagnetic alignment of all the Mn^{2+} dopants in the nanocrystal – an *exciton magnetic polaron* -- even in the absence of any external magnetic field.

[1] W. D. Rice *et al.*, Nature Nanotechnology **11**, 137 (2016).
[2] W. D. Rice *et al.*, Nano Letters **17**, 3068 (2017).

978-3-901578-31-1

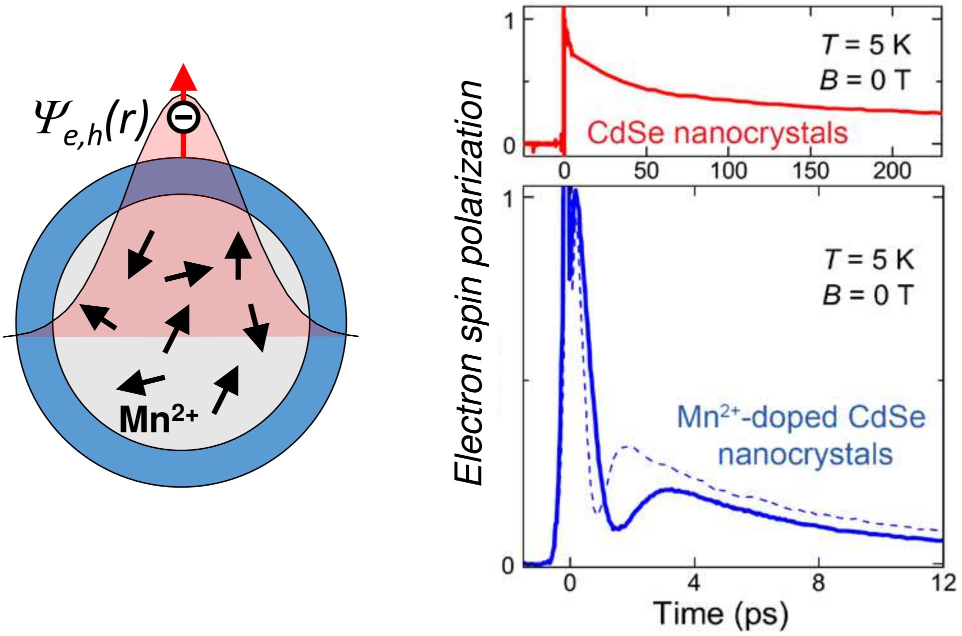

Fig.1: Left: Cartoon of a magnetically-doped CdSe nanocrystal. A single photo-generated electron and/or hole interacts with several (N ~ 5-20) embedded Mn^{2+} moments via the sp-d spin-exchange interaction. The strength of these interactions is enhanced by strong quantum confinement, which compresses the electron/hole envelope wavefunctions. Statistical sqrt(N) fluctuations of the Mn^{2+}spins lead to large effective magnetic fields B$_{eff}$ that are 'seen' by an electron. Right: Time-resolved measurements reveal very fast (100s of GHz) electron spin precession in Mn-doped CdSe nanocrystals, indicating B$_{eff}$~ 15-30 T, even in the absence of any applied field. [1]

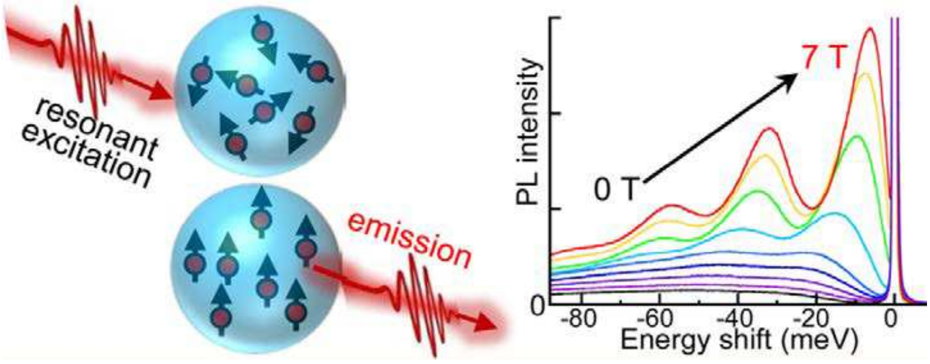

Fig.2: The formation of exciton magnetic polarons –i.e., the collective ferromagnetic alignment of all the Mn^{2+} spins in a nanocrystal -- following absorption of a single photon. The effective exchange field B$_{ex}$ 'seen' by the Mn^{2+} spins that is due to the exciton is of order 10 tesla. Magnetic polarons are revealed via the field-dependence of resonant PL spectra. [2]

Spin resonance in spin-orbit-coupled quantum dots in the weak and strong driving regimes

Giorgos Giavaras[1], Yasuhiro Tokura[1], and Keiji Ono[2]

[1]*Faculty of Pure and Applied Sciences, University of Tsukuba, Tsukuba, Ibaraki 305-8571, Japan*
[2] *Advanced Device Laboratory, RIKEN, Wako-shi, Saitama 351-0198, Japan*
e-mail: g.giavaras@gmail.com

The control over individual spin states in semiconductor quantum dots is necessary for spin-based qubits, and in this context studying electron-spin-resonance (ESR) effects induced by ac-fields is important. Understanding the role of the spin-orbit-interaction (SOI) is also important because it leads to a coherent coupling between coupled spin states.

In this work we study theoretically ESR effects in a system of two coupled quantum dots in the presence of SOI. In particular, we consider two dots in the spin blockade regime, and calculate the ESR-induced current generated by a microwave field in a constant magnetic field. For the microwave field we consider two cases: (i) an oscillating electric field and (ii) an oscillating magnetic field. By employing a Floquet-Markov open-system approach we calculate the current in the sequential tunneling regime for weak and strong driving. We identify the various features in the current generated by the two fields, for different energy detuning, constant magnetic field, and SOI strength [1].

As shown in figures 1-3, the ESR-induced current peak height has strong dependence on the constant magnetic field. For example, when the double dot is driven by an ac-electric field then at about B=0.2 T the peak height is zero for the T_+ to S transition, but it is maximum for the T_- to T_+ as well as the T_- to S transition. This result is due to the presence of the SOI that determines the populations of the singlet-triplet states, and to the fact that the ac-field tends to equalize the populations.

We also determine the ratio of the two-photon peak height over the single-photon peak height as a function of the strength of the driving field. We find regimes where this ratio follows a completely different behavior for the two cases of the driving field considered. Finally, we compare our theoretical findings with a recent experiment on a p-channel Si MOSFET device [2], and find very good qualitatively agreement (figures 4(a), (b)).

Part of this work was supported by CREST JST (JPMJCR15N2)

[1] G. Giavaras and Y. Tokura, in preparation

[2] K. Ono, G. Giavaras, T. Tanamoto, T. Ohguro, X. Hu, F. Nori, arxiv:1707.03106

978-3-901578-31-1

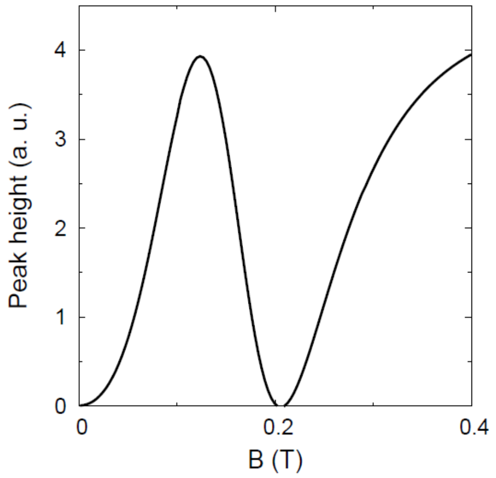

Fig.1: The peak height of the ESR-induced current as a function of the magnetic field, for the T_+ to S transition.

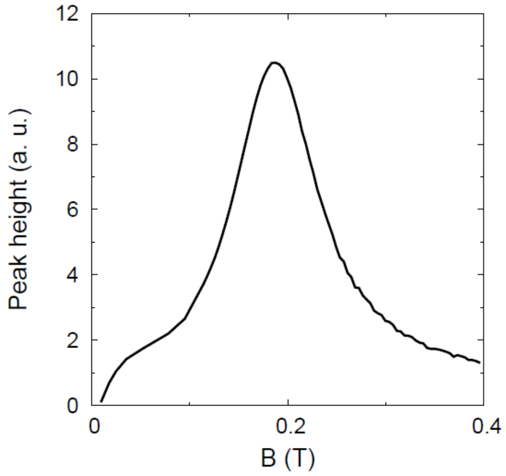

Fig.2: As in Fig.1 but for the T_- to T_+ transition.

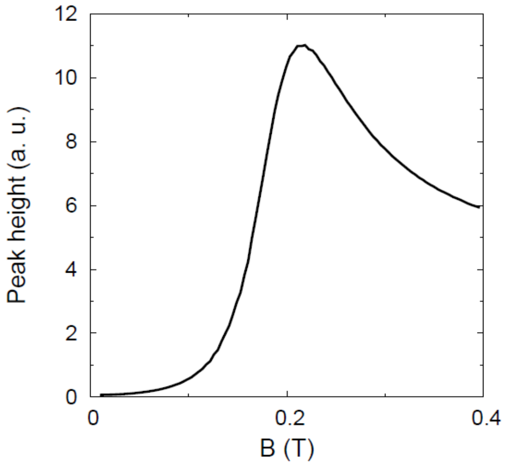

Fig.3: As in Fig.1 but for the T_- to S transition.

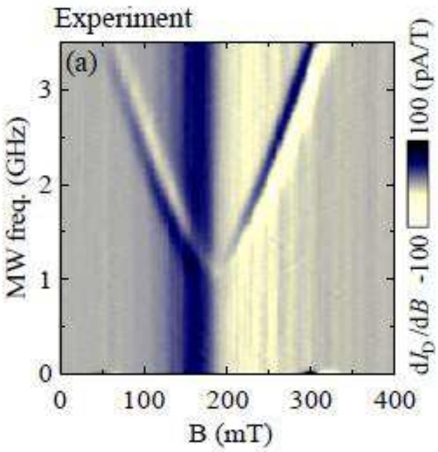

Fig.4 (a): Measured current as a function of the magnetic field and frequency of the oscillating electric field near the T_+ - S anti-crossing point.

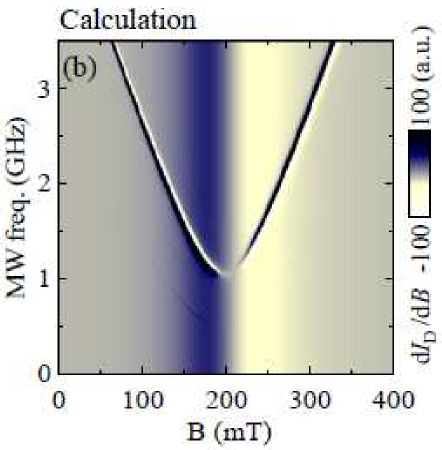

Fig.4 (b): As in Fig.4 (a) but here the calculated current is shown.

Landauer and NEGF: Plain Talk on the Proper Approach

D. K. Ferry and D. Vasileska

School of Electrical, Computer, and Energy Engineering, Arizona State University
Tempe, AZ 85287-5706 USA

As device sizes have continued to decrease, we have reached the point where extensive quantum effects are present in these devices, and are utilized for varying the band structure as a method of improving device performance. Traditionally, the Landauer formula has been the “go to” approach to determining the conductance through a nanoscale device, and the transmission is often computed from the retarded Green’s function, particularly in the case of ballistic transport through the device. This approach is still often used [1]. In the case in which scattering is present, many people still use this approach via the non-equilibrium Green’s functions (NEGF). However, continuing to compute the conductance from the simple bubble composed of the retarded and advanced Green’s functions (Fig. 1) [2] leads to significant error. The reason for this error lies in the presence of significant back-scattering in the channel of a nanoscale device. In order to correctly account for this, the conductivity bubble must be recognized as the two-particle Green’s function it is, and then determined self-consistently via the Bethe-Salpeter equation (Fig. 2) [3-5]. This process is well-known in near-equilibrium transport, where the famous (1-cosθ) for impurity scattering can be recovered *only* from the Bethe-Salpeter equation. Yet, it has been neglected in the NEGF study of nanoscale devices in recent years. In this talk, we discuss the proper application of the NEGF formalism to nanoscale devices and focus on the source and importance of the full conductivity bubble, and its impact on various transport properties of nanoscale devices.

[1] H. Horri, R. Faez, and M. Pourfath, IEEE Trans. on Electron Dev. **64**, 3459 (2017).

[2] M. P. Anantram, M. S. Lundstrom, and D. E. Nikonov, Proc. IEEE **96**, 1511 (2008).

[3] D. Vasileska, P. Bordone, T. Eldridge, and D.K. Ferry, J. Vac. Sci. Techn. B **13**, 1841 (1995).

[4] D. Vasileska, P. Bordone, T. Eldridge, and D.K. Ferry, VLSI Des. **6**, 21 (1998).

[5] D. Vasileska, C. Prasad, H. H. Wieder, and D. K. Ferry, J. Appl. Phys. **93**, 3350 (2003).

978-3-901578-31-1

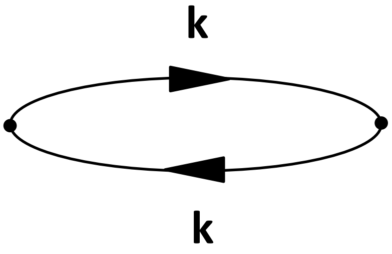

Fig.1: The simple conductivity bubble for the conductivity. It is connected at left and right to the reservoirs, and the upper line represents the retarded Green’s function, while the lower line is the adjoint of this function.

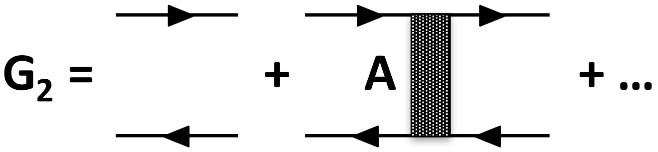

Fig.2: The proper form of the bubble is to solve the Bethe-Salpeter equation, depicted here pictorially, which includes interactions (back-scattering particularly) between the two Green’s functions of Fig. 1. (The ends of the bubble of Fig. 1 have been opened up to illustrate the full two-particle Green’s function nature of the approach.)

Novel Polaritonic Modes in Subwavelength Antenna: Applications for Nanotube Plasmonic Sensing

Slava V. Rotkin[1] and Benjamin Sofka[2]

[1] *Materials Research Institute, The Pennsylvania State University,*
Millennium Science Complex, University Park, PA 16802
[2] *Lehigh University, Department of Physics, 16 Memorial Drive East, Bethlehem, PA 18015*
e-mail: rotkin@psu.edu

The quantum optical effect of superradiance attracted substantial attention last decade, mostly due to recent successes in AMO systems. Typically, the system should include a set of quantum objects, strongly coupled to quantized radiation field. Here we explore much simpler model and show that a “sister”-effect exists in a classical system: a polarizable rod in a self-consistent electromagnetic field (an analog of a Hertz dipole, though made of non-metal material). The effect manifests itself as a series of resonances with very specific spatial oscillatory pattern. It has been interpreted in terms of hybrid polaritonic modes formed by an exciton (eigenmode of the polarizable non-metal material) mixed to a series of antenna modes (modes of an open resonator of the rod).

Figs. 1 and 2 show the polaritonic profiles of metallic NT and semiconducting NT below the excitonic resonance (negative detuning) are similar, and non-oscillatory, while above the resonance, clear spatial oscillations develop with the period quantized as inverse length of the open resonator of the NT antenna. Unexpectedly, the oscillatory hybrid modes only exist for positive detuning from the excitonic resonance, the feature not mentioned for plasmon-polaritonic hybrid modes before, due to the plasmon response function has a pole at zero frequency and does not allow non-positive detuning. The effect is further discussed for a particular example of semiconductor or metallic nanotube (NT) for plasmonics applications that may vary from FRET-like sensing[1] to near-field imaging[2].

This research has been supported by NSF (ECCS-1509786).

[1] AM. Nemilentsau, et.al, Ed: DM. Chigrin, Phot. and Nanost. 9, 381-389 (2011). AM. Nemilentsau, et.al, Phys. Rev. B82, 235411, (2010). AM. Nemilentsau, et.al, J of NanoPhotonics, 4, 041685 (2010).

[2] AM. Nemilentsau, et.al, the SPIE Newsroom, p. 1-5, (2010).

978-3-901578-31-1

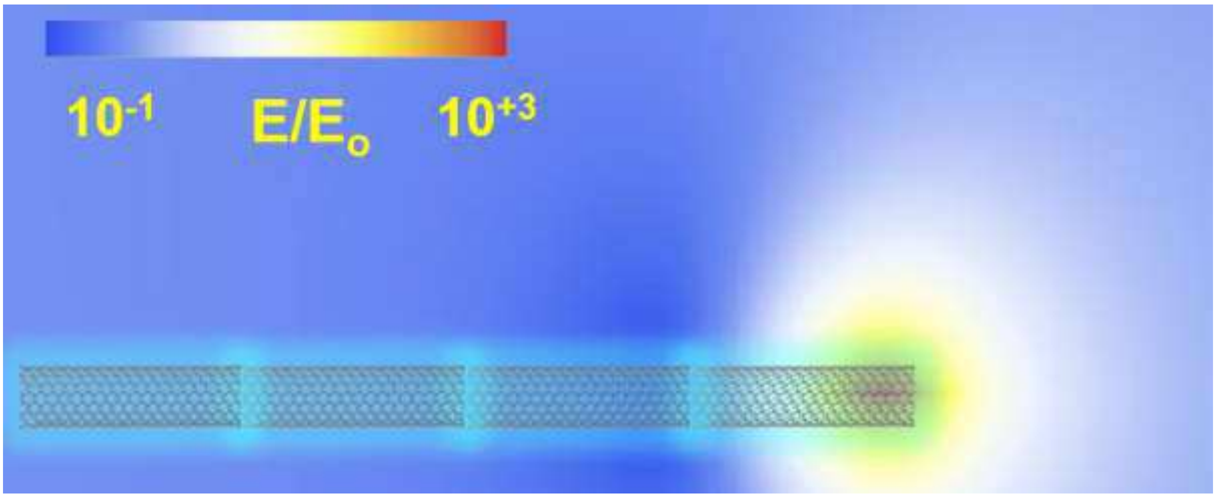

Fig.1: Near-field enhancement factor of a polaritonic mode of a metallic NT (plasmonic regime) at 1st plasmon resonance.

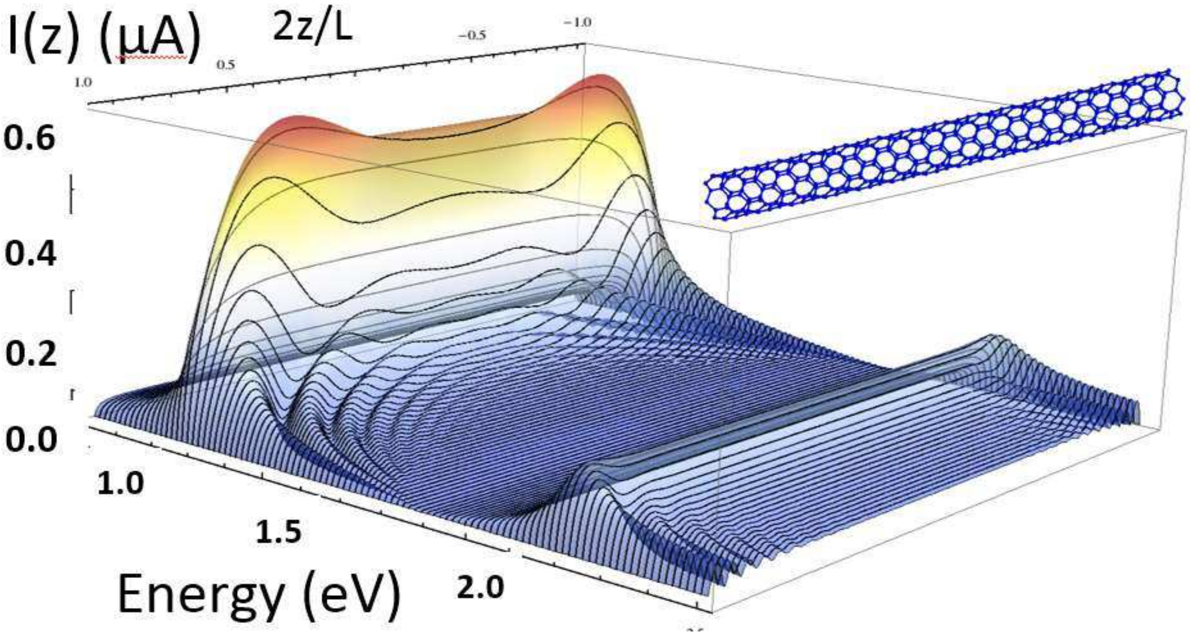

Fig.2: The spatial-frequency profile of the hybrid polariton modes of a finite-length non-metallic NT: two exciton resonances are covered (S_1 and S_2 for (6,5) NT). Oscillatory antenna modes clearly exist only above the resonance (but not below it).

Classical and Quantum Electron Evolution with a Repulsive Dopant

Mauro Ballicchia[1,2], Josef Weinbub[3], Mihail Nedjalkov[2], and Siegfried Selberherr[2]

[1] *Department of Information Engineering, Università Politecnica delle Marche,*
Via Brecce Bianche 12, 60131 Ancona, Italy
[2] *Institute for Microelectronics, TU Wien, Gußhausstr. 27-29, 1040 Wien, Austria*
[3] *Christian Doppler Laboratory for High Performance TCAD,*
Institute for Microelectronics, TU Wien, Gußhausstr. 27-29, 1040 Wien, Austria
e-mail: ballicchia@iue.tuwien.ac.at

Modeling gives a unique opportunity to study quantum effects governing nanoelectronics by comparing them to classical effects and by selectively investigating different physical conditions which characterize the transport picture. To that end, the Wigner transport model implemented by a signed particle approach [1] can be reduced to the Boltzmann transport model, when the quantum rules for particle evolution are replaced by classical ones. The role of physical conditions can then be investigated in detail, such as using classical or quantum boundary conditions in order to enable or disable the effects of quantum repulsion [2]. In this work, we investigate the classical and quantum electron evolution with a repulsive dopant potential with ViennaWD [3]. In the classical case the evolution is local (the first derivative of the potential). However, in the quantum case all derivatives of the potential control the evolution. This gives rise to non-local and tunneling effects which both can be conveniently studied by means of simulation. In our particular simulation setup, the dopant potential is placed in the center of the simulation domain ($20\text{x}30\text{nm}^2$) and has a peak energy of about 0.345eV. We inject a minimum uncertainty Wigner state [4] every 1fs with an initial kinetic energy of 0.141eV. Fig 1 and Fig. 2 show the electron density for all absorbing boundary conditions in the classical and in the quantum case, respectively. The green *isoline* shown in all figures is the potential energy of the dopant at 0.175eV. The non-locality effects of the quantum potential affect the injected electrons right after injection. Tunneling effects are identified due to the intensified spreading of the density. In Fig. 3 and Fig. 4 the current density is shown for $10 \leq y \leq 30\text{nm}$. The increasing quantum current density above the center is due to the action of the repulsive potential on the tunneling electrons. Adding classical reflecting boundaries on the lateral sides ($x = 0$ and $x = 20\text{nm}$) allows to cleanly study the effects of non-locality and tunneling without imposing effects of quantum repulsion. Fig. 5 and Fig. 6 show the current density with lateral reflecting boundaries. In this case the current's evolution path is much more closed around the dopant in the quantum case. This is attributed to the joint effect of tunneling and repulsion, since the electrons reflected from the boundary are accelerated after the dopant.

978-3-901578-31-1

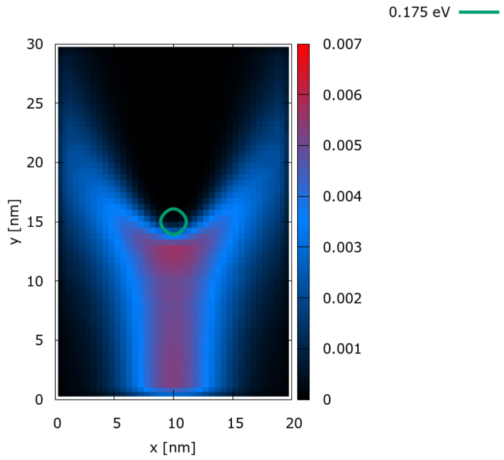

Fig. 1: Classical electron density [a.u.]; absorbing boundaries.

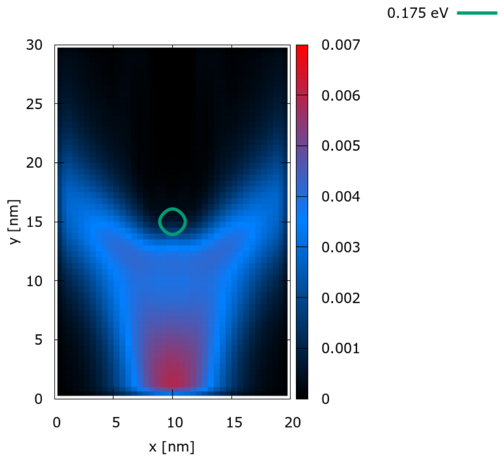

Fig. 2: Quantum electron density [a.u.]; absorbing boundaries.

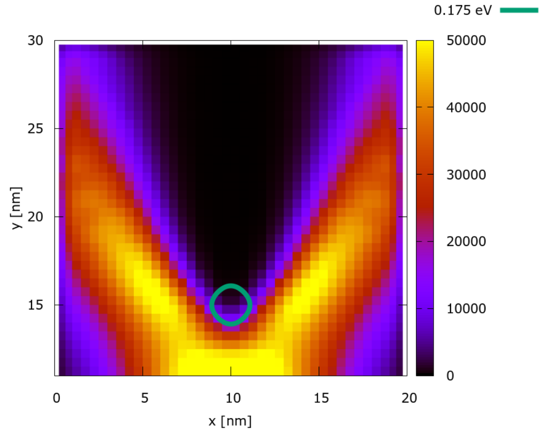

Fig. 3: Classical current density [a.u.]; absorbing boundaries (zoom).

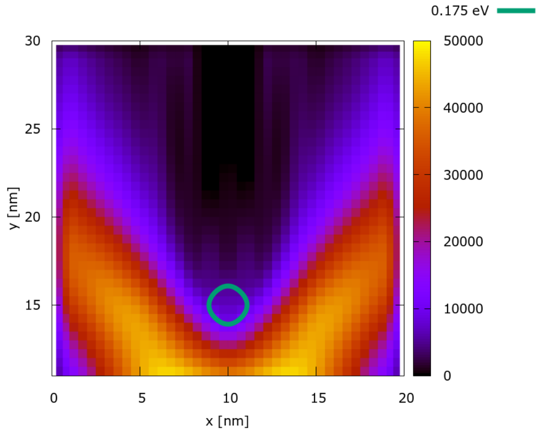

Fig. 4: Quantum current density [a.u.]; absorbing boundaries (zoom).

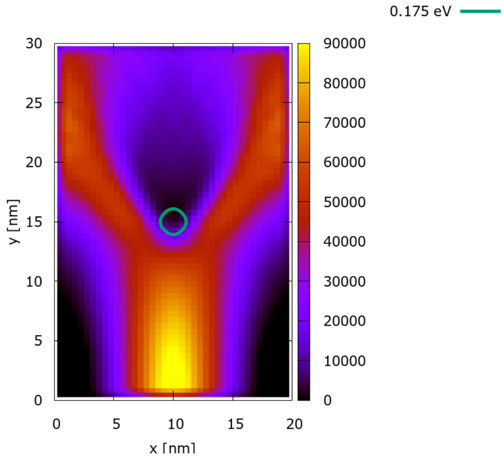

Fig. 5: Classical current density [a.u.]; lateral reflecting boundaries.

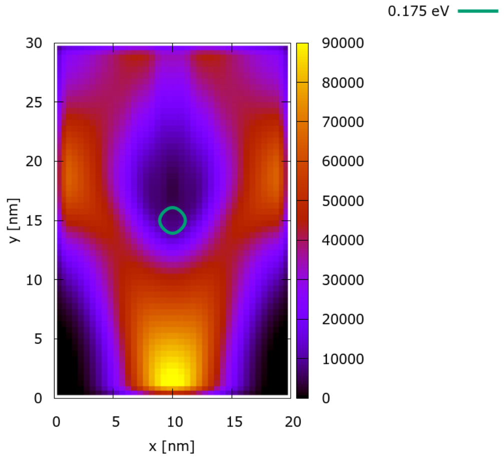

Fig. 6: Quantum current density [a.u.]; lateral reflecting boundaries.

Acknowledgment. The financial support by the Austrian Science Fund (FWF) project FWF-P29406-N30, the Austrian Federal Ministry of Science, Research and Economy, and the National Foundation for Research, Technology and Development is gratefully acknowledged. The presented computational results have been achieved using the Vienna Scientific Cluster (VSC).

[1] M.Nedjalkov et al., Springer, ISBN: 978-1-4419-8839-3 (2011)
[2] A.M. Kriman et al., Quant. Trans. in Semicond., pp. 239-287 (1992)
[3] http://viennawd.sourceforge.net
[4] D.Querlioz, P.Dollfus, Wiley-ISTE, ISBN: 978-1-84821-150-6 (2010)

Coulomb blockade effect in proximitized nanowires

Roman M. Lutchyn

Station Q, Microsoft Research, Santa Barbara, California 93106-6105, USA

Motivated by recent experiment [1], we consider a mesoscopic island consisting of a proximitized nanowire which is connected via point contacts to normal-state leads, see Fig. 1. We study transport properties of such islands in the Coulomb blockade regime as a function of an applied magnetic field [2-4]. In the presence of Rashba spin-orbit coupling, magnetic field can drive a proximitized nanowire into a topological superconducting phase [2,3]. The associated with the topological superconductivity Majorana modes significantly modify transport and lead to single-electron coherent transmission through the nanowire - a non-local signature of topological superconductivity. In this work, we focus on the case of strong hybridization of the Majorana modes with the normal leads. The induced by hybridization broadening of the Majorana zero-energy states competes with the charging energy, leading to a considerable modification of the Coulomb blockade in a nanowire contacted by two normal leads. We evaluate the two-terminal conductance as a function of the gate voltage, junctions transmission coefficients, the geometric capacitance of and the induced superconducting gap in the nanowire.

[1] S. M. Albrecht et al., Nature 531, 206 (2016)

[2] R. M. Lutchyn, J. D. Sau, and S. Das Sarma, Phys. Rev. Lett. 105, 077001 (2010).

[3] Y. Oreg, G. Refael, and F. von Oppen, Phys. Rev. Lett. 105, 177002 (2010).

[4] B. van Heck, R. M. Lutchyn, and L. I. Glazman, Phys. Rev. B 93, 235431 (2016)

[5] R. M. Lutchyn and L. I. Glazman, Phys. Rev. Lett. 119, 057002 (2017)

[6] M. Pustilnik, B. van Heck, R. M. Lutchyn, L. I. Glazman, arXiv:1706.04726 (2017)

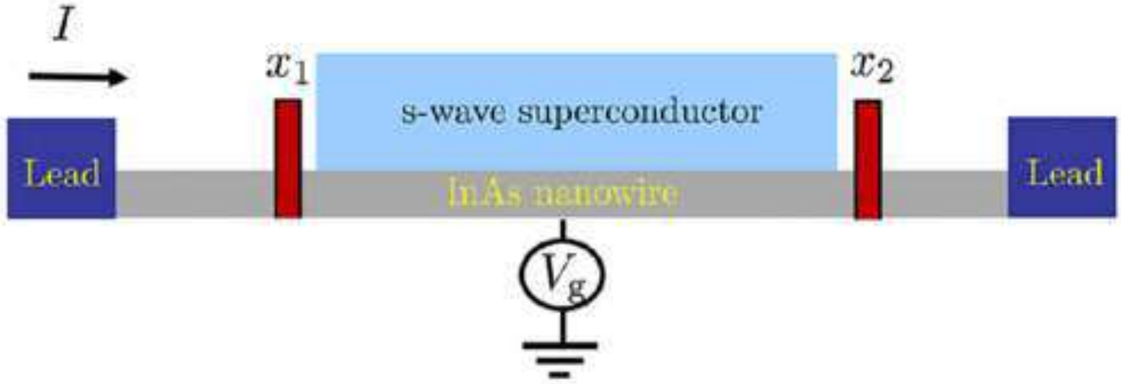

Fig.1: Schematic plot of the device: proximitized semiconductor nanowire is connected via point contacts to normal-state leads.

Chalcogenide Phase Change Device with Topological Functionalities

Junji Tominaga[1]

[1] *Nanoelectronics Research Institute, National Institute of Advanced Industrial Science and Technology (AIST), Tsukuba, 305-8565, Japan*
e-mail:j-tominaga@aist.go.jp

Non-volatile memories (NVMs) are key devices in computers to save your important information. Beside Flash memory, several new NVMs have been proposed, such as using magneto-resistance, resistance change of metal oxides, and phase change of chalcogenides. Especially, phase change random access memory (PRAM) is the most attractive NVM on the view point of switching speed, high durability and scalability. As an evidence, US companies, Intel and Micron Technology have already shipped the devices (Optane) as storage class memories since this year [1]. However, the phase change memory innovation has not been completed by Optane, rather recently shifted into the next stage. It is because by the development of interfacial phase change memory (iPCM), it was found that PRAM may be able to control electron spins in future [2, 3].

iPCM was originally developed for improving an energy conversion efficiency of a conventional PRAM, using a superlattice (SL) composed of GeTe and Sb_2Te_3 sublayers. But soon after the performance demonstration, it was found that the SL is a topological insulator [4]. The electron system in the SL is protected by both time reversal symmetry and spatial inversion symmetry. Therefore, if one of which symmetry is broken, spin property may be emerged. We have confirmed phenomena attributed to the electron spins at room temperature since 2011 [5]. Once the spin properties can be controlled, the future PRAM will receive an universal status not only for a phase change resistance change memory, but also as a spin current control transistor.

[1] https://www.intel.com/content/www/us/en/architecture-and-technology/intel-optane-technology.html

[2] J. Tominaga et al. *In Proceedings of the European Symposium on Phase Change and Ovonic Science* (E/PCOS, Aachen, Germany), pp. 148

[3] R. E. Simpson *et al. Nature Nano.* 6, 501 (2011)

[4] J. Tominaga *et al. Adv. Mater. Interfaces* **1,** 1300027 (2013).

[5] J. Tominaga *et al. Sci. Technol. Adv. Mater.* **16,** 014402 (2015).

The work was fully supported by grant no.- JPMJCR14F1 of JST/CREST.

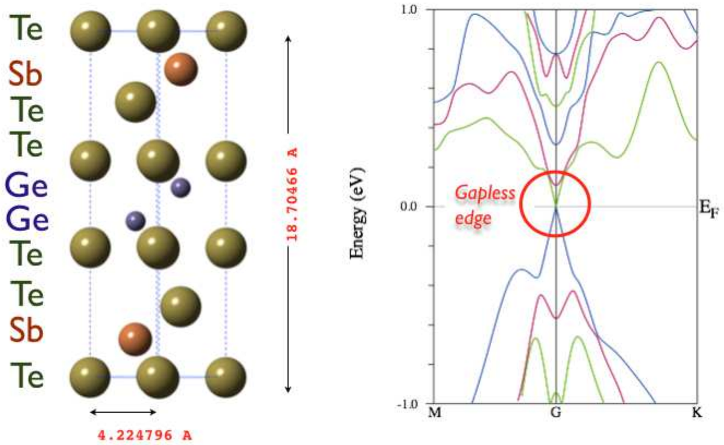

Fig.1 *a primitive cell of a hcp-type* $[(GeTe)_2(Sb_2Te_3)_1]n$ *SL structure and the electronic band structure (bulk) [4].*

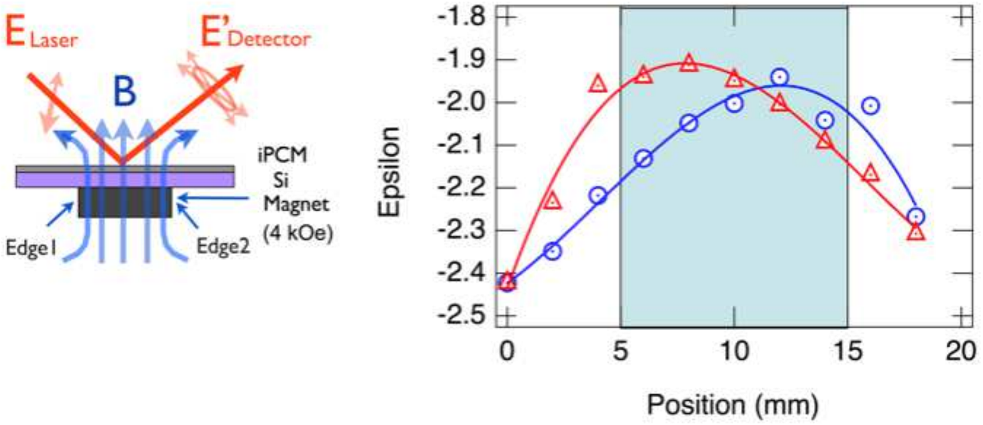

Fig.2 *Optical response of SL under a static magnetic field using an elipso meter*

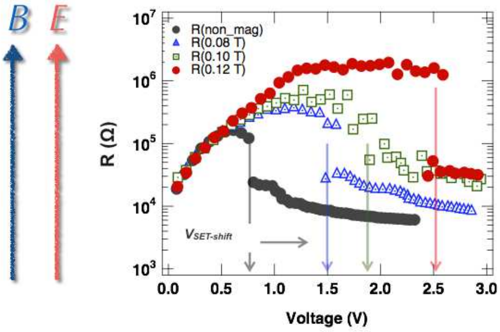

Fig. 3 *iPCM device response to a combination of electric field and magnetic field [5]*

Topological Quadrupole and Octupole Insulators

Wladimir A. Benalcazar[1], B. Andrei Bernevig[2], and Taylor L. Hughes[1]

[1] *Department of Physics and Institute for Condensed Matter Theory, University of Illinois at Urbana-Champaign, IL 61801, USA*

[2] *Department of Physics, Princeton University, Princeton, New Jersey 08544, USA*

e-mail: hughest@illinois.edu

In a recent article[1], we extended the formulation of electric polarization in crystals to higher electric multipole moments. We determined the necessary conditions under which, and minimal models in which, the quadrupole and octupole moments are topologically quantized electromagnetic observables. Such systems exhibit gapped boundaries that are themselves lower-dimensional topological phases. Furthermore, they manifest topologically protected corner states carrying fractional charge, i.e., fractionalization at the boundary of the boundary. We proposed three realistic experimental implementations of this new topological behavior that can be immediately tested. Finally, we will discuss some extensions of these multipolar systems to other 3D materials that provide new examples of topological phases and possible interesting applications.

[1] W. A. Benalcazar, B. A. Bernevig, T. L. Hughes, *Science*, **357**, 61 (2017).

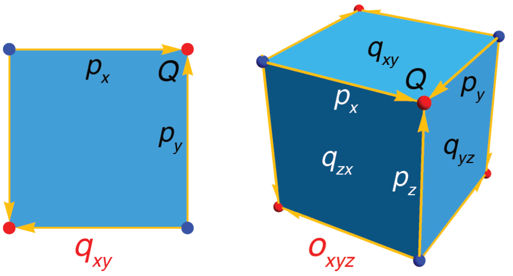

Fig.1: Schematic illustration of materials having a quadrupole moment q_{xy} (left) or an octupole moment o_{xyz} (right) and the resulting boundary polarizations and corner charges.

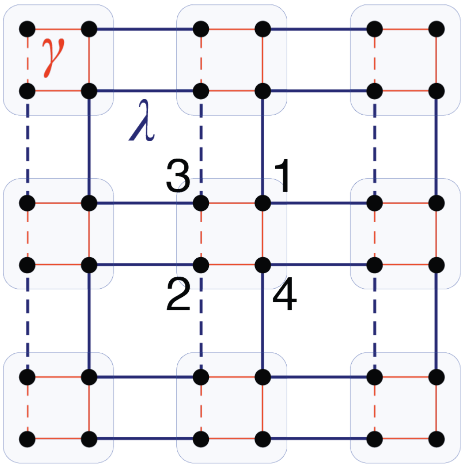

Fig.2: Illustration of a simple tightbinding representation of an insulator model with a quantized quadrupole moment q_{xy}. The dots represent electronic orbitals and the lines represent tunneling terms between electron orbitals.

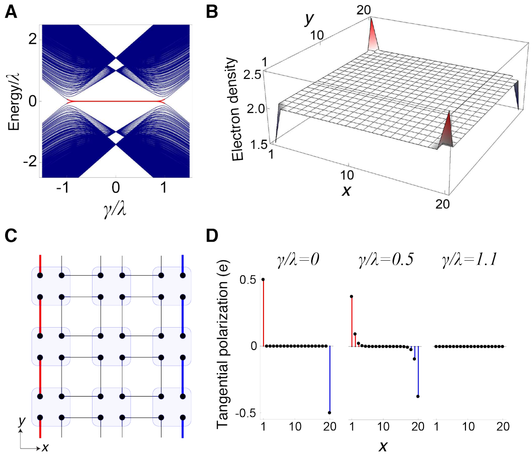

Fig.3: (A)Energy spectrum for model in Fig. 2 with open boundary conditions in both directions. Mid-gap states are localized on the corners of the sample (B) Charge density plot illustrating the fractionalized half-charge on the corners of a sample in a quadrupole pattern (C) Toy model with open boundary conditions in one direction showing the boundary insulator which can be polarized (D) Electronic polarization vs. position across the sample. This illustrates the boundary polarization when in the quadrupolar phase.

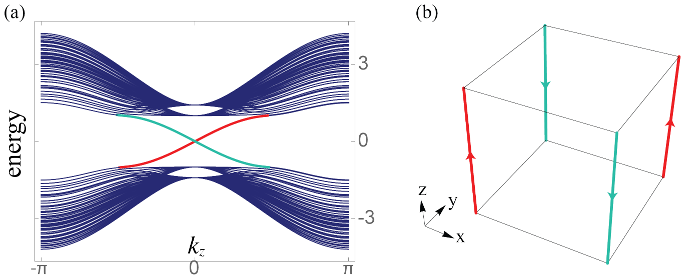

Fig.4: Features of a three dimensional extension of the quadrupole model to a model of an insulator that exhibits chiral modes on the hinges of the sample. (a) The energy spectrum with open boundaries on two sides. The mid-gap states disperse chirally as indicated in (b) and are localized on the hinges of the samples.

978-3-901578-31-1

Geometrically-induced transport phenomena in Weyl semimetals and Weyl superconductors

Takuro Kobayashi[1], Yusuke Ishihara[1], Takeshi Mizushima[1], H. Sumiyoshi[2], Atsushi Tsuruta[1], and Satoshi Fujimoto[1]

[1]*Ddepartment of Materials Engineering Science, Osaka University, Toyonaka, Osaka 560-8531, Japan*
[2]*Department of Physics, Kyoto University, Kyoto, Japan*
e-mail: fuji@mp.es.osaka-u.ac.jp (e-mail address of the corresponding author)

Weyl semimetals are characterized by the monopole charge of the Weyl points in the momentum space and the associated chiral anomaly. These features give rise to unique transport phenomena such as anomalous Hall effect, chiral magnetic effect, and negative magnetoresistance. Among them, chiral magnetic effect, i.e. generation of a charge current due to a static magnetic field, can not be realized in real solid state materials. On the other hand, it has been pointed out that the characteristic transport phenomena associated with chiral anomaly can be also induced by geometrically inhomogeneous structures such as lattice defects, dislocations, and topological textures. The important point is that when a spatial inhomogeneity generates torsion fields, they play a role similar to fictitious electromagnetic fields. In this presentation, torsional responses characterizing Weyl quasiparticles in solid state systems are discussed. In a Weyl semimetal, a torsion field induced by screw dislocation gives rise to a dissipationless charge current flowing along the dislocation line, which is referred to as the torsional chiral magnetic effect.[1] In contrast to the chiral magnetic effect, which is absent for lattice systems under a static and uniform magnetic field, the torsional chiral magnetic effect is realized for realistic solid state electron systems, and experimentally detectable via nonlocal transport measurement or the scanning SQUID measurement. Some analogous torsional responses are also possible to occur in Weyl superconductors, in which nodal Bogoliubov quasiparticles behave as Weyl fermions. For instance, topological textures of the superconducting order parameter such as a vortex and skyrmion *l*-vector textures of a p-wave pairing state can generate torsional fields acting on Weyl quasiparticles. I would like to present some recent results of geometrically-induced transport phenomena associated with chiral anomaly in Weyl superconductors.

[1] H.Sumiyoshi and S. Fujimoto, Phys. Rev. Lett 116, 166601 (2016).

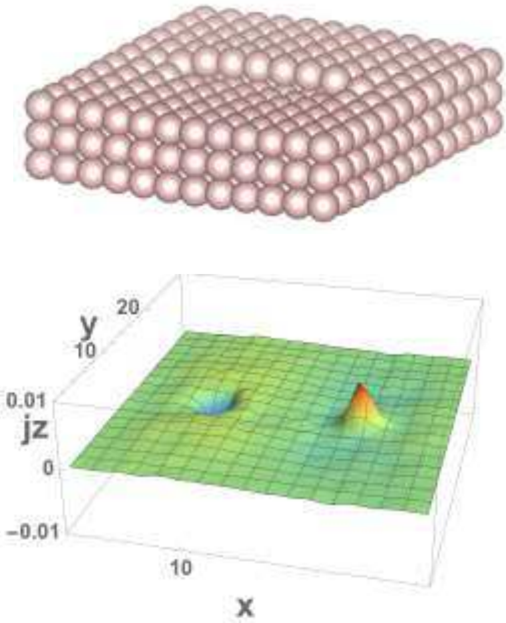

Fig.1: (Upper panel) Configuration of screw dislocation and anti-screw dislocation in a Weyl metal. (Lower panel) The distribution of dissipationless currents induced by torsional chiral magnetic effect. The currents are flowing along the dislocation lines.

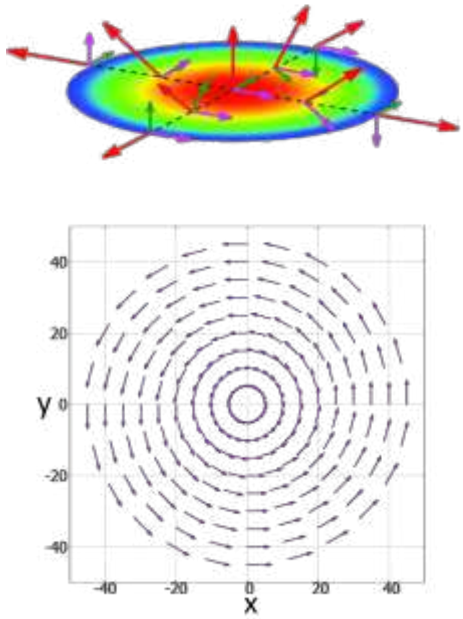

Fig.2: (Upper panel) Skyrmion textures of the order parameter of p-wave superconductivity. (Lower panel) The distribution of currents of Weyl quasiparticles induced by skyrmion textures via chiral magnetic effect.

Quantum transport in heterostructured topological materials

Masashi Kawasaki[1, 2]

[1] *Quantum Phase Electronics Center (QPEC) and Department of Applied Physics,*
The University of Tokyo, Tokyo 113-8656, Japan
[2] *RIKEN Center for Emergent Matter Science (CEMS), Wako 351-0198, Japan*
e-mail: kawasaki@ap.t.u-tokyo.ac.jp

Three-dimensional topological insulator (TI) is a new state of matter that is characterized by topologically nontrivial bulk insulating state and a Weyl electron surface state. Quantum Hall effect (QHE) on this surface state exhibits various phenomena that are not seen in conventional semiconductors. One of the prominent features is QHE under zero magnetic field called anomalous QHE realized in ferromagnetic TI [1-3]. However, one needs so far not only very low temperature (~ 50mK) but also high magnetic field in order to achieve full quantization. We have systematically examined Landau quantization and QHE in non-magnetic TI to reveal quantization at $\nu = 0$ in addition to $\nu = \pm 1$ [4, 5]. This fact gives us a simple idea of combining non-magnetic and magnetic TIs in order to achieve full quantization at higher temperature as well as under zero magnetic field. This kind of modulation doping of magnetic impurities opens tremendous opportunities in designing electronic states of Weyl system. We present stabilization of anomalous QHE at higher temperature [6, 7], quantum magneto-electric effect [8], a possible realization of Axion insulator [9,10], and direct detection of topological current [11]. Besides these phenomena related with QHE, there are numbers of interesting physics emerging in TIs, such as formation of magnetic skyrmions [12], spontaneous photocurrent [13], highly efficient spin-charge conversion [14], and current induced magnetization reversal [15]. Also explored are novel phases based on polar-ferromagnet (GeMn)Te [13] and quantum Hall effect in Dirac semimetal Cd_3As_2 [17].

This work is supported by JST-CREST JPMJCR16F1.

[1] C.-Z. Chang et al., Science **340**, 167 (2013)

[2] J. G. Checkelsky et al., Nature Physics 10, 731 (2014).

[3] X. Kou et al., Phys. Rev. Lett. 113, 137201 (2014).

[4] R. Yoshimi et al., Nature Materials 13, 253 (2014).

[5] R. Yoshimi et al., Nature Commun. 6, 6627 (2015).

[6] R. Yoshimi and K. Yasuda et al., Nat. Commun. 6, 8530 (2015).

[7] M. Mogi et al., Appl. Phys. Lett., 107, 182401(2015).

[8] K. N. Okada et al., Nature Commun. 7, 12245 (2016).

978-3-901578-31-1

[9] M. Mogi and M. Kawamura et al., Mature Mater. 16, 516 (2017).
[10] M. Mogi et al., arXiv:1708.05387
[11] K. Yasuda et al., arXiv:1707.09105
[12] K. Yasuda et al., Nature Physics 12, 555 (2016).
[13] N. Ogawa et al., Nature Commun. 7, 12246 (2016).
[14] K. Kondo et al., Nature Physics 12, 1027 (2016).
[15] K. Yasuda et al., arXiv:1612.06862
[16] M. Kriener et al., Sci. Rep. 6, 25748 (2016)
[17] M. Uchida et al., to be published.

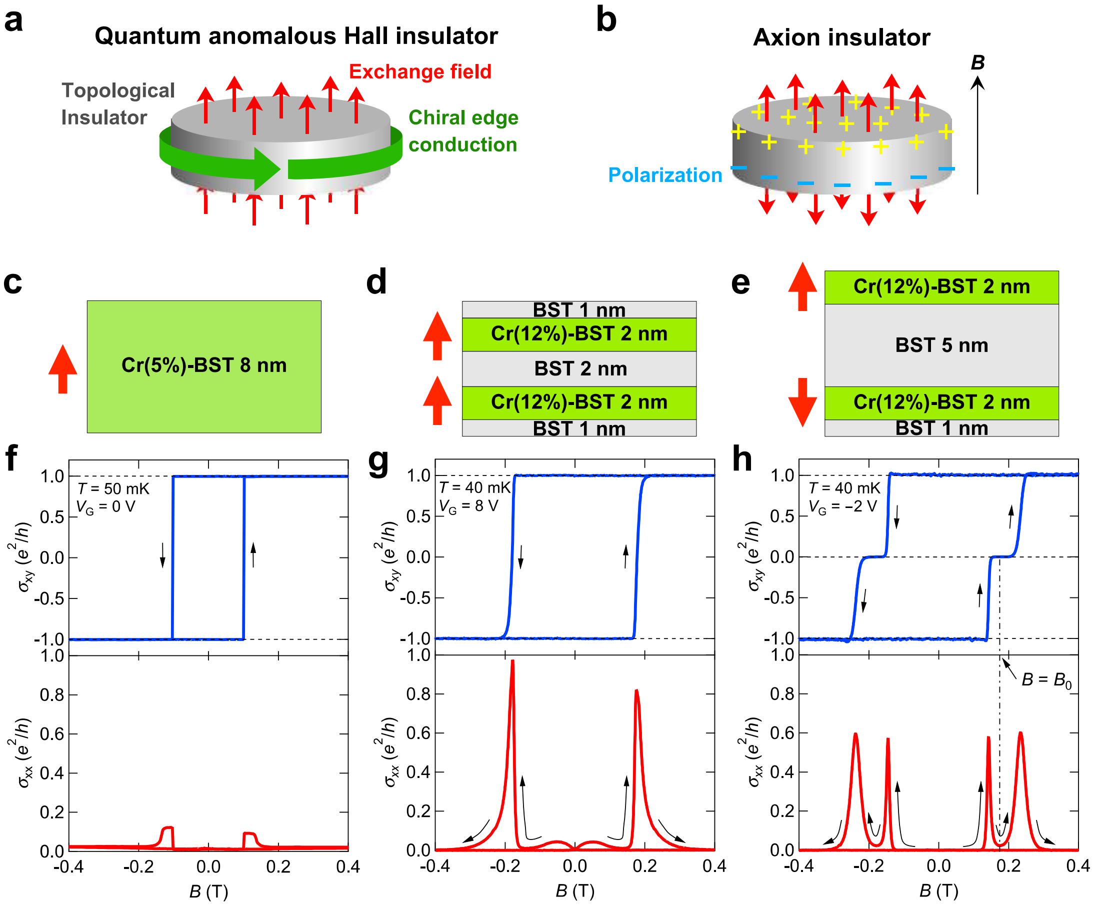

Figure 1 *Zero Hall plateau state in a magnetic topological insulator heterostructure towards an axion insulator.* ***a,b,*** *Schematic drawings of a quantum anomalous Hall (QAH) insulator (a) and an axion insulator (b) in magnetic TI thin films.* ***c–e,*** *Schematic layouts of MBE-grown Cr-modulation-doped TI* $((Bi,Sb)_2Te_3)$ *thin films used for the experiments.* ***f–h,*** *Magnetic field (B) dependence of Hall conductivity* (σ_{xy}) *and longitudinal conductivity* (σ_{xx}) *at the lowest temperature for respective samples.*

Pure- and mixed-state simulation of Dirac fermion dynamics in electromagnetic textures

Walter Pötz

Department of Physics, Karl-Franzens University of Graz, 8010 Graz, Austria
e-mail: walter.poetz@uni-graz.at

Low-energy excitations of topological insulator (TI) surfaces intrinsically are characterized by an odd number of zero-mass Dirac cones. Time-reversal-symmetry breaking induced by magnetic texture and external magnetic fields can be used to further engineer these surface states, thereby, inducing mass-gaps, domain-wall and vortex structures[1]. Non-equilibrium in conjunction with spin-momentum-locking inherently leads to spin polarization, making this system well suited for the study and utilization of spintronic effects.

Here we present results from our numerical studies of Dirac fermion propagation on TI surfaces. Our simulations are based on a single-cone second-order accurate finite-difference scheme for the (2+1)D Dirac equation[2-4]. Electro-magnetic fields are included in gauge invariant fashion. This scheme is applied to space-time resolved simulations of charge carrier dynamics on the surface of topological insulators in presence of electromagnetic texture. Both pure and mixed-state simulations have been performed. The former allow an analysis of single-particle coherent wave propagation, while the latter provide full space-time-resolved transport studies.

Our numerical results for single-electron dynamics include a microscopic analysis of transverse current build-up arising from scattering at static structural barriers (related to the Bychkov-Rashba spin-orbit effect), time-dependent potential structures, and the propagation of Dirac fermions across magnetic vortices[5-7]. Mixed-state transport studies explore the simulation of Ohmic contacts and associated particle injection, as well as absorbing boundary conditions by imaginary potentials[3,4]. Numerical examples for spin-momentum-locking are given for simple geometries, such as magnetic islands and domain walls.

[1] M. Z. Hasan et al., Rev. Mod Phys., **82**, 3045 (2010).
[2] R. Hammer et al., J. of Comp. Phys. , **265**, 50 (2014).
[3] M. Schreilechner and W. P., Comp. Phys. Comm., **204**, 43 (2016).
[4] W. P. and M. Schreilechner, J. Comp. Phys., **348**, 591 (2017).
[5] R. Hammer and W. P, Phys. Rev., **B 88**, 235119 (2013).
[6] R. Hammer et al., Appl. Phys. Lett., **102**, 193514 (2013)
[7] W. P. and R. Hammer, J. Appl. Phys., **120 (**2016).

978-3-901578-31-1

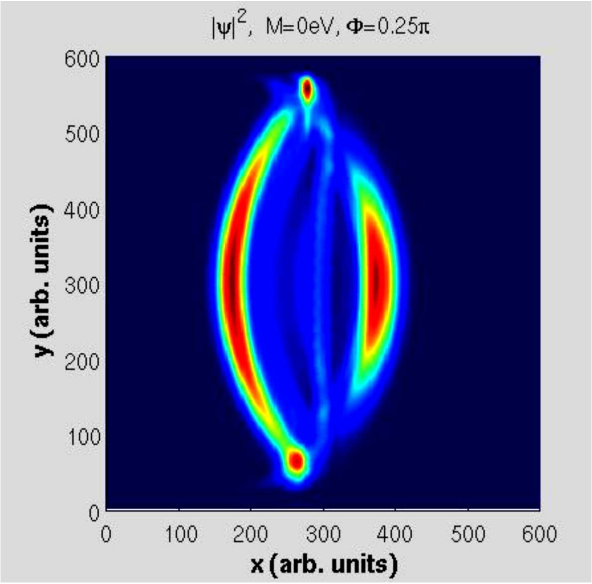

Fig.1: Scattering of a left-incident Dirac fermion wave packet at a narrow M_z mass-barrier. Clearly visible are a re-focussed transmitted contribution, as well as transverse contributions (``red dots" , near top and bottom of the simulation region).

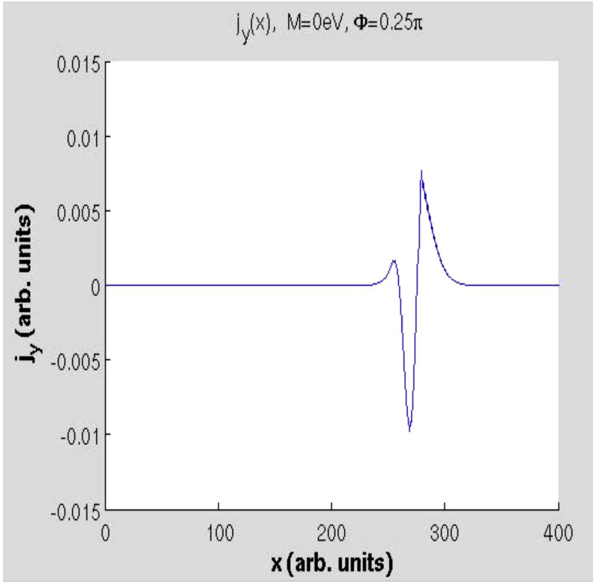

Fig. 2: Transverse current contriution j_y upon impinging at the left side (x=280) of the mass barrier (centered at position 300).

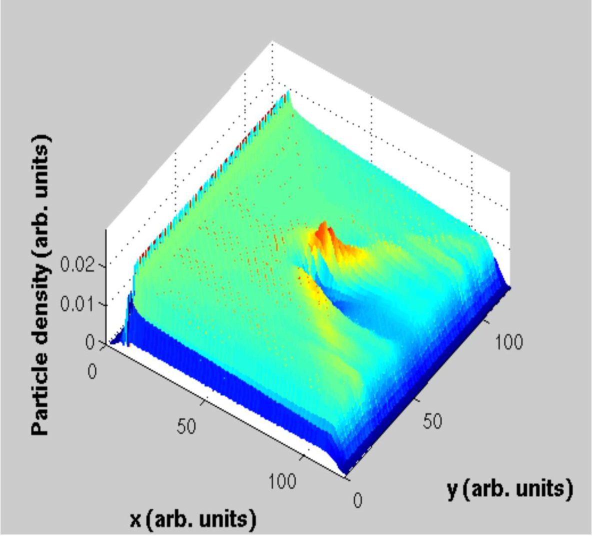

Fig.3: Scattering of Dirac fermions at a magnetic island under applied electric bias. Clearly visible is the asymmetry of the scttering process - attributed to spin-momentum locking.

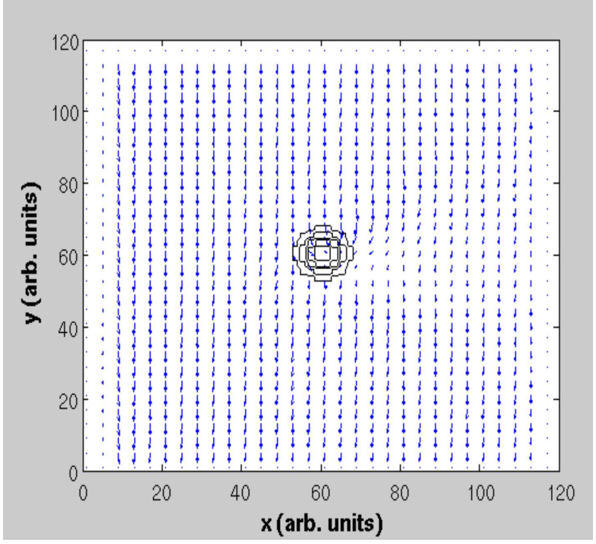

Fig.4: Associated spin texture of the Dirac fermions (blue arrows). The contour of the magnetic island (M_z>0) is indicated by black lines.

978-3-901578-31-1

Patterning Superconductivity in a Topological Insulator

Jerome T. Mlack,[1,2] Atikur Rahman,[1] Gopinath Danda,[2] Natalia Drichko,[1] Sarah Friedensen,[2] Marija Drndic [2] and Nina Markovic [1,3]

[1] *Department of Physics and Astronomy, Johns Hopkins University, Baltimore, Maryland 21218, USA*
[2] *Department of Physics and Astronomy and §Department of Electrical and Systems Engineering, University of Pennsylvania,*
Philadelphia, Pennsylvania 19104, USA
[3] *Department of Physics and Astronomy, Goucher College, Baltimore, Maryland 21204, USA*
e-mail:nina.markovic@goucher.edu

Topologically protected states in combination with superconductivity hold great promise for quantum computing applications, but the progress on electrical transport measurements in such systems has been impeded by the difficulty of fabricating devices with reliable electrical contacts. We find that superconductivity can be patterned directly into Bi2Se3 nanostructures by local doping with palladium [1]. Superconducting regions are defined by depositing palladium on top of the nanostructures using electron beam lithography followed by in situ annealing. Electrical transport measurements at low temperatures show either partial or full superconducting transition, depending on the doping conditions. Structural characterization techniques indicate that palladium remains localized in the targeted areas, making it possible to pattern superconducting circuits of arbitrary shapes in this topological material.

[1] J. T. Mlack, A. Rahman, G. Danda, N. Drichko, S. Friedensen, M. Drndic and N. Markovic, ACS Nano **11**, 5873 (2017).

978-3-901578-31-1

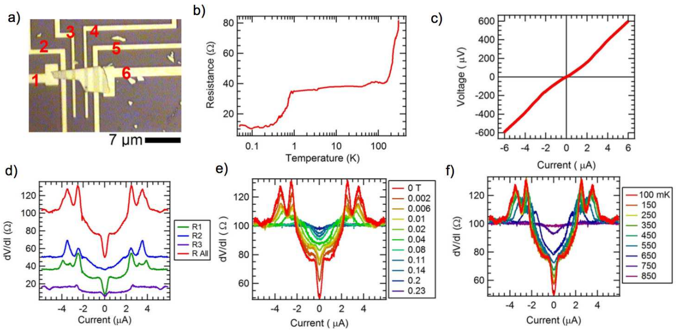

Figure 1. Sample image and the electrical transport measurements of a Pd-doped Bi_2Se_3 device after annealing.

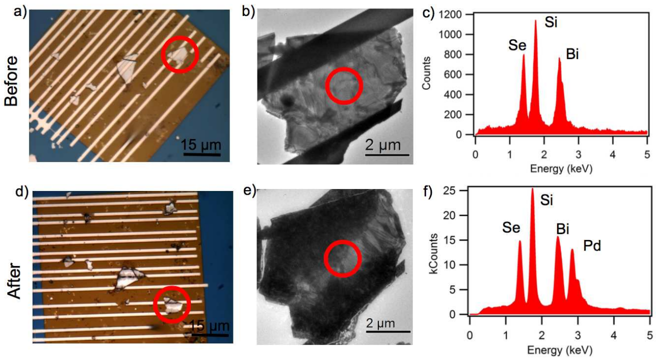

Figure 2. Images and EDS spectra of Bi_2Se_3 flakes before and after annealing.

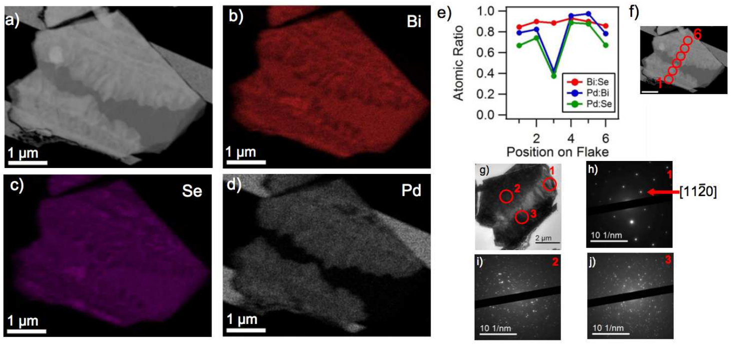

Figure 3. Elemental EDS maps of an annealed Bi_2Se_3 flake.

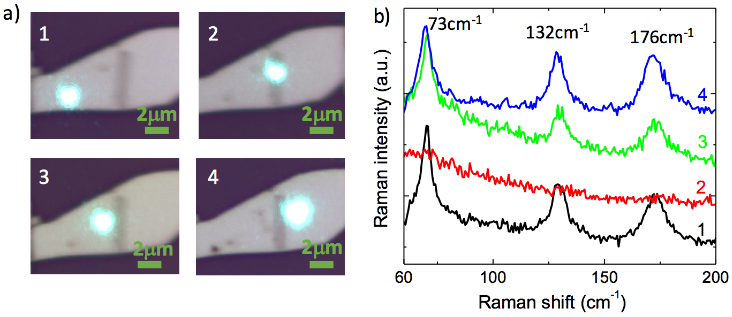

Figure 4. Images (a) and Raman spectra (b) of doped (dark gray stripe) and undoped (light gray) regions of a Bi_2Se_3 flake after annealing.

Topological Quasiparticles: Magnetic Skyrmions

Wanjun Jiang[1,2], Pramey Upadhyaya[3,4], Xichao Zhang[5], Wei Zhang[1,6], Guoqiang Yu[3],
Xiao Wang[7], M. Benjamin Jungfleisch[1], Frank Y. Fradin[1], John E. Pearson[1],
Yaroslav Tserkovnyak[4], Kang L. Wang[3], Yan Zhou[5], Xuemei Cheng[7], Olle Heinonen[1],
Suzanne G. E. te Velthuis[1], and Axel Hoffmann[1]

[1] *Materials Science Division, Argonne National Laboratory, Lemont, IL 60439, U.S.A.*
[2] *Department of Physics, Tsinghua University, Beijing, 100084, China*
[3] *Dept. of Electrical Engineering, University of California, Los Angeles, CA 90095, U.S.A.*
[4] *Dept. of Physics and Astronomy, University of California, Los Angeles, CA 90095, U.S.A.*
[5] *School of Science and Eng., The Chinese Univ. of Hong Kong, Shenzhen 518172, China*
[6] *Department of Physics, Oakland University, Rochester, MI 48309, U.S.A.*
[7] *Department of Physics, Bryn Mawr College, Bryn Mawr, PA 19010, U.S.A.*
e-mail: hoffmann@anl.gov

Magnetic skyrmions are topologically distinct spin textures and can be stable with quasi-particle like behavior, such that they can be manipulated with very low electric currents. This makes them interesting for extreme low-power information technologies [1], where data is envisioned to be encoded in topological charges, instead of electronic charges as in conventional semiconducting devices. Using magnetic multilayers we demonstrated that inhomogeneous charge currents allow the generation of skyrmions at room temperature in a process that is remarkably similar to the droplet formation in surface-tension driven fluid flows, see Fig. 1 [2]. Micromagnetic simulations reproduce key aspects of this transformation process and suggest a possible second mechanism at higher currents that does not rely on preexisting magnetic domain structures [3]. Indeed, we demonstrated this second mechanism experimentally using non-magnetic point contacts. Using this approach, we demonstrated that the topological charge gives rise to a transverse motion on the skyrmions, i.e., the skyrmion Hall effect (see Fig. 2) [4], which is in analogy to the ordinary Hall effect given by the motion of electrically charged particles in the presence of a magnetic field.

This work was supported by the U.S. Department of Energy, Office of Science, Materials Sciences and Engineering Division.

1] A. Hoffmann and S. D. Bader, Phys. Rev. Appl. 4, 047001 (2015).

[2] W. Jiang, *et al.*, Science 349, 283 (2015).

[3] O. Heinonen, *et al.*, Phys. Rev. B 93, 094407 (2016).

[4] W. Jiang, *et al.*, Nature Phys. **13**, 162 (2017).

978-3-901578-31-1

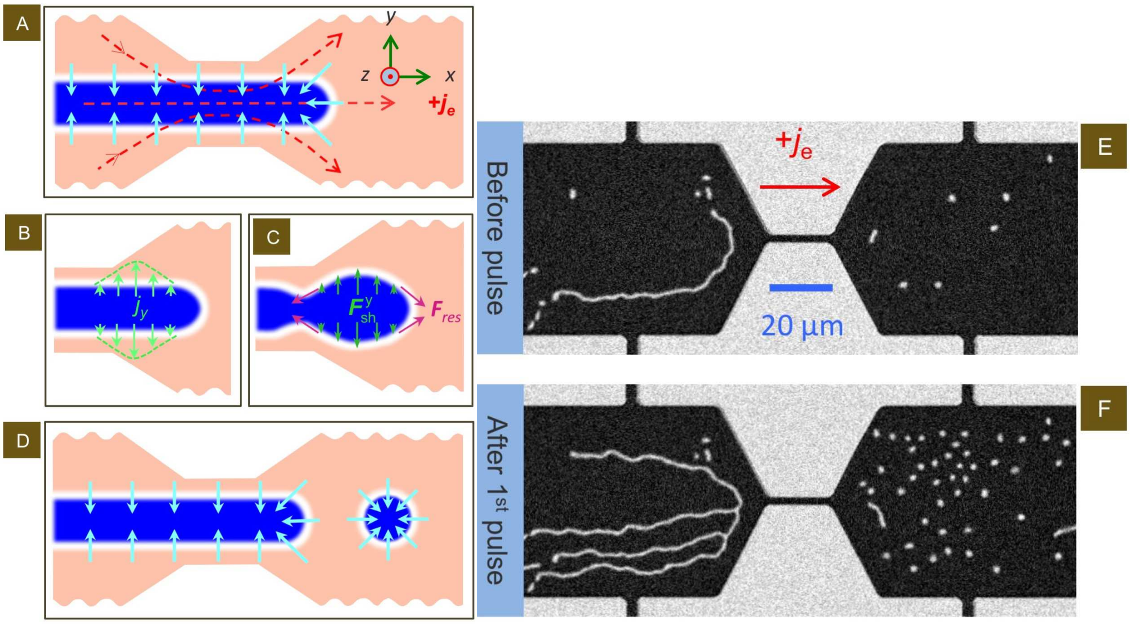

Fig.1: Transformation from chiral band domain into magnetic skyrmions enabled via inhomogeneous spin-orbit torques. (A) Inhomogeneous current distribution passing through a magnetic band domain. (B) Transverse current passing through the side walls of the magnetic band domain. (C) Expansion of band domain and increased surface tension leads /to necking instability. (D) Individual skyrmion bubble separates from band domain. Magnetooptic Kerr effect imaging of Ta/CoFeB/TaO$_x$ trilayer with a geometrical constriction (E) before and (F) after applying electric current pulse.

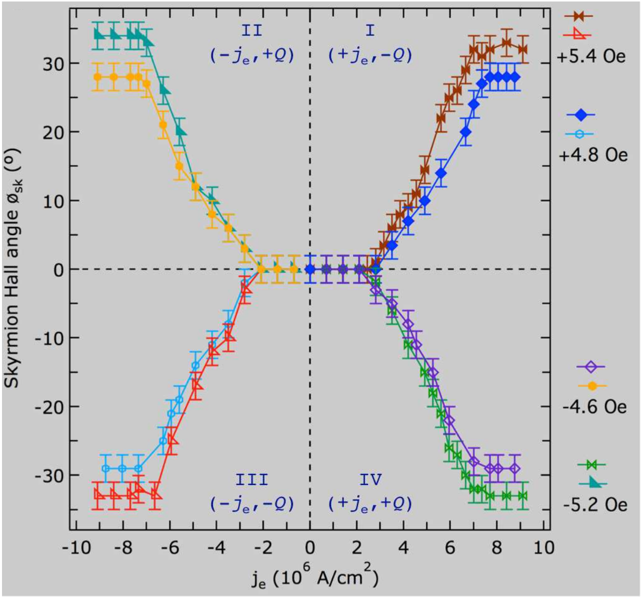

Fig.2: Skyrmion Hall angle as a function of electric current for positive and negative topological charge (determined by external magnetic field). Three different regions can be observed. At low currents the motion of skyrmion is in the creep regime and follows the direction of external force. In the intermediate, regime the spin Hall angle increases gradually until it saturates at high currents, when the skyrmion motion is in the flow regime. The saturation skyrmion Hall angle increases with larger magnetic field, which is related to the smaller skyrmion size.

Topological Mott Insulators in Certain Frustrated Lattices

Mengsu Chen, Hoi Hui and Vito Scarola

Department of Physics, Virginia Tech
Blacksburg VA 24060 USA
e-mail: scarola@vt.edu

Topological phases typically encode topology at the level of the single particle band structure. But a remarkable new class of models shows that quantum anomalous Hall effects can be driven exclusively by interactions, while the parent non-interacting band structure is topologically trivial. Unfortunately, these models have so far relied on interactions that do not spatially decay and are therefore unphysical. We study models of spinless fermions on frustrated lattices: decorated honeycomb (Fig. 1) and kagome lattices. Using complementary methods, mean-field theory and exact diagonalization, we find a robust quantum anomalous Hall phase arising from spatially decaying interactions (Fig. 2). Our finding indicates that interactions alone can, in principle, drive topologically trivial single-particle states into topological phases in certain frustrated lattices.

978-3-901578-31-1

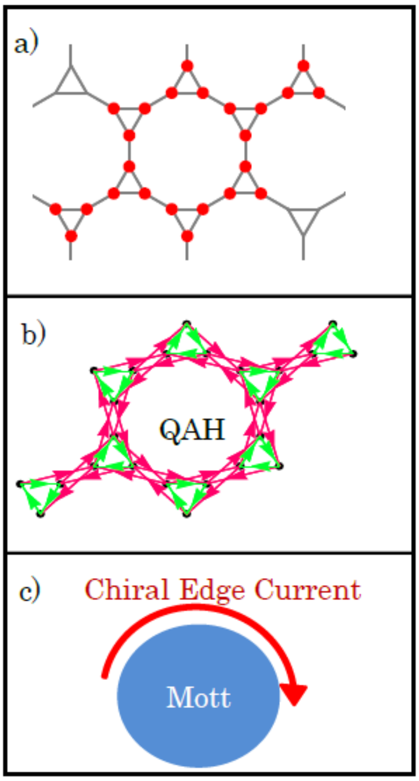

Fig.1:
(a) The decorated honeycomb lattice and the 24-site cluster (red dots) studied by exact diagonalization.
(b) The quantum anomalous Hall (QAH) pattern draws bond currents computed with arrows indicating the direction of spontaneously induced currents.
(c) Schematic of a large central Mott Insulator surrounded by a spontaneously induced edge current in the QAH phase.

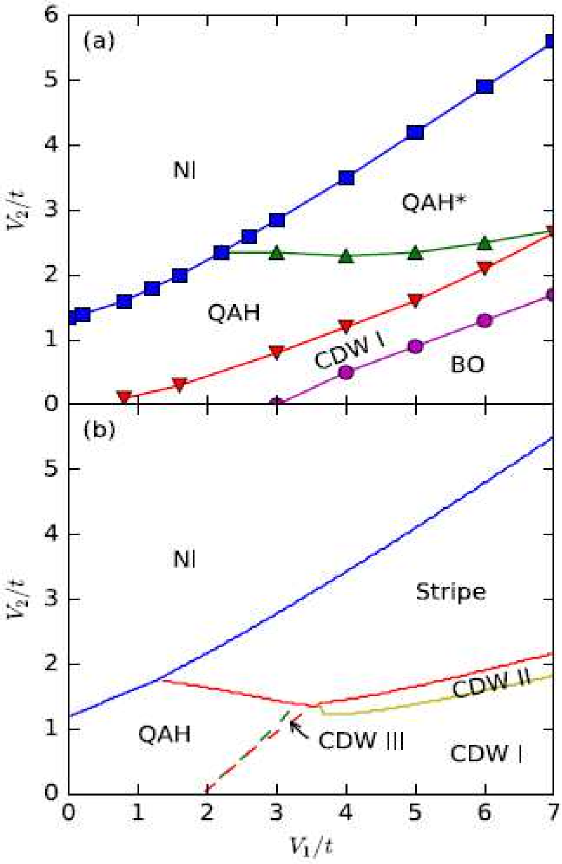

Fig.2:
(a) Phase diagram obtained using exact diagonalization of a Hubbard model on the decorated honeycomb lattice with a nearest-neighbor (V2) and next-nearest neighbor (V2) interaction in units of the nearest neighbor hopping, t. The symbols are results from calculations and the lines area guide to the eye. The nematic insulator (NI) represents a symmetry broken phase that avoids next-nearest neighbor pairs. The bond ordered (BO) phase is a uniform phase that results from the superposition of bond-ordered crystal configurations. The CDW and stripe states are topologically trivial charge ordered phases. The QAH phase denotes the topological Mott insulator with spontaneously induced chiral edge modes.
(b) The same as (a) but the lines plot transitions obtained from self-consistent mean field theory on an infinite lattice. The dashed lines indicate second order phase transitions.
The agreement between panels (a) and (b) shows strong evidence for a robust QAH phase

Towards Low-Damping Spin-Wave Media for Magnonics

Hadrian Aquino[1], Adam Papp[2], Gyorgy Csaba[2], Alexei O. Orlov[1],
Gary H. Bernstein[1], and Wolfgang Porod[1]

[1] *Center for Nano Science and Technology, University of Notre Dame, IN, USA*
[2] *Faculty of Information Technology & Bionics, Pazmany University, Budapest, Hungary*
e-mail: porod@nd.edu

Spin waves (SWs) offer intriguing possibilities for transmitting and processing information in future electronics [1][2]. Low-damping spin-wave media are required for such magnonic applications. Specifically, yttrium iron garnet ($Y_3Fe_5O_{12}$, YIG) has seen significant interest as a spin-wave propagation medium for spintronics. The magnetic properties of YIG films strongly depend upon the crystallinity of the film. Current research uses epitaxial YIG on gadolinium gallium garnet ($Gd_3Ga_5O_{12}$, GGG) due to their excellent lattice match. YIG growth on semiconductor substrates would allow for the integration of YIG-based devices with other semiconductor electronics and is therefore important to the development of spintronic devices. However, little work has been done along these lines. We report on the quality of YIG material as grown on SiO_2, as it is ubiquitous in the fabrication of circuits not only on Si, and can be deposited on any type of substrate. Our approach involves the deposition of amorphous SiO_2 on Si in a magnetron sputtering system, followed by post-deposition crystallization of the film in various conditions including annealing in a tube furnace and rapid thermal annealing. We were able to produce YIG films with high saturation magnetization in a surprisingly narrow temperature window (Fig. 1). TEM images confirm the crystallinity of the YIG film within that narrow temperature window (Fig. 2).

We will also present the design of a spin-wave-based microwave signal processing device (Fig. 3) [3]. The microwave signal is first converted into spin-wave excitations that propagate in a patterned magnetic thin-film. An interference pattern is formed in the film whose intensity distribution at the read-out points yields the spectral decomposition of the signal. We use analytic calculations and micromagnetic simulations to verify and analyze device operation.

[1] G. Csaba, Á. Papp, W. Porod. “Perspectives of using spin waves for computing and signal processing,” Physics Letters A, 381, 17 (2017).

[2] A. V. Chumak, V. I. Vasyuchka, A. A. Serga, and B. Hillebrands. "Magnon spintronics," Nature Physics 11, no. 6, 453-461 (2015).

[3] A. Papp, Ph.D. dissertation, University of Notre Dame (2017).

978-3-901578-31-1

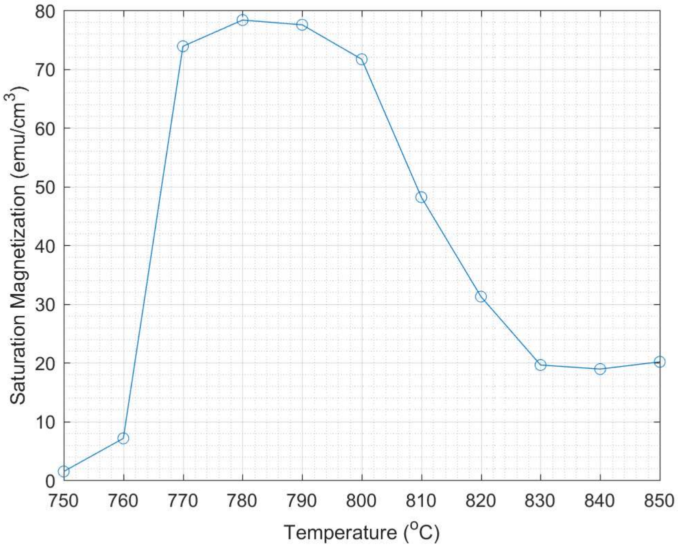

Fig.1: Saturation magnetization vs rapid thermal anneal temperature of 18 nm YIG film RF magnetron sputtered on silicon dioxide.

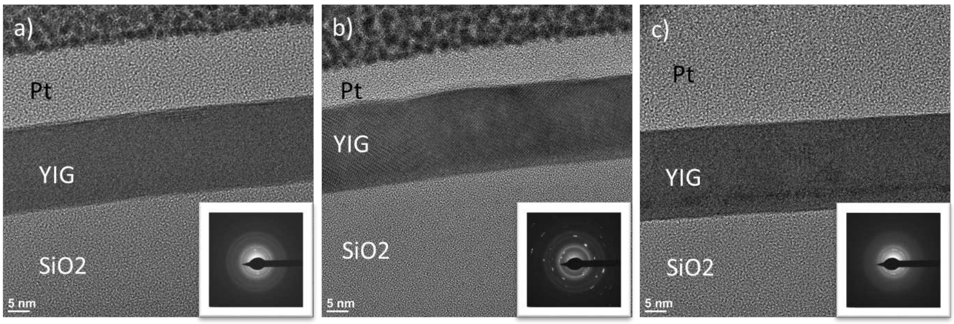

Fig.2: TEM images of 18 nm YIG film, RTA at a) 760 °C which resulted in an amorphous film, b) 790 °C with clearly visible crystallites, c) 830 °C small isolated crystallites in an amorphous film.

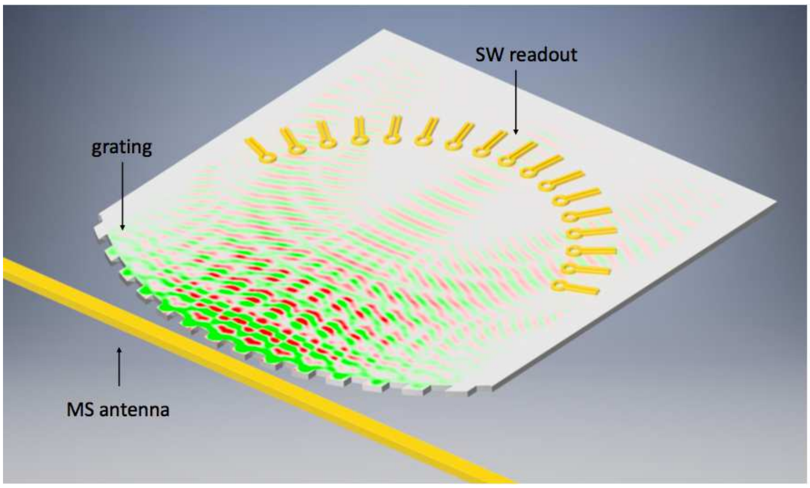

Fig.3: Schematic layout of the proposed spin-wave-based spectrum analyzer [3].

Towards reconfigurable nanomagnonic devices based on patterned spin-textures

E. Albisetti[1,2], D. Petti[2], M. Pancaldi[3], M. Madami[4], S. Tacchi[5], A. Papp[6], G. Csaba[6],
W. Porod[6], P. Vavassori[3], E. Riedo[1], R. Bertacco[1,7]

[1] CUNY-Advanced Science Research Center and City College New York, City University of New York, 85 St Nicholas Terrace, New York, New York 10031, USA.
[2] Dipartimento di Fisica, Politecnico di Milano, 20133 Milano, Italy.
[3] CIC nanoGUNE, E-20018 Donostia-San Sebastian, Spain.
[4] Dipartimento di Fisica e Geologia, Università di Perugia, Italy.
[5] Istituto Officina dei Materiali del CNR (CNR-IOM), Unità di Perugia, c/o Dipartimento di Fisica e Geologia, Perugia, Italy.
[6] Center for Nano Science and Technology, University of Notre Dame, Notre Dame, IN, 46556 USA.
[7] IFN-CNR, c/o Politecnico di Milano, 20133 Milano, Italy.
e-mail: edoardo.albisetti@polimi.it

The control of spin-waves holds the promise to enable energy-efficient information transport and wave-based computing. Conventionally, the engineering of spin-waves is achieved via physically patterning magnetic structures such as magnonic crystals and micro-nanowires. However, spatially confining and steering spin-waves at the nanoscale, which is crucial for the realization of magnonic nanodevices, proved itself extremely challenging.

We demonstrate a new concept for creating reconfigurable magnonic structures, by crafting at the nanoscale the magnetic anisotropy landscape of a ferromagnet exchange-coupled to an antiferromagnet. By performing a highly localized field cooling with the hot tip of a scanning probe microscope, magnetic structures, with arbitrarily oriented magnetization and tunable unidirectional anisotropy, are patterned without modifying the film chemistry and topography (Fig. 1). We show that, in such structures, the spin-wave excitation and propagation can be spatially controlled at remanence (Fig. 2), and can be tuned by external magnetic fields. [1,2] Furthermore, we show that we are able to confine and steer spin-waves propagating within patterned magnetic domains and domain walls, paving the way towards the use of nanoscale spin-textures for exciting and manipulating magnons in reconfigurable nanocircuits.

[1] E. Albisetti et al., Nat. Nanotechnol., **11** 545–551 (2016).

[2] E. Albisetti et al., AIP Advances, **7**(5), 55601 (2017).

978-3-901578-31-1

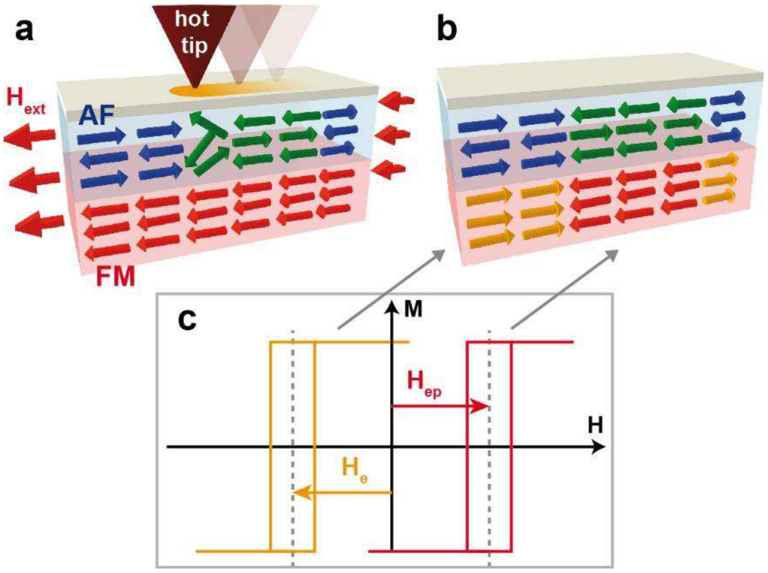

Fig.1: a. Schematic of the tam-SPL writing process on a ferromagnet (FM)/antiferromagnet (AF) exchange bias system: a highly localized field cooling is performed by sweeping a heated AFM tip in presence of an external magnetic field. b. Magnetic configuration of the sample after writing: the spin-textures in the ferromagnet are stabilized by the local exchange bias. c. Local ferromagnetic hysteresis loops from the patterned (red loop) and non-patterned (yellow loop) areas of the sample.

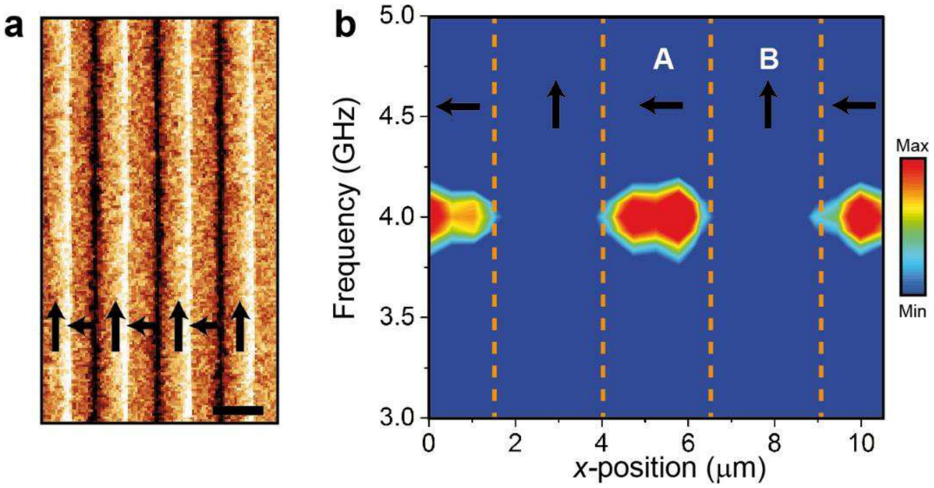

Fig.2: a. MFM image of the magnonic structures, consisting of 2.5 μm wide tracks with alternated 0° and 90° oriented remanent static magnetization (black arrows). Scale bar: 4 μm. b. One-dimensional map of the spin-wave intensity measured at remanence by μ-BLS along the x-direction on the sample of panel a. The black arrows indicate the direction of the magnetization, the orange dashed lines mark the domain walls. Spin-waves are efficiently excited within tracks of type A.

Surface Patterned Magnetic Thin Films for Multiferroic and Exchange Bias Device Application

Goran Rasic[1], Justin Schwartz[2], and Branislav Vlahovic[1]

[1] *Department of Physics, North Carolina Central University, Durham, NC 27707, USA*
[2] *Department of Materials Science and Engineering, North Carolina State University, Raleigh, NC 27606, USA*
e-mail: grasic@nccu.edu

We use innovative design at the nanoscale to alter and improve the physical properties of ferroic materials for device application. Textured $NiFe_2O_4$ (NFO) thin films were deposited at room temperature by chemical solution deposition onto c-plane sapphire substrates and patterned using nanoimprint lithography [1-4]. Significant coercivity reduction (up to 90% as compared to planar film) in sol-gel fabricated polycrystalline $NiFe_2O_4$ thin films was achieved by patterning the surface in a corduroy pattern [1-4]. By patterning the surface we are able to alter the minimum energy configuration of the system and domain wall propagation. Building on these results using similar principles we can improve number of devices based on ferroic material properties. The focus is on patterning the interface between two different materials to improve the coupling between them and thus improving the overall device response. The two main areas of interest are magnetoelectric devices (control and detection of magnetic fields with electronic devices and vice-versa) and exchange bias devices for memory applications. Both of these effects have great promise but suffer from low end response due to weak interface coupling. Combining these and other suitable materials with piezoelectrics (PZT) and antiferromagnets (NiO, CoO) can help improve response of magnetic sensors, memories, field generators, and other devices.

[1] G. Rasic et al., MRS Comm., **6(4)**, 397 (2016).
[2] G. Rasic et al., Phys. Status Solidi (a), **212**, 449 (2015).
[3] G. Rasic et al., IEEE Mag. Lett., **5**, 1 (2014).
[4] G. Rasic et al., MRS Comm., **3**, 207 (2013).

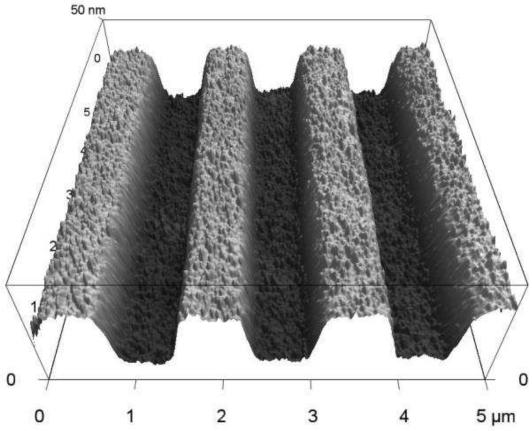

Fig.1: Atomic force microscopy scan showing the surface topography of patterned NiFe$_2$O$_4$ film.

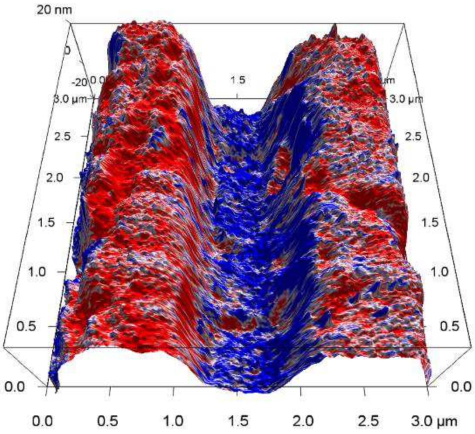

Fig.2: Magnetic force microscopy scan overlaid over topography of a patterned film. Magnetic fields oriented in opposite directions and colored red and blue respectively.

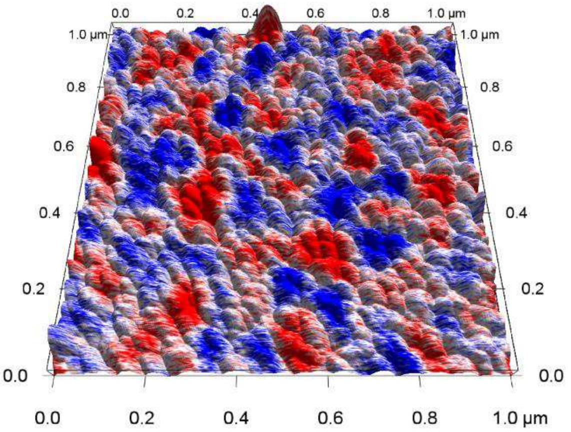

Fig.3: Magnetic force microscopy image overlaid over topography of a planar film. Magnetic fields oriented in opposite directions and colored red and blue respectively.

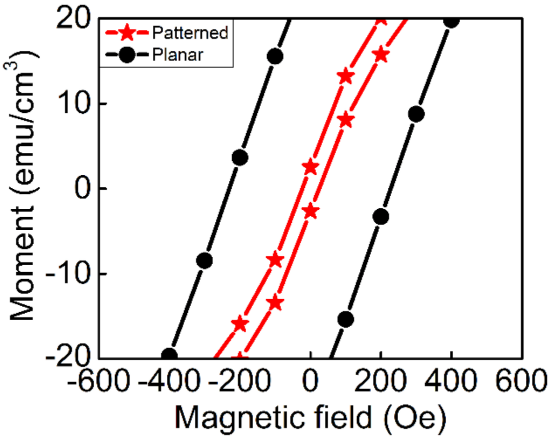

Fig.4: Magnetization hysteresis measurements of planar and patterned NiFe$_2$O$_4$ thin films.

978-3-901578-31-1

Transport in topological insulators and topological superconductors

Ewelina Hankiewicz

Physics Department, Wurzburg University, Germany
e-mail: hankiewicz@physik.uni-wuerzburg.de

Topological insulators (TIs) have a bulk energy gap that separates the highest occupied band from the lowest unoccupied band while gapless energy electronic states that are protected by time reversal symmetry live at the edge (2D TIs) or surface (3D TIs). When doped with the magnetic impurities the TIs show the quantum anomalous Hall effect i.e. a single circulating chiral mode at the boundary of 2D TI. Interestingly, in the odd space-time dimensions, one would expect that the formation of the quantum anomalous Hall effect is directly connected to the parity anomaly. We prove theoretically this relation and discuss the experimental consequences [1].

On the other hand, a topological insulator in the proximity to an s-wave superconductor is the prefect material to detect signatures of Majorana fermions. S-wave superconductor on the top of the surface states of 3D TI generates s-wave and p-wave pairing mixture in the surface state due to the spin-momentum locking [2,3]. We predict that in the Josephson junction setup, namely superconductor (SC) /surface state of topological insulator/superconductor (SC), existence of this p-wave component leads to novel features in transport like superconducting Klein tunneling i.e. the perfect transmission of hybridized Majorana states for normal incidence, the non-sinusoidal current phase relation [3] and unusual phase-dependent thermal conductance in SQUIDS (see Figs. 1,2) [4]. Further, we propose the experimental setups to observe signatures of Majorana fermions in the ac Josephson effect on TI hybrid structures [3,4,5] and in superconductors on hexagonal lattices [6].

[1] J. Böttcher and E. M. Hankiewicz, arXiv:1607.07768 (2016).

[2] Liang Fu and C. L. Kane, Phys. Rev. Lett. **100**, 096407 (2008).

[3] G. Tkachov and E. M. Hankiewicz, Phys. Rev. B **88**, 075401 (2013).

[4] B. Sothmann and E. M. Hankiewicz Phys. Rev. B **94**, 081407(R) (2016).

[5] R. S. Deacon, J. Wiedenmann, E. Bocquillon, F. Domínguez, T. M. Klapwijk, P. Leubner, C. Brüne, E. M. Hankiewicz, S. Tarucha, K. Ishibashi, H. Buhmann, and L. W. Molenkamp, Phys. Rev. X **7**, 021011 (2017).

[6] L. Elster, C. Platt, R. Thomale, W. Hanke, and E. M. Hankiewicz, Nature Comm.**6**, 8232 (2015).

978-3-901578-31-1

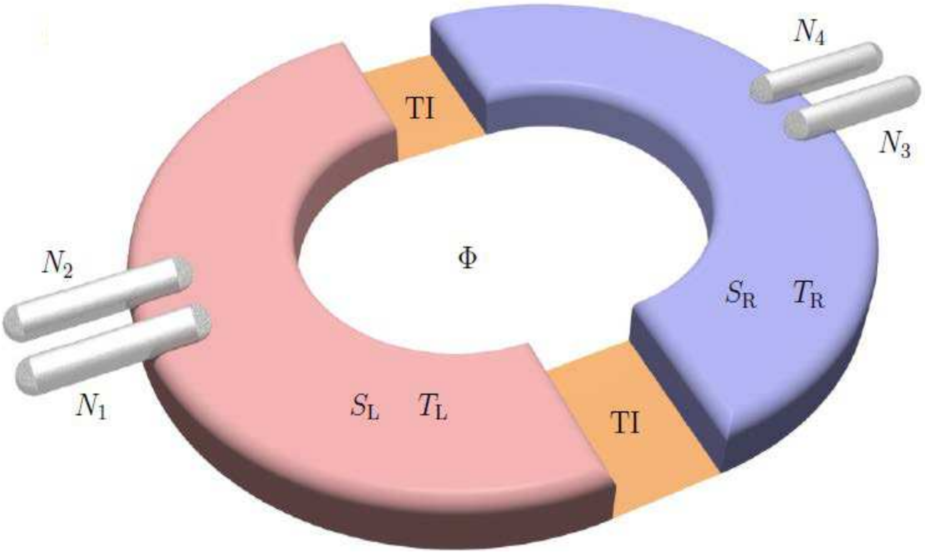

Fig.1 SQUID geometry to detect the phase- dependent heat currents

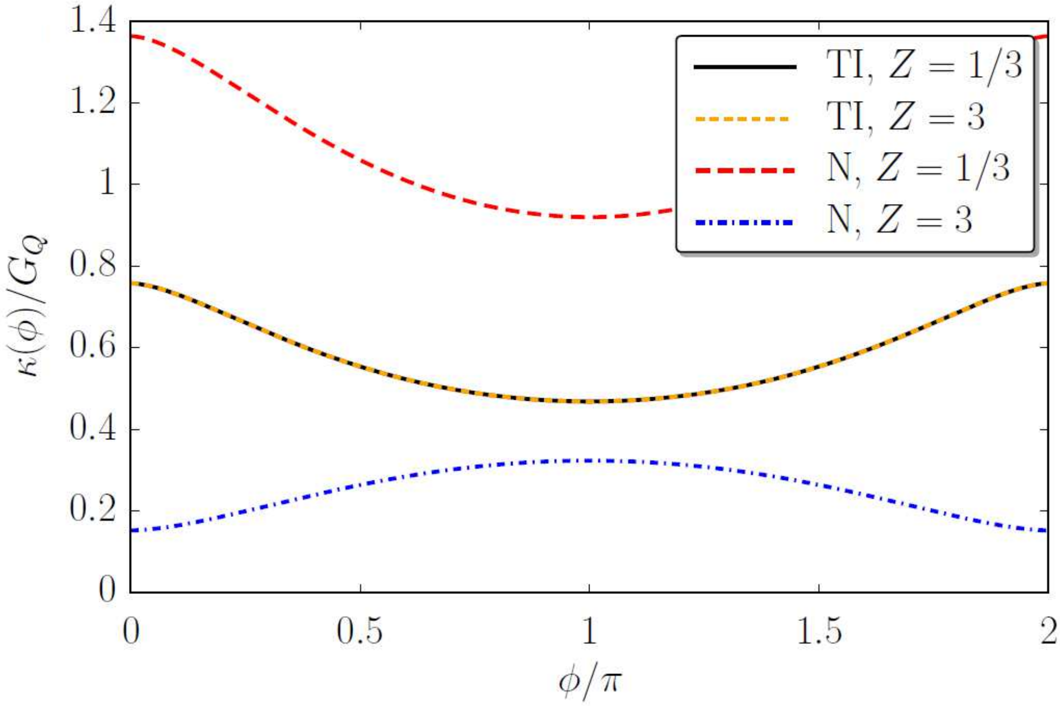

Fig,2 Phase dependence of the thermal conductance in units of thermal conductance qunatum GQ for short one-dimensional SC-normal-SC (SC-N-SC) and SC-TI-SC Josesphson junctions for different interface strenght Z.

978-3-901578-31-1

Development of a new platform to realize high order non-Abelian excitations

Aleksandr Kazakov[1], Tai-Lung Wu[1], Zhong Wan[1], Ken W. West[2], Loren N. Pfeiffer[2], and Leonid P. Rokhinson[1]

[1] *Department of Physics and Astronomy, Purdue University, West Lafayette, Indiana, USA*
[2] *Department of Electrical Engineering, Princeton University, Princeton, NJ, USA*
e-mail: leonid@purdue.edu

I will introduce a new concept based on the ferromagnetic transition in a quantum Hall regime where manipulation of topological defects may be possible via reconfigurable network of domain walls. We pursue two systems, one based on magnetic semiconductor CdTe:Mn, and one based on GaAs high mobility heterostructures, where we developed gate control of quantum Hall ferromagnetic transitions. Such control allows formation of isolated domain walls which consist of counter-propagating edge states of opposite polarization. Apart from interesting spintronics applications, these re-configurable domain walls, coupled to superconducting contacts, can form a new platform where Majorana fermions, higher-order non-Abelian excitations parafermions, and, possibly, Fibonacci fermions (non-Abelian particles that can perform universal gate operations) can be created, braided, manipulated and fused.

A. Kazakov, et al., Phys. Rev. B **94**, 075309 (2016)
A. Kazakov, et al., Phys. Rev. Lett. **119**, 046803 (2017)

978-3-901578-31-1

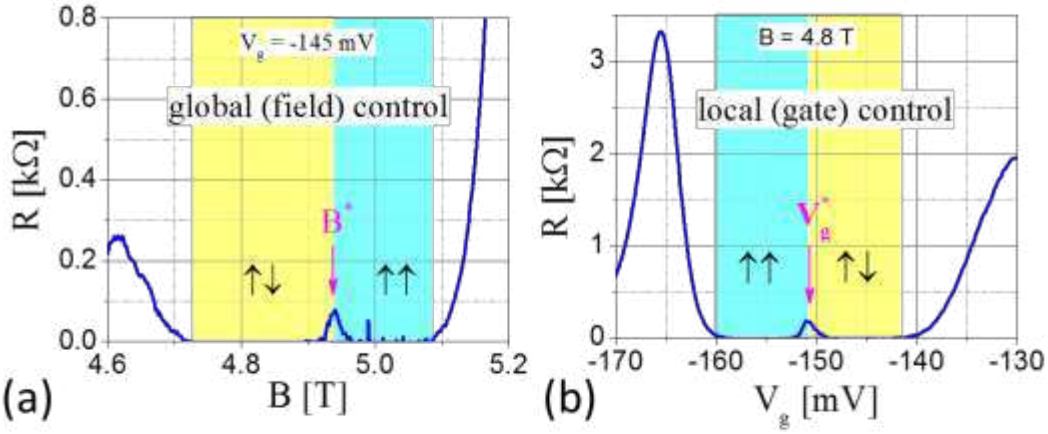

Fig.1: Field and gate control of FQHE spin transition. Resistance near ν = 2/3 state is measured as a function of (a) magnetic field B at a constant gate voltage V g or (b) as a function of V g at a constant B in a Hall bar sample from wafer A. In yellow regions the 2D gas is unpolarized with CFs levels $\Lambda_{1,\uparrow}$ and $\Lambda_{1,\downarrow}$ filled. In cyan regions 2D gas is fully polarized with CFs residing in $\Lambda_{1,\uparrow}$ and $\Lambda_{2,\uparrow}$ levels. B^* and V_g^* mark the spin transition.

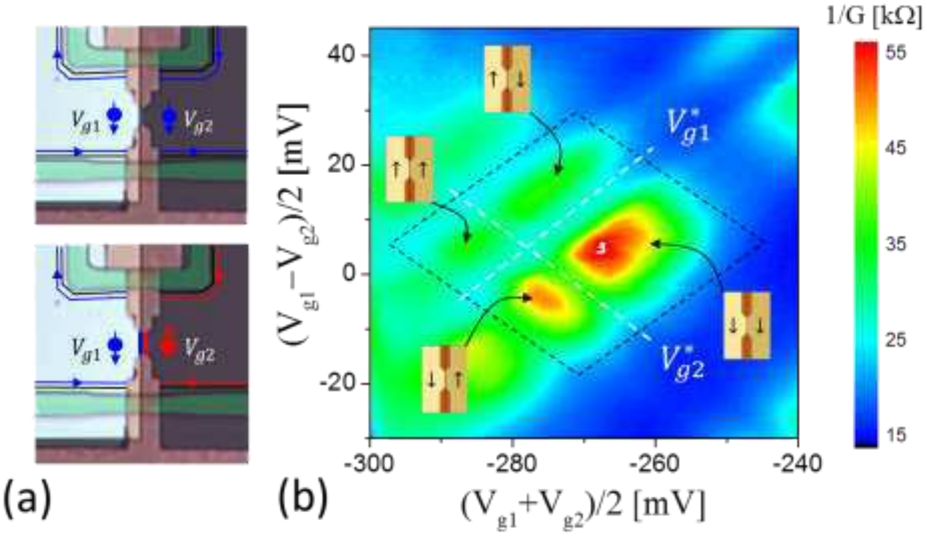

Fig.2: (a) An optical image of a multi-gate sample. Brown colored regions are Ohmic contacts separated by 5 μm in this device. Etched areas without 2D gas are colored green, they completely enclose contact pads. The light and dark regions are overlapping gates V_{g1} and V_{g2}, the gates also overlap with contacts. Edge channels are shown schematically for different $\nu = 2/3$ polarizations under the gates. (b) Resistance is measured between two central contacts in the vicinity of $\nu = 2/3$ at B = 6.3 T. The $\nu = 2/3$ state is outlined by a black dashed line. White dashed lines highlight spin transitions under the two gates. The $\nu = 2/3$ region is divided into four quadrants with different polarization of the topmost CF Λ-level.

High-Voltage Al_2O_3/Ta_2O_5 Heterostructure Metal/Insulator/Insulator/Metal (MIIM) Diodes

D.Z. Austin, M. Jenkins, K. Holden, John F. Conley, Jr.

*School of EECS, Oregon State University, Corvallis, OR, *jconley@eecs.oregonstate.edu*
e-mail: jconley@eecs.oregonstate.edu

Thin heterostructure dielectric tunnel barriers have recently enabled enhanced low-voltage current asymmetry ($\eta_{asym} = I^-/I^+$) and non-linearity (f_{NL}) in MIIM tunnel diodes for applications such as rectenna based energy harvesting.[1-4] In this work, we investigate thick bi-layers of Al_2O_3 and Ta_2O_5 for high-voltage applications such as antenna diodes for plasma-induced damage protection and one-time programmable non-volatile memory logic.

Al_2O_3/Ta_2O_5 bilayer stacks were deposited via atomic layer deposition (ALD) without breaking vacuum. Al_2O_3:Ta_2O_5 thickness ratios of 1:1, 1:2, 1:3, 1:5, and 1:9 were fabricated with Al_2O_3 fixed at 30 nm and Ta_2O_5 varied from 30 - 270 nm (Figs. 1 and 2).

I-V behavior (Fig. 3) and asymmetry (Fig. 4) are both found to be a strong function of the Al_2O_3/Ta_2O_5 thickness ratio. The maximum asymmetry ratio and voltage are tuned by the Ta_2O_5 thickness, increasing from $\eta_{asym\text{-}max}$ ~10^3 at ~19 V for the 1:1 ratio devices to $\eta_{asym\text{-}max}$ ~10^5 at ~52 V for the 1:9 ratio (Fig. 4). Trends in conduction and η_{asym} are explained by the asymmetric barrier (Fig. 2) created by the pairing of Al_2O_3 and Ta_2O_5, and are dominated by Fowler-Nordheim tunneling (FNT) through the Al_2O_3 barrier and defect based Frenkel-Poole emission (FPE) conduction through the Ta_2O_5. FNT through the Al_2O_3 is confirmed by a constant Al_2O_3 electric field / effective tunnel distance versus Ta_2O_5 thickness plot (Fig. 5). Because the FNT onset voltage is dependent (independent) on the Ta_2O_5 thickness under positive (negative) bias, controlling the Ta_2O_5 thickness controls the maximum asymmetry and the voltage which it occurs.

This work demonstrates that ALD bilayers may be used to effectively engineer the reverse breakdown voltage, maximum η_{asym}, and operating range of high voltage MIM diodes. Due to low temperature fabrication, high voltage diodes are of interest for implementation in CMOS back end of the line as well as for large area electronics

The authors acknowledge support of ON Semiconductor and NSF CSMC

[1] Maraghechi et al., Appl. Phys. Lett. 99, 253503 (2011).
[2] Maraghechi et al., Appl. Phys. Lett. 100, 113503 (2012).
[3] N. Alimardani and J.F. Conley, Jr., Appl. Phys. Lett. 102, 143501 (2013).
[4] N. Alimardani and J.F. Conley, Jr., Appl. Phys. Lett. 105, 082902 (2014).

978-3-901578-31-1

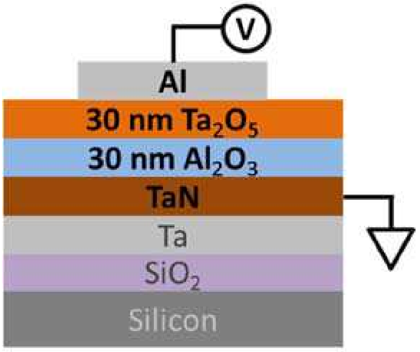

Fig. 1: Cross sectional schematic of the basic MIIM device structure.

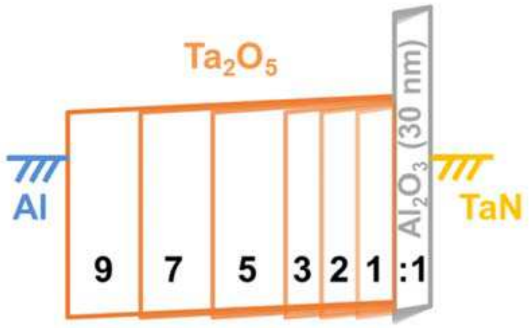

Fig. 2: Asymmetric equilibrium band diagrams representing the various Ta_2O_5:Al_2O_3 thickness ratio devices. Al_2O_3: $E_G = 8.7$ eV, $\chi = 1.4$ eV, $\kappa = 8.7$; Ta_2O_5: $E_G = 4.5$ eV, $\chi = 3.2$ eV, $\kappa \sim 26$

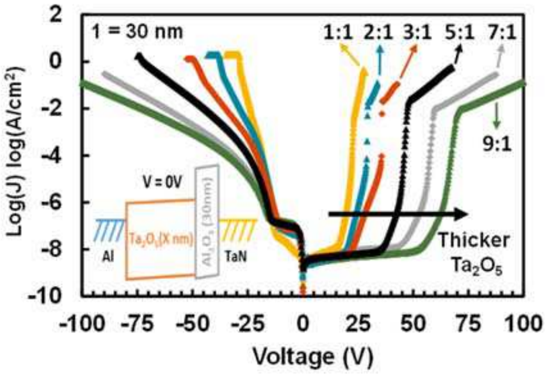

Fig. 3: I-V for all Al_2O_3/Ta_2O_5 thickness ratio devices. Under positive bias, *reverse* diode current for all devices remains low until the onset of FNT through Al_2O_3 layer, followed by rapid increase until Al_2O_3 breakdown, upon which current becomes limited by FPE through the Ta_2O_5. The "knee" voltage marking the onset of FNT through Al_2O_3 is controlled by the Ta_2O_5 thickness - a larger voltage drops across thicker Ta_2O_5 layers reduces the drop across the Al_2O_3. For small negative bias, <-15 V, the *forward current is higher for thicker* Ta_2O_5 *layers*, a somewhat counter-intuitive result explained by the asymmetry of the band diagram and Schottky emission over the Al_2O_3. Beyond -15V, current is lower for thicker Ta_2O_5 layers, in line with expectations. Unlike positive bias, the onset of negative bias FNT through the Al_2O_3 is relatively independent of the Ta_2O_5 thickness, but again followed by Al_2O_3 breakdown and finally FPE limited conduction through Ta_2O_5 at high negative bias.

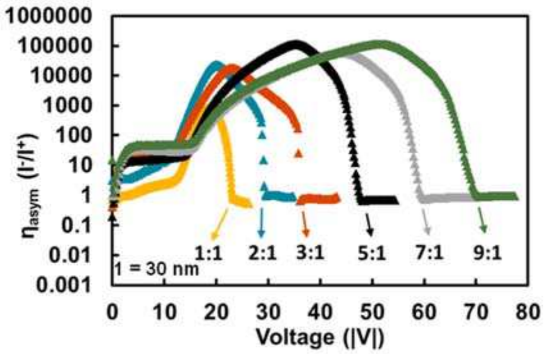

Fig. 4 Log$|\eta_{asym}|$ vs. V for devices from Fig. 3. The onset of FNT through Al_2O_3 at positive bias (Fig. 3) causes asymmetry to drop rapidly.

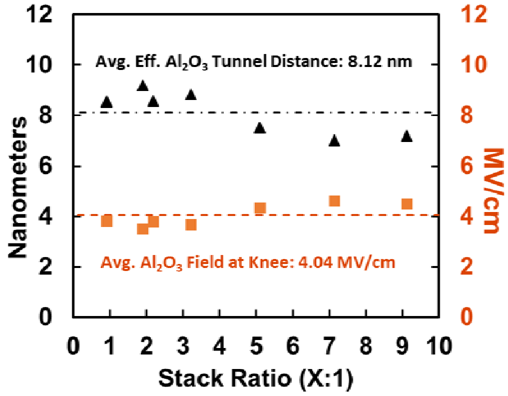

Fig. 5: Plot of Al2O3 effective tunnel distance and electric field at the positive bias FNT onset "knee" versus Ta2O5 thickness ratio.

The reverse Al2O3 breakdown voltage also increases with increasing thickness of the Ta2O5 layer, from ~20 V for the 1:1 ratio to ~67 V for the 1:9 ratio devices.

For small magnitude negative (forward) bias, in the range of 0 to -15 V, the diode forward current is higher for thicker Ta_2O_5 layers, a somewhat counter-intuitive result explained by the asymmetry of the band diagram and Schottky emission over the Al_2O_3. Beyond -15V, forward current is lower for thicker Ta_2O_5 layers, in line with expectations. Unlike positive bias, the onset of negative bias FNT through the Al_2O_3 is relatively independent of the Ta_2O_5 thickness, but again followed by Al_2O_3 breakdown and finally FPE limited conduction at high negative bias.

P-1

Cu Migration During Light-Soaking Experiments

D. Guo[1], A.R. Shaik[1], I. Sankin[2], D. Krasikov[2] and D. Vasileska[1]

[1] *School of Electrical, Computer and Energy Engineering,*
Arizona State University, Tempe, AZ 85287-5706, USA
[2] *First Solar, Perrysburg, OH, 43551, USA*
e-mail: vasileska@asu.edu

Nearly all PV technologies exhibit changes in device performance under extended illumination, or “light soaking”, although the magnitude and the trend of these changes are not always the same among different technologies. Experiments on both commercial modules and research cells based on CdTe technology have shown improvement of cell performance under light stress conditions for up to 20 hours [1]. Many accredited such phenomena to the passivation of traps and migration of Cu ions, however no simulations were previously done to confirm any of these mechanisms. We use the in-house developed 1D Unified Solver [2] to simulate self-consistently the effects of illumination, bias and temperature on the evolution of defect profiles during stress and the resulting performance changes of the device.

The light stress is typically performed after the dark storage of solar devices. Therefore, to prepare the initial system for light soaking simulations, first, we simulate the equilibrium of the defects in CdTe cells under dark without any bias at 65°C. In equilibrium, most of the Cu_i^+ is pushed away from the depletion region, due to the built-in potential of the p-n diode. As a result, more uncompensated acceptors appear in the junction area. Cu_{Cd} acceptor is partially ionized in the quasi-neutral region, while it is completely ionized in the depletion region due to low density of holes in that area.

Under light stress condition with applied forwards bias of 0.8V (maximum power point), the defect equilibrium changes in the following way: (1) Cu_i^+ moves closer to the main junction due to the forward bias, reducing the uncompensated acceptor doping density in the depletion region, (2) part of the ionized defects (Cu_i^+ and Cu_{Cd}^-) are converted into the neutral state after capture of light-generated free carriers, (3) the zero-bias depletion region width increases because of the reduced p-doping in the junction area, (4) the carrier collection efficiency improves, thus increasing the performance. More details of these findings will be given in the presentation.

[1] M. Gostein, L. Dunn, *37th IEEE PVSC*, pp. 3126–3131, 2011.

[2] D. Guo, T. Fang, A. Moore, D. Brinkman, R. Akis, I. Sankin, C. Ringhofer, and D. Vasileska, *IEEE Journal of Photovoltaics*, Vol. 6 (5), pp. 1286-1291 (2016).

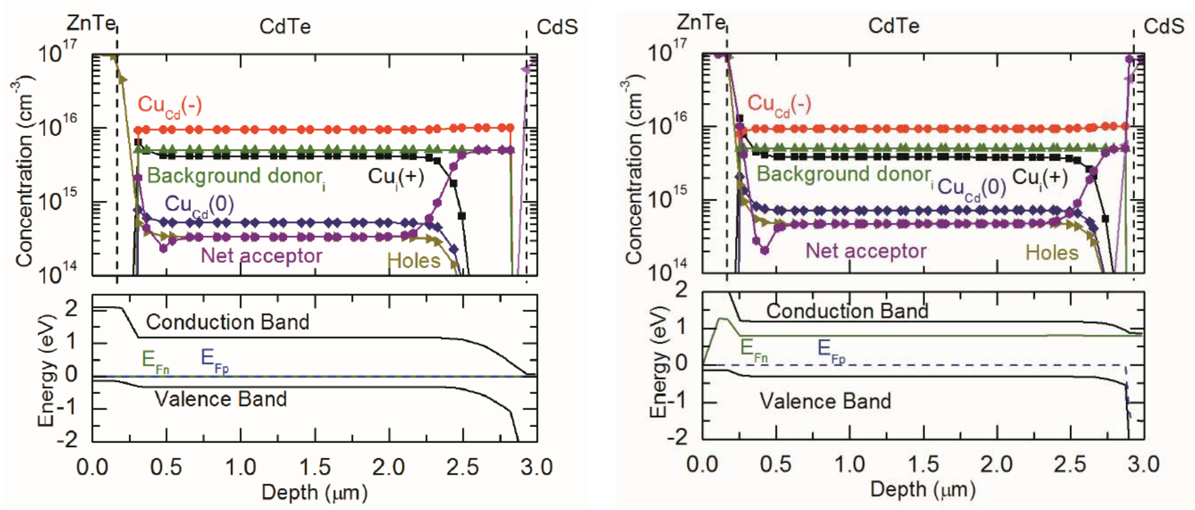

Figure 1: Simulated concentrations of defects and free carriers and device energy bands in the dark (left) and under light soak conditions (right) at 65°C.

Table I. List of stress conditions.

Soak	**Illumination**	**Voltage Bias**	**Mechanism**
A	1 Sun	0.8 V	Both
B	1 Sun	0.0 V	Passivation
C	Dark	0.8 V	Migration
D	Dark	0.0 V	None
E	1 Sun	0.8 V	No Migration
F	1 Sun	0.8 V	10^{-12} cm^2/s
G	1 Sun	0.8 V	10^{-13} cm^2/s

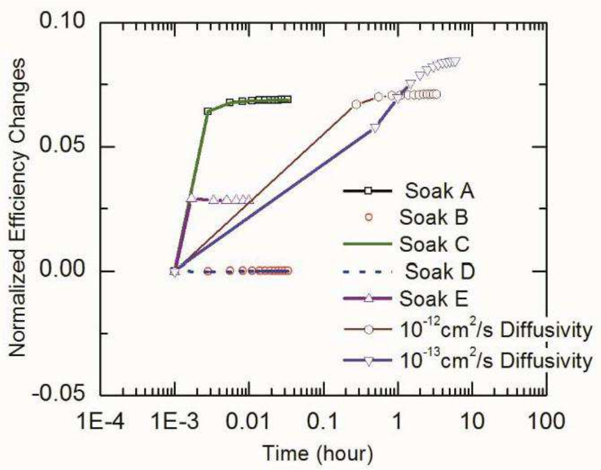

Figure 2: Device performance changes as a function of soaking time with various conditions.

P-2

Computational analysis of chemical mechanical polishing process for GaN substrate with step structure

Takuya Igarashi, Jingxiang Xu, Yusuke Ootani, Nobuki Ozawa, Momoji Kubo

Institute for Materials Research, Tohoku University, Sendai, Miyagi 980-8577, Japan
e-mail: takuya.igarashi@imr.tohoku.ac.jp

The chemical mechanical polishing (CMP) is a promising technique for efficient planarization of a GaN substrate which has high hardness and chemical stability. However, the detailed CMP mechanism remains unclear because the CMP process is a multi-physics phenomena including the atomic-level mechanical polishing and chemical reactions. A full understanding of the CMP mechanism is essential for designing efficient CMP process. In order to understand the atomic-level CMP mechanism, we developed a tight-binding quantum chemical molecular dynamics simulator[1] and apply it to the GaN CMP. In this study, we perform the CMP simulations of the GaN substrate with a step structure using a nano-diamond (ND) abrasive grain. We use OH radicals as the active species.

Firstly, we perform relaxation calculation of H_2O molecules on a clean GaN(0001) surface with a step structure while adding OH radicals. Wurtzite GaN has two types of steps, one is tri-coordinated N atom and the other is Ga-Ga dimer (Fig. 1). After the relaxation, the tri-coordinated N atoms are terminated by H atoms and the Ga-Ga dimers are dissociated by the OH termination and Ga-OH-Ga bonds are formed. Furthermore, topmost Ga atoms on the terrace are terminated by OH group (Fig. 2).

Secondly, we perform the CMP simulation on the relaxed GaN substrate with the nano-diamond (ND) abrasive grain (Fig. 3). Fig. 4 shows the snapshots of the CMP simulation. At first, the step-edges of Ga-OH-Ga bonds are distorted by the ND abrasive grain and N atom next to the Ga-OH-Ga bond forms a C-N-Ga bond between the GaN substrate and the ND abrasive grain (Fig. 4a). The N atom binding to the ND abrasive grain is removed from the GaN substrate and the O atom in the OH group at the surface is intruded into the vacant N site (Fig. 4b). Then, intrusion of O atom occurs at the other step-edge in the same process and the oxidation of the surface proceed (Fig. 4c). Moreover, the Ga atoms in the oxidized region at the step-edges bind to the ND abrasive grain and are removed from the GaN substrate with the sliding of the ND abrasive grain (Fig. 4d). In conclusion, we found that the removing of N atoms induces the oxidation of the GaN substrate and GaN CMP process proceed from the oxidized region at the step-edge.

[1] K. Kawaguchi, T. Aizawa, Y. Higuchi, N. Ozawa, M. Kubo, Proceeding of International Conference on Planarization/CMP Technology, 39-41 (2014)

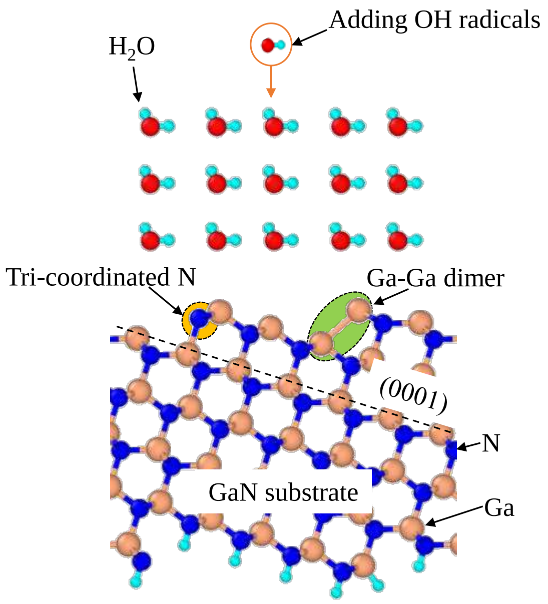

Fig.1: Calculation model of the GaN substrate with the step structure.

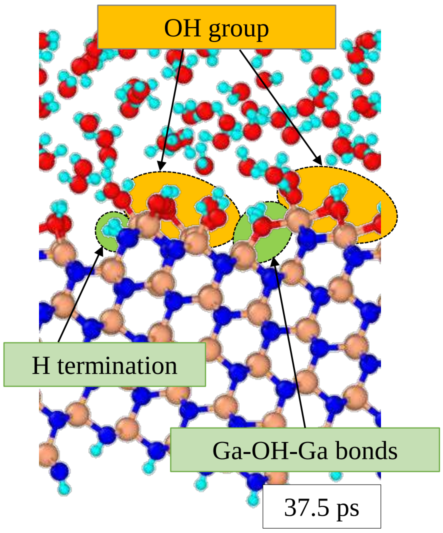

Fig.2: Snapshot of the relaxation calculation of the GaN substrate at 37.5 ps.

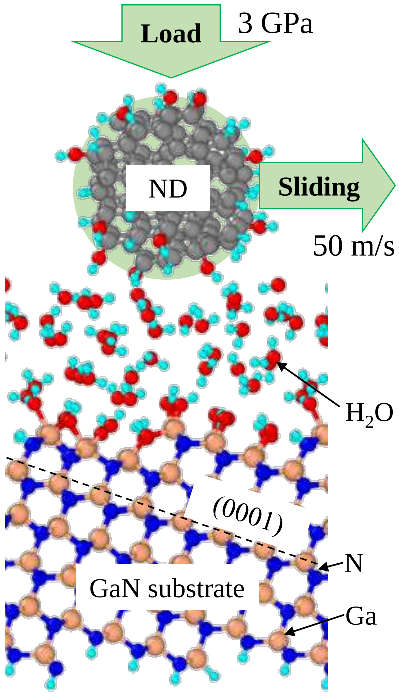

Fig.3: CMP simulation model of the GaN substrate with the step structure using the ND abrasive grain.

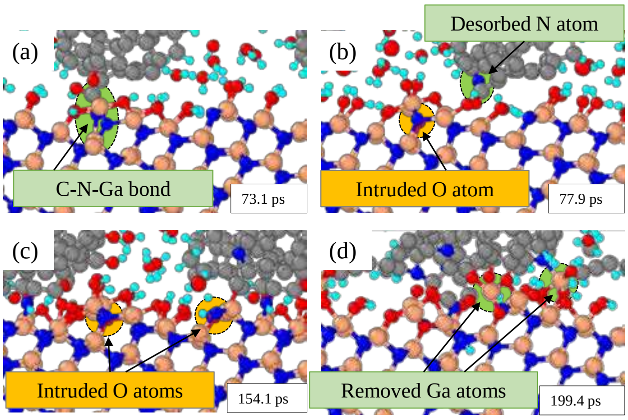

Fig.4: Snapshots of the CMP simulation of the GaN substrate at (a) 73.1 ps, (b) 77.9 ps, (c) 154.1 ps, and (d) 199.4 ps.

978-3-901578-31-1

P-3

Molecular Dynamics Study on Chemical Wear Process of Amorphous Silica in Humidity Environment

Naoki Takahashi, Yang Wang, Jingxiang Xu, Yusuke Ootani, Nobuki Ozawa
and Momoji Kubo

Institute for Materials Research, Tohoku University, Sendai, Miyagi 980-8577, Japan
e-mail: naoki.takahashi@imr.tohoku.ac.jp

Friction of silica is known to be important in nanotechnology fields such as NEMS/MEMS devices. It is reported that the wear amount of silica increases as humidity increases due to chemical reactions between silica and water molecules [1]. Thus, it is necessary to clarify the chemical wear mechanism to develop the device as expected. However, *in-situ* observation of atomic-scale phenomena in experiments is very difficult, and therefore simulations are required to elucidate the wear mechanism. In this study, sliding simulation of amorphous silica substrates with water molecules was carried out by molecular dynamics (MD) method with ReaxFF force field in order to investigate the influence of the chemical reactions on wear characteristics.

Fig. 1 shows the model of the sliding simulation. A normal load applied to the upper substrate along the $-z$ direction was maintained 3 GPa. The upper substrate was moved at a velocity of 100 m/s along the x direction. In order to reproduce humidity environment, 2000 water molecules were placed at the sliding interface.

The result of sliding simulation shows that the Si-O-Si bridge bonds connecting upper and lower substrates were formed around a contact area of the asperities (Fig. 2). Accordingly, the length of the Si-O bond in the amorphous silica substrate increased by the shearing force (Fig. 3a). Then, the H_2O molecule attacked the Si-O bond (Fig. 3a) and broke not the bridge bond but the Si-O-Si bond in the substrate through a hydrolysis reaction as $\text{Si-O-Si} + H_2O \rightarrow \text{Si-OH} + \text{Si-OH}$ (Fig. 3b). Subsequently, the shearing force caused another hydrolysis reaction between Si-O bond in the substrate and water molecule (Fig. 3b). Finally, Si atom dissociated from the amorphous silica substrate as $Si(OH)_4$ molecule (Fig. 3c). By the repeating these mechanisms, wear debris were formed as shown in Fig. 4. Therefore, we concluded that chemical wear at the sliding interface was due to the formation of Si-O-Si bridge bonds and hydrolysis reaction by water molecules.

[1] X. Wang et al., ACS Appl. Mater. Inter., **7**, 14785 (2015).

978-3-901578-31-1

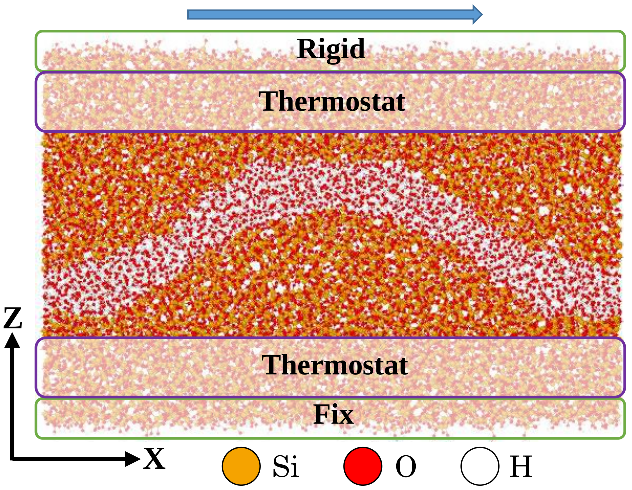

Fig.1: Model of Sliding Simulation.

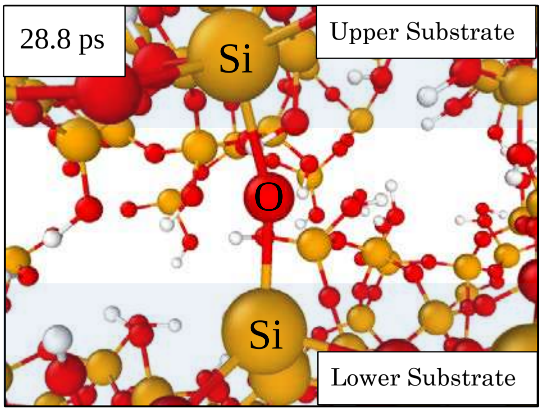

Fig.2 : Snapshot of Si-O-Si Bridge Bonds.

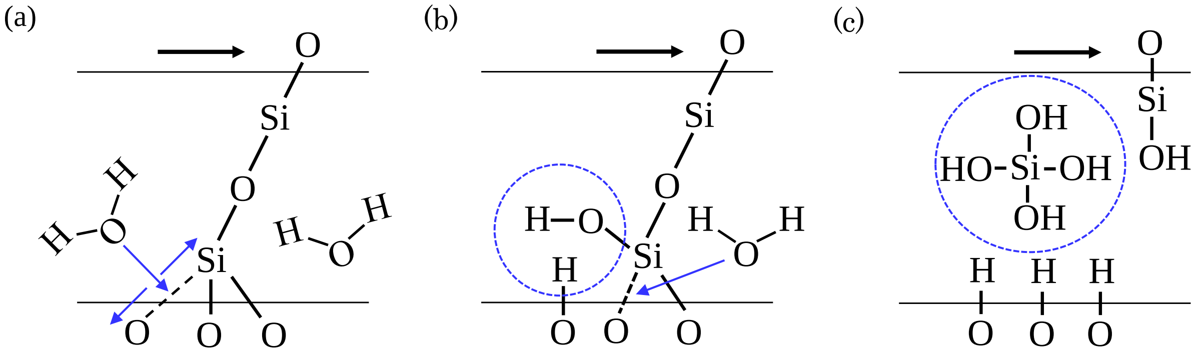

Fig.3: Mechanism of Hydrolysis Reaction between Amorphous Silica Substrate and Water Molecules.

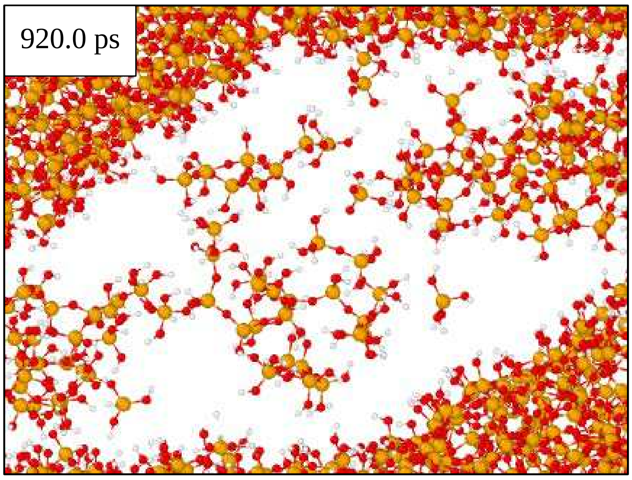

Fig.4: Snapshot of Wear Debris. (water molecules are not shown)

978-3-901578-31-1

P-4

Effect of Tribochemical Reactions on Super-Low Friction Properties of Carbon Nitride Thin Films as Investigated by Tight-Binding Quantum Chemical Molecular Dynamics Simulations

Miho Nakamura[1], Takeshi Tsuruda[1], Seiichiro Saito[2], Jingxiang Xu[1], Yusuke Ootani[1],
Nubuki Ozawa[1], Koshi Adachi[3], and Momoji Kubo[1]

[1] *Institute for Materials Research, Tohoku University, Sendai 980-8577, Japan*
[2] *Fracture and Reliability Research Institute, Graduate School of Engineering,*
Tohoku University, Sendai 980-8579, Japan
[3] *Department of Mechanical System Engineering, Graduate School of Engineering,*
Tohoku University, Sendai 980-8579, Japan
e-mail: miho.nakamura@imr.tohoku.ac.jp

Recently, much attention has been given to the ceramic lubricants for realizing super-low friction in automotive engines, aerospace instruments etc. Experimentally, it was discovered that carbon nitride (CNx) thin films give super-low friction. However, the super-low friction mechanism of CNx has not been clarified, experimentally. Therefore, in the present study we employed our tribology simulator based on the tight-binding quantum chemical molecular dynamics method to reveal the reason for the super-low friction mechanism of CNx.

Fig. 1 shows the snapshots of the friction simulation result under 1 GPa load. This simulation result shows low friction coefficient of 0.05. We clarified that hydrogen-hydrogen repulsion is the reason for the super-low friction. Next, we performed the friction simulation of CNx under water environments. Fig. 2 shows the snapshots of the simulation result under 1 GPa load. This result indicates the generation and evaporation of NH_3 molecules by the tribochemical reaction of CNx and water molecules. The NH_3 generation was also observed by the previous experiments. Here, we propose that the generation and evaporation of NH_3 molecules from the CNx thin films give low density diamond-like carbon (DLC) thin films. Low density DLC thin films have high Csp^2/Csp^3 ratio, leading to much graphite-structure. Therefore, we simulated the friction coefficient of high and low Csp^2/Csp^3 DLC (Fig. 3). Then, we revealed that high Csp^2/Csp^3 DLC gives lower friction coefficient because of the less generation of C-C bonds at the friction interface. Therefore, we concluded that generation and evaporation of NH_3 molecules from the CNx thin films give high Csp^2/Csp^3 DLC and then it leads to the super-low friction coefficient. Finally, we suggest that the acceleration of the tribochemical reactions is very effective to reduce the friction coefficient of CNx.

[1] M. I. De Barros Bouchet, J. M. Martin, J. Avila, M. Kano, K. Yoshida, T. Tsuruda, S. Bai, Y. Higuchi, N. Ozawa, M. Kubo, and M. C. Asensio, Sci. Rep., 7 (2017) 46394.

978-3-901578-31-1

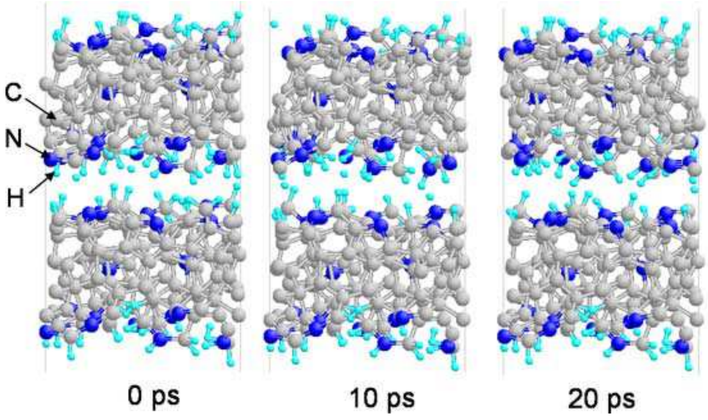

Fig. 1 Friction Simulation of H-terminated CNx

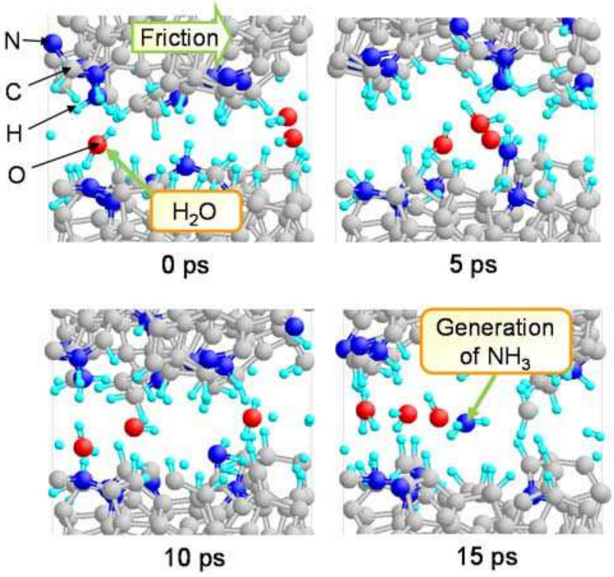

Fig.2 Friction Simulation of H-terminated CNx under water environments

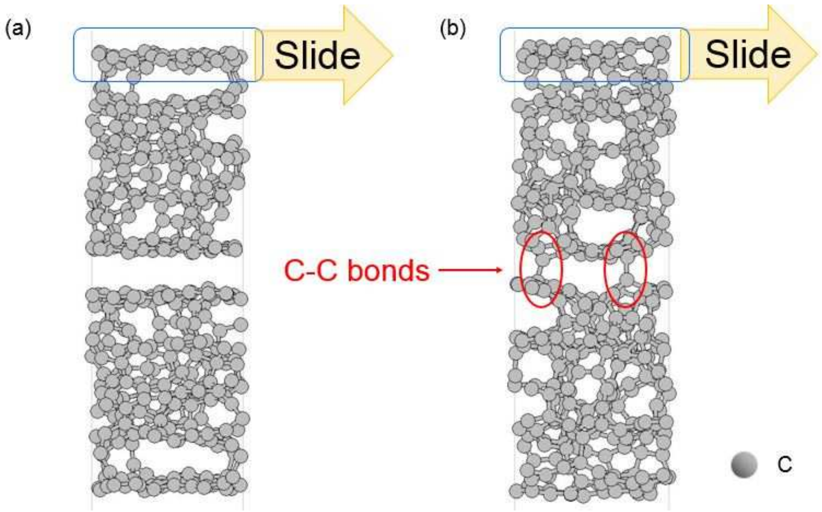

Fig. 3 Friction Simulation of (a) High Csp^2/Csp^3 DLC and Low Csp^2/Csp^3 DLC

P-5

Oxidative Degradation of Carbon Nanotubes and Extraction of Encapsulated 1D Materials

Haruka Omachi[1,2], Miho Yamagishi[1], Masachika Kato[1], Ryo Kitaura[1], and Hisanori Shinohara[1,3]

[1] *Department of Chemistry, Graduate School of Science, Nagoya University, Nagoya 464-8602, Japan*
[2] *Research Center for Materials Science, Nagoya University, Nagoya, 464-8602, Japan*
[3] *Institute for Advanced Research, Nagoya University, Nagoya, 464-8602, Japan*
e-mail: noris@nagoya-u.jp

Carbon nanotubes (CNTs) have cylindrical structure which provide an ideal cavity to create one-dimensional (1D) nanomaterials. Recently, we have established synthesis of thin single-wall BN-nanotubes and diamantane polymers inside CNT [1,2]. However, since the synthesized 1D materials are remained inside CNTs, it is hard to reveal the actual properties of 1D materials. Hence, removal of the CNT shell is required to isolate encapsulated 1D nanomaterials. In this research, we developed oxidative decomposition of CNTs under mild conditions.

We initially carried out the optimization of reaction conditions. After screening of a lot of oxidant, it was found that some of suitable organic oxidants were effective and the decomposition of CNTs proceeded even at room temperature. With the reaction progress, absorption spectra of CNTs were gradually decreased (Figure 1). Most of peaks were finally disappeared after 24 hours. Interestingly, D/G ratio was improved in early stage of the reaction (Figure 2). The decomposition was indicated to have high selectivity, as the reaction start from defects of the CNT shells. We then demonstrated the extraction of C_{60} fullerene from C_{60}@SWCNT nano-peapod by using this CNT decomposition technology (Figure 3).

We established decomposition of CNTs with a suitable organic oxidant. Reaction proceeded at room temperature with the high selectivity. Extraction of encapsulated fullerenes inside CNTs was also realized. Isolation of other encapsulated 1D nanomaterials will be accomplished in near future.

[1] R. Nakanishi, *et al.*, *Sci. Rep.* **3**, 1385 (2013).
[2] Y. Nakanishi, *et al.*, *Angew. Chem., Int. Ed.*, **54**, 10802 (2015).

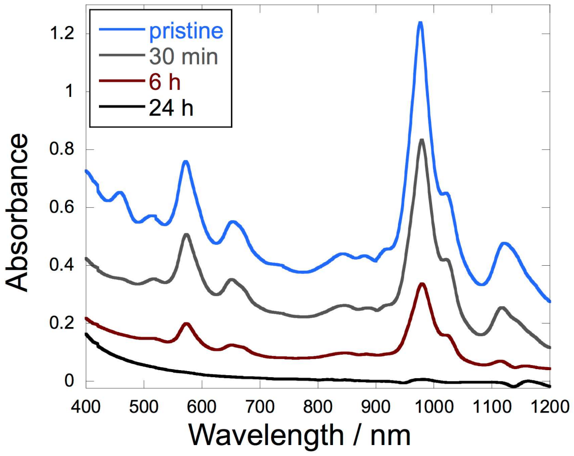

Fig.1: UV-Vis-NIR spectra of initial CNT dispersion and reacted dispersion at each reaction time (30 min, 6 h, and 24 h).

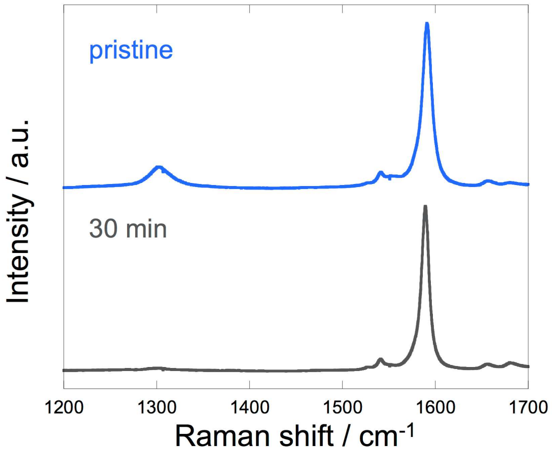

Fig.2: Raman spectra of initial CNT dispersion and reacted dispersion for 30 min.

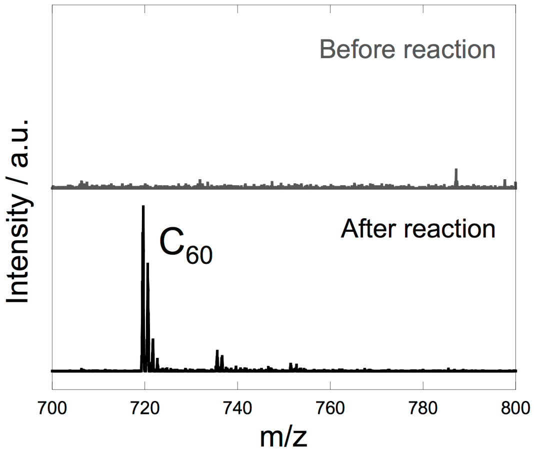

Fig.3: Mass spectra of toluene extraction before and after the decomposition treatment of C_{60}@SWCNT..

978-3-901578-31-1

P-6

Tunnel barrier formation in suspended multi-walled carbon nanotubes by Ga focused ion beam irradiation.

Tomohiro Yamaguchi[1], Norizzawati Mohd Ghazali[1,2], Hiroshi Tomizawa[1], Katsuya Suzuki[1,3],
Noriyuki Hagiwara[1,3], Seiji Akita[4], and Koji Ishibashi[1,2,3,5]

[1] *Advanced Device Laboratory, RIKEN, 2-1 Hirosawa, Wako, Saitama 351-0198, Japan*
[2] *Malaysia-Japan International Institute of Technology, Universiti Teknologi Malaysia, Malaysia*
[3] *Graduate School of Advanced Integration Science, Chiba University, Chiba, Japan*
[4] *Department of Physics and Electronics, Osaka Prefecture University, Osaka, Japan*
[5] *RIKEN Center for Emergent Matter Science (CEMS), Saitama, Japan*
e-mail: tyamag@riken.jp

Carbon nanotubes have attracted a great deal of attention as a material for quantum dot (QD)-based devices owing to their small diameter. One of the key techniques indispensable for fabrication of functional nanodevices based on QDs is to form the desired tunnel barriers with high controllability and reproducibility. The fabrication and characterization of tunnel barriers formed in MWNTs on substrate by Ar atom beam [1] or Ga focused ion beam (FIB) [2] irradiation technique have been studied. In this presentation, we report tunnel barrier formation in MWNTs suspended between metal electrodes by irradiation of Ga FIB.

Suspended MWNT samples were prepared by the mechanical transfer technique. The two-terminal resistance before the irradiation was in range of 10-20 kΩ at room temperature for all samples. We investigated the ion dose and the nanotube diameter dependence of the resistance change after irradiation. The resistance change increases with increasing Ga ion dose. Under the same dose, the resistance change is strongly dependent on the nanotube diameter. The resistance after irradiation is proportional to $1/d^2$, where d is the nanotube diameter. To estimate the height of formed tunnel barriers, we study temperature dependence of current under low bias voltage (Arrhenius plot) and voltage dependence (Fowler-Nordheim plot) at low temperature. It is shown that the barrier height has a positive correlation with the resistance at room temperature that can be controlled by the ion dose and the nanotube diameter.

Our results show that we can form tunnel barriers in MWNTs with enough controllability and reproducibility, and demonstrate the potential of our techniques to fabricate complex QD-based nanodevices.

[1] H. Tomizawa et al., J. Appl. Phys. **118**, 044306 (2015).
[2] H. Tomizawa et al., Nanotechnology **28**, 1 (2017)

P-7

High thermal conductivity of carbon nanotube sheets for future thermal interface materials

Shinichi Hirose[1], Daiyu Kondo[1], Koichi Suzuki1[1] Seiki Sakuyama[1] and Taisuke Iwai[1]

[1] *Devices & Materials Laboratories, Fujitsu Laboratories Ltd., 10-1 Morinosato-Wakamiya,*
Atsugi, Kanagawa 243-0197, Japan
e-mail: hirose.shinichi@jp.fujitsu.com

Thermal interface material (TIM) which are used to connect thermally between a heat spreader and a processor tip with carbon nanotubes (CNTs) is a good candidate of next generation TIM due to their high performance regarding thermal and mechanical properties. Actually, individual CNTs including single-walled CNTs and multi-walled CNTs have extremely high thermal conductivity around 3000 W/mK [1, 2], which were synthesized at a relatively high temperature around several thousands degrees Celsius (ºC) by arc discharge method. On the other hand, CNT-TIM composed of vertically-aligned CNTs does not always show high thermal conductivity due to their poor density and low quality. As-grown vertically-aligned CNTs are utilized to be directly applied to CNT-TIM after growth on a substrate at a relatively low temperature by chemical vapor deposition (CVD). Therefore, one cannot obtain vertically-aligned CNTs with higher quality at the stage of CNT growth by CVD method around 650ºC to obtain vertically-aligned CNTs on a substrate, although higher temperature during CVD process leads to higher quality of CNTs.

In this paper, we demonstrated annealing process to improve a quality of CNT sheets and compare thermal conductivity of CNT sheets with indium films, which are generally used as TIM. After annealing above 2000ºC, SEM images (figure 1) indicated that morphology of CNT sheets composed of vertically-aligned CNTs seemed to be unchanged. However, it was clear that the Raman spectra of CNT sheets was found to be improved better than that before annealing shown in figure 2 and 3. Furthermore, the thermal conductivity of CNT sheets including the thermal resistance at the interface was estimated to be above 80 W/mK after 2600 ºC, and better than that of indium film. This remarkable improvement of the thermal conductivity might be originated from improvement in quality of CNTs, which was supported by the Raman measurement. Furthermore, CNT sheets showed much higher mechanical properties than that before annealing. Our results indicate that CNT sheets after annealing above 2000ºC is really promising for future TIM.

[1] J. Hone, M. Whitney, C. Piskoti and A. Zettl, Phys. Rev. B, **59**, R2514 (1999).

[2] P. Kim, L. Shi, A. Majumdar and P.L. McEuen, Phys. Rev. Lett., **87**, 215502 (2001).

978-3-901578-31-1

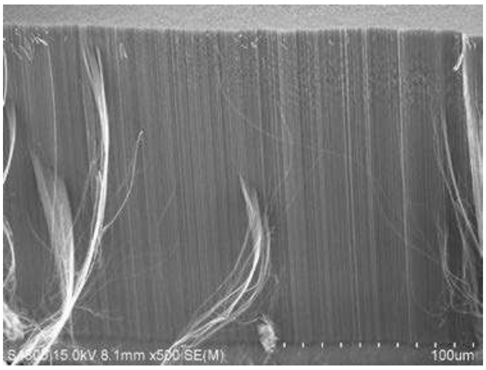

Fig.1(a): SEM images of CNT sheets after annealing process at 2600 ℃.

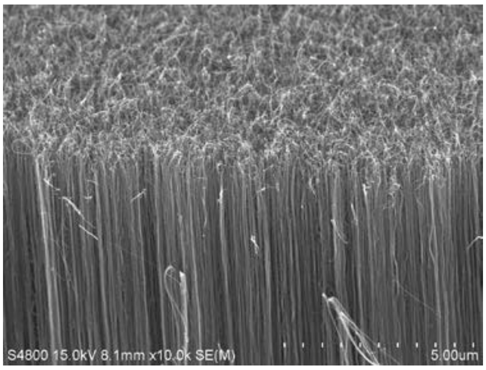

The Fig.1(b): SEM images of CNT sheets after annealing process at 2600 ℃.

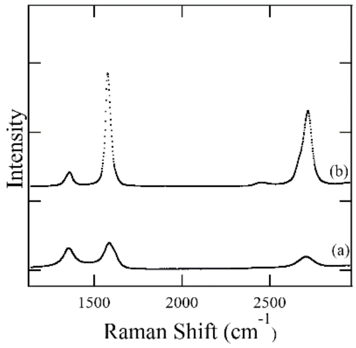

Fig.2: Raman spectra of CNT sheets (a) before and (b) after annealing process at 2600 ℃.

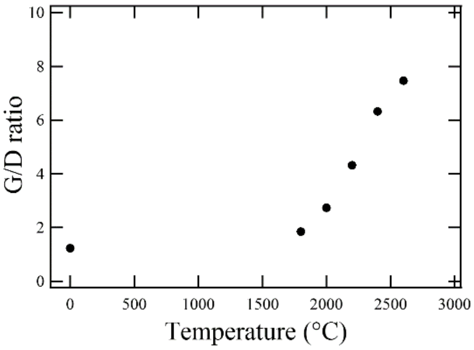

Fig.3: G/D ratios of CNT sheets dependent on annealing temperatures.

P-8

Geometric structures of Al nanoparticles adsorbed on graphene under an external electric field

Manaho Matsubara[1] and Susumu Okada[1]

[1] *Graduate School of Pure & Applied Sciences, University of Tsukuba, Tsukuba 305-8571, Japan*
e-mail: mmatsubara@comas.frsc.tsukuba.ac.jp

Graphene has been receiving a lot of attention from not only the low-dimensional science but also the electronic device engineering due to its unique structural and electronic properties. In addition to the intrinsic unique electronic properties of graphene, graphene exhibits further variation in their electronic structure by forming hybrid structures with foreign materials and external environments, owing to the modulation of the electrostatic potential on graphene by these foreign materials. An external electric field also modulate the electronic structure of graphene and their hybrids. In the electronic devices, the hybrid structures of graphene with foreign materials, such as environmental nanoparticles, and the external electric field are essential for controlling their functionalities. In our previous work [1], hybrids such as charged nanoparticles adsorbed on the graphene surfaces cause the peculiar electronic properties under the carrier injection by the gate electrode. Thus, in this work, we aim to elucidate geometric structures of Al nanoparticles adsorbed on graphene under the excess electron or hole injected by a counter electrode simulating graphene-based FET structures, using the density functional theory combined with the effective screening medium method (Fig.1).

Our calculations showed that the stable position of Al nanoparticles under the excess electrons/holes are sensitive to the carrier species and their relative arrangement with respect to the counter electrode (Fig.2). The electron injection in hybrids increase the equilibrium spacing between the nanoparticle and graphene, irrespective of the relative arrangement of nanoparticle to the electrode. In contrast, for the hole doping, the equilibrium spacing monotonically decrease with increasing the number of hole when the nanoparticle is situated at the opposite surface of graphene to the electrode, while it has a minimum value under the hole concentration when the nanoparticle is sandwiched between graphene and electrode (Fig. 3). The distribution of the accumulated carrier also depends on the mutual arrangement of the nanoparticles to the electrode (Fig.4).

[1] M. Matsubara, S. Okada, Appl. Phys. Express **10**, 025101, (2017).

978-3-901578-31-1

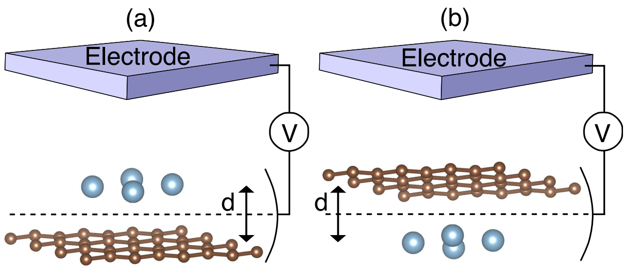

Fig.1: A structural model of Al nanoparticles adsorbed on graphene with the FET structure. Large and small balls denote Al and C atoms, respectively. Slabs situated above the hybrid consisting of graphene and Al nanoparticle denote the counter electrodes which is simulated by the ESM.

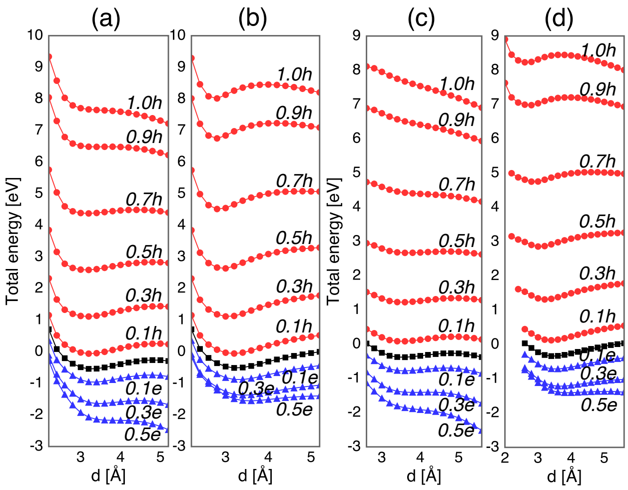

Fig.2: Total energies of Al_4 adsorbed on graphene with (a) electrode-Al-graphene and (b) electrode-graphene-Al arrangements as a function of the spacing between Al_4 and graphene with carrier concentrations from 0.5e to 1.0h. Total energies of Al_3 adsorbed on graphene with (c) electrode-Al-graphene and (d) electrode-graphene-Al arrangements as a function of the spacing between Al_3 and graphene with carrier concentrations from 0.5e to 1.0h. In each panel, filled squares, circles, and triangles denote the total energies of neutral, hole-doped, and electron-doped conditions, respectively.

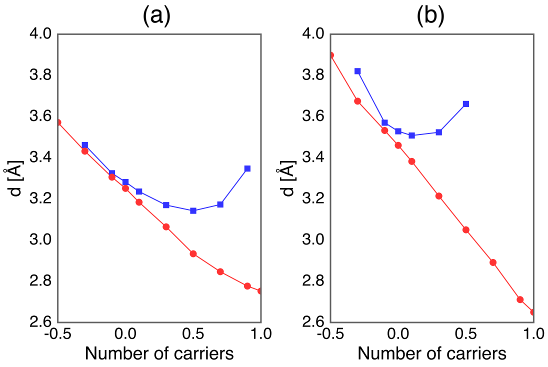

Fig.3: Equilibrium spacing between Al nanoparticles and graphene as a function of the carrier concentration for (a) Al_4 and (b) Al_3 nanoparticles. In each panel, the circles and squares denote the spacing with the electrode-graphene-Al and electrode-Al-graphene arrangements.

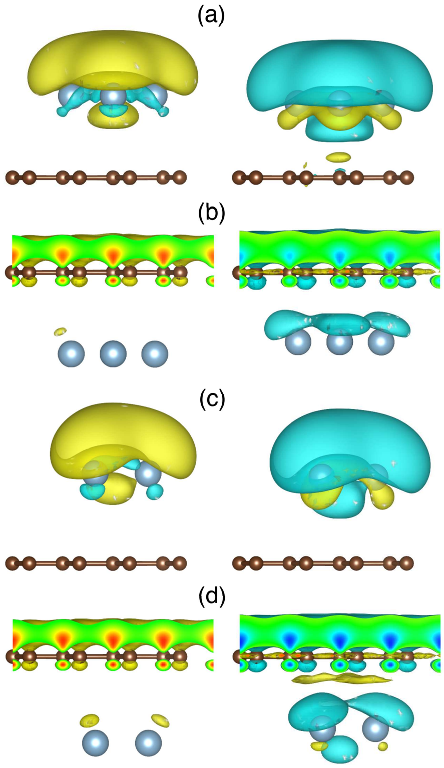

Fig.4 Isosurfaces of the distribution of the accumulated electron and hole by the gate electrode in graphene-Al_4 hybrids in which the Al_4 is adsorbed (a) above and (b) below the graphene layer to the electrode. Isosurfaces of the distribution of the accumulated electron and hole by the gate electrode in graphene-Al_3 hybrids in which the Al_3 is adsorbed (c) above and (d) below the graphene layer. In each figure, the left and right panels show the isosurfaces under 0.3e and 0.5h doping, respectively. Yellow and blue isosurfaces denote the region where the electron and hole increase, respectively. Small and large balls denote C and Al atoms, respectively.

P-9

Coexistence of Dirac cones and Kagome flat bands in porous graphene

Mina Maruyama[1], Nguyen Thanh Cuong[2], and Susumu Okada[1]

[1] *Graduate School Pure and Applied Sciences, Univ. Tsukuba, 1-1-1 Tennodai, Tsukuba, Ibaraki 305-8571, Japan*
[2] *International Center for Young Scientist (ICYS) and International Center for Materials Nanoarchitectonics (MANA), National Institute for Materials Science (NIMS), 1-1 Namiki, Tsukuba, Ibaraki 305-0044, Japan*
e-mail: mmaruyama@comas.frsc.tsukuba.ac.jp

Polymerization and oligomerization of hydrocarbon molecules can provide structurally well-defined π electron network. The electronic structures of such polymers and oligomers strongly depend on the combinations of hydrocarbon molecules and polymer chains. Phenalenyl ($C_{13}H_9$ consisting three benzene rings with D_3 symmetry) is one possible candidate as a constituent unit of such magnetic materials. The three-fold symmetry of the phenalenyl network causes honeycomb networks of radical spins or non-bonding state to be distributed on phenalenyls with appropriate interconnect units, leading to interesting electron systems. In this work, we aim to theoretically investigate the electronic and magnetic properties of the possible structures of 2D porous hydrocarbon networks of sp^2 C obtained by assembling phenalenyl molecules in a hexagonal manner with phenyl interconnects using density functional theory with the generalized gradient approximation.

Figure 1 shows the optimized structures of 2D porous hydrocarbon networks consisting of phenalenyl connected via phenyl under the hexagonal cell parameter of 1.94 nm. We find that the phenalenyl units retained a planar structure as their stable conformations. As illustrated in Fig. 1, two phenalenyl units per unit cell form a hexagonal lattice in which phenyl units connect adjacent phenalenyl units through covalent bonds like those of graphene. Simultaneously, three phenyl units form a Kagome lattice in which phenalenyl acts as an interunit bond. As shown in Figure 2, the porous hydrocarbon sheet is a zero-gap semiconductor with a pair of linear dispersion bands at E_F. In addition to the linear dispersion bands, we find three bunched states just above and below the linear dispersion bands. One of the three branches exhibits the perfect flat band nature while the remaining two have finite band dispersion, being consistent with their Kagome band structure. Because of narrow band width of the Dirac cones, the sheet exhibits spin polarization localized on phenaleneyl parts. Figure 3 illustrates spin densities of network. The polarized radical spin on the phenaleneyl unit has the antiferromagnetic (AF) and ferromagnetic (F) states, and the AF state is more stable than the F state by 13.9 meV per unit cell.

978-3-901578-31-1

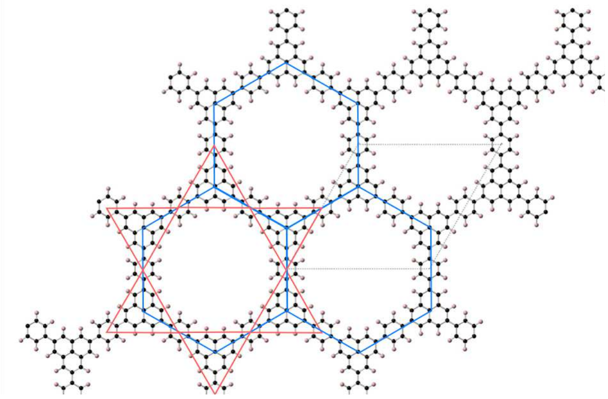

Fig.1: Optimized structures of porous graphene consisting of phenalenyl and phenyl.

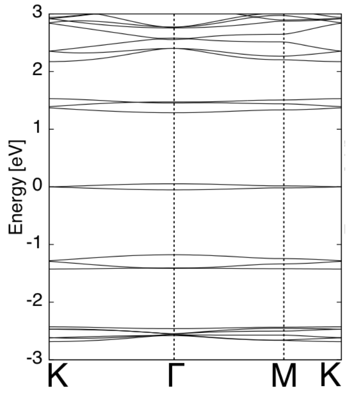

Fig.2: Electronic structures of porous graphene consisting of phenaleneyl and pheyl.

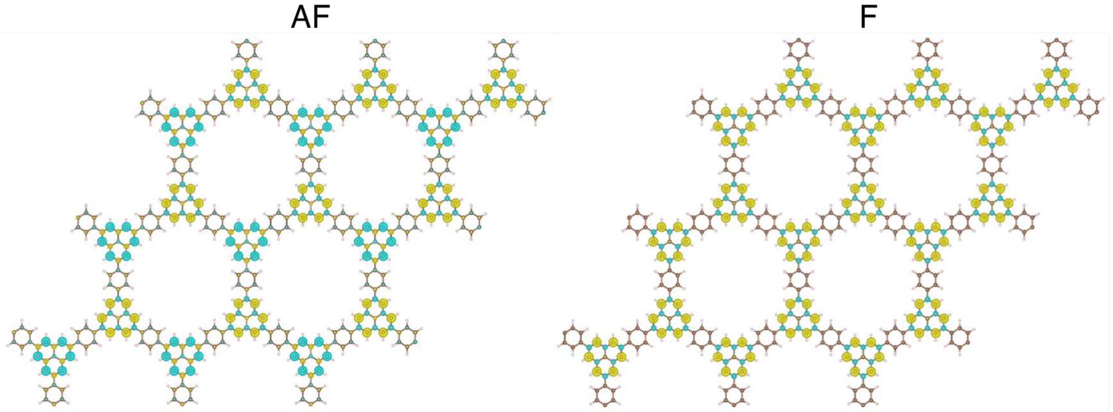

AF

F

Fig.3: Spin densities of porous graphene consisting of phenalenyl and phenyl.

P-10

Electrostatic potential properties of edge-functionalized graphene nanoribbon under the external electric field

Yanlin Gao and Susumu Okada

Graduate School of Pure and Applied Sciences, University of Tsukuba, Tsukuba, Ibaraki 305-8571, Japan
e-mail:ylgao@comas.frsc.ac.jp

Graphene has attracted a great deal of attention in the fields of nanoscience and nanotechnology due to its peculiar physical property and extensive application prospects. With high aspect ratio, high electrical conductivity, and high chemical stability, graphene is thought to be a promising candidate for a field emission source in field emission devices. In the ambient condition, edges of graphene are usually terminated by functional groups, depending on the environment. In this work, we investigated the electrostatic properties of edge-functionalized zigzag graphene nanoribbon (ZGNR) by ketone, aldehyde, hydrogen or carboxyl groups to elucidate how the edge functional groups affect the field electron emission from the functionalized edges, using the density functional theory (DFT) combined with the effective screening medium method.

Figure 1(a) shows the structure model for simulating the field emission from the edges of functionalized ZGNR. The ribbons are located in front of the planar electrode with 5 Å vacuum spacing. Our DFT calculations show that functional groups affect the critical electric field resulting in the field emission at which the electrostatic potential at the electrode crosses the Fermi level [Fig. 1(b)]. Figure 2 shows the critical electric field as a function of the work function of functionalized zigzag edges. The critical electric filed is proportional to the work function of these functionalized edges except the hydroxylated edge. The hydroxylated edge possesses the highest critical electric field, despite the edge possesses the smallest work function among the edges studied here. To clarify the physical origin of the anomalous behavior of hydroxylated edge, we give contour and vector plots of electrostatic potential and electric field for functionalized edges of these graphene nanoribbons (Fig. 3). The electric field concentrates at the functionalized edge of graphene, and the local the field distribution depends on the functional group species. For the hydroxylated edge, we find a potential peak outside the edge and in the vacuum region, leading to an opposite electric field to the external electric field in the vacuum region between the potential peak and the graphene edge. Thus, the potential peak in vacuum region causes the large critical electric field for field emission, although the hydroxylated edge possesses the smallest work function.

978-3-901578-31-1

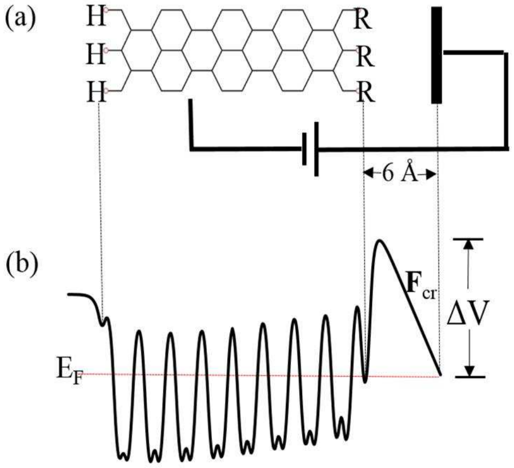

Fig. 1: (a) A structural model and (b) schematic diagram of the electrostatic potential for functionalized graphene nanoribbon under the electric field..

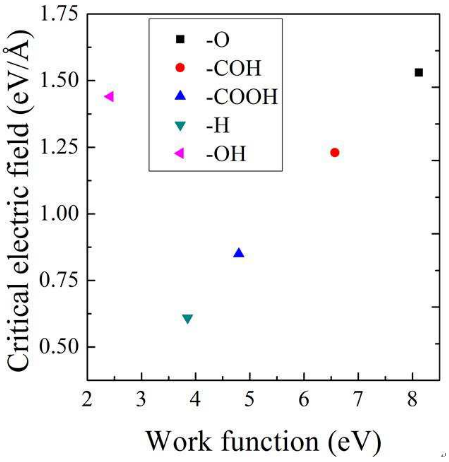

Fig. 2: Critical electric field for the electron emission from edge-functionalized ZGNR as a function of work function.

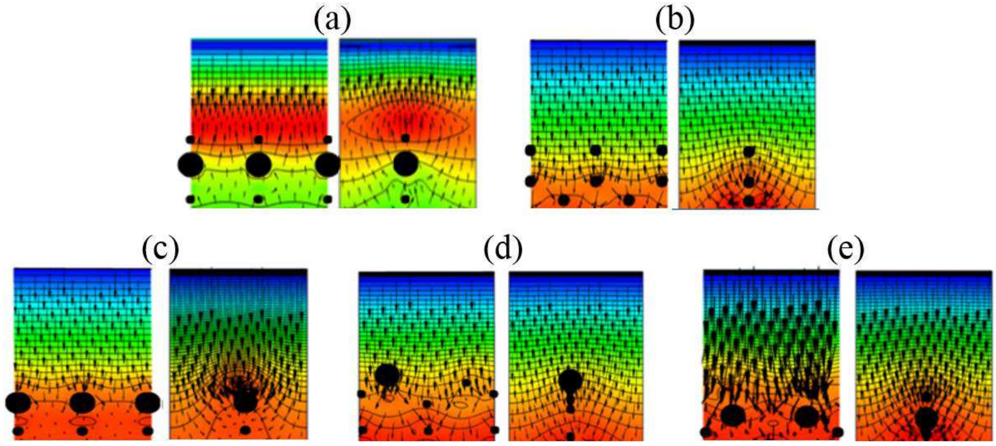

Fig.3: (a) Contour and vector plots of electrostatic potential and electric field, respectively, of ZGNRs functionalized by (a) hydroxyl, (b) H, (c) ketone, (d) aldehyde, and (e) carboxyl functional groups under the critical electric field for the electron emission. The left and right panels in each figure correspond to the parallel and vertical planes of ZGNRs, respectively.

P-11

Bottom-up approach for edge-fluorinated graphene nanoribbons

Hideyuki Jippo[1,2], Junichi Yamaguchi[1,2], Shintaro Sato[1,2], Hironobu Hayashi[3], Hiroko Yamada[3], Mari Ohfuchi[1,2]

[1] *Fujitsu Laboratories Ltd. and* [2]*Fujitsu Limited, 10-1 Morinosato-Wakamiya, Atsugi, Kanagawa 243-0197, Japan*
[3] *Graduate School of Materials Science, Nara Institute of Science and Technology (NAIST), 8916-5, Takayama-cho, Ikoma, Nara 630-0192, Japan*

e-mail: jippo.hideyuki@jp.fujitsu.com

For graphene-based electronics, it is important to modulate the electronic properties of graphene nanoribbons (GNRs). The modulation can be realized by, for instance, chemical modification of the edges of the GNRs. A bottom-up synthesis [1] is one of the promising approaches for obtaining edge-functionalized GNRs, since the precursor molecules define the structures of the GNRs with the atomic precision. In this study, we have attempted edge-fluorination of GNRs using the bottom-up approach [2].

Figure 1 shows an expected reaction scheme from precursor molecules of HFH-DBTA to HFH-7AGNRs via HFH-polyanthrylenes. However, our scanning tunneling microscopy (STM) and X-ray photoelectron spectroscopy (XPS) measurements as shown in Fig. 2 indicate that the GNRs fabricated on Au(111) surface have no fluorinated edges, while the C-F bonds are still observed in the polyanthrylenes. The defluorination occurred during the cyclodehydrogenation process from the polyanthrylenes to the GNRs.

We performed the first-principles calculations to reveal the mechanism of the dissociation of the strong C-F bond. Figure 3 shows the most stable geometry of the HFH-polyanthrylene on Au(111). We have found that the activation energies E_a, which are calculated using the nudged elastic band method, are approximately 80 kJ/mol and 40 kJ/mol for the reactions of I0→I1 and I1→I2 (Fig. 4, 5), respectively. These reactions can proceed at the annealing temperature in our experiments. We have also found that the intermediated H-C-F structure significantly weaken the C-F bond. The E_a of the benzene with the H-C-F structure is lower by ~400 kJ/mol than that of the fluorobenzene (Fig. 6). The defluorination can proceed via the H-C-F structure at the edge during the cyclodehydrogenation.

These results suggest that it is important to design precursors considering the structural transformation during the reaction process for synthesizing edge-functionalized GNRs.

[1] J. Cai et al., Nature **466**, 470 (2010). [2] H. Hayashi et al., ACS Nano **11**, 6204 (2017).

This research was supported by JST CREST Grant Number JPMJCR15F1, Japan.

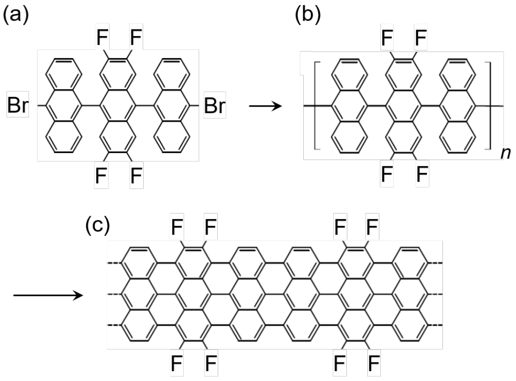

Fig.1: Expected reaction scheme from (a) HFH-DBTA to (c) HFH-7AGNR via (b) HFH-polyanthrylene.

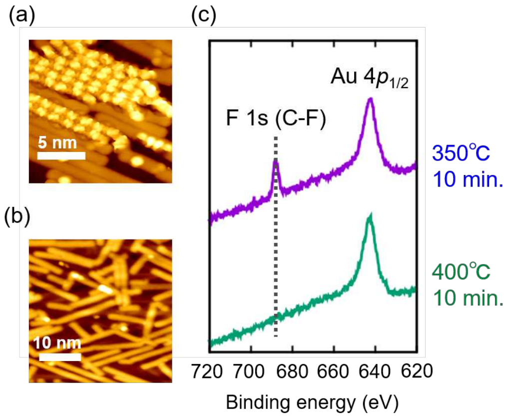

Fig.2: STM topographic images for HFH-DBTA deposited on Au(111) after annealing at (a) 350 ℃ and (b) 400 ℃ for 10 min. The bright aligned periodic protrusions and the dark ribbons indicate the polyanthrylenes and the GNRs, respectively. (c) XPS spectra of HFH-DBTA deposited on Au(111) after annealing at two temperatures.

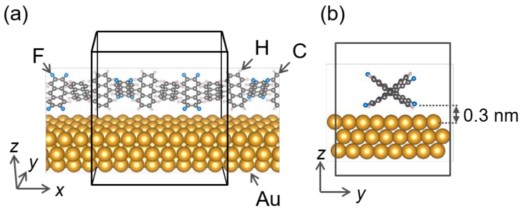

Fig.3: (a) Oblique and (b) side views of the calculated structural model of the HFH-polyanthrylene on three Au(111) layers. The region enclosed by the black lines represents the unit cell.

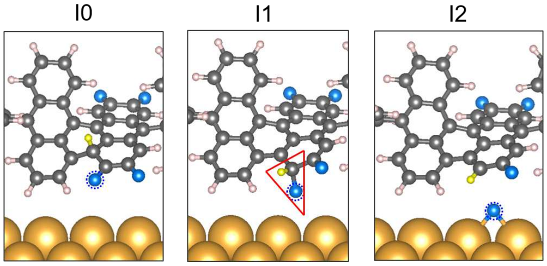

Fig.4: Optimized geometries of the intermediate states of I0, I1, and I2 along the C-F dissociation path. The migrating H atom and dissociating F atom are represented by the yellow sphere and the blue dotted circle, respectively. The red triangle in the I1 state indicates the H-C-F structure.

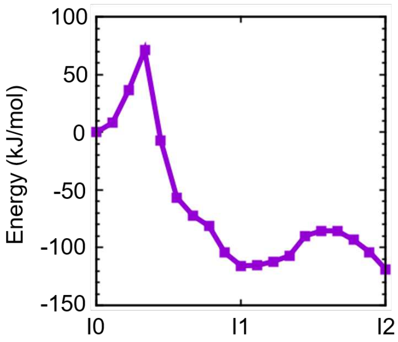

Fig.5 Minimum energy path of the reactions of I0→I1→I2.

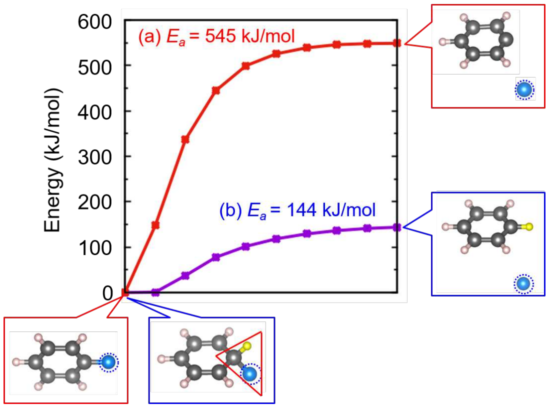

Fig.6: Minimum energy path of the C-F dissociation from (a) the fluorobenzene and (b) the benzene with the H-C-F structure.

P-12

High Thermoelectric Power in B_3N_3-doped Graphene

Nguyen Thanh Cuong[1], Susumu Okada[2]

[1] *International Center for Young Scientists, National Institute for Materials Science, Tsukuba, 305-0044, Japan*
[2] *Graduate School of Pure and Applied Sciences, University of Tsukuba, Tsukuba, 305-8571, Japan*
e-mail: NGUYEN.Thanhcuong@nims.go.jp

Thermoelectric energy conversion is one of the important and effective energy harvesting technology to convert waste heat into electric power. The efficiency of a thermoelectric materials is determined by the dimensionless figure-of-merit $ZT=S^2\sigma T/(K_e+K_{ph})$, when S, σ, T, K_e, K_{ph} are the Seebeck coefficient, the electrical conductivity, the absolute temperature, the electronic and phonon thermal conductivity, respectively. A promising strategy for the enhancement of thermoelectric performance is reducing the dimensionality of materials that could remarkably enhance the Seebeck coefficient due to the quantum confinement effect [1]. In this work, we demonstrate that atomic-layer materials with high Seecbeck coefficient ($\sim 10^3$ μV/K) could be achieved by embedding B_3N_3 into graphene.

Based on first-principles density functional theory simulations, we design novel B_3N_3-doped graphene sheet through the polymerization of BN-phenanthryne molecules, as shown in Figure 1. By embedding B_3N_3 into the hexagonal carbon network, the B_3N_3-doped graphene sheet exhibits semiconducting characteristics with a direct band-gap of 0.64 eV (Figure 2). On the other hand, we also find that B_3N_3-doped graphene exhibits high Seebeck coefficient of 10^3 (μV/K) at room temperature (Figure 3) that could be ascribed to the unique density of states. In addition, using relaxation time of electron $\tau=1.3\times10^{-13}$ (s) [2], the highest thermopower factor ($S^2\sigma$) of this atomic-layer material is estimated about 5.8 (mW/mK^2) (Figure 4), comparable to that of commercial Bi_2Te_3 (4 mW/mK^2). These findings demonstrate that B_3N_3-doped graphene is a promising atomic-layer material for thermoelectric devices.

[1] L. D. Hicks, M. S. Dresselhaus, Phys. Rev. B, **47**, 12727 (1993).

[2] P. H. Jiang et al., Carbon, **113**, 108 (2017).

978-3-901578-31-1

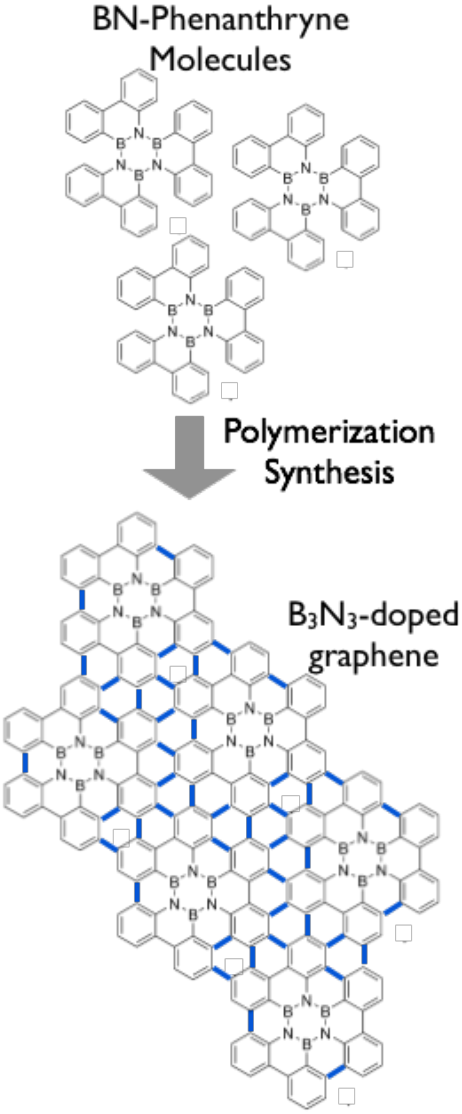

Fig.1: The diagram of B_3N_3-doped graphene sheet by covalent assembling of BN-Phenanthryne molecules.

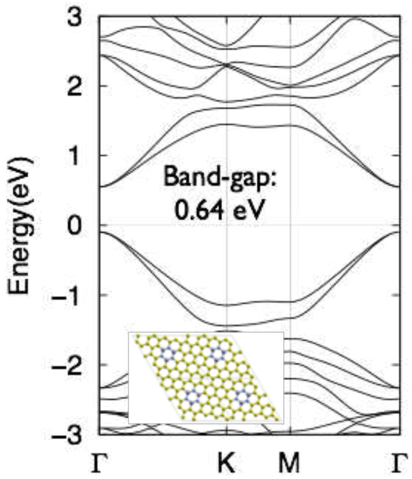

Fig 2: Energy band structure of B_3N_3-doped graphene.

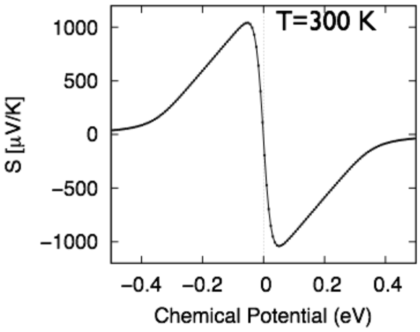

Fig 3: The in-plane Seebeck coefficient at 300 K as a function of the chemical potential for B_3N_3-doped graphene.

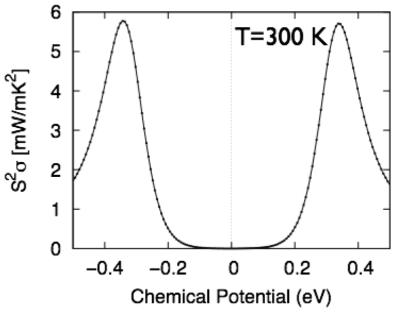

Fig 4: The in-plane thermopower factor at 300 K as a function of the chemical potential for B_3N_3-doped graphene.

P-13

Controllable tunneling of electron and hole in van der Waals assembly

Dongil Chu, Chang-Soo Park, and Eun Kyu Kim

Quantum-Function Research Laboratory and Department of Physics, Hanyang University,
Seoul 04763, South Korea
e-mail: ek-kim@hanyang.ac.kr

Recently, the artificial van der Waals (vdW) heterostructures made from semiconducting transition-metal dichalcogenides (TMDs) and other ultrathin 2D crystals have emerged as promising materials. The discoveries of that have led to the diverse interesting and novel physical phenomena [1]. Assembling these vdW materials into three-dimensional (3D) heterostructures with atomic precision enables the creation of a host of novel functional devices via layer-by-layer construction with TMDs possessing different band gaps. Indeed, there are many possible combinations by utilizing hexagonal boron nitride (hBN), graphene, and tungsten disulfide (WS_2), etc., to build electronic and optoelectronic devices, such as binary TMD heterointerfaces for p-n junction diodes [2]. It is primarily favorable to design new transistor architectural by assembling diverse vdW materials into 3D with superior performance in terms of on/off ratio, as well as subthreshold swing.

In this study, we introduce a new conceptual tungsten disulfide-based tunneling device, namely “carristor”. By combining a thin hexagonal boron nitride tunnel barrier and graphene in an out-of-plane stack, multiple superior performances in terms of current on/off ratio, rectification ratio, and ideality factor can be achieved. The devices operation relies on the tunability of the surface potential of WS_2 at the atomically abrupt interface (Fig. 1). The output curve reveals strong non-linear response showing a rectification ratio approximately 100,000 and ideality factor 1.2 (Fig.2). Figures 3 and 4 illustrate the output and transfer characteristics of the devices under different gate biases, respectively. The external electric field resulting from the silicon back-gate determines the output curves to obtain rectification ratio over a range of 10 ~ 400,000. Moreover, a high on/off ratio of 3.6×10^6 is demonstrated at room temperature.

[1] A. K. Geim and I. V. Grigorieva, “Van der Waals heterostructures”, *Nature* **499**, 419-425 (2013).

[2] D. Chu, Y. H. Lee, and E. K. Kim, “Selective control of electron and hole tunneling in 2D assembly”, *Sci. Adv*. **3**, e1602726 (2017).

978-3-901578-31-1

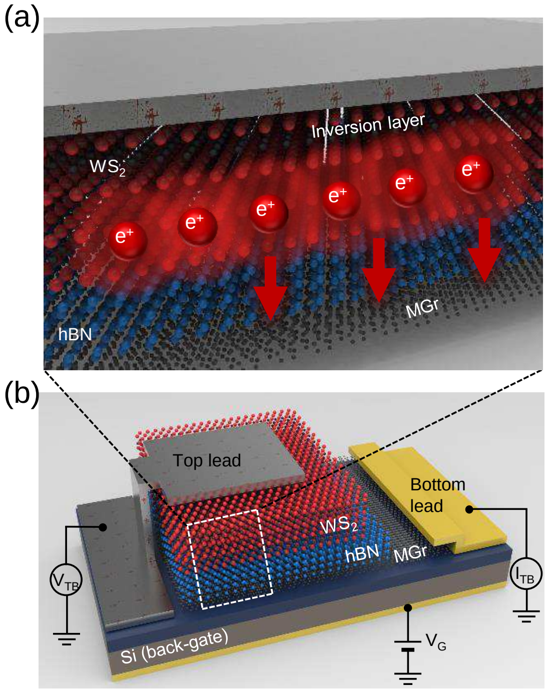

Fig.1: Illustration of semimetal-insulator-semiconductor-carristor and the characterization of the device structure. (a) Schematic illustration of an MIS-C under the state of forming an inversion of holes for tunneling. 'e+' represents hole carrier. (b) Schematic representation of the carristor layout and electrical connections for electrical transport measurements.

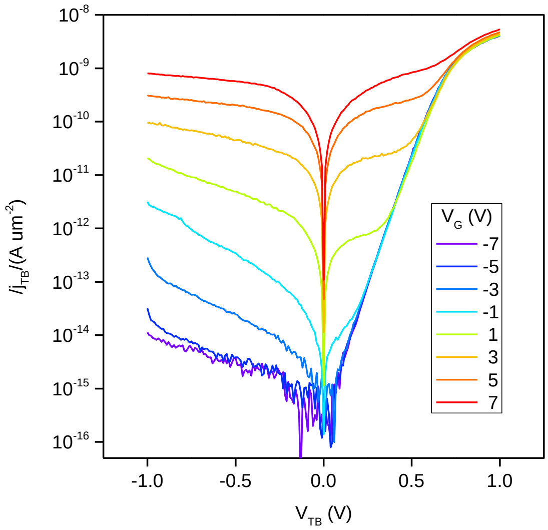

Fig.3: Semi-log scale of I_{TB}-V_{TB} output curves for different back-gate voltages with an active contact area of 50 µm^2.

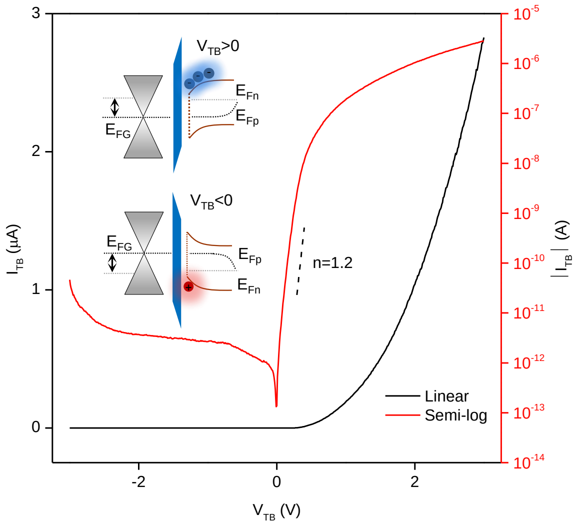

Fig.2: I_{TB}-V_{TB} output curve measured across the heterostructure (between leads T1 and B1) showing an ideality factor of 1.2; the silicon back-gate was set to ground during the measurements. Inset: Schematic of the energy band diagram of a vertically stacked MIS-C under forward (top) and reverse (bottom) bias conditions. Symbols are E_{FG}: graphene Fermi level, E_{Fn} (E_{Fp}): quasi-Fermi level for electrons (holes).

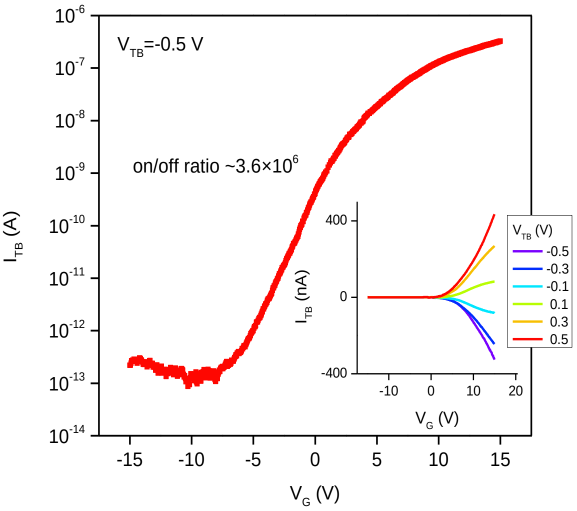

Fig.4: Room-temperature semi-log I_{TB}-V_G transfer characteristics of an MIS-C at V_{TB}=-0.5 V. Inset: The corresponding linear scale I_{TB}-V_G at various V_{TB}.

978-3-901578-31-1

P-14

Ferromagnetic and semiconducting properties from cobalt oxide adsorbed graphene

Chang-Soo Park[1], Kyung Su Lee[1], Dongil Chu[1], Juwon Lee[2], Yoon Shon[2], and Eun Kyu Kim[1*]

[1] *Department of Physics and Quantum-Function Research Laboratory, Hanyang University, Seoul 04763, Korea*

e-mail: ek-kim@hanyang.ac.kr

[2] *Quantum Functional Semiconductor Research Center, Dongguk University, Seoul 04620, Korea*

Ferromagnetic semiconductors have attracted much interest because they are considered as good candidates for a next generation electronic devices with an application of electron spin [1-3]. For the functional application of materials, ferromagnetic semiconductors should keep the ferromagnetic ordering at room temperature for ordinary electron device working. Dietl et al. had reported the room temperature ferromagnetic properties with T_c over 300K in semiconductors in a theoretical method [4]. Ferromagnetism at room temperature has also been reported in carbon related materials. In addition, graphene has the high mobility and excellent material properties and has become a hot issue for future spin electronic devices. In this study, we report the ferromagnetic semiconductor properties of a metal oxide adsorbed graphene using electrochemical method.

[1] H. Ohno et al., Appl. Phys. Lett. **69,** 363 (1996).

[2] H. Ohno, Science **281,** 951 (1998).

[3] G. A. Prinz, Science **282,** 1660 (1998).

[4] T. Dietl et al., Science **287,** 1019 (2000).

978-3-901578-31-1

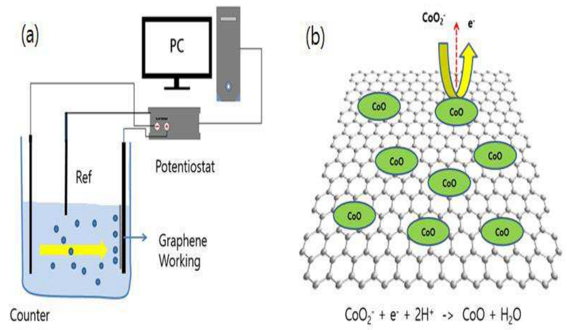

Fig.1: (a) Schematic of electrochemical procedure and (b) CoO adsorption onto graphene by electrochemical method.

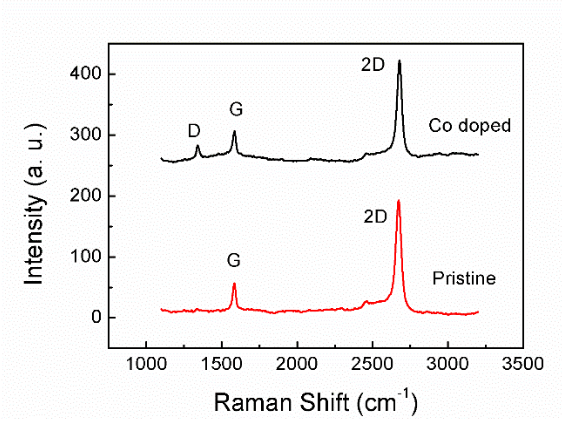

Fig.2: Raman spectra of the pristine and the CoO adsorbed graphene film.

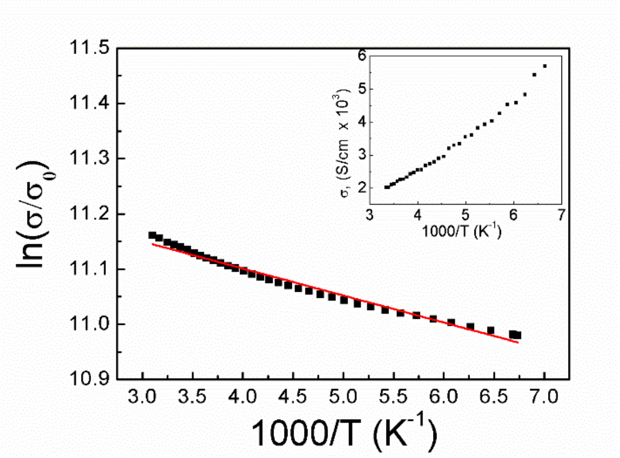

Fig.3: Temperature dependent conductivity of graphene adsorbed with CoO. The inset shows a metallic behavior of pristine graphene.

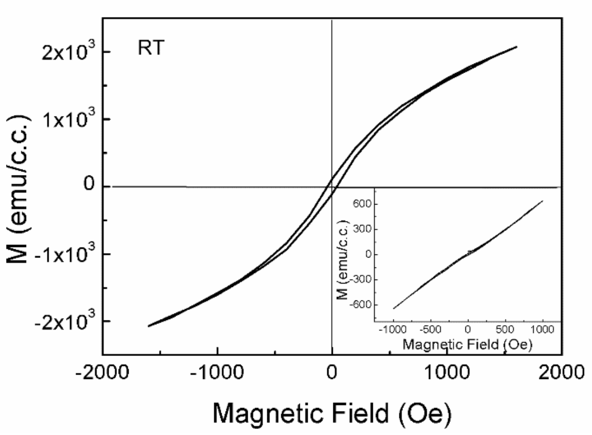

Fig.4 Ferromagnetic hysteresis characteristics of the CoO adsorbed graphene with various magnetic fields.

P-15

Electric double layer light emitting diode of WSe2/MoSe2 in-plane heterostructures

Yuhei Takaguchi[1], Jiang Pu[2], Yu Kobayashi[1], Taishi Takenobu[2],
Yutaka Maniwa[1], Yasumitsu Miyata[1],

[1] *Department of Physics, Tokyo Metropolitan University, Hachioji 192-0397, Japan*
[2] *Department of Applied Physics, Nagoya University, Nagoya 464-8603, Japan*
e-mail: ymiyata@tmu.ac.jp

Transition metal dichalcogenide (TMDC) atomic layers have attracted attention because of their unique spin-valley physics and future applications in electronics and opto-electronics Especially, the semiconductor heterostructures based on TMDCs is expected to be useful to realize high-performance devices including light-emitting diodes and tunnel field-effect transistors. For this purpose, we have developed growth processes of various in-plane heterostructures based on TMDC atomic layers [1]. Recently, Pu et al. reported a simple way to generate light emission in semiconductors using electric double layer [2]. By combining these techniques, in this study, we have fabricated the electric doublelayer light emitting diodes (EDLEDs) based on WSe_2/$MoSe_2$ in-plane heterostructures.

WSe_2/$MoSe_2$ in-plane heterostructures was grown on sapphire substrates by using two- steps chemical vapor deposition (CVD) processes as reported previously [1]. First, monolayer WSe_2 was grown using WO_3 and Se, and then, monolayer $MoSe_2$ was grown from the edge of WSe_2 with MoO_2 and Se. Optical image and PL spectra is shown in Fig.1 and Fig.2. Cr/Au electrodes were then deposited on the samples by using a shadow mask or photolithography. To fabricate EDLEDs, ion gel was spin coated on the sample [2], and an illustration of device is shown in Fig.3. As shown in Fig.4 and Fig.5, the device shows strong light emission from the WSe_2/$MoSe_2$ interface by applying voltage at two electrodes (Fig. 5). We also found that electroluminescence (EL) spectrum shows a relatively broad peak than photoluminescence (PL) of WSe_2 and $MoSe_2$ monolayer (Fig. 6). In the presentation, we will show the details of sample preparation and discuss a mechanism of EL in the present EDLEDs.

[1] Y. Kobayashi et al., Sci. Rep., 6, 31223 (2016). [2] J. Pu et al., Adv. Mater. , 29, 1606918 (2017).

978-3-901578-31-1

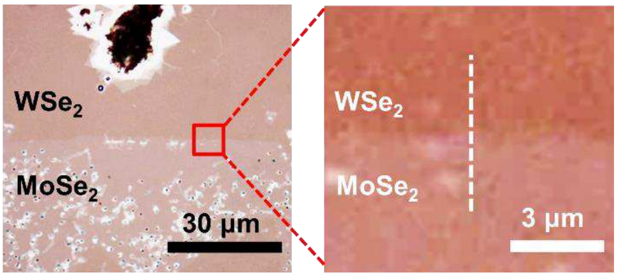

Fig.1: Optical image of WSe$_2$/MoSe$_2$ in-plane heterostructure .

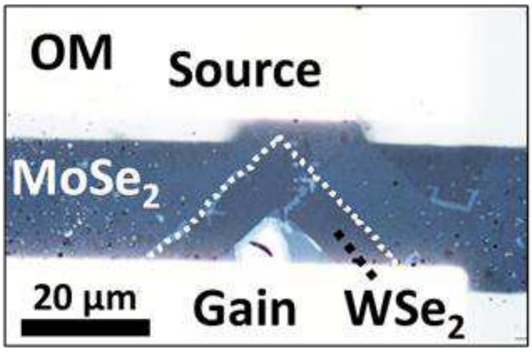

Fig.4: Optical image of WSe$_2$/MoSe$_2$-based EDLED device.

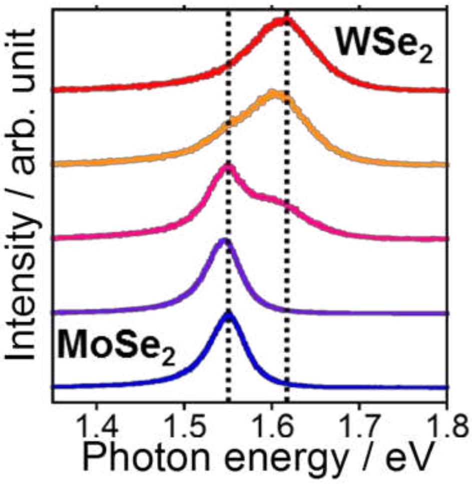

Fig.2: PL spectra of WSe$_2$/MoSe$_2$ in-plane heterostructure

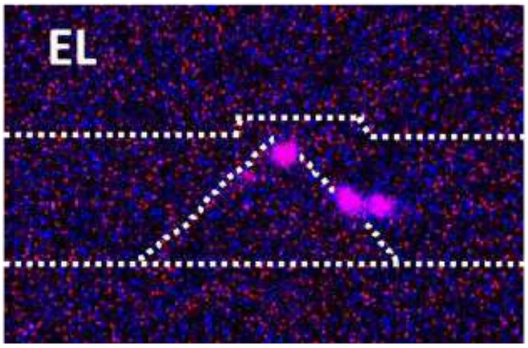

Fig.5 Electroluminescence (EL) images of WSe$_2$/MoSe$_2$-based EDLED device. Arrows indicate the observed EL.

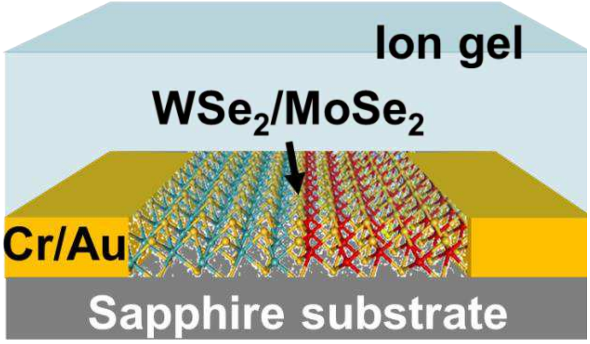

Fig.3: Illustration of WSe2/MoSe2-based EDLED device.

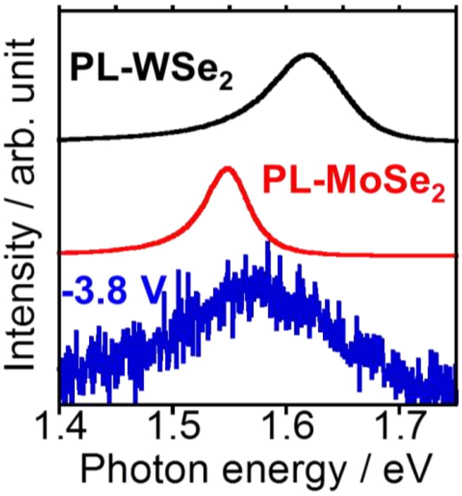

Fig.6: EL spectrum of the EDLED device, and photoluminescence (PL) spectra of WSe$_2$ and MoSe$_2$ monolayers.

978-3-901578-31-1

P-16

Growth and characterization of Re-doped MoS_2 monolayers

Shintaro Yoshimura[1], Yu Kobayashi[1], Shoji Yoshida[2], Naoya Okada[3], Toshifumi Irisawa[3],
Takahiko Endo[1], Yutaka Maniwa[1], Hidemi Shigekawa[2], and Yasumitsu Miyata[1]

[1]Department of Physics, Tokyo Metropolitan University, Hachioji 192-0397, Japan
[1]Faculty of Pure and Applied Sciences, University of Tsukuba, Tsukuba 305-8573, Japan
[3]Nanoelectronics Research Institute, AIST, Tsukuba 305-8568, Japan
e-mail: ymiyata@tmu.ac.jp

To control the semiconducting properties of two-dimensional chalcogenides, understanding of the role of impurities is an important issue. In a previous study, first-principles calculations predict the formation of acceptor and donor levels by replacing Mo atoms in molybdenum disulfide (MoS_2) with other elements such as Nb and Re atoms [1]. So far, several studies have reported the increase of hole concentration and the formation of impurity level by Nb doping in MoS_2 and WS_2 [2, 3]. In our previous study, we also found that Re atoms can be replaced with Mo atoms in MoS_2 and revealed the formation of impurity level by using scanning tunneling spectroscopy. In this study, we have prepared large single crystals of Re-doped monolayer MoS_2, and have investigated their electrical and optical properties.

Re-doped monolayer MoS_2 crystals were grown on silicon substrates with halide-assisted chemical vapor deposition (CVD) [3, 4]. As shown in optical microscope images (Figs.1, 2), the growth of large-area single crystals are achieved for both undoped and Re-doped monolayer MoS_2. In the Re-doped samples, the Raman intensity of LA mode at 227 cm^{-1} increases probably due to the lowering of symmetry of crystal by Re doping (Fig.3) [5]. Furthermore, a novel emission peak is observed around 1.6 eV at room temperature (Fig.4). This peak can be assigned to the emission derived from localized exciton due to its saturation behavior under high power excitation as reported previously [3]. We have also found that field-effect transistors of Re-doped MoS_2 shows ambipolar behavior unlike the conventional n-type monolayer MoS_2 (Figs.5, 6). This result suggests that acceptor levels can be formed in monolayer MoS_2 by Re doping. In the presentation, we will discuss the details of Re doping on the optical and electrical properties of monolayer MoS_2.

[1] K. Dolui et al., Phys. Rev. B, **88**, 075420 (2013).
[2] J. Suh et al., Nano. Lett., **14**, 6976 (2014).
[3] S. Sasaki et al., Appl. Phys. Express, **9**, 071201 (2016).
[4] S. Li et al., Appl. Mater. Today, **1**, 60 (2015).
[5] S. Mignuzzi et al., Phys. Rev. B, **91**, 195411 (2015).

978-3-901578-31-1

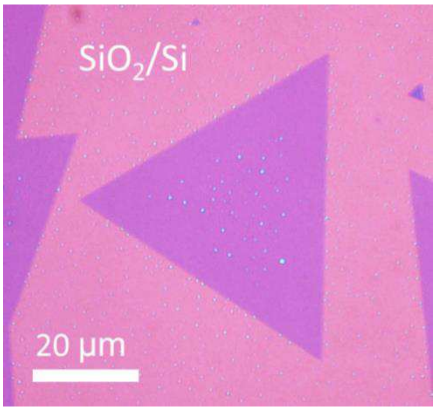

Fig.1: Optical microscope images of undoped MoS$_2$ monolayer.

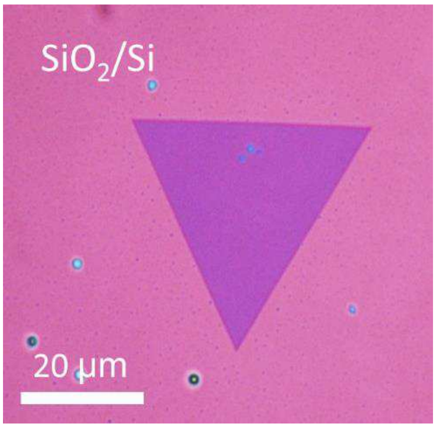

Fig.2: Optical microscope images of Re-doped MoS$_2$ monolayer.

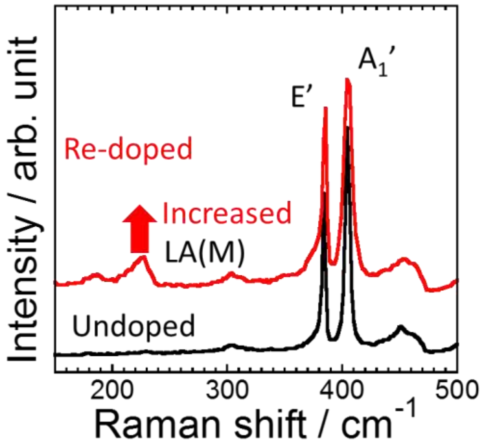

Fig.3: Raman spectra of undoped and Re-doped MoS$_2$ monolayers.

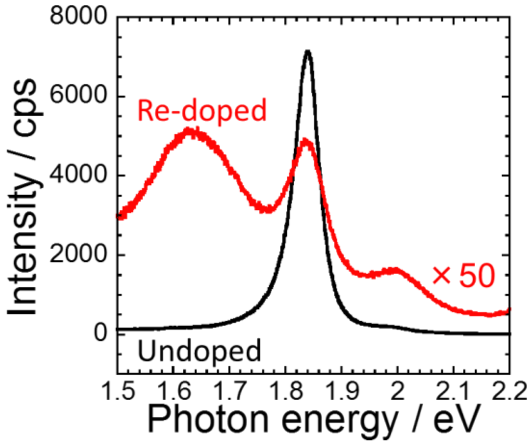

Fig.4: PL spectra of undoped and Re-doped MoS$_2$ monolayers.

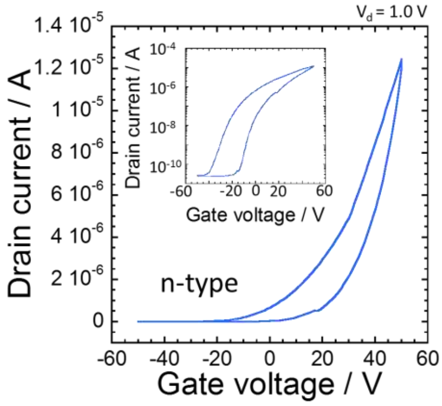

Fig.5: Drain current vs gate voltage of undoped MoS$_2$ monolayer.

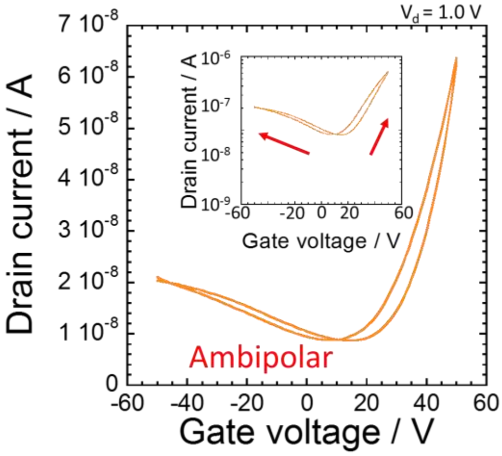

Fig.6: Drain current vs gate voltage of Re-doped MoS$_2$ monolayer.

P-17

Growth and characterization of transition metal dichalcogenides using halide-assisted MOCVD

Yu Kobayashi[1], Shoji Yoshida[2], Kota Murase[2], Naoya Okada[3], Toshifumi Irisawa[3],
Yutaka Maniwa[1], Hidemi Shigekawa[2], Yasumitsu Miyata[1]

[1]*Department of Physics, Tokyo Metropolitan University, Hachioji 192-0397, Japan*
[2]*Faculty of Pure and Applied Sciences, University of Tsukuba, Tsukuba 305-8573, Japan*
[3]*Nanoelectronics Research Institute, AIST, Tsukuba 305-8568, Japan*
e-mail: ymiyata@tmu.ac.jp

Chemical vapor deposition (CVD) is one of the most powerful techniques for growth of large-area transition metal dichalcogenide (TMDC) atomic layers and their heterostructures. In particular, Kang et al. recently reported the growth of large-area and uniform TMDC films using organic compound-based precursors with high vapor pressure [1]. Because of their high controllability of supply rate, this progress motivates us to fabricate TMDC-based heterostructures through multi-step metal-organic CVD (MOCVD) processes. In this work, we have developed a simple and effective way to produce uniform and high-quality monolayer MoS_2 and WS_2 films using halide-assisted MOCVD.

Monolayer MoS_2 (WS_2) are grown by using organic sulfide and molybdenum (tungsten) compounds. Our MOCVD system is displayed in figure 2. To improve the sample quality, we have investigated the effect of alkali metal halides (AMHs) such as NaCl as the growth promoters. The effects of AMHs are suggested to be the removal of water, the formation of volatile oxyhalides, and the surface modification previously [1-3]. Figure 2-5 show optical, atomic force microscope (AFM) and scanning tunneling microscope (STM) images and grain size histograms of MoS_2 grown with and without AMHs in MOCVD. We found that the use of AMHs improves various parameters including grain size, uniformity of layer number, nucleation density, and defect density of MOCVD-grown TMDCs. Unlike the previous studies [1,2], no oxygen atoms are included in the present precursors, and thus, the different mechanism is required to explain the halide-assisted growth in the present case. In the presentation, we will discuss the role of AMHs in MOCVD growth and show the details of optical and electrical properties of samples.

[1] K. Kang et al., Nature, **520**, 626 (2015),
[2] S. Li, et al. Appl. Mater. Today, **1**, 60 (2015),
[3] H. Kim et al., Nano Lett., Nano Lett., **17**, 5056–5063 (2017).

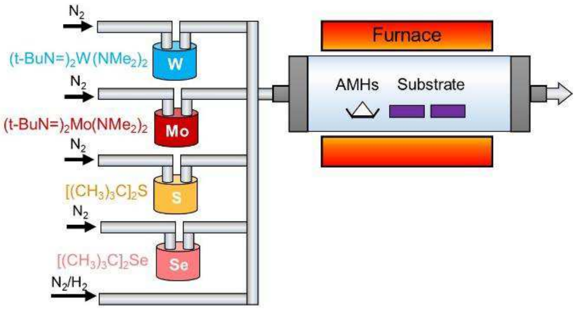

Fig.1: Schematic illustration of MOCVD system.

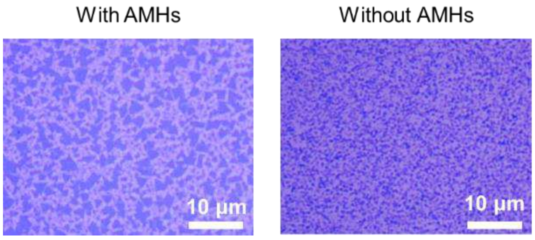

Fig.2: Optical images of MOCVD grown MoS_2 with and without AMHs on SiO_2/Si.

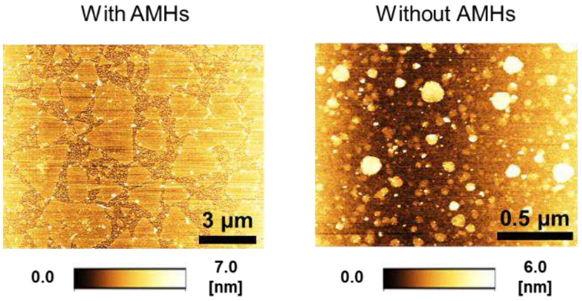

Fig.3: Height images of MOCVD grown MoS_2 with and without AMHs on SiO_2/Si.

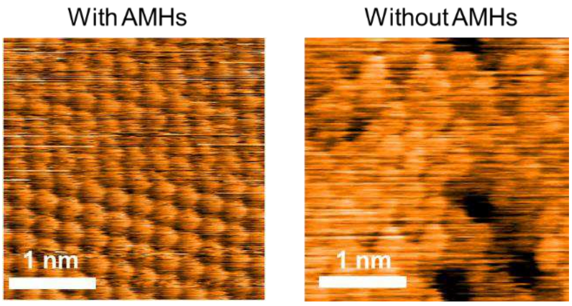

Fig.4: Scanning tunneling microscope images of MOCVD grown MoS_2 with and without AMHs on graphite.

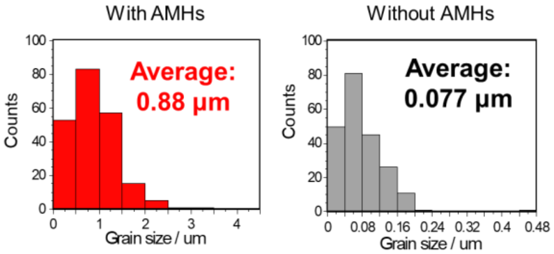

Fig.5: Histograms of MOCVD grown MoS_2 with and without AMHs on SiO_2/Si.

P-18

Cubic Nonlinearity of Transition Metal Dichalcogenides Atomic layer

Tikaram Neupane, Sheng Yu, Bagher Tabibi, and Felix Jaetae Seo*

Advanced Center for Laser Science and Spectroscopy, and Center for Atmospheric Research and Education, Department of Physics, Hampton University, Hampton, Virginia 23668, USA
e-mail: jaetae.seo@hamptonu.edu

The nonlinear absorption properties of TMDCs depend on the electronic bandgap. The monolayer of TMDCs has a direct bandgap which is wider than the indirect bandgap present in the bilayer/ multilayer. The change of bandgap plays an important role in the nonlinear absorption process which is described by Jablonski diagrams that may include two-step absorption with one-photon for each step, or two-photon absorption to the real final state through a virtual intermediate state. In the one-photon excitation case, the electric dipole transition from initial to final state is allowed due to different parities between these states. This implies that the ground-state absorption cross-section is larger than the excited-state absorption cross-section which results in saturable (negative) absorption (SA) as shown in figure 1. However, in the two-photon excitation case, the electric dipole transitions from initial to final state are allowed via virtual intermediate state due to same parities between the initial and final states. Here, the excited-state absorption cross-section is larger than the ground-state absorption cross-section which causes reverse saturable (positive) absorption (RSA) as shown in figure 2. Therefore, changes from RSA to SA and vice versa, is determined by the number of layers corresponding to the bandgap of TMDCs. The atomic layers with SA can be utilized for laser Q-switch and mode-locker, while the atomic layers with RSA can be utilized for optical power limiter [1, 2]. Acknowledgement: This work is supported by ARO W911NF-15-1-0535, NSF HRD-1137747, and NASA NNX15AQ03A.

[1] T. Neupane et al., Transition of Saturable and Reverse Saturable Absorptions between Monolayer and Bilayer/Multilayer, (In preparation).
[2] Y. Li et al., Laser Photon. Rev. **9,** 427 (2015).

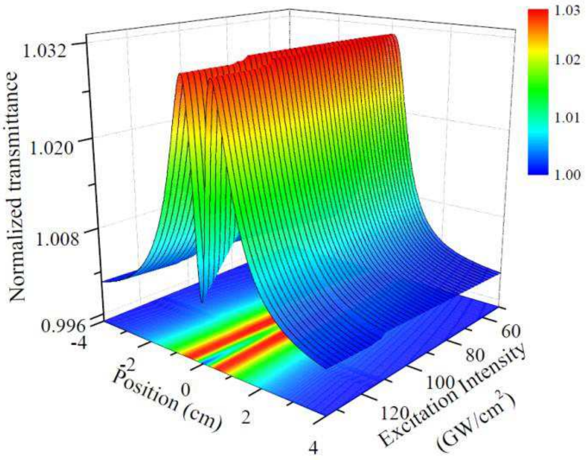

Fig.1. Nonlinear transmittance as the functions of sample position and excitation intensity results SA for bilayer/or multilayer of MoS_2.

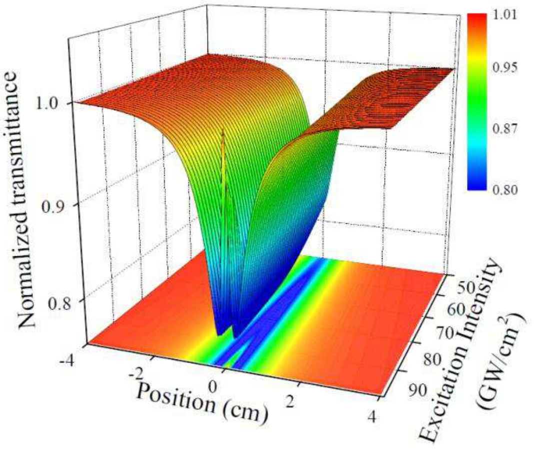

Fig.2. Nonlinear transmittance as the functions of sample position and excitation intensity results RSA for monolayer of MoS_2.

978-3-901578-31-1

P-19

Phonon and Intensity induced Exciton Dephasing of TMDC Atomic Layer

Tikaram Neupane, Sheng Yu, Bagher Tabibi, and Felix Jaetae Seo*

Advanced Center for Laser Science and Spectroscopy, and Center for Atmospheric Research and Education, Department of Physics, Hampton University, Hampton, Virginia 23668, USA
e-mail: jaetae.eso@hamptonu.edu

The exciton polarization dephasing time, T_2, in two-dimensional transition metal dichalcogenides are of great interest for optoelectronic applications including ultrafast modulation, switching, and information processing. The exciton dephasing process occurs through coherence loss of exciton polarization and population decay. The coherence loss of exciton polarization is mainly due to the coupling strength of both exciton-exciton and exciton-phonon interaction. The exciton-phonon coupling is dominant at higher temperature that generates a larger phonon density. At a higher temperature, larger phonon scattering occurs which may lead to faster exciton dephasing. The exciton-exciton coupling may have a significant contribution at a higher excitation intensity due to a larger exciton density generated in the material. As excitation intensity increases, a larger exciton elastic collision causes faster exciton dephasing. Therefore, the contribution of exciton-phonon and exciton-exciton coupling to the total dephasing time in WSe_2 monolayer was analyzed as functions of temperature and excitation intensity. The dephasing time of WSe_2 atomic layer in the range of a few picosecond to sub-picosecond may be utilized for optoelectronic modulator or switching [1,2]. The longer dephasing time of exciton or electron in the WSe_2 atomic layer with valley photonic chirality may pave the prospective quantum information processing. Acknowledgment: This work is supported by ARO W911NF-15-1-0535, NSF HRD-1137747, and NASA NNX15AQ03A.

[1] T. Neupane et al., “Exciton Dephasing of Two-dimensional Atomic Layers,” (In preparation).
[2] G. Moody et al., Nat. Commun. **6**, 9315 (2015).

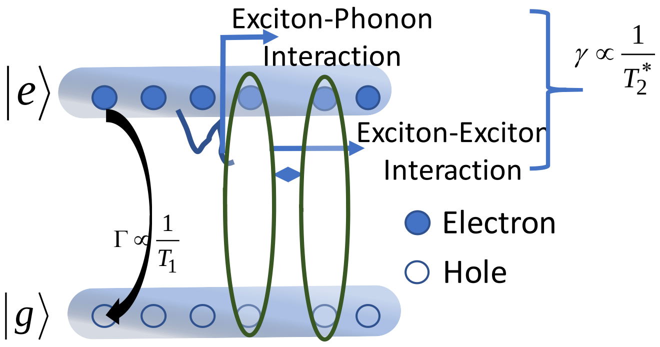

Fig 1. Dynamics of exciton dephasing including population decay process

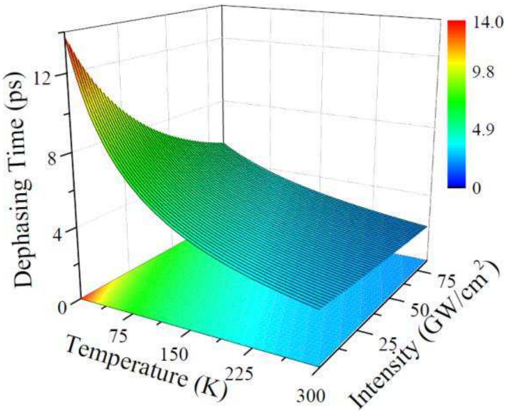

Fig.2: Exciton dephasing time as functions of temperature and excitation peak intensity.

978-3-901578-31-1

P-20

PIEZOELECTRICITY OF 2-DIMENSIONAL MoS_2/WSe_2 HETEROSTRUCTURE

Sheng Yu, Tikaram Neupane, Bagher Tabibi, and Felix Jaetae Seo*

Advanced Center for Laser Science and Spectroscopy, and Center for Atmospheric Research and Education, Department of Physics, Hampton University, Hampton, Virginia 23668, USA
e-mail: jaetae.seo@hampton.edu

Two-dimensional atomic monolayers of transition-metal dichalcogenides have an intrinsic piezoelectricity due to the inversion asymmetry of crystal structure. The piezoelectricity of atomic monolayer has a strong angular dependence along the armchair directions of 0, 120, and 240 degrees in the hexagonal structure. This article presents the piezoelectronicity of n-type MoS_2 / p-type WSe_2 heterostructure atomic layers as shown in figure 1 a and b. The offset energies of conduction band minimum and valence band maximum between n-type MoS_2 and p-type WSe_2 are 0.77 and 1.11 eV, respectively. The interlayer energy difference between n-type conduction band minimum and p-type valence band maximum is 0.71 eV. The output voltages, polarization strength change due to the applied strain, of partial vertical heterostructure were 0.137 eV and 0.183 eV for 4% and 8% tensile strain along the transport (armchair) direction, respectively. The piezoelectricity also depends on the number of layers, orientation between the layers, and partial or full stacking. The piezo output voltage was significantly reduced as the number of atomic layers was increased due to the large reduction of band offset. The output voltages of $(MoS_2)_1(WSe_2)_1$ and $(MoS_2)_2(WSe_2)_2$ were 0.239 V and 0.193 V for the 8% tensile strain along the armchair direction. The heterostructure with AB stacking displayed relatively a larger output voltage compared to that with AA stacking. However, the polarization strength in the depletion region for AC stacking was reduced for the applied tensile stain. Acknowledgment: This work is supported by ARO W911NF-15-1-0535, NSF HRD-1137747, and NASA NNX15AQ03A.

978-3-901578-31-1

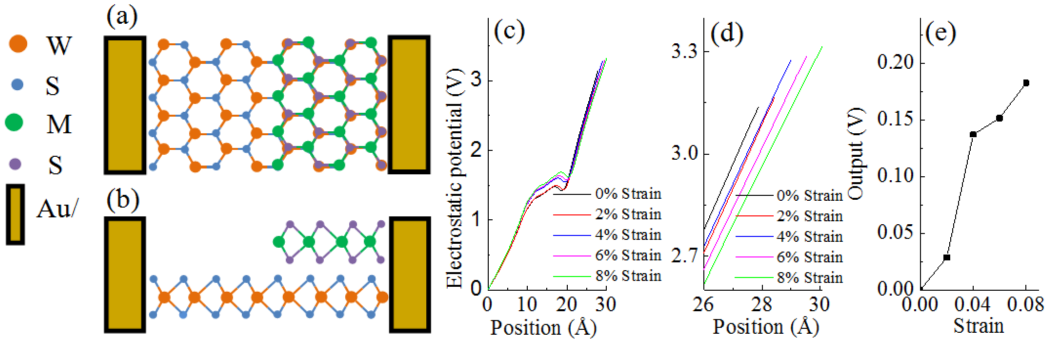

Figure 1: Schematic sketches of partial vertical heterostructure of WSe_2 and MoS_2 atomic layers in (a) top and (b) side views. Electrostatic potential distribution between the electrodes for (c) whole heterostructure region and (d) region near right electrode; and (e) output voltage as a function of strain.

P-21

Electrical characteristics of positively and negatively charged protein adsorption to epitaxial graphene film on SiC substrate

Yasuhide Ohno, Yoshiaki Taniguchi, and Masao Nagase

Graduate School of Technology, Industrial and Social Sciences, Tokushima University,
Tokushima, Tokushima 770-8506, Japan
e-mail: ohno@ee.tokushima-u.ac.jp

Epitaxial graphene film synthesized on a SiC substrate by Si atom sublimation is one of the most promising candidates for forming large-area, single-crystal graphene film [1, 2]. Although the electrical characteristic changes by protein adsorption onto the graphene surface is essential for the graphene-based sensors, it is difficult to distinguish the electrical influence from the protein adsorption and other effects such as resist residues during device fabrication process, ionized impurities in the substrate, and contact resistance, and so on. In this work, we investigated that the negatively and positively charged protein adsorption to the epitaxial graphene film.

The monolayer graphene films were prepared by heating 10 mm square 4H-SiC (0001) substrates at 1650 °C for 5 min in Ar 100 Torr atmosphere using rapid thermal annealing. Thereafter, in order to obtain electric characteristics only in the region immersed in the solution, a 6-terminal graphene Hall bar having a 3 mm square channel was formed by a typical stencil mask lithography with PET film and air plasma etching as shown in Fig. 1(a). Such fabrication processes need no photo and e-beam resist, hence, the device are free from these residues. Since the Hall mobility exceeded 1,000 cm^2/(Vs) and the carrier type was n type, these results show that these devices were a typical high quality graphene films on a SiC substrate. Bovine serum albumin (BSA; isoelectric point: 5.3) were used as a target protein. We prepared the BSA solution with 10 mM acetate (pH 4.0) and borate buffer solution (pH 9.0), which contained positively and negatively charged BSAs, respectively. To measure the transfer characteristics, we used a Ag/AgCl reference electrode as a top gate electrode.

Figure 2 shows transfer characteristics (I_D-V_G) of the epitaxial graphene FETs after the various concentration of BSA introduction. The transfer characteristics shifted in the negative gate voltage direction with increasing the concentration of negatively and positively charged BSA, indicating that the electrical characteristic change from protein adsorptions does not depend on the isoelectric point of the protein but direct charge transfer from the adsorbed proteins.

[1] T. Aritsuki et al., Jpn. J. Appl. Phys. **55**, 06GF03 (2016).

[2] Y. Ohno et al., Jpn. J. Appl. Phys. **55**, 06GF09 (2016).

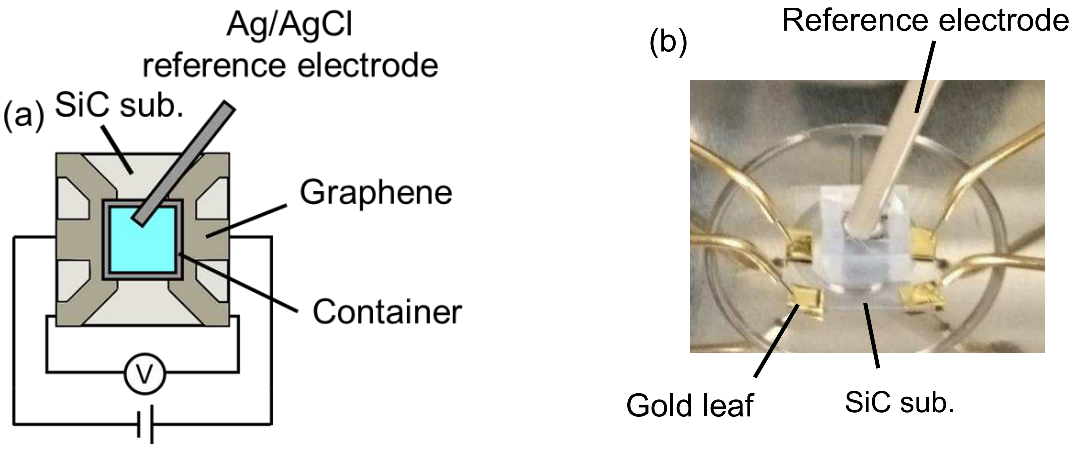

Fig. 1: (a) Schematic diagram of the measurement setup and (b) photograph of the measurement.

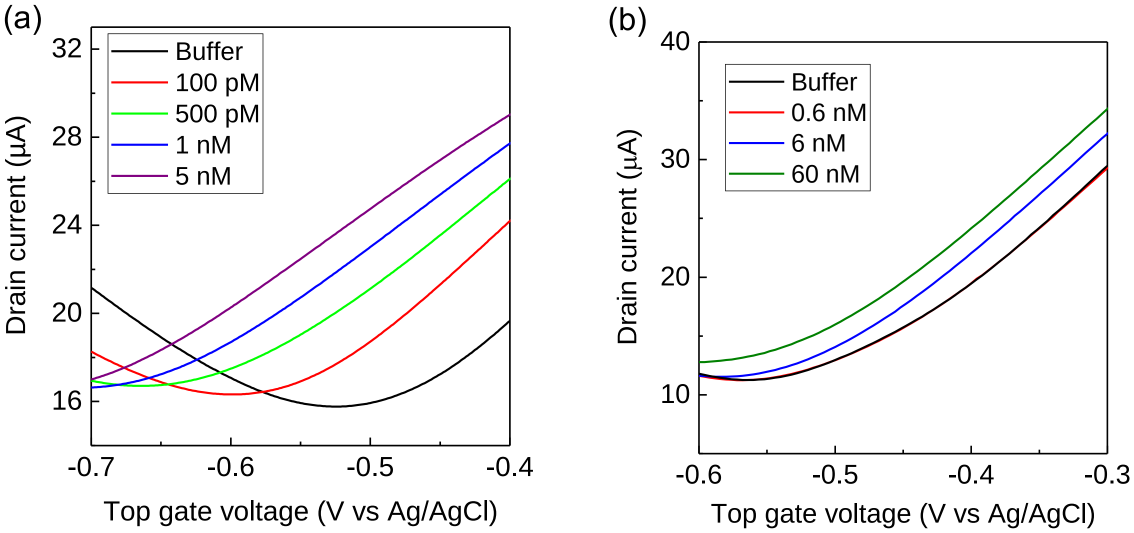

Fig. 2: Transfer characteristics of an epitaxial graphene FET for buffer solution and various concentrations of (a) positively and (b) negatively charged BSA.

P-22

Surface resonance soliton in phosphorene

G. T. Adamashvili

Department of Physics, Technical University of Georgia, Kostava str. 77, 0179, Georgia
e-mail: guram_adamashvili@ymail.com

Surface plasmon polariton (SPP) is a surface optical wave which undergoes a strong enhancement and spatial confinement of its wave amplitude near an interface of two-dimensional layered structures. Phosphorene (single-layer black phosphorus) and other two-dimensional anisotropic phosphorene-like materials are recognized as promising materials for potential future applications of SPPs. A theory of an optical soliton of self-induced transparency for SPP propagating in monolayer or few-layer phosphorene is developed. Starting from the optical nonlinear wave equation for surface TM-modes interacting with a two-dimensional layer of atomic systems or semiconductor quantum dots and a phosphorene monolayer (or other two-dimensional anisotropic material), we have obtained the evolution equations for the electric field of the pulse [1]. In this case, one finds that the evolution of these pulses become described by the damped Bloch-Maxwell equations. For SPP fields, solitons are found to occur. Explicit relations of the dependence of solitons on the local media, phosphorene anisotropic conductivity, transition layer properties and transverse structures of the SPP, are obtained and will be given. It is shown that the phosphorene conductivity reduces exponentially the amplitude of the surface soliton of SIT in the process of propagation. The direction of propagation corresponding to the maximum and minimum damping of the amplitude are assigned along the armchair and zigzag directions of black phosphorus nano-film, respectively. The most rapid damping of the intensity occurs when the polarization of pulse is along the armchair direction.

[1] G. T. Adamashvili and D. J. Kaup, Phys. Rev. A, **95,** 053801 (2017).

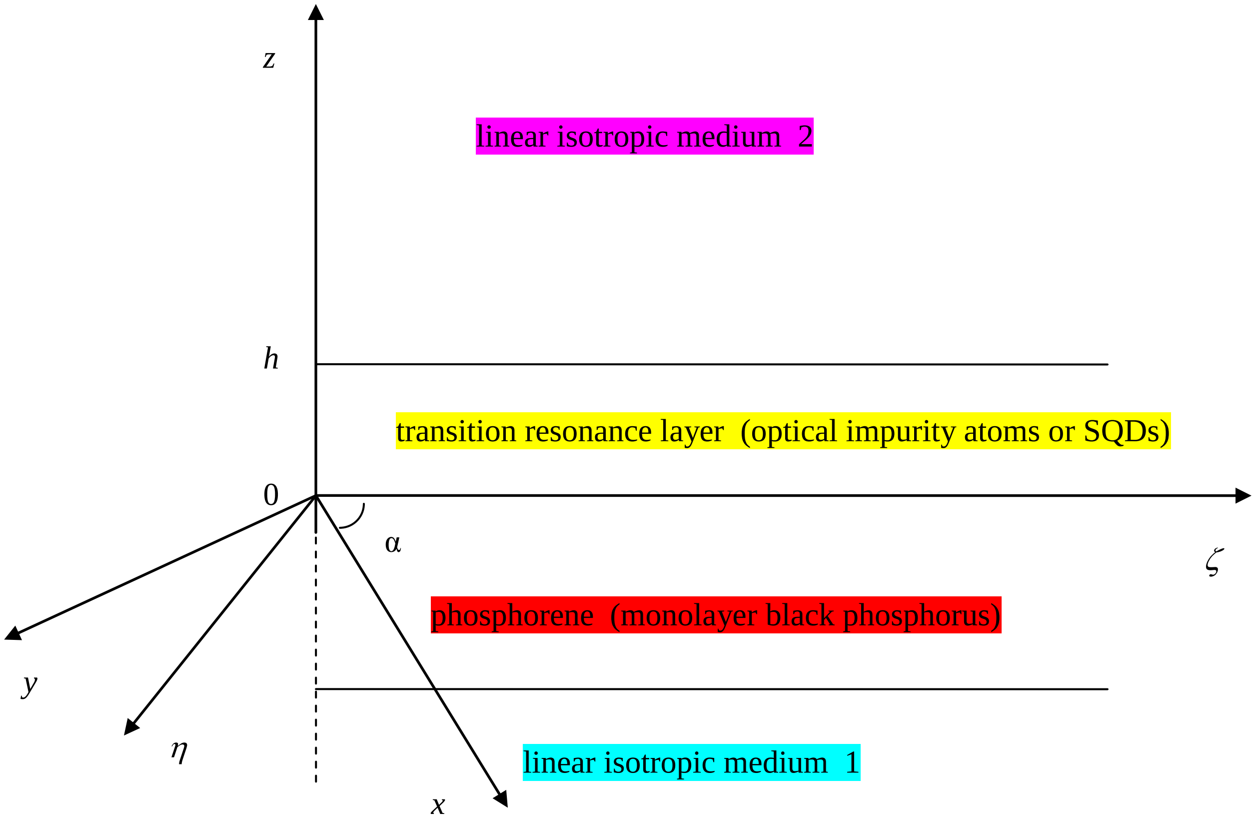

The direction of the propagation of the TM SPP along axis ζ. The coordinate axes ζ, η, x and y lie in a single plane perpendicular to the z axis. The x-direction (or armchair direction) and y-direction (or zigzag direction) are perpendicular to the z axis. The vector of the electric field, **E**, of the SPP TM-mode lies in the ζ z -plane. The vector of the associated magnetic field, **H**, is parallel to the η-axis. The transition layer, of thickness h, contains SQDs or optical impurity atoms. The phosphorene is sandwiched between the transition layer and medium 1. The vector of polarization **P** of the impurity atoms or SQDs points along axis ζ. α is the angle between axes x and ζ.

978-3-901578-31-1

P-23

Amplitude control of MoS_2 cantilever by electrostatic driving

Daiki Yoshikawa, Yuga Miyamoto, Kuniharu Takei, Takayuki Arie, and Seiji Akita
Department of Physics and Electronics, Osaka Prefecture University,
Sakai, Osaka 599-8531, Japan
e-mail: yoshikawa-4@pe.osakafu-u.ac.jp

Two-dimensional atomic layers are attracting attention as many useful device materials due to their unique electrical, optical and mechanical properties. Among others, transition metal dichalcogenide (TMDC) such as molybdenum disulfide (MoS_2) is expected to be applied to high performance nanoelectromechanical system (NEMS), because it has a bandgap depending on the number of layers unlike graphene. Thus, the resonance frequency of MoS_2 mechanical resonator would be modulated by photoinduced effect, which depends on the wavelength of light. Here, we investigate a cantilevered MoS_2-NEMS on the planar substrate actuated by electrostatic force under light irradiation.

Figure 1 shows a device structure of the cantilevered MoS_2-NEMS supported by SU-8. A pair of electrodes for the actuation of the cantilever is placed underneath the SU-8 support. To actuate the MoS_2 cantilever, DC + AC bias (V_{AC} or V_{DC}) was applied to the electrodes, where a wavelength 532 nm laser light was used for the probe of the vibration. Figure 2 shows a resonance curve of the cantilevered MoS_2-NEMS. At V_{AC}=1 V, the resonance frequency and Q factor are 811.5 kHz and 940, respectively. Figure 3 shows V_{AC} dependence of the resonance characteristics. The amplitude increases with increasing V_{AC} with the resonance frequency around 811 kHz. In case of V_{DC} + V_{AC}, the amplitude at the resonance increases linearly with increasing either V_{AC} or V_{DC} as shown in Figs.4 and 5. Under the linear oscillation regime with small vibration amplitude, these linear dependence can be explained by a simple model, where the cantilevered MoS_2 acts as the intermediate electrode in two series capacitor. by a simple model equivalent circuit using one capacitor.

Finally, we examined the influence of the photoinduced effect on the amplitude of the MoS_2 cantilever, where the laser intensity was varied from 9.2 to 12.2 μW. As shown in Fig. 6, the vibration amplitude at resonance is successfully modulated by the photoinduced effect, where the resonance amplitude increases with the laser light.

Acknowledgements This work was partially supported by KAKENHI Grant Number 16H00920, 16K14259, 16H06504 and 17H01040.

[1] A. Yoshinaka et al, Appl. Phys. Lett. **98**, 133103 (2011).

978-3-901578-31-1

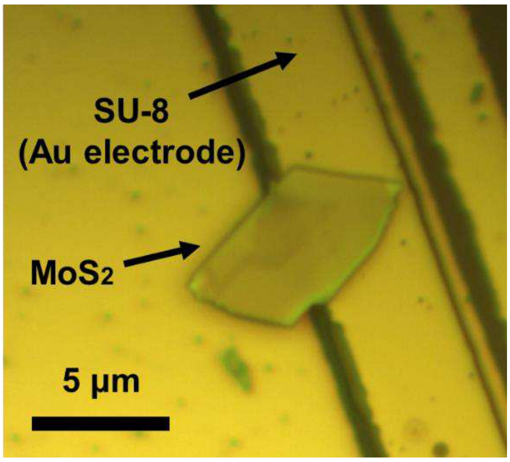

Fig. 1: Microscope image of the cantilever MoS_2*-NEMS*

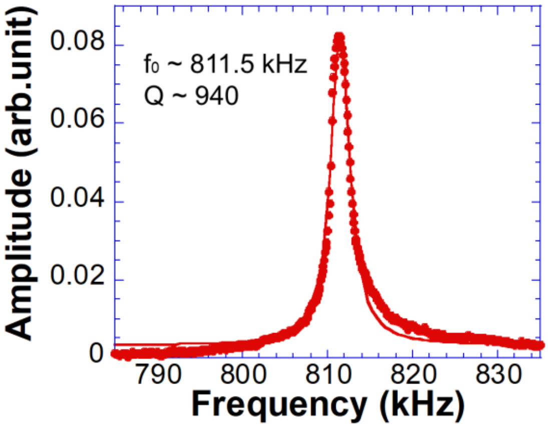

Fig. 2: Resonance curve at $V_{AC}=1$ *V and fixed* $V_{DC}=0$ *V*

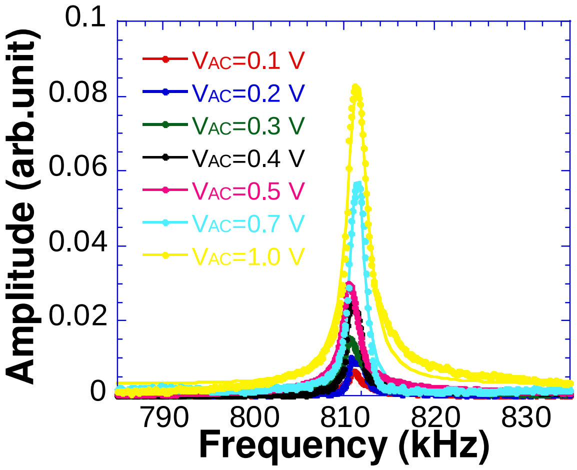

Fig. 3: Resonance curve at $V_{AC}=0.1$*, 0.2, 0.3, 0.4, 0.5, 0.7, 1 V respectively and fixed* $V_{DC}=0$ *V*

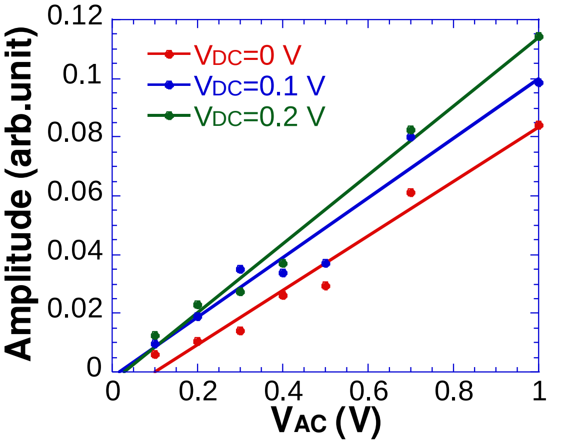

Fig. 4: Amplitude control of the cantilever MoS_2 *by each* V_{AC} *fixed* $V_{DC}=0$*, 0.1, 0.2 V*

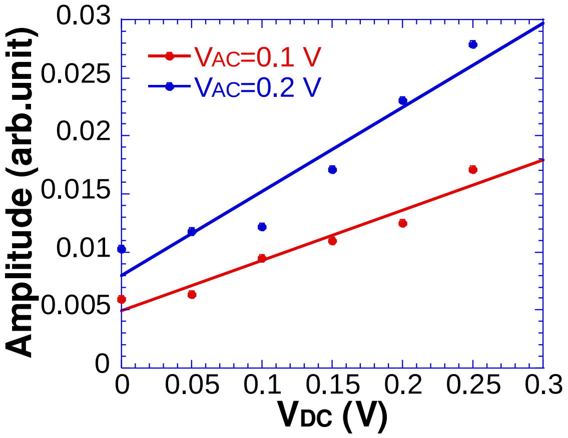

Fig. 5: Amplitude control of the cantilever MoS_2 *by each* V_{DC} *fixed* $V_{AC}=0.1$*, 0.2 V*

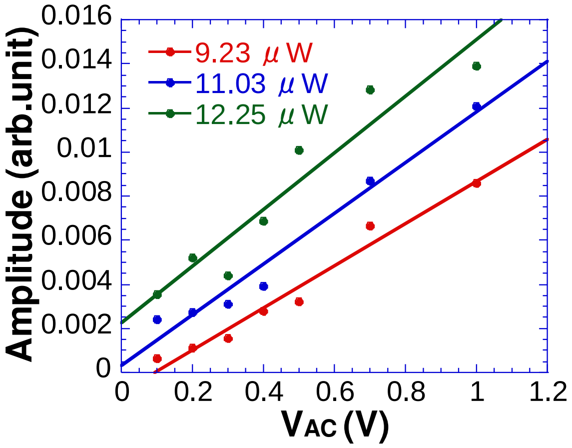

Fig. 6: Influence on amplitude control of the cantilever MoS_2 *changing the laser intensity*

P-24

Universality of Self-Heating in Disordered Transparent Conductor Networks

Sajia Sadeque[1,3], Aaditya Candadai[2,3], Yu Gong[1,3], Amir K Ziabari[1,3], Kerry Maize[1,3], Ali Shakouri[1,3], Timothy Fisher [2, 3], David B. Janes[1, 3]

1. *School of Electrical and Computer Engineering, Purdue Univ., West Lafayette, IN, US*
2. *School of Mechanical Engineering, Purdue University, West Lafayette, IN, US*
3. *Birck Nanotechnology Center, Purdue University, West Lafayette, IN, US*

e-mail: janes@purdue.edu

Nanostructured transparent conducting electrodes (TCEs) may be suitable replacements for transparent conductive oxides due to their comparable transparency and sheet resistance and good flexibility and mechanical strength. In nanowire (NW) and hybrid NW-graphene networks [1-3], NW-NW junctions represent transport bottlenecks. Understanding the properties of these junctions and their connectivity within the network is key to understanding and controlling electrical properties. Local self-heating within the network can provide information on the coupled electro-thermal response and on local conduction pathways and overall distributions.

This study employs high resolution transient thermoreflectance (TR) imaging [4] to resolve self-heating transients at microscopic hotspots corresponding to individual NW-NW junctions within a silver NW network (Fig. 1). Time constants of less than 1 µs are observed (Fig 2). Line scans along crossing NWs at various delay times (Fig. 2), show a distribution peaked near the NW-NW junction, with a FWHM of ~ 500nm - 1 µm. Extending previous work on time-averaged behavior [5], the temperature distributions (Fig. 3) have been analyzed in both the short-time (local self-heating) and long-time (macroscopic heat spreading) regimes. A single distribution function (Weibull) can be used to fit the measured distributions over both time regimes, with shape and scale parameters varying smoothly as the time response evolves (Fig. 4). The observation of universality in random networks could enable new approaches for understanding conduction in this class of percolation networks.

[1] S. De *et al.*, *ACS nano,* vol. 3, no. 7, pp. 1767-1774, 2009.

[2] R. Chen, *et al.*, *Advanced Functional Materials,* vol. 23, no. 41, pp. 5150-5158, 2013.

[3] S. R. Das, *et a.l*, Nanophotonics, 2016, doi: 10.1515/nanoph-2016-0036.

[4] K. Maize, *et al.*, in *Twenty-fourth Annual IEEE Semiconductor Thermal Measurement and Management Symposium, 2008. Semi-Therm 2008.* pp. 55-58.

[5] S. R. Das, *et al.*, Nano Lett., 2016, 16 (5), pp 3130–3136.

978-3-901578-31-1

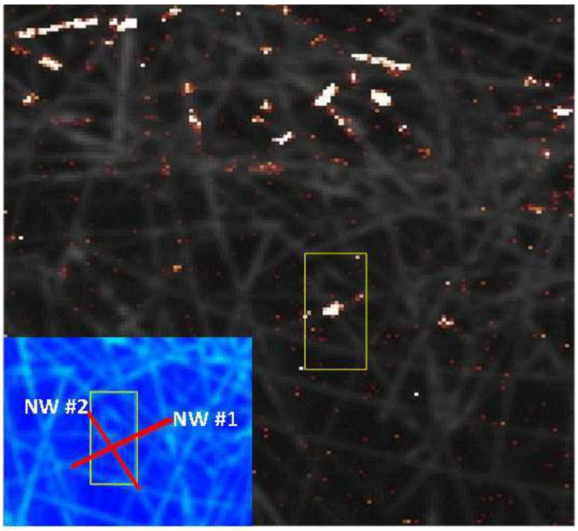

Fig.1: TR image (ΔT) superimposed on grayscale CCD image to show hotspots at NW-NWjunctions. (inset) False color CCD image, with two crossing NWs highlighted with red lines (rectangles are same region).

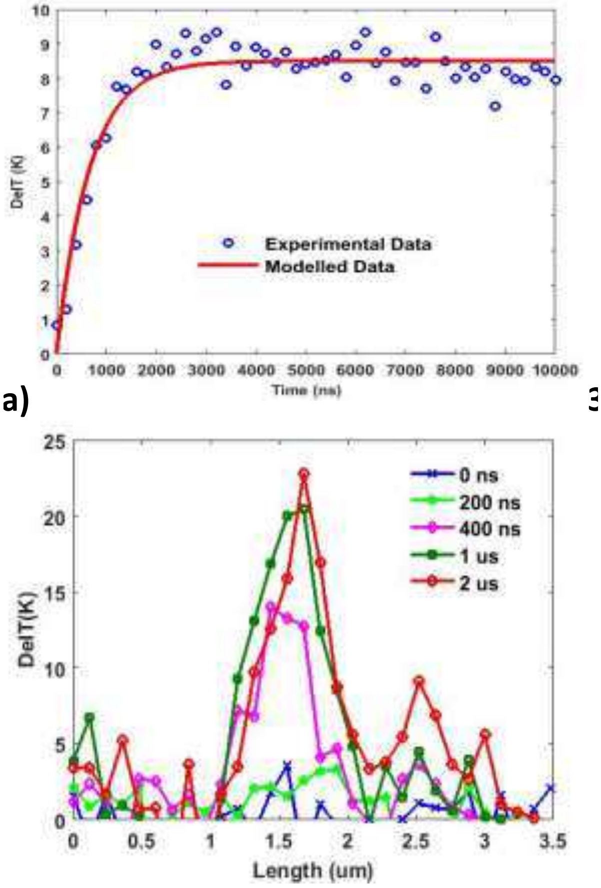

Fig.2: (top)Thermal transient response of a microscopic hotspot during heating cycle; (bottom) Measured ΔT profiles along one NW at various time delays.

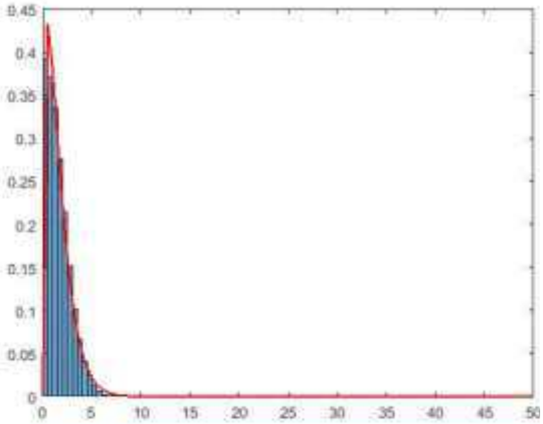

Fig.3. Histogram of temperature rise at 200 ns and corresponding Weibull fit (solid curve). Weibull distribution is given by:

$$f = \beta/\alpha\ (x/\alpha\ )^{\beta-1}\ \exp -(x/\alpha)^{\beta}$$

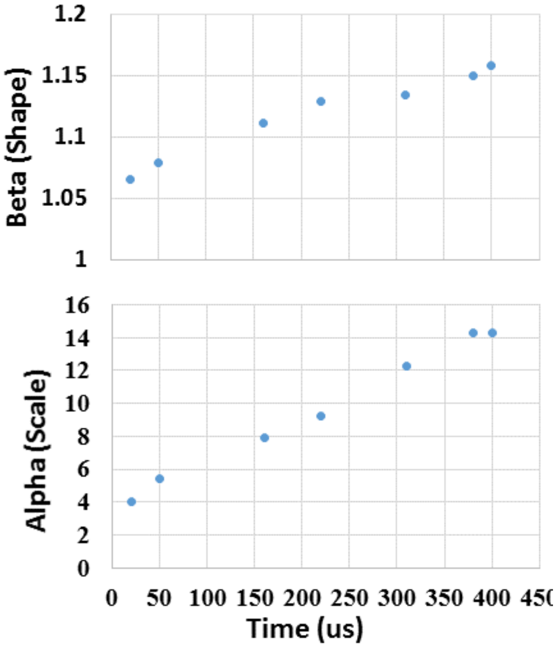

Fig.4 Time evolution of shape and scale parameters for Weibull distribution. Short-time (< 10 µs) regime reflects local self-heating, with long-time regime corresponding to heat spreading.

978-3-901578-31-1

P-25

Landau-Zener tunneling problem for particles in periodic systems

Ryuji Takahashi[1], Naoyuki Sugimoto[2]

[1] *Condensed Matter Theory Laboratory, RIKEN, Wako, Saitama 351-0198, Japan*
[2] *Department of Applied Physics, The University of Tokyo, Tokyo 113-8656, Japan*
e-mail: ryuji.takahashi@riken.jp

The tunneling phenomenon represents one of the most characteristic features of quantum mechanics, which cannot be described by classical physics. One of the descriptions of these phenomena, the Landau-Zener (LZ) tunneling problem plays an important role for quantum tunneling in nanoscale systems. To obtain the transition probability, the LZ formula is widely used, and conventionally, for quantum particles in periodic systems, this formula is derived on the basis of the *k.p* approximation, which is valid for the small gap and small wavenumber. Therefore, it is not sufficient for the calculation of the tunneling probability by the LZ formula, when we take into account the nonlinear effect due to the lattice.

In this presentation, we report the LZ tunneling problem for particles bound in the periodic lattice [1]. To this end, for general periodic systems, we construct the path integral based on the Bloch and Wannier functions in the presence with an external force F, and the transition amplitude is calculated for a simple one-dimensional lattice model with a constant gap Δ and lattice constant a. Then, we find that the tunneling probability in bulk periodic systems becomes drastically larger than that by the LZ formula P_{LZ}. In Fig. 1, the calculation result of the transition probability P is shown as a function of the magnitude of the nearest-neighbor hopping integral v in the right vertical axis, and the left vertical axis shows the ratio between P and P_{LZ}. These results are calculated for $\Delta/aF = 10$. As shown in the results, the transition probability P becomes even more than 100 times larger than that of the LZ formula P_{LZ}. This enhancement is prominent for small values of the external field F or small hopping integral v compared with the gap, and comes from the difference between the Dirac and the periodic dispersions. In addition, when the lattice effect is strong, another analytical formula of the tunneling probability is given with a different behavior from the Landau-Zener formula.

[1] Ryuji Takahashi and Naoyuki Sugimoto, *Phys. Rev. B* 95, 224302(2017).

978-3-901578-31-1

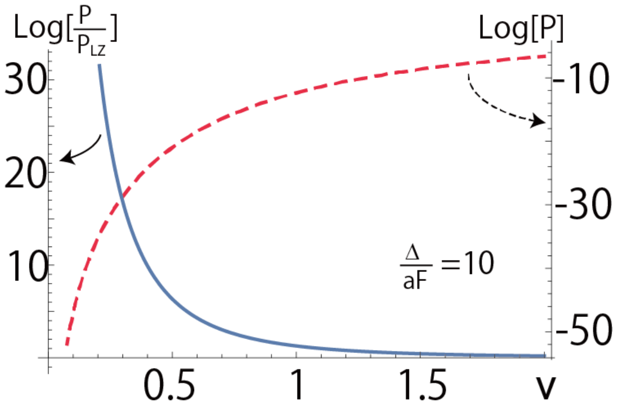

Fig.1: The right and left vertical axes show values of the transition probability P and the ratio P/P_{LZ} *for =Δ/aF= 10, respectively. The probability with the lattice effect P is much larger than* P_{LZ}*. The hopping integral v is shown in units of* Δ.

978-3-901578-31-1

P-26

Nuclear spin polarization and resistively-detected nuclear magnetic resonance in quantum point contact

Tomosuke Aono[1], Peter Stano[2,3], Minoru Kawamura[2] , Keiji Oono[2], and Takashi Komine[1]

[1] *Faculty of Engineering, Ibaraki University, 4-12-1 Nakanarusawa, Hitachi 316-8511, Japan*
[2] *RIKEN Center for Emergent Matter Science, Wako 351-0198, Japan*
[3] *Institute of Physics, Slovak Academy of Sciences, 84511 Bratislava, Slovakia*

e-mail: tomosuke.aono.ee@vc.ibaraki.ac.jp

In a quantum point contact (QPC) system, the electron-electron interaction induces spin correlations of conduction electrons. The correlations change the nuclear spin distribution near the QPC center. Recently the magnetization of conduction electron is measured by the resistively detected NMR (RDNMR) [1]. In this work, we discuss the dynamical nuclear spin polarization (DNP) due to the current through QPCs.

When an external magnetic field B_{ex} is applied, the QPC potential is spin-dependent, described by an S-matrix S_{QPC}. The hyperfine interaction between conduction electrons and nuclei induces the spin flip-flop processes. The spin-flip rate is calculated by the Fermi's golden rule using S_{QPC}. The value of the DNP, p, is determined by the rate equation for the nuclear spin [2].

Figure 1(a) shows the distribution of p when $G \simeq e^2/h$. The black arrow indicates the direction of the current. The DNP distribution changes its sign at the QPC center; $p < 0$ for the upstream side of the QPC while $p > 0$ for the downstream side. This DNP reverses its orientation when the direction of the current is reversed as shown in (b). The DNP distribution comes from the scattering processes for conduction electrons as shown in Figs. 1(c) and (d). When $G=e^2/h$, up spin electrons can pass through the QPC. When an electron with the down spin that flips to the up spin before the transmission, it induces the down DNP, while the electron flips its spin after the transmission, it induces the up DNP.

We discuss electron transport under the DNP structure in Fig. 1(a-b). The effective magnetic field $B = B_{\mathrm{ex}} + B_{\mathrm{N}}$ is $B > B_{\mathrm{ex}}$ for $p < 0$ and $B < B_{\mathrm{ex}}$ for $p > 0$, since the Overhauser field $B_{\mathrm{N}} < 0$ for $p > 0$. The conductance under the DNP is calculated with and without the NMR, denoted by G(NMR), and G(w/o NMR), respectively. It is shown that $\Delta G = G(\mathrm{NMR}) - G(\mathrm{w/o\ NMR})$ is proportional to the shot noise and $\Delta G > 0$ for weak Coulomb interactions. When the Coulomb interaction is strong, ΔG can change its sign.

[1] M. Kawamura, K. Ono, P. Stano, K. Kono, and T. Aono, Phys. Rev. Lett. 115, 036601 (2015).
[2] A. Singha, M. H. Fauzi, Y. Hirayama, and B. Muralidharan, Phys. Rev. B 95, 115416 (2017).

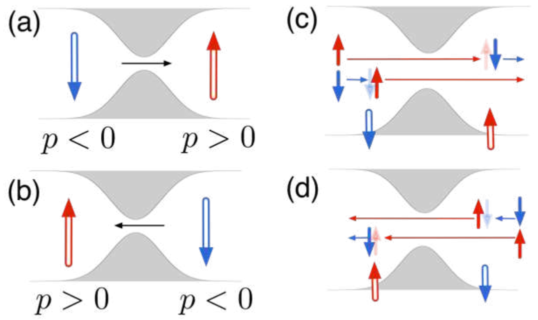

Fig.1:(a-b) DNP distribution; (c-d) Scattering processes of conduction electrons in (a) and (b), respectively

P-27

Numerical simulation of s- and p-wave superconductor heterostructures within the (1+1)D Bogoliubov-de Gennes equation

M. Schwendt, F. Atteneder, F. Zierler, and W. Pötz

Department of Physics, Karl-Franzens University of Graz, 8010 Graz, Austria
e-mail: walter.poetz@uni-graz.at

The original Bogoliubov-de Gennes (BdG) equation offers a mean-field description of spatially inhomogeneous s-wave superconductors, capturing physical effects, such as Andreev reflection and Andreev bound states[1,2]. Spectral analysis of the Andreev-reflected particle beam has been used to identify the type of superconductor[3]. Due to their inherent particle-hole symmety, BdG-type equations have received renewed interest in connection with Majorana fermion realization. Experimental efforts are striving for realization of nanostructures emulating Kitaeev chains[4].

In this work we report on the simulation of s- and p-wave superconductor-heterostructures in (1+1)D within the Crank-Nicholson propagator. In particular, we address the problem of open simulation boundaries and offer two alternative solutions: exact transparent (T) and perfectly-matched-layer (PML) boundary conditions (BCs). The former are constructed in full compatibility with the underlying discretization and formally provide an exact solution to absorbing BCs[5]. Numerical complexity arises from the need for inverse Z-transformations in the effort to, essentially, compute the dynamics in the outside domains in parallel. For the latter, a complex material is constructed by coordinate extension into the complex plane, applied to the interior domain of the physical system[6]. This complexity is used to dampen wave contributions travelling towards the simulation boundaries. PML-BCs readily lend themselves to extension to higher spatial dimensions, whereas, the great numerical efforts associated with the T-BC approach seem to be prohibitive in this regard.

Numerical examples demonstrating successful implementation of absorbing boundary conditions are given for Andreev reflection: single Andreev reflection at a metal-superconductor interface, and multiple Andreev reflections at metal-superconductor double interfaces. Spectral analysis yields information on the underlying electronic structure[8]. Both s- and p-wave superconductors are treated.

[1] P. G. de Gennes, Superconductivity of Metals and Alloys (Westview Press, 1964).
[2] Ying Liu and Zhi-Qiang Mao, Physica C, **514,** 339 (2015).
[3] F. Laube et al., Phys. Rev. Lett., **84**, 1595 (2000).
[4] A. Yu Kitaev, Phys.-Usp., **44,** 131 (2001).
[5] A. Zisowsky et al., ZAMM Z. Angew. Math Mech., **85**, 793 (2005).
[6] J.-P. Berenger, Comp. Phys., **114** (1), 185 (1994).
[7] M. Schwendt, Transparent boundary conditions for Bogoliubov-de Gennes equations in (1+1)D, Master Thesis, University of Graz (2017).
[8] F. Atteneder et al. unpublished.

978-3-901578-31-1

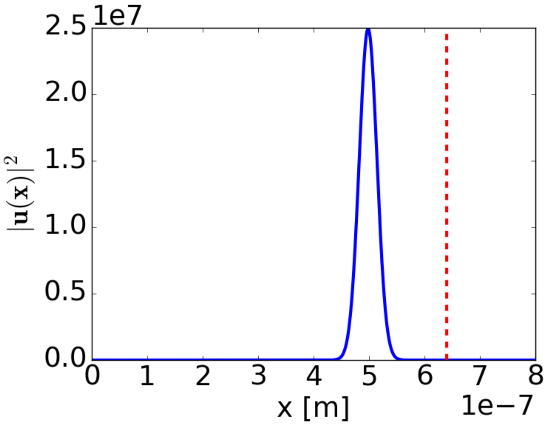

Fig.1: Andreev reflection at a metal to s-wave superconductor interface (red dashed line) using T-BCs: high-energy incident electron wave-packet.

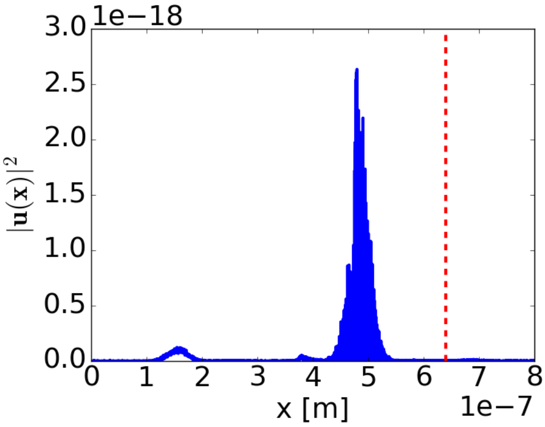

Fig.2: Andreev reflection at a metal to s-wave superconductor interface: surviving electron wave-packet back-reflected from the right simulation boundary (note the change in scale).

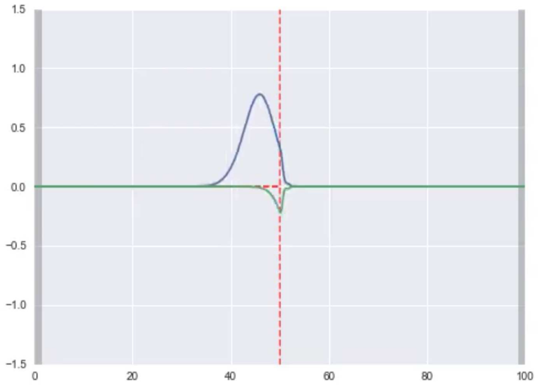

Fig.3: Andreev reflection at a metal to p-wave superconductor interface (red dashed line) using PML-BCs: onset of reflection, incident electron wave-packet in blue, reflected hole wave packet in green.

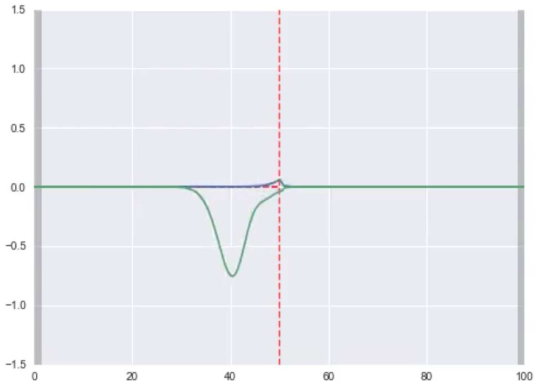

Fig.4: Andreev reflection at a metal to p-wave superconductor interface (red dashed line): near completion of reflection.

978-3-901578-31-1

P-28

Thermionic Cooling Devices Based On AlGaAs/GaAs Heterostructures

Aymen Yangui*, Marc Bescond, and Kazuhiko Hirakawa

[1] *Quantum Semiconductor Electronics Lab (Hirakawa Group), Institute of Industrial Science,*
University of Tokyo, 4-6-1 Komaba, Meguro-ku, Tokyo 153-8505, Japan
**e-mail: yangui@iis.u-tokyo.ac.jp*

In the modern electronics, energy saving and thermal management technologies are becoming extremely important. For example, very-large-scale integration are now approaching their physical limits, because materials cannot tolerate the heat dissipated in the circuits.1 In addition, energy-efficient cooling technology is also desired because of the environmental concern. Therefore, thermal control has become increasingly important in the designed operation of electronic equipment and the development of new efficient cooling technologies is indispensable for future progress in electronics. In the present work, we present a theoretical and experimental investigations of a semiconductor heterostructure refrigerator (SHR) initially proposed in 2005 by Chao et al.2 This device structure is based on a concept of "thermionic cooling" by coupling tunneling injection with thermionic extraction (Fig. 1). The electron transport in this device is due to resonant tunneling and subsequent thermionic emission. Cold electrons are injected into the active region by resonant tunneling through an injector potential barrier and subsequently removed from the active region by a thermionic process above a thick potential barrier that works as an extractor barrier and serves as a thermal wall to reduce the heat backflow into the active region (Fig 1). This rather simple electronic transport process efficiently removes heat from the quantum well layer and works as a refrigerator. Our first theoretical and experimental results show a lattice temperature drop ~ 20 mK and an electron temperature drop ~ 15 K under 100 mV bias voltage, at room temperature. More experiment and numerical analysis will be performed in order to optimize the performances of the device and to reach the highest thermionic cooling efficiency.

[1] Rhyner, R.; Luisier, M. Nano Letters 2016, 16, (2), 1022-1026.

[2] Chao, K. A.; Larsson, M.; Mal'shukov, A. G.; C., L.; A., S.; E., B. J. Applied Physics Letters 2005, 87, (2), 022103.

978-3-901578-31-1

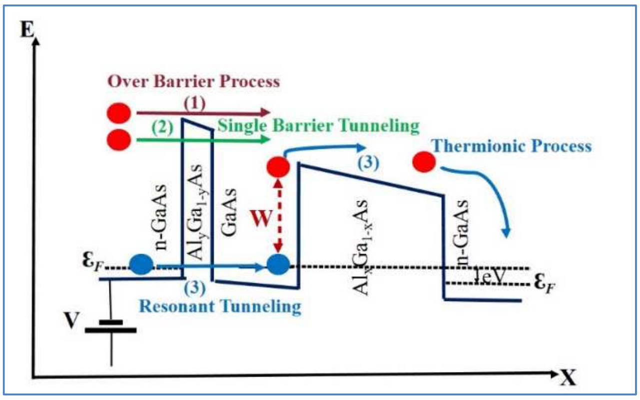

Fig.1: Physical processes for the operation of the SHR. (1) Over barrier process, (2) single barrier tunneling process, and (3) resonant tunneling/thermionic process.

P-29

Field-induced crystallization of $Ge_2Sb_2Te_5$ amorphous studied by strong THz pulses

Yasuyuki Sanari[1], Yuta Saito[2,3], Kento Uchida[1], Takehiro Tachizaki[4], Koichiro Tanaka[1],
Junji Tominaga[2,3], Muneaki Hase[3,5], and Hideki Hirori[6,7]

[1]*Dept. Phys., Kyoto Univ.,* [2]*Nanoelectronics Research Inst., AIST,* [3]*JST-CREST,* [4]*Dep. Eng., Tokai Univ.,* [5]*Div. Appl. Phys., Univ. Tsukuba,* [6]*ICR, Kyoto Univ.,* [7]*JST-PRESTO*

Chalcogenide alloys, such as $Ge_2Sb_2Te_5$ (GST) and the interfacial phase change memory (iPCM) material, are very important materials for nonvolatile memory devices [1-4], because the phase transition between the amorphous and crystalline states exhibits a large difference in electrical resistance and may occur on ultrafast timescales by applying electrical pulses [5]. The measurement on the dynamics of nucleation and growth under high electric fields should play a vital role in clarifying the microscopic mechanism of the phase-change transformations [6]. In this study, we investigated the crystallization dynamics of a GST amorphous sample by irradiating with strong THz pulses [7]. The sample is composed of GST amorphous layer, ZnS-SiO_2 cap layer, Si substrate and Au antennas array (shown in Fig.1). A finite-difference time-domain calculation shows that Au antennas enhance the peak THz electric field to the order of 1 MV/cm at the center of antenna gap. Figure 2 shows optical microscope image of the sample irradiated with 86000 shots of THz pulse. Raman spectroscopy (Fig. 3) reveals that the reflectivity changes in Fig. 2 are caused by THz field-induced crystallization of the sample [8]. The elongated crystallization growth along the electric field direction implies that the higher conductivity of the crystal area than that of the amorphous one concentrates the electric field and Joule heat produced by surge current increases the temperature at the edge of the crystalized area, leading to prompt crystallization.

[1] A. V. Kolobov *et al.*, Nat. Mater. 3, 703 (2004).
[2] J. Tominaga *et al.*, Sci. Technol. Adv. Mater. 16, 014402 (2015).
[3] R. E. Simpson *et al.*, Nat. Nanotech. 6, 501 (2011).
[4] 3D-X-Point memory (Octane) from Intel & Macron Technology for storage class memories has already been commercialized since this May. (See the website as reference [https://www.micron.com/about/our-innovation/3d-xpoint-technology].)
[5] P. Zalden *et al.*, Phys. Rev. Lett. 117, 067601 (2016).
[6] M. Simon *et al.*, J. Appl. Phys. 108, 064514 (2010).
[7] H. Hirori *et al.*, Appl. Phys. Lett. 98, 091106 (2011).
[8] P. Nemec *et al.*, Mater. Chem. Phys. 136, 935 (2012).

978-3-901578-31-1

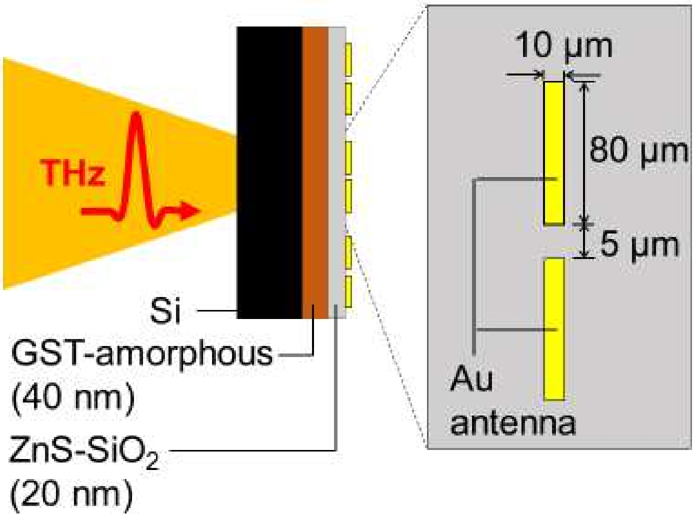

Fig.1: Experimental setup. Au antenna enhances THz electric field at 5µm gap. GST amorphous films of 40 nm thickness were sputter deposited at room temperature onto Si(100) substrates. ZnS-SiO$_2$ cap prevents GST from oxidation and Au diffusion.

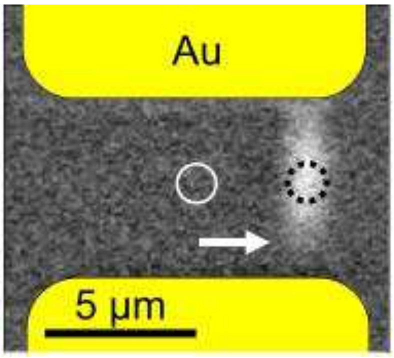

Fig.2: Optical microscope image of sample after THz irradiation. The presented images were obtained by averaging over 20 images (460 shots) centered with the 86000 shots. White arrows indicate the edge of the crystallized area.

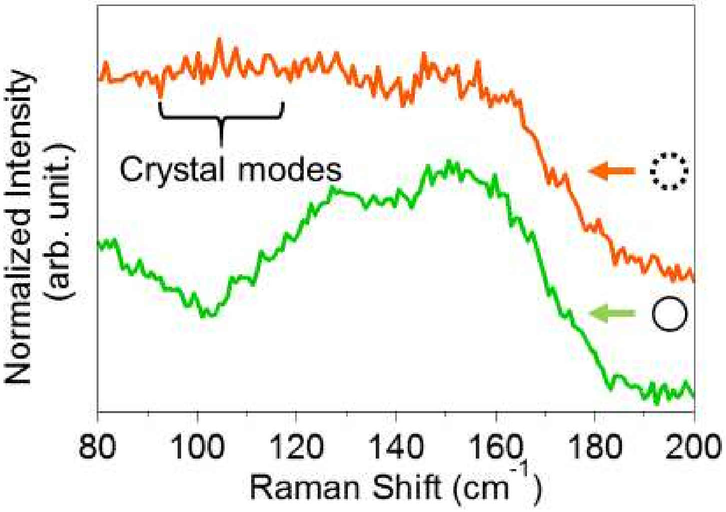

Fig.3: Raman spectra of the sample. Modes originating GST crystal around 110 cm $^{-1}$ *(*A_1 *mode of* $GeTe_4$*,* $E_g(2)$ *mode of* Sb_2Te_3*) was observed in the area showing reflectivity changes indicated by the dashed circle in Fig.2 [8].*

P-30

Inverse tunneling of free vacuum electrons into a solid

Peng Zhang[1], and Tony Pan[2]

[1]*Department of Electrical and Computer Engineering, Michigan State University, East Lansing, Michigan 48824-1226, USA*
[2] *Modern Electron, Bellevue, Washington 98007, USA*
e-mail: pz@egr.msu.edu

The field emission heat engine (FEHE) is a novel thermionic converter to directly convert heat into electricity with high efficiency. By applying strong electric fields on the anode and/or cathode to set up quantum tunneling barriers, the escaped electrons from a hot cathode with energies lower than the surface vacuum level will transit the vacuum gap, and “inverse tunnel” into the cooler anode [1,2]. This process produces electrical power output when the converter is connected to an external load. This paper presents an exact analytical theory for the inverse tunneling of free vacuum electrons through a triangular potential barrier into a metal [3]. Both exact electron wave functions and the transmission probability are obtained analytically, and compared with those for classical field emission (c.f. Figs. 1 and 2). It is found that the inverse tunneling probability is the same as that of the field emission of electrons from metal into vacuum, for the same incident electron energy, metal properties (work function, Fermi energy), and applied electric field. The theory is extended to the more general three-dimensional (3D) model, where the electron travels at arbitrary direction with an oblique angle to both the front and the back of the potential barrier.

P. Zhang was supported by AFOSR Grant No. FA9550-14-0309 through a subcontract from the University of Michigan.

[1] R. A. Hyde, J. T. Kare, N. P. Myhrvold, T. S. Pan, and L. L. W. JR, US8575842 B2 (5 November 2013).

[2] T. Pan, H. Busta, R. Gorski, and B. Rozansky, in 2014 27th Int. Vac. Nanoelectron. Conf. IVNC (2014), pp. 147–148.

[3] P. Zhang and T. Pan, AIP Adv. **7**, 065307 (2017).

978-3-901578-31-1

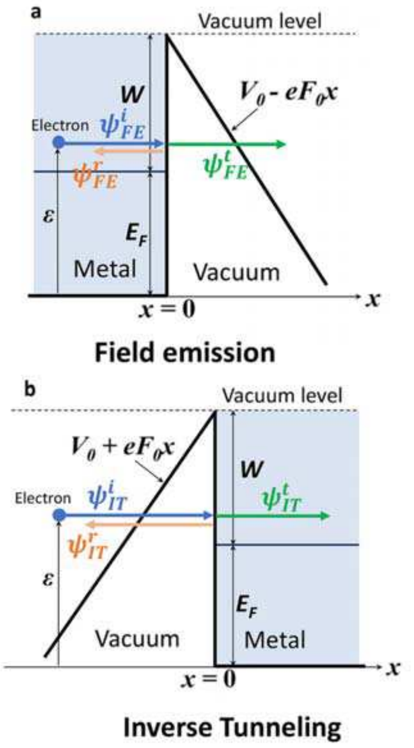

Fig.1: (a) Field emission, and (b) Inverse tunneling. The metal-vacuum interface is located at $x = 0$. The metal has Fermi level E_F and work function W, with $V_0 = E_F + W$. The external DC electric field is F_0. The initial electron energy is at ε. The incident electron wave is ψ^i, the transmitted and reflected electron waves are ψ^t and ψ^r respectively.

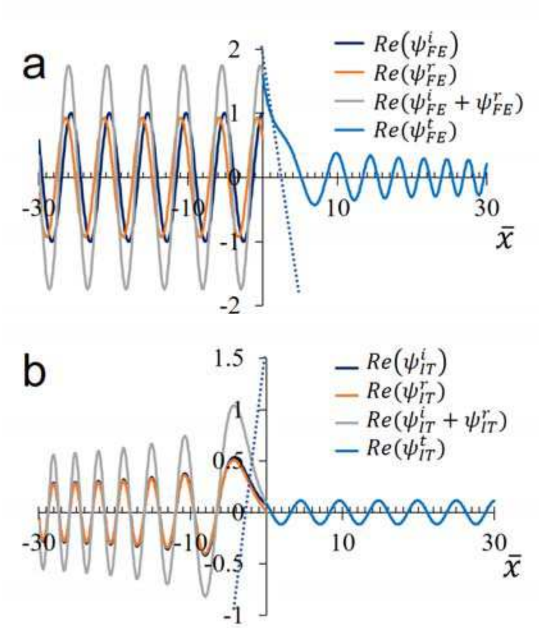

Fig.2: Electron wave function for (a) Field emission, and (b) Inverse tunneling. In the calculation, we assume $E_F = W$, $\varepsilon = 1.5\ W$, and $F_0 = 0.2W$. The incident electron wave is ψ^i, the transmitted and reflected electron waves are ψ^t and ψ^r respectively. The dashed lines indicates the location of the potential barrier.

P-31

Growth and characterization of GaSb quantum nanostructures by solid-source molecular beam epitaxy

Yasushi Shoji[1], *and Yoshitaka Okada*[1]

[1] *Research Center for Advanced Science and Technology, The University of Tokyo,*
Meguro-ku, Tokyo 153-8904, *Japan*
e-mail: shoji@meb.rcast.u-tokyo.ac.jp

III-V semiconductor quantum nanostructures (QNs) such as quantum dot (QD), wire (QWi), and ring (QR) have attracted interest due to excellent optical properties. In particular, QNs with type-II band alignment have been expected to be applied in light receiving devices, since they are capable of responding to infrared photon and realizing long carrier lifetime. A GaSb/GaAs is one of the material systems forming of type-II band alignment. In this study, we investigated the structural properties of GaSb QDs and QRs grown at several conditions. The samples were fabricated on semi-insulating GaAs (100) substrates by molecular beam epitaxy (MBE). A 250 nm-thick GaAs buffer layer was grown with As flux of 2.0×10^{-3} Pa, after the thermal cleaning of the surface at 580°C. Then, GaSb of 2.5 MLs was grown on Sb terminated surface at 480°C. The Sb flux in growing a GaSb layer was varied from 1.4×10^{-5} to 11.5×10^{-5} Pa. The Ga flux and GaSb growth rate were 1.6×10^{-5} Pa and 0.6 um/h, respectively. After the growth of GaSb layer, As soaking of 1.0×10^{-3} Pa was applied from 0 to 30 sec. Figure 1 shows the atomic force microscopy (AFM) images of GaSb layer grown with Sb flux of (a) 1.4×10^{-5} Pa, (b) 3.7×10^{-5} Pa, and (c) 11.5×10^{-5} Pa, respectively. These samples were fabricated without As soaking. It can be seen that 2-dimensional layer was formed for the sample grown with Sb flux of 1.4×10^{-5} Pa. This reason is considered that GaAsSb layer was grown by the influence of As atoms remained in the MBE chamber. In the other samples, though the formation of 3-dimensional islands was observed from AFM images, the shape of QNs differed with Sb flux. Figure 2 shows the photoluminescence (PL) spectra of GaSb QDs grown at different Sb flux. The PL intensity for GaSb QDs grown with Sb flux of 3.7×10^{-5} Pa is higher than that of QDs formed with Sb flux of 11.5×10^{-5} Pa. These results suggest that excess supply of Sb changes the growth mode of GaSb QDs, and it causes the non-radiative recombination centers. Finally, we investigated the change of GaSb QN shape during As soaking. Figure 3 (a) - (d) show the AFM images of the GaSb QNs applied with As soaking from 0 to 30 sec. In this study, all GaSb QNs changed to ring shape by As soaking of 22 sec or higher. The change of shape is reported to be due to desorption of Sb from GaSb QNs which takes place by As/Sb exchange [1,2]. Figure 3 (e) shows enlarged images of QNs observed in Fig. 3 (b). For the sample applied with As soaking of 10 sec, a mixed structure of QNs different in degree of progress in the transition from QD to QR was formed. We found that the shape change of QN due to As soaking takes place from the edge. The exchanges of Sb and As atoms tend to occur at weak bonds between Ga and Sb. Therefore, the transition mechanism from QD to QR is thought to be involved in strain distribution of GaSb QNs.

[1] S. Kobayashi et al., Jpn. J. Appl. Phys. **43**, No. 5B (2004).

[2] W.-H. Lin et al., IEEE Photonics Technol. Lett. **24**, 1203 (2012).

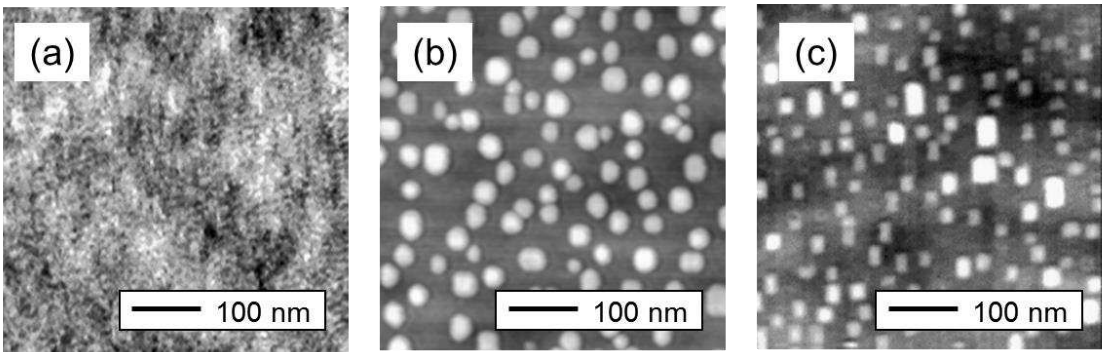

Fig.1: AFM images of GaSb layer grown with Sb flux of (a) 1.4 ×10^{-5} Pa, (b) 3.7 ×10^{-5} Pa, and (c) 11.5 ×10^{-5} Pa, respectively.

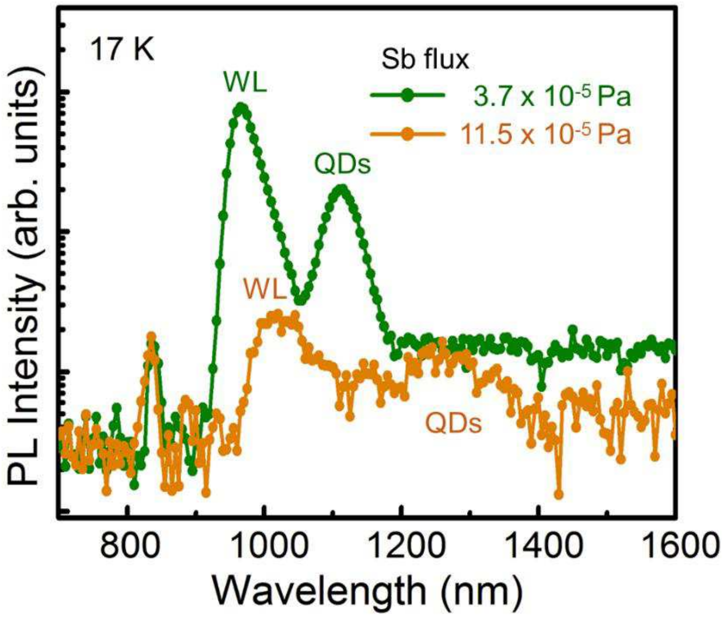

Fig.2: PL spectra of GaSb QDs grown with different Sb flux. The PL measurement was also carried out at low temperature of 17 K using a closed-cycle cryostat. The signals located at around 1000 nm are the emission from wetting layer (WL).

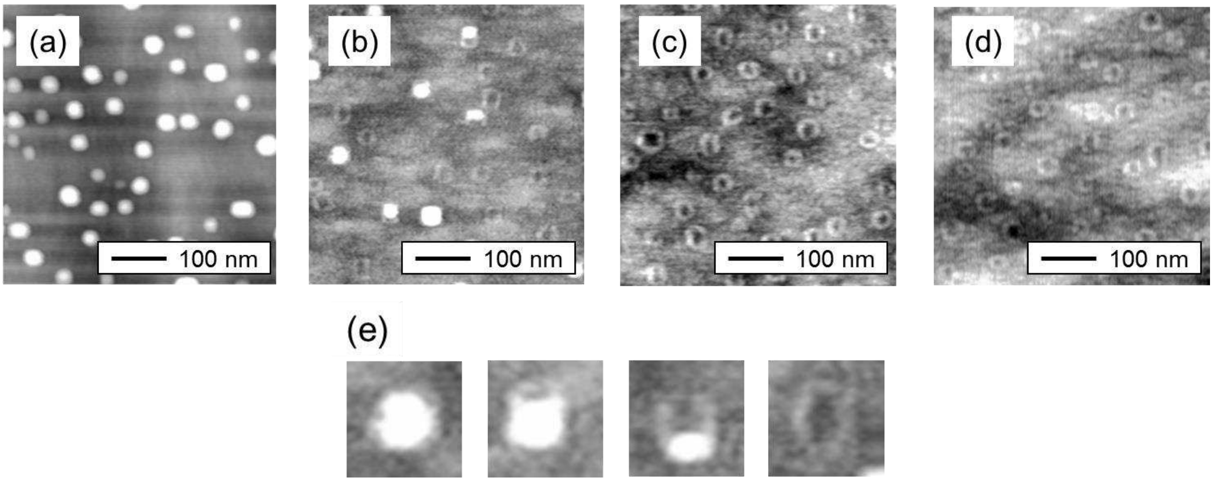

Fig.3: (a) - (d) show the AFM images of the GaSb QNs applied with As soaking from (a) 0 sec, (b) 10 sec, (c) 22 sec, and (d) 30 sec. (e) shows enlarged image of QNs observed in Fig.3 (b).

P-32

Effect of sulfur passivation using aqueous and alcoholic ammonium sulfide solutions on the specific contact resistivity of Ni contact to InAs layer epitaxially grown on $In_{0.56}Ga_{0.47}As$ epilayer.

[1]

Sim-Hoon Youk[1], Han-Soo Jang[1], and Chel-Jong Choi[1]*

School of Semiconductor and Chemical Engineering, Semiconductor Physics Research Center (SPRC), Chonbuk National University, Jeonju 561-756, Republic of Korea

*email : cjchoi@jbnu.ac.kr

We have investigated the effect of sulfur passivation using aqueous and alcoholic ammonium sulfide solutions on the specific contact resistivity of Ni contact to InAs layer epitaxially grown on $In_{0.56}Ga_{0.47}As$ epilayer. Prior to 50 nm-thick Ni deposition using DC sputtering system, InAs epilayer was treated at room temperature in the aqueous or in alcoholic ammonium sulfide solution for 100 sec. The aqueous and alcoholic ammonium sulfide solutions were prepared using the dilution of ammonium sulfide by water and isopropyl alcohol in the ratio of 1:100 by volume, respectively. The specific contact resistivity of Ni/InAs contact with alcoholic ammonium sulfide treatment was much lower than that with aqueous ammonium sulfide one, of which values were 4.09×10^{-9} and 1.06×10^{-7} Ωcm^2, respectively. From X-ray photoelectron-spectroscopy analysis, As-S/As-In bonding ratios were calculated to be 3.1 and 0.8 for the InAs surfaces chemically treated by alcoholic and aqueous ammonium sulfide solutions, respectively, implying that alcoholic ammonium sulfide treatment was more effective in the sulfur passivation of InAs surface than aqueous ammonium sulfide treatment. The ultraviolet photoelectron spectroscopy measurements revealed that the work function of alcoholic ammonium sulfide treated InAs surface was higher than that of aqueous ammonium sulfide treated InAs one. Based on XPS and UPS results, the improvement of specific contact resistivity of the Ni/InAs contact through alcoholic ammonium sulfide surface treatment could be due to the reduction of contact barrier height between Ni and InAs associated with better sulfur passivation of InAs surface.

978-3-901578-31-1

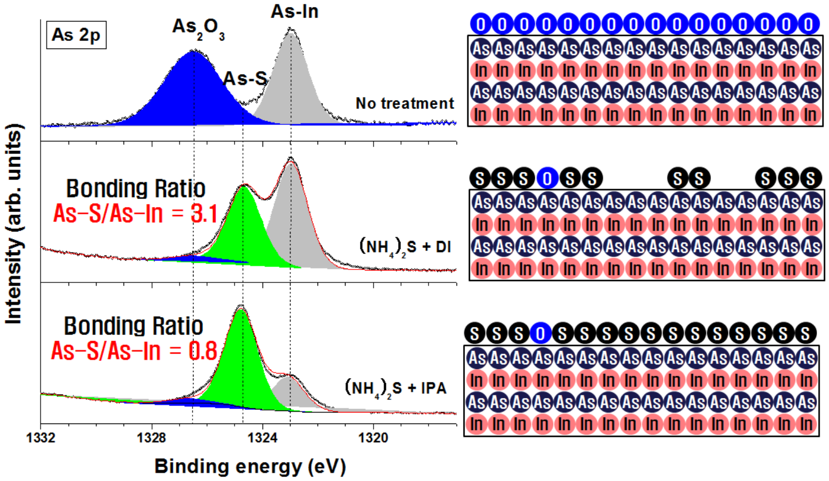

Fig1. XPS analysis and illustration for surface treatment of Ni contact to InAs layer epitaxially grown on In$_{0.56}$Ga$_{0.47}$As epilayer

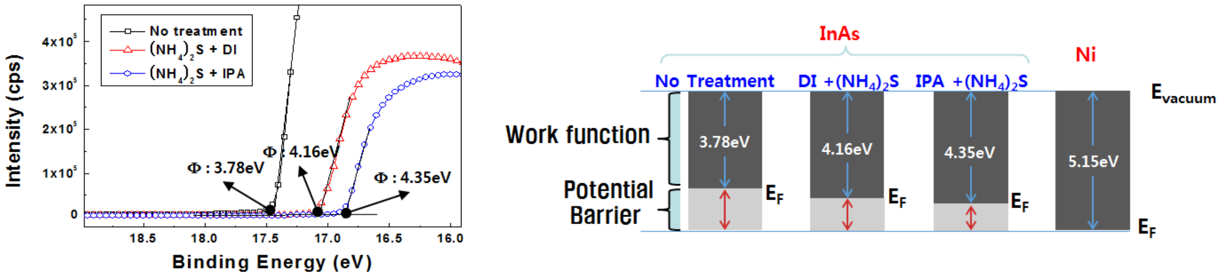

Fig2. UPS analysis and illustration for the band diagram based on UPS result

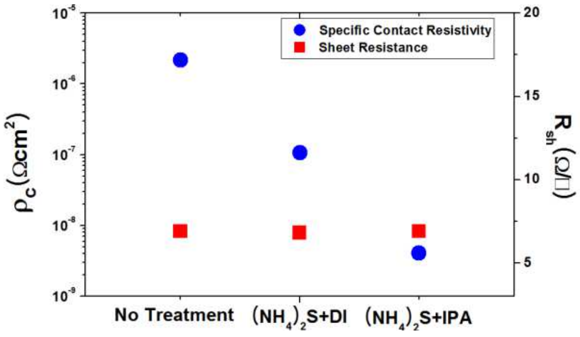

Fig.3 specific contact resistivity and sheet resistance for surface treatment of Ni contact to InAs layer epitaxially grown on In$_{0.56}$Ga$_{0.47}$As epilayer

P-33

Microstructural and electrical properties of Ni stanogermanides formed on $Ge_{0.92}Sn_{0.08}$ epi-layer grown on Si(100) substrate

Han-Soo Jang[1], Sim-hoon Yuk[1], Yeon-Ho Kil[1], Kyu-Hwan Shim[1] and Chel-Jong Choi[1]*

[1]*School of Semiconductor and Chemical Engineering, Semiconductor Physics Research Center (SPRC), Chonbuk National University, Jeonju 561-756, Republic of Korea*

**email : cjchoi@jbnu.ac.kr*

We present a comprehensive study on the microstructural and electrical properties of Ni stanogermanides formed on $Ge_{0.92}Sn_{0.08}$ epi-layer grown on Si(100) substrate. For the formation of Ni-stanogermanides, 30 nm-thick Ni film was deposited on $Ge_{0.92}Sn_{0.08}$ film, followed by rapid thermal annealing (RTA) process at the temperatures in the range of 300 – 600 °C for 30 s under N_2 ambient. Ni-rich stanogermanide ($Ni_3(Ge_{1-x}Sn_x)$) phase with cubic structure was formed after RTA at 300 °C, above which Ni-mono stanogermanide ($Ni(Ge_{1-x}Sn_x)$) was the only phase formed as a result of solid-state reaction between Ni and $Ge_{0.92}Sn_{0.08}$. The RTA process at 400 °C led to the formation of $Ni(Ge_{1-x}Sn_x)$ film having relatively uniform surface and interface morphologies, allowing the minimum value of sheet resistance. The samples annealed above 500 °C underwent the severe structural degradation of $Ni(Ge_{1-x}Sn_x)$ without maintaining film continuity known as agglomeration, resulting in a rapid increase in the sheet resistance. Regardless of RTA temperature, secondary ion mass spectroscopy (SIMS) results combined with energy dispersive X-ray spectroscopy (EDX) line profiling showed the segregation of Sn atoms near surface and interface region, indicating that the amount of Sn atoms were out-diffused during Ni-stanogermanides process. In particular, laterally confined Se atoms which were distributed along interface between $Ni(Ge_{1-x}Sn_x)$ island and $Ge_{0.92}Sn_{0.08}$ film was observed in the sample annealed at 600 °C.

978-3-901578-31-1

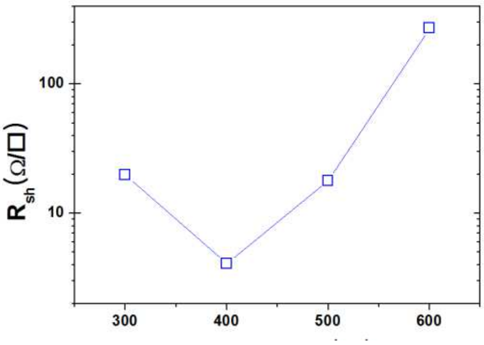

Fig1. Sheet resistance of Ni-GeSn samples annealed at various temperatures for 60 seconds

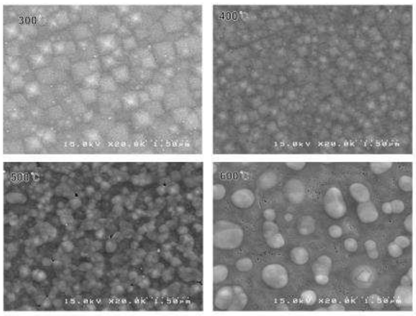

Fig2. SEM image of Ni-GeSn samples annealed at various temperatures for 60 seconds

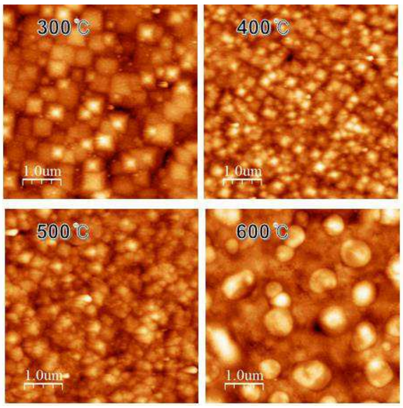

Fig3. AFM image of Ni-GeSn samples annealed at various temperatures for 60 seconds

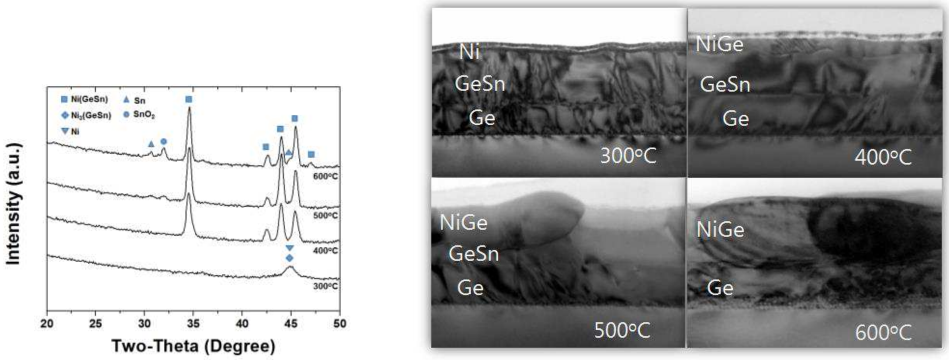

Fig4.XRD result and TEM image of Ni-GeSn samples annealed at various temperatures for 60 seconds

978-3-901578-31-1

P-34

Numerical Study of Quantum Efficiency of Quantum-Dot Intermediate-Band Solar Cells under Infrared Light Illumination

Katsuhisa Yoshida, and Yoshitaka Okada

Research Center for Advanced Science and Technology, The University of Tokyo, Meguro-ku,
Tokyo 152-8904, Japan
e-mail: yoshida@mbe.rcast.u-tokyo.ac.jp

Quantum-dot intermediate-band solar cell (QD-IBSC) has attracted due to its potential for a high energy conversion efficiency over 60% [1]. The quantum efficiency (QE) measurement with infrared(IR) biasing light has been employed to characterize the key feature of QD-IBSC - the two-step photon absorption via IB (see Fig. 1 a). The detailed discussion of the light biased QE, however, has not been developed. In this study, we simulated IR light biased QE by using the self-consistent drift-diffusion method for IBSC [2] with including an electron capturing process by IB (non-radiative process) as illustrated in Fig. 2, and studied the capturing effect on QE. Figures 1 and 2 summarize the equations, the device structure and the calculation condition employed in this study. QE was calculated by taking a difference of current densities with and without monochromatic light illumination, and by dividing that difference by the product of elementary charge and incident photon flux density of the monochromatic light as described in Fig. 3.

Figure 4 shows calculated QEs with and without IR light illumination under short-circuit condition. In standard QE results (Fig. 4 a), the cell with a shorter capturing time shows a larger QE in a spectral range for the optical transition between IB and the valence band (VB). It indicates photo-generated IB electrons from VB can easily excite into the conduction band (CB) through the CB-IB non-radiative process and finally can be extracted to the contract. As a result, the shape of QE in the wavelength range for IB-VB photon absorption resembles the absorption coefficient of IB-VB (red curve in Fig. 4 a). In the spectral range for CB-VB optical excitation, the short time constant degrades QE. For ideal IBSC operation in which there is no fast capturing process ($1/\tau < 10^{10}$ s^{-1}), QE in IB-VB excitation range should be negligibly small. Under the IR light illumination (Fig. 4 b), the ideal cell has a significant QE enhancement due to the optical electron excitation from IB to CB by IR light, while the cell with a short capturing time does not show a clear increase. Therefore, by taking a difference of QEs with and without IR bias light, we can evaluate the ability of the two-step photon absorption in QD-IBSCs.

[1] Y. Okada et al., Appl. Phys. Rev., **2**, 021302 (2015).

[2] K. Yoshida et al., J. Appl. Phys., **12**, 084510 (2012).

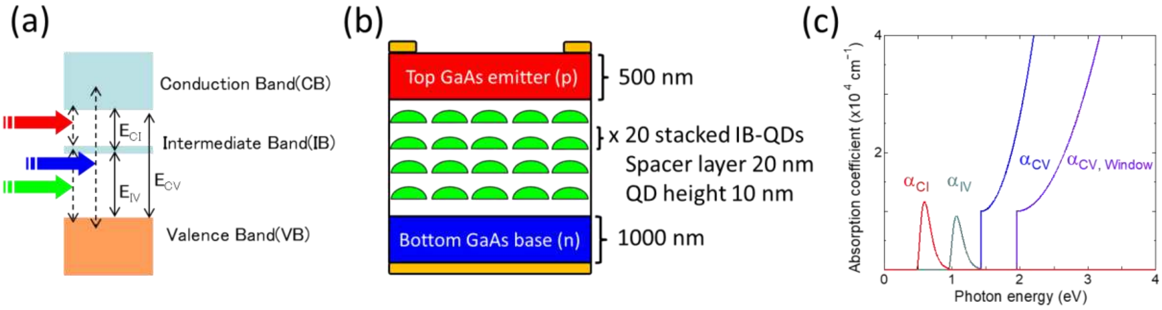

Fig.1: (a) Schematic of IBSC operation concept. E_{CV}, E_{IV}, and E_{CI} are CB-VB, IB-VB, and CB-IB energy gaps, respectively. The thick arrows with colors indicate incident lights with different wavelengths. (b) Schematic of the QD-IBSC structure employed in this study. GaAs material parameters are used. The top-emitter and the bottom-base layers have artificial window layers to suppress surface recombinations. E_{CV}, E_{IV}, and E_{CI} are 1.43, 0.95 and 0.48 eV, respectively. Window layers have the energy gap of 2.0 eV. (c) Absorption coefficients for each band-to-band optical transition. $\alpha_{CV,Window}$ is the coefficient of the window layers.

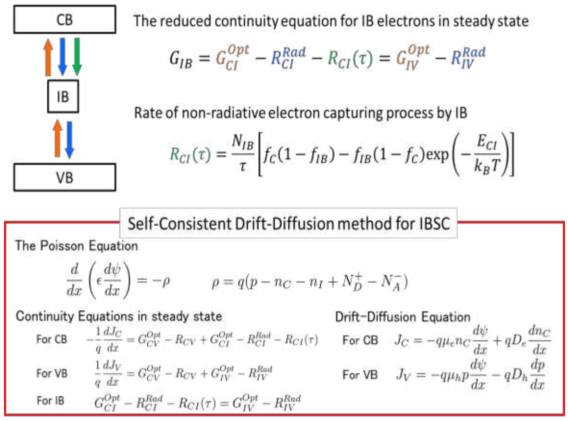

Fig.2: The self-consistent drift-diffusion method for QD-IBSC with including the electron capturing process $R_{CI}(\tau)$ by IB. G^{Opt} and R^{Rad} are optical carrier generation and radiative recombination rates, respectively. The definition of other symbols are the same shown in Ref. [2].

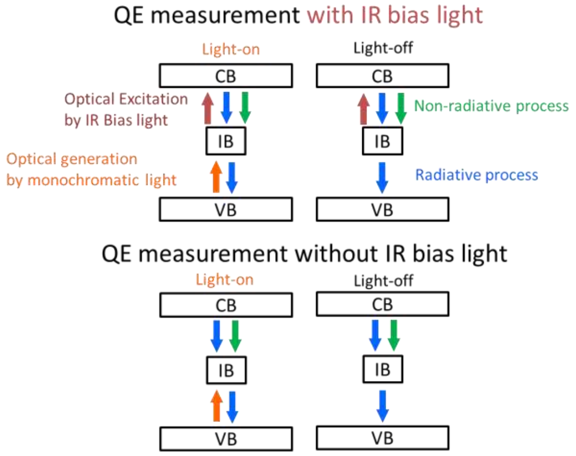

Fig.3: Schematics of QE calculation (top) with and (bottom) without IR bias light. QE is calculated by taking a difference of current densities of the cell with and without monochromatic light illumination and dividing that difference by the product of elementary charge and incident photon flux of the monochromatic light.

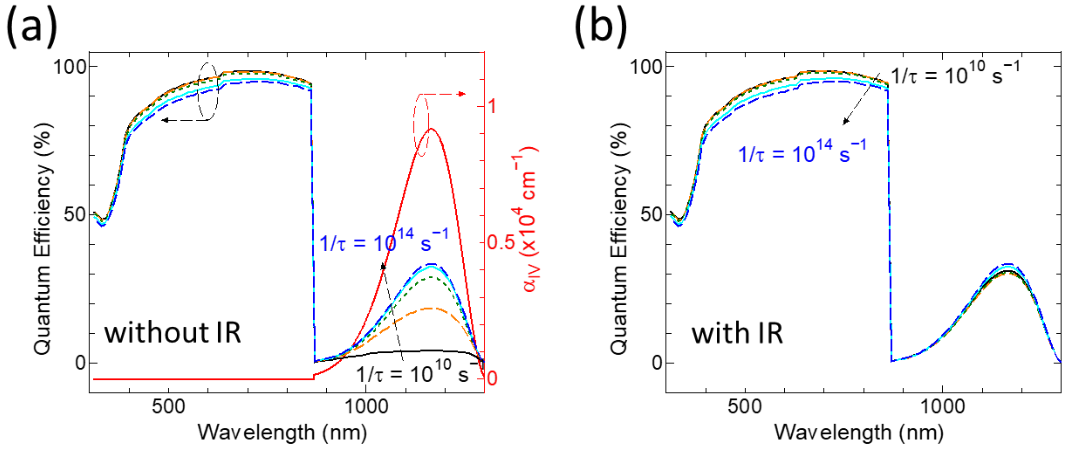

Fig.4: Calculated QEs (a) without and (b) with IR bias light illumination under short-circuit condition. IR light incidents to the cell with the power of 5 mW/cm^2 and the energy of 0.5 eV to only excite IB electrons to CB. The values of the capturing time constant τ are $10^{-10}, 10^{-11}, 10^{-12}, 10^{-13}$ and 10^{-14} s. A red curve shown in (a) shows the absorption coefficient of IB-VB α_{IV}. The shape of QE with a short time constant resembles α_{IV} in the wavelength range for IB-VB optical carrier generation.

P-35

A method of predicting pattern with etch rate of non-pattern wafer using ion beam etching

Jongsoon Park[1,2], Jongkyu Kim[1], Sangkuk Kim[1], Woohyun Lee[1], Ilhyeong Lee[1], Jongchul Park[1], Kyongsub Shin[1], Seokwoo Nam[1] and Heeyeop Chae[3]

[1] *Process Development Team 1, Samsung Electronics, Republic of Korea*
e-mail: puddinggu@*skku.edu*
[2] *School of Semiconductor and Display Engineering, Sungkyunkwan University (SKKU), Republic of Korea*
[3] *School of Chemical Engineering, Sungkyunkwan University (SKKU),Republic of Korea*

Magnetic Random Access Memory (MRAM) receive attention the most promising candidate for the next-generation memory to replace the conventional non-volatile memory. For this reason, physical and electrical properties of Magnetic Tunneling Juction (MTJ) have been evaluated and studied widely for a long time as a basic switching core materials in MRAM device. With the research of the magnetic and electrical properties of the MTJ materials, the method of MTJ patterning technology is also has been developed by lots of research groups and the semiconductor companies. Various etching technologies for patterning process to make a isolated pattern is developed and suggested for the purpose of mass production of MRAM patterning.

Among them, Ion Beam Etching (IBE) technology using the ion sputtering with noble gas is considered as a one of the promising and powerful candidate of MTJ patterning technology. IBE method has own several fundamental advantage compared to the conventional RIE plasma. In IBE equipment, plasma source and wafer surface is physically separated each other, so radical species which is the main degradating factor cannot react at MTJ material during the sputtering process.

In this paper, we studied on the phenomenon of sputtering surface during the IBE process between non pattern wafer and pattern wafer. Incident angle was changed for the purpose of examining the ion scattering at the wafer surface and the chamber itself. Beam divergence in scattering chamber was also studied and normalized according to distance between wafer and grid of the IBE chamber. Based on this, we analyzed the phenomenon of non uniformity at isolated pattern profile with the different position of the wafer using tilted ion beam etching process. Finally, we were able to predict the profile change during the patterning process using the tilted ion beam etching system, and also we could obtain the same results at 40nm isolated pattern.

978-3-901578-31-1

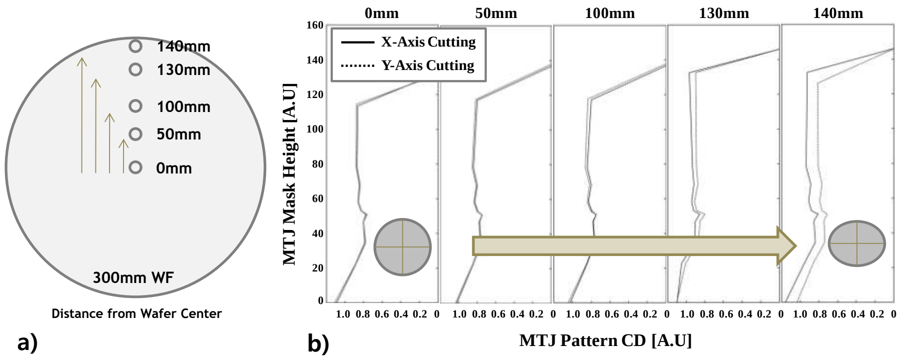

Figure 1. This graph show a results about the measurement of profile dimension by TEM. a) The position of the 12 inch wafer in the analyzed profile. b) x axis and y axis is represents each profile CD. According to the distance from the center, Gap between x-axis and y-axis are getting bigger

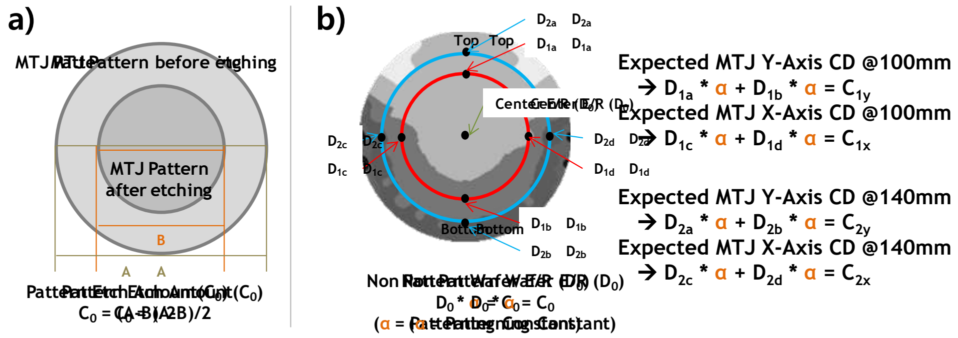

Figure 2. It is to explain how to create predictive models. a) Critical Demension(CD) of the pattern is measured at the different points of the wafer twice, before and after the etch. b) Non-pattern Etch Rate(E/R) was confirmed, and the correlation coefficient was extracted by matching with the difference of CD and E/R.

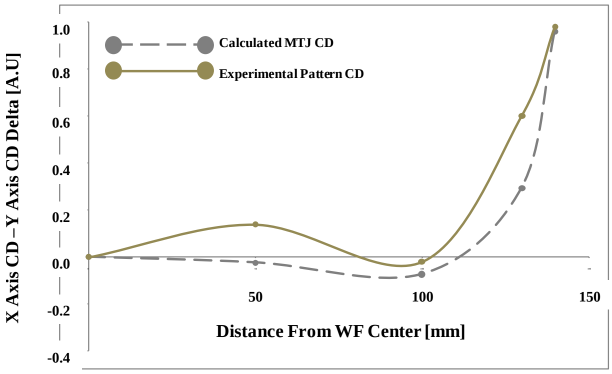

Figure 3. This figure shows a comparison between experimental data and calculated data

Quantum Control Over Diamond Qubits Using a Mechanical Resonator

Evan MacQuarrie[1], *Huiyao Chen*[1], *Matt Otten*[1], *Tanay Gosavi*[1], *Sunil Bhave*[2], *Stephen Gray*[3], *Gregory D. Fuchs*[1]

[1] Cornell University, Ithaca, NY 14853 USA
[2] Department of Electrical and Computer Engineering, Purdue University, West Lafayette, IN 47907, USA
[3] *Center for Nanoscale Materials, Argonne National Laboratory, Argonne, Illinois 60439, USA*
e-mail: gdf9@cornell.edu

Creating and studying coherent interactions between disparate solid-state quantum systems is a challenge at the intersection of atomic physics, condensed matter physics, and engineering. In general, different physical realizations of a quantum bit (qubit) operate at different frequencies, on different size scales, and couple to different fields. Nonetheless, efforts to create "hybrid quantum systems" are appealing because they could enable a quantum concert – were parts are played by different physical qubits that each offer the best performance in a particular area. There is a growing consensus that mechanical motion is a "plastic" degree of freedom for solid-state qubits, with the potential to form a coherent interface between them, and with light. This has motivated intense research into the coherent interactions between mechanical resonators and qubits formed from photons, trapped atoms, superconducting circuits, quantum dots, and nitrogen-vacancy (NV) centers in diamond, to name a few. I will describe our experiments to coherently couple NV center spins to gigahertz-frequency mechanical resonators using dynamic crystal lattice strain. In high-quality diamond mechanical resonators, we demonstrate coherent Rabi oscillations of NV center spins driven by mechanical motion instead of an oscillating magnetic field [1, 2]. Furthermore, we show that the mechanical resonator is a resource to prolog the NV center's spin coherence [3]. We also examine how strain can be used to control NV centers through their excited-state, both the room temperature spin-strain coupling [4] and the extremely strong low temperature orbital-strain coupling [5].

[1] E. R. MacQuarrie *et al.*, Phys. Rev. Lett. **111**, 227602 (2013).

[2] E. R. MacQuarrie *et al.*, Optica **2**, 233 (2015).

[3] E. R. MacQuarrie *et al.*, Phys. Rev. B **92**, 224419 (2015).

[4] E. R. MacQuarrie *et al.*, Nat. Commun. **8**, 14358 (2016).

[5] H. Chen *et al.*, in preparation (2017).

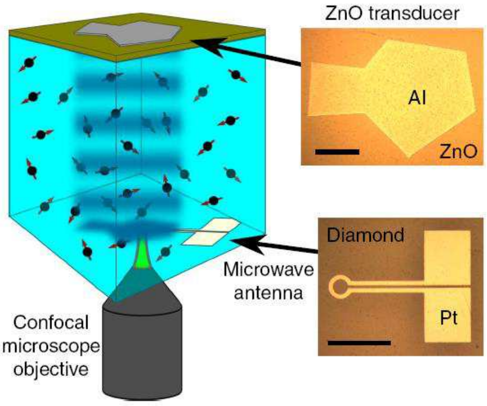

Fig.1: Schematic diagram of high-overtone bulk-mode acoustic resonator (HBAR) fabricated from single crystal diamond. On one face is a piezoelectric transducer to launch acoustic waves, and on the opposite face is a microwave antenna for conventional magnetic resonance control. Figure from [4].

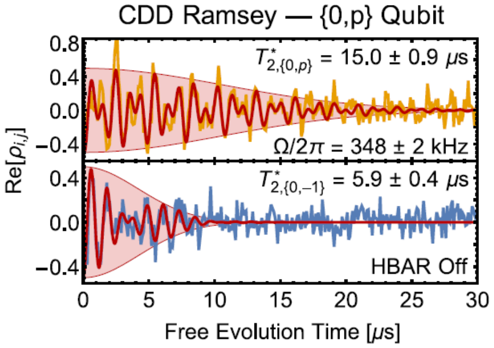

Fig.4: Ramsey coherence, T_2^*, for an NV center spin that is mechanically driven with a Rabi field of $\Omega/2\pi$ =348 kHz as compared to its bare Rabi coherence. Even weak mechanical Rabi driving prolongs the spin coherence by more than a factor of 2. Figure from Ref. [3].

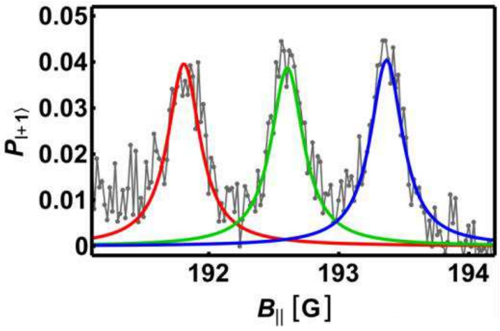

Fig.2: Spectroscopy of mechanically-driven spin transitions from m_s=–1 to m_s= +1. The three peaks are for each nitrogen I=1 nuclear spin sublevel. Figure from Ref. [1].

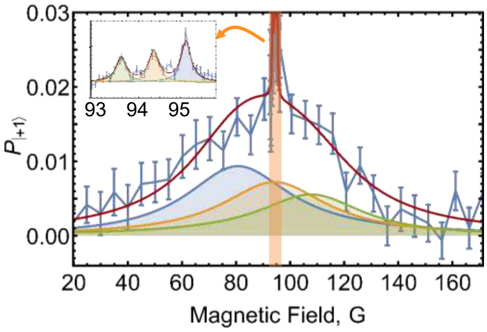

Fig.5 Spectroscopy of mechanically driven spin transitions in both the ground-state and the excited-state manifold at room temperature. Figure from Ref. [4].

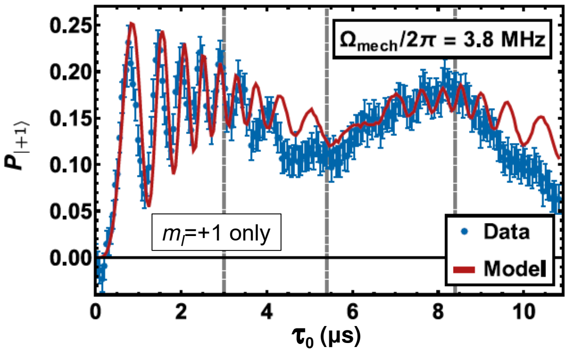

Fig.3: Coherent Rabi oscillations of an NV center spin ensemble driven in the m_s= +1 to –1 manifold with a mechanical resonator. Figure taken from Ref. [2].

978-3-901578-31-1

Modular Anomalies in (2+1) and (3+1)-Dimensional Edge Theories

Moon Jip Park[1,2], Chen Fang[3], B. Andrei Bernevig[4] and Matthew J. Gilbert[1,2,5,6]

[1]*Department of Physics, University of Illinois at Urbana-Champaign, Urbana, Illinois 61801, USA*
[2] *Micro and Nanotechnology Laboratory, University of Illinois at Urbana-Champaign, Urbana, Illinois 61801, USA*
[3] *Institute of Physics, Chinese Academy of Sciences, Beijing 100190, China*
[4] *Department of Physics, Princeton University, Princeton, New Jersey 08544, USA*
[5] *Department of Electrical and Computer Engineering, University of Illinois at Urbana-Champaign, Urbana, Illinois 61801, USA*
[6] *Ming Hsieh Department of Electrical Engineering, University of Southern California, Los Angeles, CA 90089, USA*

e-mail: matthewg@illinois.edu

The classification of topological phases of matter in the presence of interactions is an area of intense interest. One possible means of classification is via understanding the behavior of the partition function under the application of the modular transformation. When the modular transform is applied to a partition function, the presence of an anomalous phase arising in the edge theory of a D-dimensional system, or modular anomaly, signals the presence of a (D+1)-D non-trivial bulk. In this work, we discuss the modular transformations of conformal field theories along a (2+1)-D and (3+1)-D edge. Using both numerical and analytic methods, we show that chiral complex free fermions in (2+1)-D and (3+1)-D are modular invariant. However, we show that when a (3+1)-D edge theory is coupled to a background $U(1)$ gauge field that a modular anomaly is present and that this is the manifestation of a quantum Hall effect in a (4+1)-D bulk. We conclude by further showing that using modular transformations, we find that the edge theory of a (4+1)-D insulator with spacetime inversion symmetry and fermion number parity symmetry for each spin becomes modular invariant when 8 copies of the edge exist.

978-3-901578-31-1

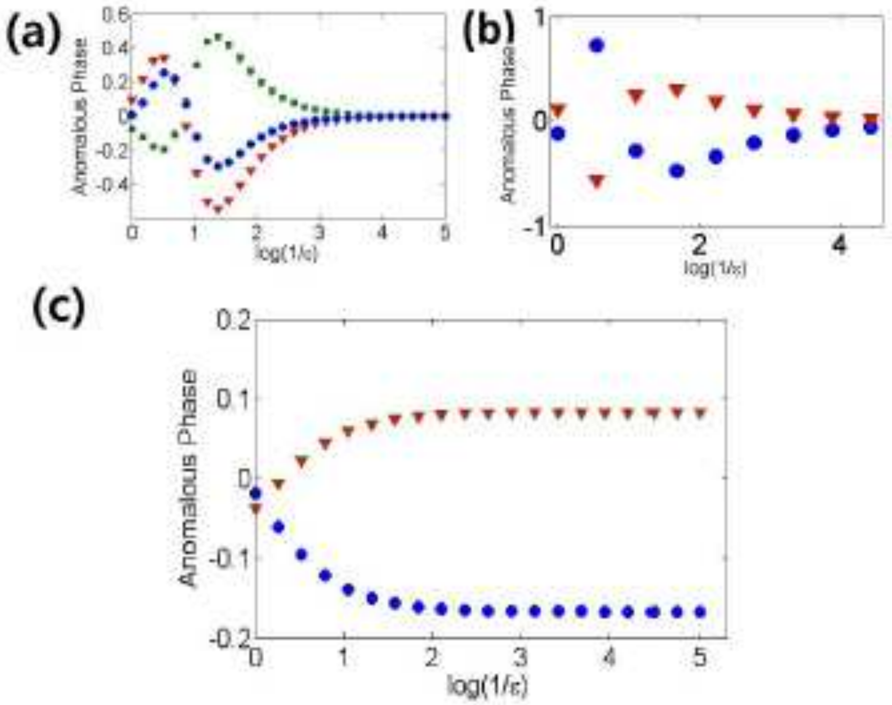

Fig. 1: Calculation of the numerical regularization scheme for: (a) T transformation, one part oft he modular transformation, of (2+1)-D chiral edge (b) *T* transformation of the (3+1)-D chiral edge (c) (3+1)-D chiral dege with a magnetic field. Each of the lines in the plots represent different boundary conditions, periodic (0) and anti-periodic (0.5). In (a), blue circles, red triangles and green squares represent (λ_1, λ_2) = (0, 0), (0.5, 0) and (0.5, 0.5) respectively. In (b), blue circles and red triangles represent (λ_1, λ_2, λ_3) = (0, 0, 0) and (0.5, 0, 0) respectively. In (c), blue circles and red triangles represent (λ_1, λ_2, λ_3) = (0.5, 0, 0) and (0, 0, 0) respectively. We include sufficient numbers of high energy states within each calculation oft he energy cutoff until the anomalous phase value converges. In (a) and (b) all choices of boundary conditions converge to zero indicating modular invariance. When the magnetic field is inserted, the anomaly approaches tot he value (1/6, -1/12) in accordance with our predictions.

Quantum Dots and Spin Qubits based on Silicon Tunnel Field-effect Transistors

Satoshi Moriyama[1], Takahiro Mori[2], Keiji Ono[3]

[1] *International Center for Materials Nanoarchitectonics (MANA), National Institute for Materials Science (NIMS), 1-1 Namiki, Tsukuba, Ibaraki 305-0044, Japan.*
[2] *Nanoelectronics Research Institute (NeRI), National Institute of Advanced Industrial Science and Technology (AIST), Central 2, 1-1-1Umezono, Tsukuba, Ibaraki 305-8568, Japan.*
[3] *Center for Emergent Matter Science, RIKEN, 2-1 Hirosawa, Wako, Saitama 351-0198, Japan.*
e-mail: MORIYAMA.Satoshi@nims.go.jp

Quantum dots (QDs) are attractive for quantum information devices which operate with the coherent manipulation of single-electron charge and spin in solid state systems. The most of the state-of-the-art spin qubits based on QDs operates at temperatures < 0.1 K in dilution refrigerators, which limits the expansion of quantum information technology. Here, we propose and demonstrate a high-temperature operable QD and spin-qubit based on silicon-on-insulator (SOI) tunnel field-effect transistors (TFETs) with deep levels [1]. QD transport in TFETs can be realized by using the single-particle deep-level states as QDs (Fig. 1). The deep levels are intentionally introduced into the transport channel by the ion implantation of Al-N complex impurities [2]. Regarding the QD devices, we measured the short channel SOI-TFETs with the channel length of 60–80 nm. We observed room-temperature single-electron transport through the implantation-induced atomic-size QDs embraced in TFETs. Furthermore, some of the devices exhibited double-QD behavior which is produced by the combination of deep and shallow levels. Fig. 2 shows the photon-assisted tunneling in a resonant tunneling peak as an evidence of the double QD transport. Fig. 3(a) shows the electron spin resonance (ESR) of a single-spin in the spin-blockade region in double QDs under continuous microwave irradiation. The ESR response was observable up to 12 K, as shown in Fig. 3(b). Also, with pulse-modulated microwave driving in the spin-blockade region, Rabi oscillations as time-ensemble measurements were observed. These results indicate that spin qubits in SOI-TFETs have advantages in realizing the high-temperature operation of quantum computing with high-density integration with established silicon technology.

[1] K. Ono, T. Mori, and S. Moriyama, submitted.

[2] T. Mori *et al*., MRS Commun., available in online, https://doi.org/10.1557/mrc.2017.63.

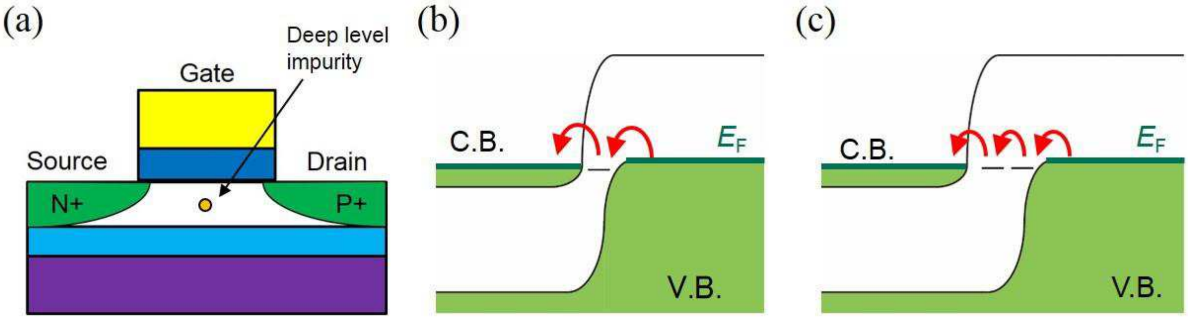

Fig. 1: (a) Schematic picture of the TFET devices with deep level impurities in transport channel. This is a P-type TFET having the n-type source and p-type drain electrode. TFET regulates current flow through the pn junction by modulating the tunnel barrier by gate electrostatic control. (b, c) Schematic band diagram of single-electron transport via a single (b) and double (c) deep level states. C.B., V.B., and E_F denote the conduction band, valence band, and Fermi energy of the electrode, respectively.

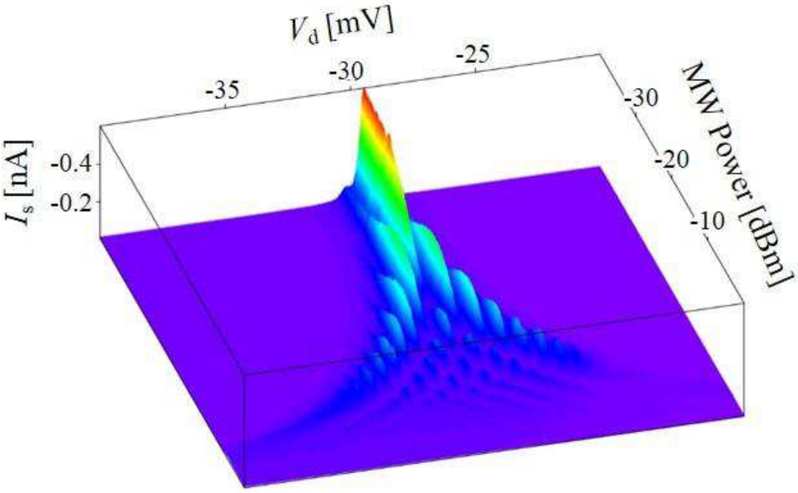

Fig. 2: The source current (I_s) as a function of drain voltage (V_d) and incident microwave power. Microwave frequency was fixed at 27.68 GHz. The measurement was performed at 1.5 K. Clear features of photon-assisted tunneling were observed with a resonant tunneling peak, i.e., multiple-photon absorption and emission in double QDs.

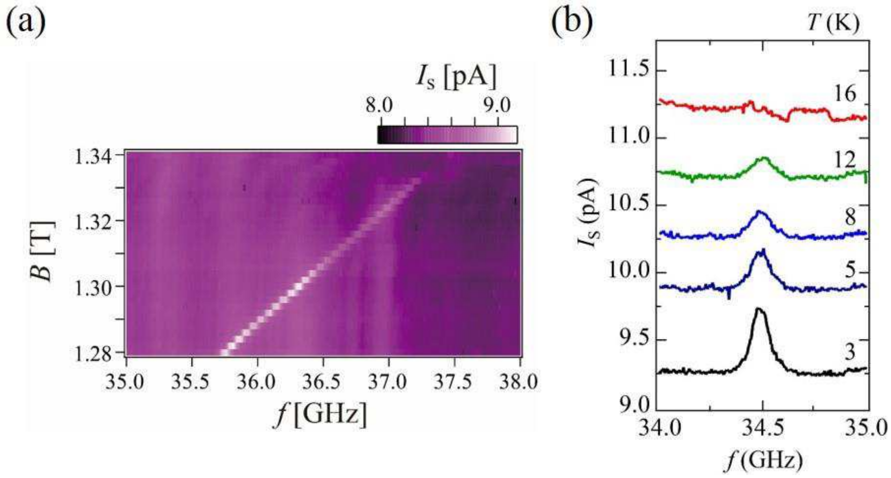

Fig. 3: (a) I_s as a function of the microwave frequency and the magnetic field in a spin-blockade transport region in double QDs. The measurement was performed at 1.5 K. Single-electron spin resonance was observed in the spin-blockade regime. (b) The temperature dependence of the single-electron spin resonance with fixed B = 1.220 T.

978-3-901578-31-1

Superconducting qubit-oscillator circuit beyond the ultrastrong-coupling regime

Fumiki Yoshihara[1], Tomoko Fuse[1], Sahel Ashhab[2], Kosuke Kakuyanagi[3], Shiro Saito[3], and Kouichi Semba[1]

[1] *National Institute of Information and Communications Technology, Koganei, Tokyo, Japan*
[2] *Qatar Environment and Energy Research Institute, Hamad Bin Khalifa University, Qatar Foundation, Doha, Qatar*
[3] *NTT Basic Research Laboratories, NTT Corporation, Kanagawa, Japan*
e-mail: fumiki@nict.go.jp

The interaction between an atom and the electromagnetic field inside a cavity has played a crucial role in the historical development of our understanding of light-matter interaction and is a central part of various quantum technologies. The emergence of superconducting qubits has allowed the realization of strong and ultrastrong coupling between artificial atoms and cavities. If the coupling strength g becomes as large as the atomic and cavity frequencies (Δ and ω respectively), the energy eigenstates including the ground state are predicted to be highly entangled. This qualitatively new regime can be called the deep-strong-coupling regime.

By inductively coupling a superconducting flux qubit, which has a large magnetic dipole moment due to its macroscopic persistent current states, and an LC oscillator, which has a large zero point fluctuation current, via a Josephson junction coupler with large Josephson inductance as shown in Fig. 1, we have realized deep-strong coupling between the qubit and the oscillator [1]. The spectra obtained in the spectroscopy measurement (Fig. 2) were well fitted by the Hamiltonian of the quantum Rabi model, which describes a system consisting of a two-level atom and a harmonic oscillator without rotating-wave approximation, and the parameters are obtained to be $g/\omega > 1$ and $g/\Delta \gg 1$. We also found that the qubit frequency is suppressed more than 90% from its original value. This can be considered as a huge Lamb shift of the flux qubit due to the deep-strong coupling to the vacuum-fluctuation current of the LC oscillator.

Our results provide a basis for ground-state-based entangled pair generation and open a new direction of research on strongly correlated light-matter states in circuit quantum electrodynamics.

[1] F. Yoshihara and T. Fuse et al., Nature Phys. **13**, 44 (2017).

978-3-901578-31-1

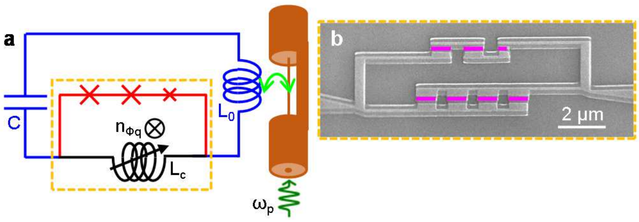

Fig. 1: **Superconducting qubit-oscillator circuit. a** Circuit diagram. A superconducting flux qubit (red and black) and a superconducting LC oscillator (blue and black) are inductively coupled to each other by sharing a tunable inductance (black). **b** Scanning electron microscope image of the qubit including the coupler junctions located at the orange rectangle in **a**. Josephson junctions are represented by magenta rectangles. The coupler, consisting of four parallel Josephson junctions, is tunable via the magnetic flux bias through its loop.

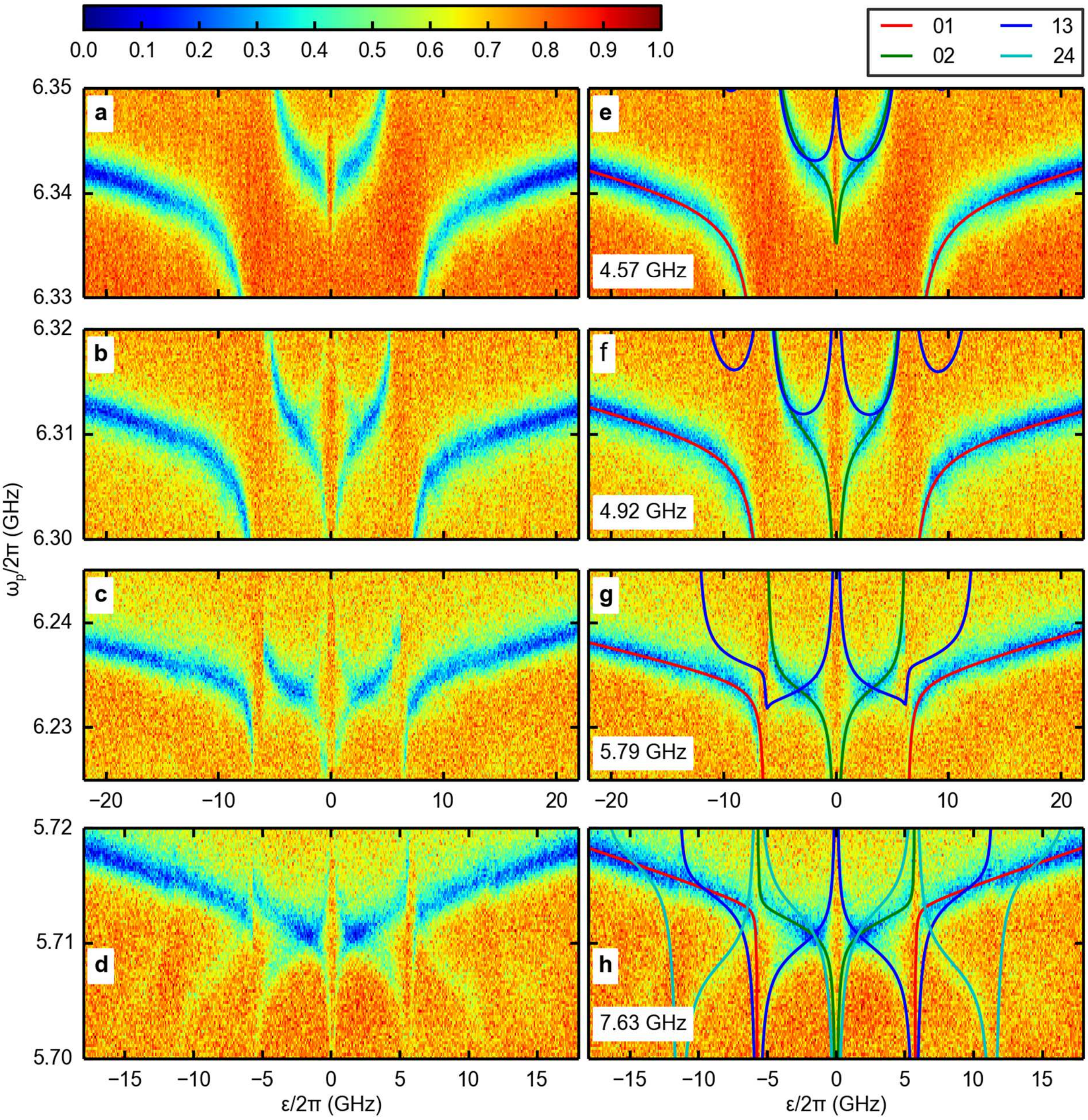

Fig. 2: **Transmission spectra.** The normalized amplitude of the transmission spectra (with calculated transition frequencies in the right panels). The red, green, blue, and cyan lines indicate the transitions $|0\rangle \rightarrow |1\rangle$, $|0\rangle \rightarrow |2\rangle$, $|1\rangle \rightarrow |3\rangle$, and $|2\rangle \rightarrow |4\rangle$, respectively. Here, $|0\rangle$ stands for the ground state and $|n\rangle$ with $n \geq 1$ stands for the nth excited state of the coupled circuits. The values of $g/2\pi$ are written in the panels.

Helical states and spin-orbit coupling in InAs nanowire-based devices

S. Heedt[1], N. T. Ziani[2], F. Crepin[2], A. Bringer[1], M. Kammermeier[3], P. Wenk[3], J. Schubert[1],
W. Prost[4], J. Schliemann[3], D. Grützmacher[1], B. Trauzettel[2], and Th. Schäpers[1]

[1] *Peter Grünberg Institut (PGI-9, PGI-1), JARA-FIT Jülich-Aachen Research Alliance,*
Forschungszentrum Jülich, Germany
[2] *Institute of Theoretical Physics and Astrophysics, University of Würzburg, Germany.*
[3] *Institute for Theoretical Physics, University of Regensburg, Germany*
[4] *Solid State Electronics Department, University of Duisburg-Essen, Germany*
e-mail: th.schaepers@fz-juelich.de

Semiconductor nanowires, fabricated by a bottom-up approach, are very promising as building blocks for future nano-scaled electronic and spintronic devices. In addition, they are also very interesting objects for studying fundamental quantum phenomena, such as Majorana physics. The latter was recently found to be relevant for the realization of future fault-tolerant quantum computers. In this respect spin-orbit coupling plays an important role, since it is essential to form a so-called helical gap, one of the prerequisites to create Majorana states. In InAs nanowires spin-orbit coupling is relatively strong, owing to the lack of inversion symmetry and the low band gap. Two types of spin-orbit coupling are relevant, i.e. spin-orbit coupling due to structural inversion asymmetry (Rashba effect) and bulk inversion asymmetry (Dresselhaus contribution). In InAs devices comprising gate electrodes (Fig.1) the electrical as well as the spin transport can be controlled. The Dresselhaus spin-orbit contribution is rather intrigue, due to its complex spatial dependency. Therefore, we performed theoretical calculations of the energy dispersion and the corresponding spin-density (Fig. 2). Experimentally, information on spin-orbit coupling is gained by weak-antilocalization measurements. These results are fitted to a theoretical model, in order to quantify the strength of the Dresselhaus as well as the Rashba contribution (Fig.3) [1]. On InAs nanowires controlled by a set of top-gate electrodes ballistic transport is investigated. By varying the gate voltage distinct conductance steps due to quantized conductance are observed (Fig.4). We found indications of a helical gap indicated by the dip feature in the first conductance plateau (Fig.4) [2].

[1] M. Kammermeier, P. Wenk, J. Schliemann, S. Heedt, Th. Schäpers, Phys. Rev. B, **93**, 205306 (2016).
[2] S. Heedt, N. T. Ziani, F. Crepin, W. Prost, S. Trellenkamp, J. Schubert, D. Grützmacher, B. Trauzettel, Th. Schäpers, Nature Physics, **13**, 563 (2017).

978-3-901578-31-1

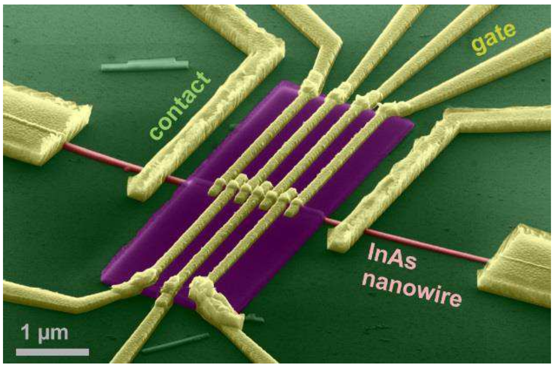

Fig.1: InAs nanowire device with source-drain electrodes and multiple top gates strongly coupled to the nanowire via a LaLuO$_3$ high-k dielectric layer.

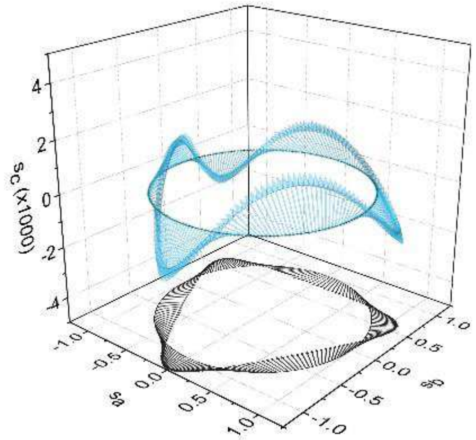

Fig.2: Calculated modulation of the spin density in an InAs nanowire due to Dresselhaus spin-orbit coupling for a state with total angular momentum j=3/2.

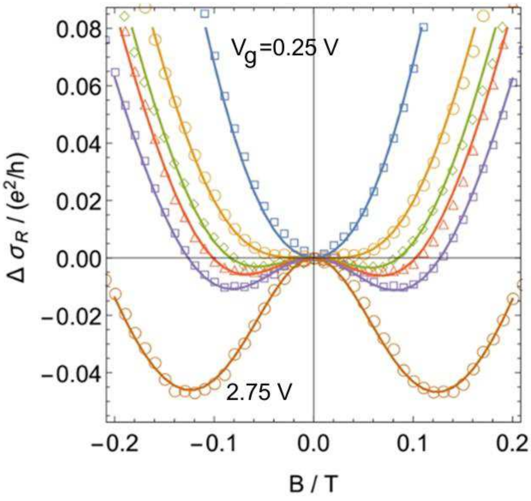

Fig.3: Gate-controlled crossover from positive to negative magnetoconductivity, i.e. weak localization to weak anti-localization, in a (111) InAs nanowire. The gate voltage V_g was varied from 0.25V to 2.75V. The symbols correspond to the experimental data, while the lines represent the theoretical values. In the theoretical calculation the strength of the Rashba as well as the Dresselhaus coupling parameter was adjusted to fit to the experimental data.

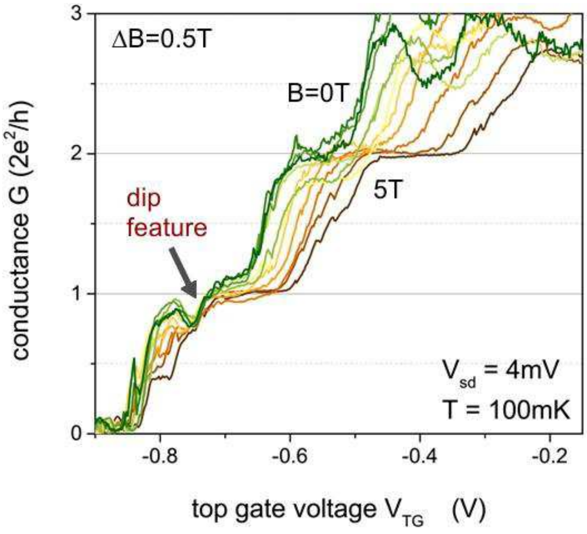

Fig.4: Quantized conductance as a function of top gate voltage measured on the InAs nanowire device shown in Fig. 1. The magnetic field was varied as a parameter from B=0 to 5T. A dip feature is found on the first plateau of the quantized conductance, which is attributed to spin helical transport.

Nanowire quantum dots coupled with a superconducting microwave resonator

Rui Wang[1], Russell Deacon[1,2], Jun Yao[3], Charles Lieber[3,4], and Koji Ishibashi[1,2]

[1] *Advanced Devie Laboratory, RIKEN, 2-1, Hirosawa, Wako, Japan*
[2] *Center for Emergent Matter Science (CEMS), RIKEN, 2-1, Hirosawa, Wako, Japan*
[3] *Deparment of Chemistry and Chemical Biology and* [4]*School of Engineering and Applied Sciences, Harvard University, Cambridge, Massachusetts 02138, USA*
e-mail: kishiba@riken.jp

To realize a strong quantum mechanical coupling between quantum bits (qubits) and a resonator would be useful for manipulating quantum information stored in different forms. For example, a flux qubit coupled to a photon in a microwave resonator could transfer its quantum information back and forth with a spin qubit which is also coupled to a resonator. The former has actually demonstrated, but the latter has not because interaction between a spin and a photon is small. It could be realized with a help of the spin-orbit interaction that mediate the interaction between them in the double quantum dots.

In this work, we fabricate double quantum dots with a Ge/Si core-shell nanowire (NW) that are located in between the signal and ground line of the superconducting co-planar wave guide resonator [1]. Before studying the spin-resonator interaction, we study charge-resonator interaction. The double dots are formed by applying positive gate voltages on the finger gates underneath the NW with a hBN film in between them. The microwave transmission was measured through the sample that was set in a dilution refrigerator, and resonance properties, such as the resonant frequency, phase and amplitude, are plotted as functions of the gate voltages to each dot and the coupling strength between the double dots. We could realize two different regimes where the coupling strength between the dots was larger or smaller than the resonator frequency. In both cases, we observed the frequency shift as the qubit detuning was changed. By fitting the frequency shift with a model calculation, we found that the decoherence rate of the double dots were larger than the coupling strength between the double dot and a photon in both regimes, NOT making the system in a strong coupling regime. It could be improved by setting the double dots in the sweet spot where the detuning is zero at the resonator frequency. Besides, we could increase the coupling strength by increasing the characteristic impedance of the waveguide, which is being tried.

[1] Wang R, Deacon R S, Car D, Bakkers E P A M and Ishibashi K, *Appl. Phys. Lett.* **108**, 203502, 2016

978-3-901578-31-1

Full counting statistics theory for cross correlation of quantum entanglement current noise in double S/N/N capacitively-coupled single electron transistor with ohmic impedance in Coulomb blockade regime

Yukimi Kanai[1], Takeshi Inagaki[2] and Shuichi Iwabuchi[1]

[1]*Department of Physics, Graduate School of Humanities and Sciences,*
Nara Women's University, Nara 630-8506, Japan
[2] *Faculty of Health Science, Butsuryo College of Osaka, Sakai, Osaka 593-8328, Japan*
e-mail:iwabuchi@cc.nara-wu.ac.jp

Recently, much interest has been shown for quantum entanglement of electrons in solid state systems. Beyond the exploration of nonlocal quantum effects through the test of Bell's inequality, a controlled generation and manipulation of electronic entanglement is of great importance for quantum information and computation schemes. So far many experimental and theoretical studies have been reported on current and cross correlation of current noise or nonlocal differential conductance[1, 2, 3]. At present stage it is safely be said that the common recognition that the charging effect is crucially important to extract and control entangled information in the ultra-small solid state entangler (SSE) has been established. In [3] non-perturbative theory of full counting statistics (FCS) for Cooper pair splitter (CPS) *in the absence of realistic electromagnetic environment effect due to ohmic resistance* has been reported[3]. Although they took Coulomb interaction into account, they failed to reflect Coulomb blockade related features ((charging effect) on their subgap results (both currents and current noise correlation) even in the case superconducting gap energy is larger than charging energy. From experimental point of view, on the other hand, physics of bunching and anti-bunching in CPS in a whole subgap region has not been sufficiently clarified probably because of experimental difficulties.

We present the Nambu-Gor'kov and Schwinger-Keldysh theory of FCS for the *double S/N/N C-SET* as shown in FIG.1, which is more general and realistic SSE than CPS treated in [3]. The theory properly takes account of *infinite order tunneling processes in the presence of arbitrarily large charging effect as well as electromagnetic environment effect due to ohmic resistance* (in Caldeira-Leggett spirit[4]), so that it enables one to discuss physics of bunching and anti-bunching nature of SSE with arbitrarily large effective transmission probability and environmental ohmic impedance at finite temperatures in Coulomb blockade regime.

We drive analytical expression for *cumulant generation function (CGF)* and obtain analytical expressions for *currents due to various mechanisms* and *current noise cross correlation* $S_{LR}(\omega = 0)$ as cumulants from CGF. Tentative results are shown in FIG.2 and FIG.3. We discuss in detail and clarify in what situation we can expect bunching or anti-bunching nature of the entanglement showing dependencies on *various bias conditions*, *effective tunneling probability* and *environmental ohmic impedance* of each of left and right C-SETs in a whole subgap region. Furthermore, we also discuss the difference in bunching and anti-bunching nature between present SSE and SSE with *Majorana physics* realized by replacing S with topological superconductor based on the similar theoretical analysis given here.

References

[1] For example, G. Falci, D. Feinberg, and F. W. J. Hekking, Europhys. Lett. **54** 255 (2001); P. Recher and D. Loss, Phys. Rev. Lett. **91**, 267003 (2003)

[2] V. Bubanja and S. Iwabuchi, Phys. Rev. B **84**, 094501 (2011); V. Bubanja, M. Yamamoto, and S. Iwabuchi, Phys. Rev. B **94** 184515 (2016)

[3] D. Chevallier, J. Rech, T. Jonckheere, and T. Martin, Phys. Rev. B **83**, 125421 (2011); J. Rech, D. Chevallier, T. Jonckheere, and T. Martin, Phys. Rev. B **85**, 035419 (2012)

[4] A. O. Caldeira and Leggett, Phys. Rev. Lett.46, 26 (1981); Gert-Ludwig Ingold and Yu. V. Nazarov,"Charge Tunneling Rates n Ultrasmall Junctions" in *Single Charge Tunneling* ed. by H. Grabert and M. H. Devoret (NATO ASI series B: Physics Vol.294, Plenum Press)

978-3-901578-31-1

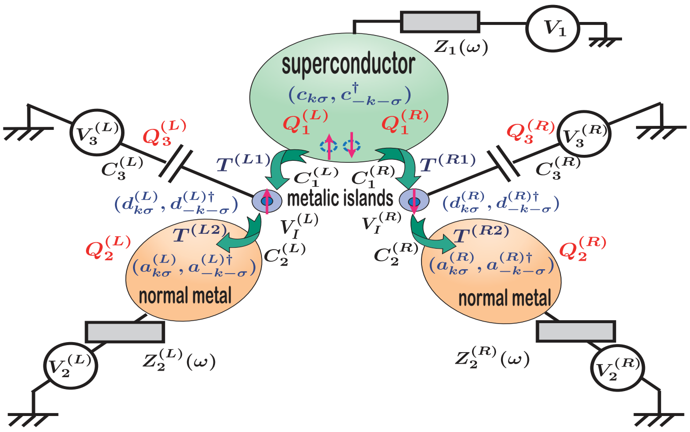

FIG.1: Model of SSE. *S/N/N double C-SET* with arbitrarily large charging energy and electromagnetic environmental ohmic impedance.

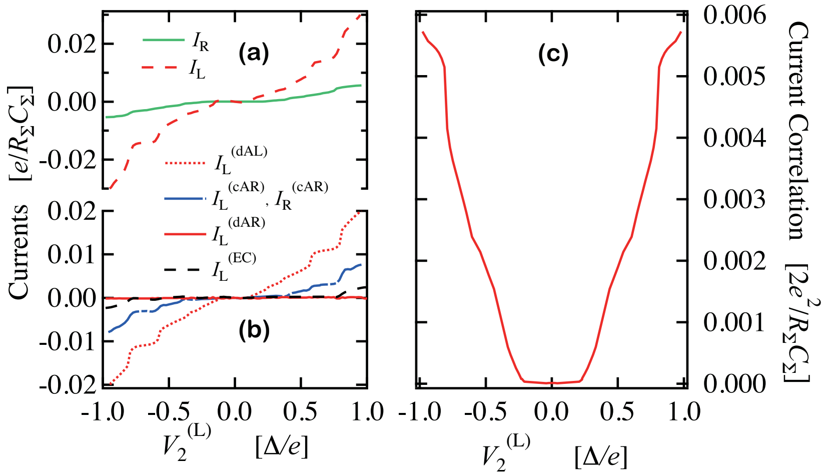

FIG.2: Tentative results for relatively low transmission probability and environmental ohmic resistance. (a)Current, (b) current components and (c) corresponding current noise cross correlation as a function of bias voltage $V_2^{(\mathrm{L})}$ with $V_2^{(\mathrm{R})} = 0$. The bunching correlation of current noise can be expected over a wide range of bias voltage in this case.

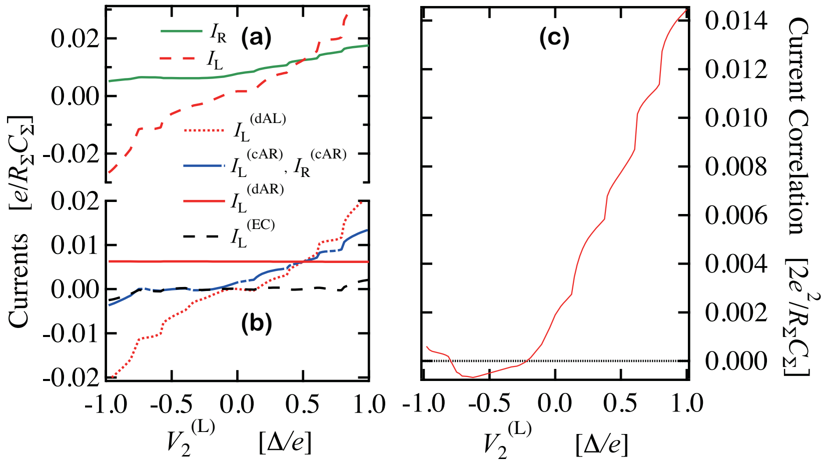

FIG.3: Tentative results for relatively low transmission probability and environmental ohmic resistance. Parameters are the same as FIG.2 but with bias voltage $V_2^{(\mathrm{L})} = 0$ and $V_2^{(\mathrm{R})} = 0.5\Delta/e$ (Δ: gap energy of superconductor). The anti-bunching correlation of current noise can be expected only in a narrow region near Coulomb gap for crossed Andreev current in this case.

978-3-901578-31-1

Beyond Moore's Computing (BMC): Fundamental Downscaling Limit of Field-effect Transistors and New Possibilities for Continued Increase of Computing Power

Denis Mamaluy

Sandia National Laboratories,
Non-conventional Computing Technologies,
Albuquerque, New Mexico, 87185
e-mail: mamaluy@sandia.gov

We have previously predicted that within next 15 years a fundamental down-scaling limit for CMOS technology and other Field-Effect Transistors (FETs) will be reached [1]. Specifically, we demonstrated that at room temperatures all FETs, irrespective of their channel material, will start experiencing unacceptable level of thermally induced errors around 5-nm gate lengths as illustrated at Figure 1. These findings were confirmed by performing 3D fully quantum-mechanical transport simulations using the CBR method [2-4] for a variety of 6-, 5- and 4-nm gate length devices, optimized to satisfy high-performance logic specifications by ITRS [4]. The tremendous deflationary influence of Moore's law on the global economy is yet to be fully appreciated [5], it is clear, however, that when the density of transistors stops increasing, the exponential decline of the price per function in computing is also going to stop resulting in far-reaching and likely disruptive economic processes. In this work we discuss the two principal paths forward to *continue* increasing the computing power after the end of CMOS/FET scaling is reached (Figure 2): I) continue the density increase with a *selected class* of novel devices, including single-electron devices; II) attempt to gain exponential decreases in power consumption per operation with the fixed device density. We will also discuss a plan (BMC "Big Idea") that 8 national laboratories have presented to DOE to facilitate BMC development, including the creation of Multiscale Codesign Framework (MCF) (Figure 3).

1. D. Mamaluy, X. Gao, Appl. Phys. Lett. **106**, 193503 (2015).
2. D. Mamaluy, D. Vasileska, M. Sabathil, T. Zibold, and P. Vogl, Phys. Rev. B **71**, 245321 (2005).
3. H. R. Khan, D. Mamaluy, and D. Vasileska, IEEE Trans. Electron Devices **54**, 784 (2007).
4. X. Gao, D. Mamaluy, E. Nielsen, et al., J. Appl. Phys. **115**, 133707 (2014).
5. http://www.itrs2.net/2013-itrs.html; ITRS 2014-2015 Reports.
6. http://www.itrs2.net/uploads/4/9/7/7/49775221/irc-itrs-mtm-v2_3.pdf, "More-than-Moore" white paper.

978-3-901578-31-1

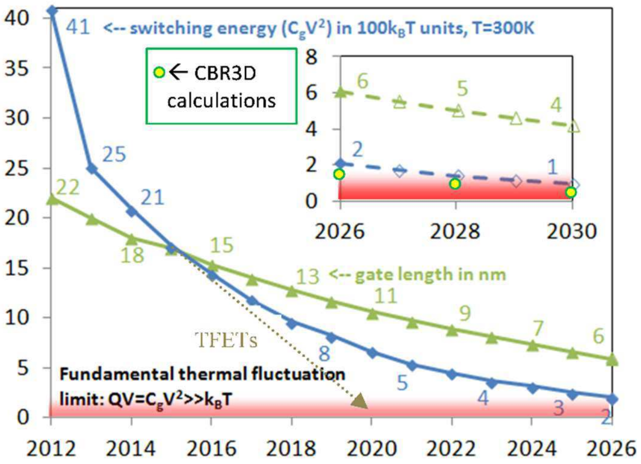

Figure 1. Switching energy (in 100kT, T=300K units) vs gate length (nm) per ITRS projections and CBR3D calculations (yellow circles).

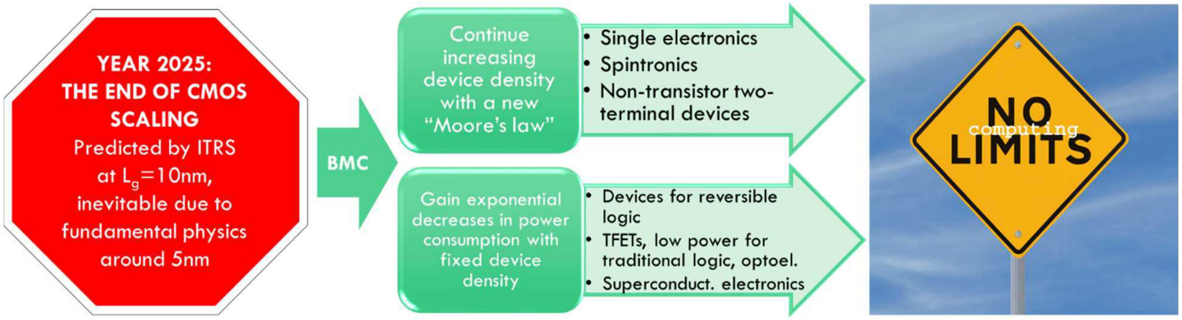

Figure 2. Two paths forward after the end of CMOS scaling

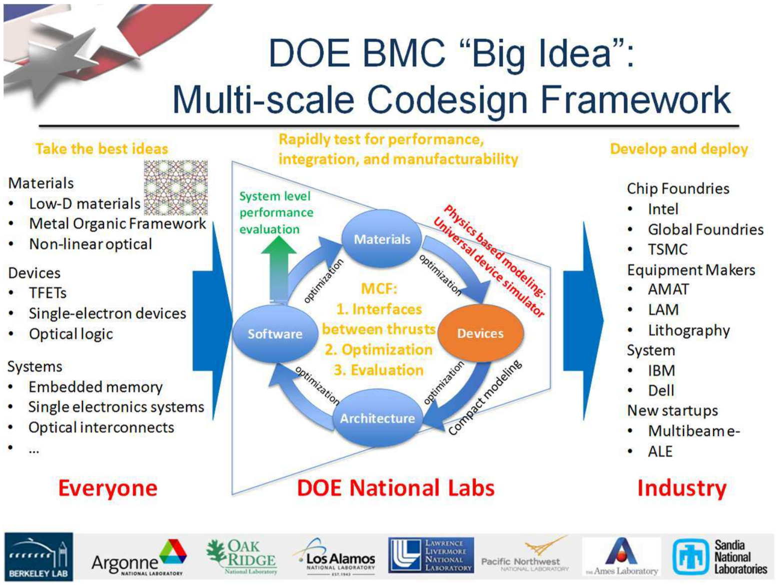
DOE BMC "Big Idea":
Multi-scale Codesign Framework

Take the best ideas

Materials
- Low-D materials
- Metal Organic Framework
- Non-linear optical

Devices
- TFETs
- Single-electron devices
- Optical logic

Systems
- Embedded memory
- Single electronics systems
- Optical interconnects
- ...

Everyone

Rapidly test for performance, integration, and manufacturability

System level performance evaluation

Materials

Devices

Architecture

Software

optimization

Physics based modeling: Universal device simulator

Compact modeling

MCF:
1. Interfaces between thrusts
2. Optimization
3. Evaluation

DOE National Labs

Develop and deploy

Chip Foundries
- Intel
- Global Foundries
- TSMC

Equipment Makers
- AMAT
- LAM
- Lithography

System
- IBM
- Dell

New startups
- Multibeam e-
- ALE

Industry

Figure 3. The framework for the entire-stack optimization and evaluation of different device technologies.

978-3-901578-31-1

The Role of Interface Roughness on the Electron Mobility in Nanoscale Devices: A Green's Function Approach

G. Kannan and D. Vasileska

School of Electrical, Computer and Energy Engineering
Arizona State University, Tempe, AZ 85287-5706, USA
e-mail: vasileska@asu.edu

A state-of-the-art simulator for the calculation of the low-field mobility in inversion layers is presented in this work that accounts for the collisional broadening of the electronic states via the solution of the Dyson Equation for the retarded Green's function (GF). Self-consistent Born approximation is used for the calculation of the self-energy contributions due to Coulomb, surface-roughness, acoustic and non-polar optical phonon scattering. Bethe-Salpeter integral equation is solved for the calculation of the conductivity, i.e. mobility. Simulated mobility results for three generations of MOSFET devices are in agreement with available experimental data. At nanoscale dimensions, we find that surface-roughness scattering dominates the collisional broadening of the states and the renormalization of the spectrum [1,2].

The 1D Schrödinger-Poisson solver uses the density of states calculated via the solution of the Dyson equation to compute the sheet charge density in various subbands, and therefore the total QM charge density in the device. This forms the self-consistent outer loop of the solver. The inner loop consists of the Green's functions solver that solves for the retarded sub-band Green's function self-consistently to compute the corresponding self-energy. Once the collisional broadening of the states and the renormalizations of the spectrum are calculated, the subband density of states function (DOS) is calculated by integrating the spectral density function over the momentum states, thus giving the updated value of the energy dependent subband "real" DOS. This, in turn, allows for the calculation of the sheet electron density in the outer loop.

Thus, for every iteration of the outer Schrödinger-Poisson loop, the subband energies, sub-band wavefunctions and the overlap integrals are updated as an input for the inner GF loop, which then iterates in itself for self-consistency. Once the value of the sheet charge density and the potential is finally calculated for the given gate voltage, the conductivity is evaluated using the Green-Kubo approach by the self-consistent solution of the subband polarizability function. The effective mobility is then calculated from this conductivity. In this work, Message Passing Interface (MPI) is used to parallelize the code for time efficiency.

[1] D. Vasileska and D. K. Ferry, *IEEE Trans. Electron Devices* **44**, 577-83 (1997).
[2] G. Kannan and D. Vasileska, *J. Appl. Physics*, in press.

978-3-901578-31-1

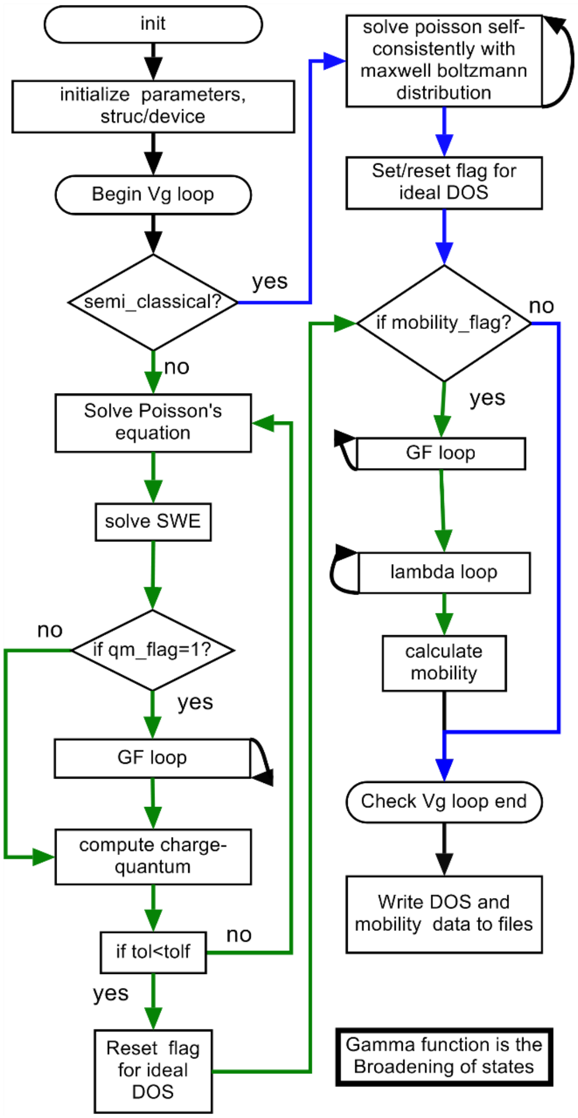

Figure 1. Flow-chart of the main code.

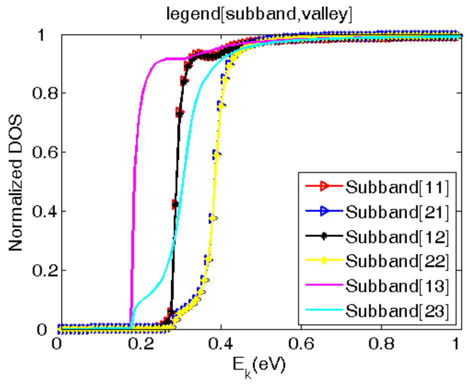

(a)

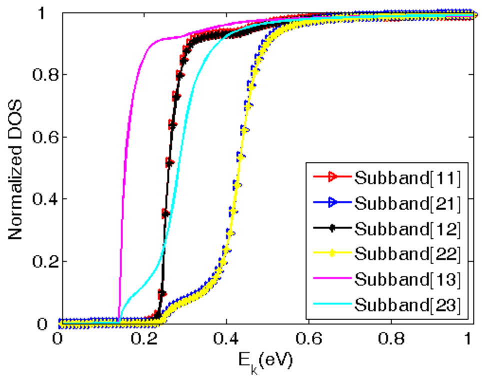

(b)

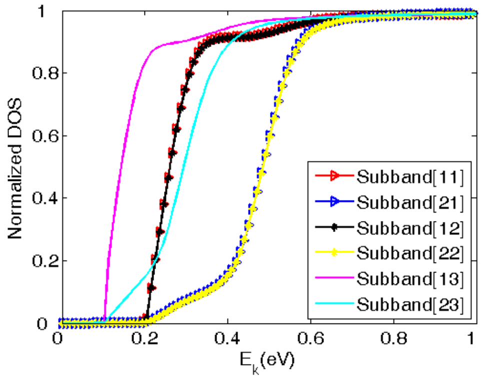

(c)

Figure 2. DOS for different substrate concentrations corresponding to different device generations: (a) 2.0×10^{16} cm^{-3}, (b) 7.7×10^{17} cm^{-3}, (c) 2.4×10^{18} cm^{-3}.

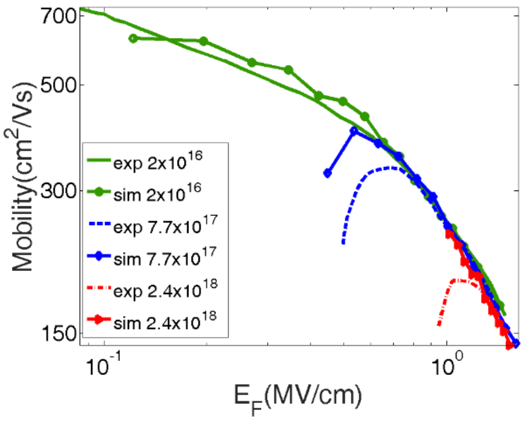

Figure 3. Simulated mobility results vs. transverse electric field (E$_F$) for different doping generations. Also shown here are the experimental data values from Takagi *et al*. (*IEEE Trans. Electron Dev*. **41**(12) (1994): 2357-2362.)

Study on Low Friction of Silicon Carbide under Water Lubrication: Molecular Dynamics Analysis

Fumiya Nakamura, Naoki Takahashi,Yang Wang, Jingxiang Xu,Yuske Ootani, Nobuki Ozawa and Momoji Kubo

Institute for Materials Research, Tohoku University, Sendai, Miyagi 980-9577, Japan
e-mail: fumiya.nakamura@imr.tohoku.ac.jp

Water is the lubricant which has the characteristic of low environmental burden. It is known that silicon carbide (SiC) shows quite low friction coefficient when it slides in water [1]. Understanding of its mechanism is essential to improve friction characteristic for practical use and application. However, it is difficult to observe directly such a complicated phenomenon including friction and chemical reaction by experiments. Therefore, in this study, molecular dynamics (MD) simulation using reactive force field (ReaxFF) was conducted to analyze the effects of H_2O molecules on the friction mechanism of amorphous silicon carbide (a-SiC).

Fig. 1 shows the model used in the MD simulations. We prepared the models with 0, 50, 100, and 200 of water molecules at the friction interface. The bottom layer atoms of the lower substrate were fixed and topmost layer atoms of the upper substrate were given a constant pressure (3 GPa) in the z-axis direction and slid for 500 ps at 50 m/s in the x-axis direction.

In the model without water molecules, the space between the upper and the lower substrate was separated by the hydrogen atoms terminated on the surface at 0 ps (Fig. 2 (a)). Then, the hydrogen atoms were diffused and the formation of the interfacial bonds between the lower and the upper substrates was observed at 500 ps (Fig. 2 (b)). In the 50 water molecule model, the formation of bonds between the upper and the lower substrates was observed during the friction (red circles in (Fig. 3(a)). The water molecules dissociated at the friction interface, and the a-SiC surface was oxidized (Fig. 3(b)). This phenomenon seems to be the initial process of the generation of the SiO_2 layer. In the 100 and 200 water molecule models (Fig.4 and 5), no formation of bonds between the upper and the lower substrates occurred and there was almost no change in friction interface during the friction. Next, we investigated the change in the number of water molecules during the friction. Fig. 6 shows variation of the number of water molecules in each model. The number of H_2O almost did not change in the 100 and 200 water molecule models, whereas it decreased gradually from 0 ps to 500 ps in the 50 water molecule model. From these results, it was found that the amount of water molecules at the friction interface of a-SiC plays an important role in forming the bonds between the substrates through chemical reactions and changing friction interface structure.

[1] M. Chen et al., Tribol. Lett, **11**, 23 (2001).

978-3-901578-31-1

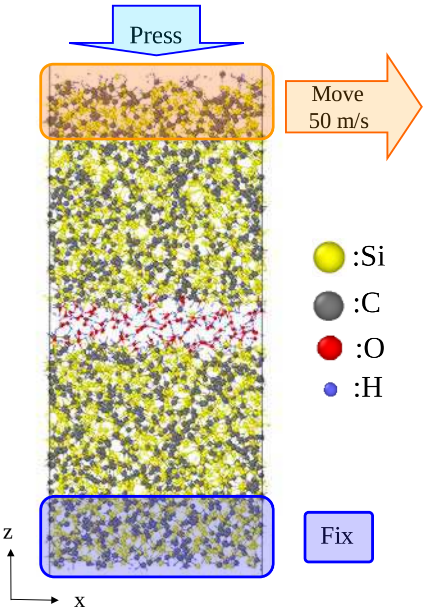

Fig.1: Simulation model of sliding interface of SiC in water.

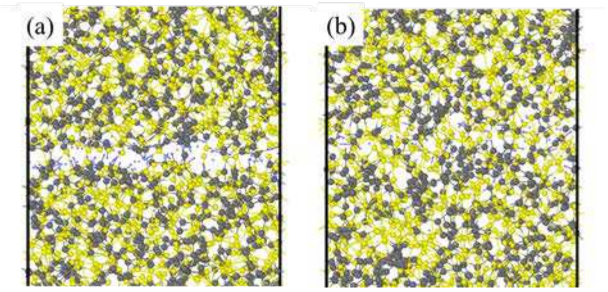

Fig.2: Snapshots of the model without water molecule at (a) 0 ps and (b) 500 ps.

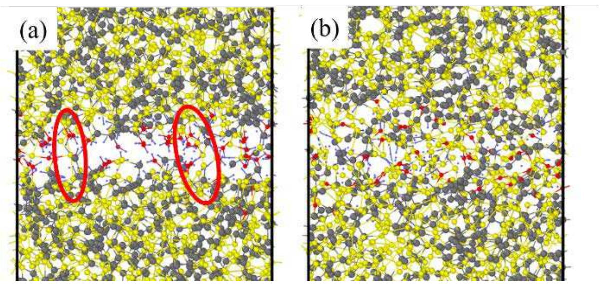

Fig.3: Snapshots of the model with 50 water molecules at (a) 100 ps and (b) 500 ps.

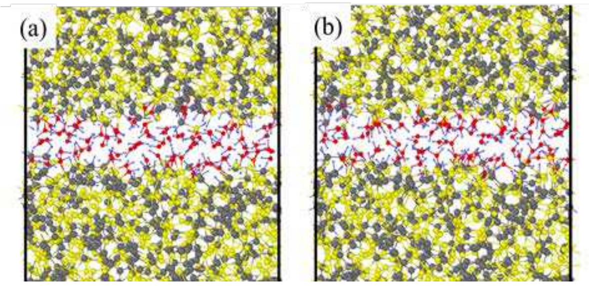

Fig.4: Snapshots of the model with 100 water molecules at (a) 0 ps and (b) 500 ps.

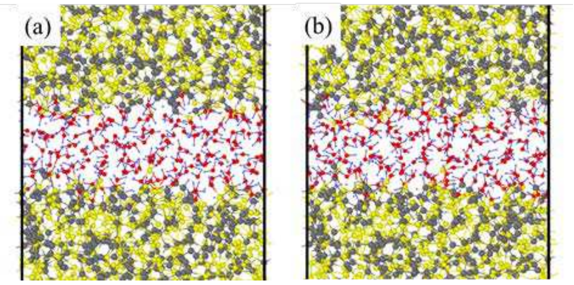

Fig.5: Snapshots of the model with 200 water molecules at (a) 0 ps and (b) 500 ps.

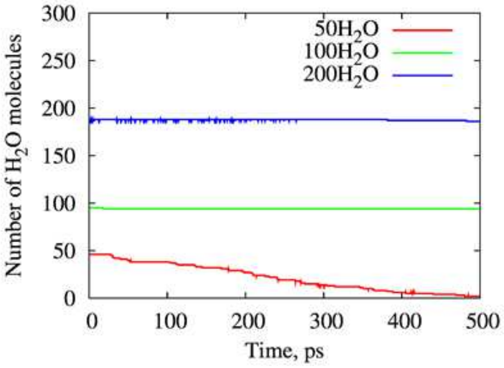

Fig.6: Variation of the number of water molecules in each model.

Authour Index (1/2)

A
Albisetti, E. * · · · · 127
Adamashvili, G.T. · · · · 179
Ando, A · · · · 57
Aono, T. · · · · 187
Aso, Y. · · · · 67
Aytan, E. · · · · 95
B
Balandin, A. · · · · ii
C
Conley, Jr., J.F. · · · · 135,ii
Crooker, S. * · · · · 97
D
Das, Saptarshi * · · · · 47
Demkov, A. A. * · · · · 25
F
Fabian, J. · · · · 83
Ferry, D. K. · · · · 101,ii
Fuchs, G. D. * · · · · 207
Fujimoto, S. · · · · 113
Fukui, N. * · · · · 65
G
Gao, Y. · · · · 155
Giavaras, G. · · · · 99
Gilbert, M.J. · · · · 209,ii
Goodnick, S. · · · · 19,i,ii,iv
H
Hankiewicz, E. · · · · 131
Higashikawa, M. * · · · · 27
Hirose, S. · · · · 149
Hoffmann, A. * · · · · 121
Hughes, T. L. · · · · 111
I
Igarashi , T. · · · · 139
Inoue, T. · · · · 61
Ishibashi, K. · · · · 217,ii
J
Janes, D. B. · · · · 69,183,ii
Jang, H-S. · · · · 201
Jariwala, D. * · · · · 9
Jippo, H. · · · · 157
Jonker, B · · · · 11,i,ii
K
Kanai, Y. · · · · 219
Kanda, A. · · · · ii
Kawabata, S. · · · · 37
Kawakami, R. K. * · · · · 79
Kawasaki, M. * · · · · 115
Khitun, A. · · · · 81
Kiehl,R. * · · · · 91
Kim, E.K. · · · · 161
Klimov, V.I. · · · · 43,ii
Kobayashi, Y. · · · · 169
L
Lee, C. * · · · · 71
Levy, J. * · · · · 33
Lutchyn,R.M. * · · · · 107
Luther, J.M. * · · · · 17
M *
Machida, T. · · · · 5,i,ii
Mamaluy, D. · · · · 221
Markovic. N. · · · · 119
Maruyama, M. · · · · 153
Matsubara, M. · · · · 151
Matsumoto, K. · · · · i,ii,iv
Miyata, Y. * · · · · 41
Moriyama, S. * · · · · 211
N
Nakamura, F. · · · · 225
Nakamura, M. · · · · 143
Nguyen Thanh, C. · · · · 159

∗ invited speaker

Authour Index　(2/2)

O
Ohno,Y. · · · · 177
Oiwa, A. · · · · 45
Okada, S. · · · · 55
Omachi, H. · · · · 145
Ordonez, R. C. · · · · 15
Orlov, A.O. · · · · 77
Otsuji, T. · · · · 29
P
Park, C. · · · · 163
Park, J. · · · · 205
Petrou, A. · · · · 13
Porod, W. · · · · 125,ii
Pötz, W. · · · · 117,189
R
Rasic, G. · · · · 129
Reed, M. · · · · ii
Richter, C. A. * · · · · 1
Riechert, H. * · · · · ii
Rokhinson, L.P. · · · · 133
Rotkin, S. V. · · · · 103
Ryzhii, V. · · · · 31
S
Sachrajda, A. · · · · 75
Sanari, Y. · · · · 193
Sato, S. * · · · · 59
Scarola, V. · · · · 123
Schäpers, Th. * · · · · 215
Selberherr, S. · · · · 87,i,ii
Semba, K. · · · · 51
Seo, F.J. · · · · 63,171,173,175
Shiraishi, M. * · · · · 85
Shoji, Y. · · · · 197
Sugaya, T. · · · · 23
Sugiyama, M. * · · · · 21
Sverdlov, V. · · · · 93,ii
T
Takaguchi, Y. · · · · 165
Takahashi, N. · · · · 141
Takahashi, R. · · · · 185
Takesue, H. * · · · · 49
Tominaga, J. * · · · · 109
V
A.N. * · · · · 7
Vasileska, D. · · · · 137,223
W
Weinbub, J. · · · · 105,i,ii
Wolkow, R. A. * · · · · 53
Wong, W.S. · · · · 73
Y
Yamaguchi, T. · · · · 147
Yangui, A. · · · · 191
Yoshida, K. · · · · 203
Yoshihara, F. · · · · 213
Yoshikawa, D. · · · · 181
Yoshimura, S. · · · · 167
Youk, S-M. · · · · 199
Z
Zhang, P. · · · · 195
Zhang, X. * · · · · 3
Zhang, Y. · · · · 35
Zhao, H. * · · · · 39
Žutic, I. · · · · 89

∗ invited speaker

978-3-901578-31-1

ISBN 978-3-901578-31-1
9 783901 578311 >